DEGRADATION OF SEAWATER-MIXED CEMENT PASTE: MD SIMULATION OF C-S-H BEHAVIOUR AND EXPERIMENTAL STUDY

UMAR HAYAT

PhD

The Hong Kong Polytechnic University

2026

The Hong Kong Polytechnic University

Department of Civil and Environmental Engineering

Degradation of Seawater-mixed Cement Paste: MD Simulation of C-S-H Behaviour and Experimental Study

UMAR HAYAT

A thesis submitted in partial fulfilment of the requirements for the degree of Doctor of Philosophy

November 2025

CERTIFICATE OF ORIGINALITY

I hereby declare that this thesis is my own work and that, to the best of my knowledge and belief, it reproduces no material previously published or written, nor material that has been accepted for the award of any other degree or diploma, except where due acknowledgement has been made in the text.

_____ (Signed)

Umar Hayat (Name of student)

ABSTRACT

Concrete is the most widely used man-made construction material, serving as the backbone for infrastructure such as buildings, bridges, pavements, pipelines, and dams. However, its substantial demand places unsustainable pressure on freshwater resources, a challenge that is particularly critical in regions where freshwater is already scarce, such as the Middle East, North Africa, and remote islands. In such coastal and island environments, the limited availability of freshwater makes the use of seawater as a mixing water for concrete construction a practical and often necessary alternative. However, the use of seawater as mixing water introduces high concentration of seawater ions into the concrete. While numerous studies have established that seawater typically expedites setting and improves early compressive strength, its long-term durability remains a primary concern for structural service life. This concern primarily arises from the chemical interaction between seawater and concrete due to the presence of multiple aggressive ions in seawater, such as chloride, sulphate, magnesium, and carbonate, which can lead to complex degradation mechanism. Despite extensive research, the mechanistic understanding of these processes, particularly ion transport, interfacial phenomena, and phase degradation at the atomic and macroscale levels, is still inadequate. To address these fundamental knowledge gaps, this thesis employs an integrated approach of molecular dynamics (MD) simulations and long-term experimental studies to elucidate the multiscale mechanisms of ion transport, water stability, and phase degradation in seawater-mixed cement paste. The investigation is structured in four parts.

First, MD simulations used to investigate the atomistic-level ion transport of NaCl within the pores of calcium silicate hydrate (C-S-H) gel, the primary binding phase of hydrated cement paste. The influence of pore size (35-95Å) and temperature (275-350 K) on ionic

transport was thoroughly investigated using a tobermorite-based model. The results indicate that NaCl transport is significantly accelerated by the increase of both pore size and temperature. The smaller pores and high temperature create a filtration effect, facilitating deeper water penetration while limiting the entry of Na^+ and Cl^- ions. Moreover, increased pore size and elevated temperatures accelerate Na-Ca cation exchange, resulting in the release of Ca^{2+} from C-S-H surface.

Building on these transport mechanisms, the second part investigates how the retained water inside C-S-H pores responds to drying, as water stability has a direct impact on ionic mobility and cohesion. This section investigates the desorption of water from NaCl solutions confined within C-S-H gel nanopores, a mechanism that governs drying shrinkage and salt crystallisation in cement-based materials. Both canonical (NVT) and isothermal-isobaric (NPT) ensembles were employed to investigate the underlying mechanisms of water desorption, considering various Ca/Si ratios (1.2, 1.4, 1.6, 1.8, and 2.0). The desorption mechanism was found to be largely independent of the Ca/Si ratio.

To understand how this interfacial ion accumulation directly impacts mechanical performance, the third section investigates the effect of seawater ions on the nanoscale cohesion and mechanical properties of C-S-H, relating transport and desorption to structural performance. MD simulations were used to investigate how interfacial distance and cation type (Na^+, K^+, Mg^{2+}) affect shear cohesion and tensile properties of C-S-H. Results show that pure C-S-H exhibits the highest strength, while partial substitution reduces performance in the order: CSH $\approx$ CSH_Mg > CSH_Na > CSH_K. Shear strength decreases sharply with increasing interfacial distance, vanishing beyond 0.32 nm when water transitions from bilayer to trilayer and becomes mobile. Tensile tests reveal consistent trends, with pure C-S-H displaying superior strength, stiffness, and ductility.

Finally, to understand the degradation mechanism at larger scale, a complementary year-long experimental study was conducted in fourth part that explain how these mechanisms emerge in real seawater cement pastes under aggressive ions exposures. In this study, seawater-mixed cement pastes were exposed for one year to 5% chloride, 5% sulphate, and combined chloride-sulphate solutions containing Na^+, K^+, Ca^{2+}, and Mg^{2+} cations. The phase assemblage, microstructure, and micromechanical properties were systematically investigated using complementary analytical techniques. The results show that chloride attack primarily promotes Friedel's salt formation without severe decalcification, whereas $MgCl_2$ causes significant portlandite (CH) depletion, brucite formation, and C-S-H degradation. Sulphate attack results in extensive formation of ettringite and gypsum, accompanied by calcium leaching, with $MgSO_4$ identified as the most aggressive among the sulphate solutions. The exposure to combined chloride-sulphate solutions intensified these processes, especially the exposure to $MgCl_2$+$MgSO_4$ system causes the most pronounced deterioration.

An improved understanding of seawater-cement interactions across multiple scales will enable the development of predictive models for long-term durability, supporting the design of sustainable concrete for marine infrastructures and contributing to resource efficiency in water-stressed regions.

Key Words: Molecular dynamic simulation; Seawater-mixed concrete; Durability of concrete; C-S-H gel pore; Mass transport; Confined solution

PUBLICATIONS ARISING FROM THE THESIS

The thesis is submitted for the Degree of Philosophy at The Hong Kong Polytechnic University. The work was carried out during the years 2022 to 2025 in the Department of Civil and Environmental Engineering.

Journal papers related to the thesis:

U. Hayat, E. Duque-Redondo, M.-F. Kai, H. Manzano, J.G-Dai. (2025). Desorption of water from aqueous solution confined in C-S-H gel pore: A molecular dynamics study. Construction and Building Materials, 490, 142602.

U. Hayat, M.-F. Kai, H.-B A, J.-X Liew, J.G-Dai. (2024). Atomic-level investigation into the transport of NaCl solution in porous cement paste: The effects of pore size and temperature. Journal of Building Engineering, 86, 108976.

U. Hayat, E. Duque-Redondo, M.-F. Kai, H. Manzano, J.G-Dai. (2025). Influence of seawater ions on nanoscale cohesion and mechanical properties of calcium silicate hydrate (C-S-H). Materials and Structures. Under Review.

U. Hayat, E. Duque-Redondo, M.-F. Kai, H. Manzano, J.G-Dai. (2025). The change of phase assemblage of seawater cement paste subjected to chloride and sulfate attack. (To be submitted).

Conference paper/abstracts

U. Hayat, E. Duque-Redondo, M.-F. Kai, H. Manzano, J.G-Dai. Influence of seawater ions on nanoscale cohesion and mechanical properties of calcium silicate hydrate (C-S-H). 2nd international conference on atomistic simulation of cementitious materials 2025, Nanjing, China

U. Hayat, M.-F. Kai, J.G-Dai, Y. Dong, T. Yu. Evaporation of water from NaCl solution confined in C-S-H gel pore using MD study: Effects of Ca/Si, Ninth Asia-pacific conference on FRP in structures 2024, Adelaide, Australia.

U. Hayat, H. Manzano, M.-F. Kai, J.G-Dai. Understanding the impact of major seawater ions on the chloride transport in cement paste: A molecular dynamic study. 1st international conference on atomistic simulation of cementitious materials 2024, Singapore

U. Hayat, M.-F. Kai, J.G-Dai. Understanding the impact of major seawater ions on the chloride transport in cement paste: A molecular dynamic study. Nanotechnology in Construction Materials - NICOM8, 2024, Catania, Italy

U. Hayat, M.-F. Kai, J.G-Dai. Effect of temperature on the transport of sodium chloride solution in the calcium silicate hydrate gel: A molecular dynamic study. Sixth International Workshop on Seawater Sea-sand Concrete (SSC) Structures Reinforced with FRP Composites 2023, Hong Kong

ACKNOWLEDGEMENTS

Alhamdulillah, all praise to Almighty ALLAH ﷻ, the creator of the universe, for giving me the strength and blessed me with the knowledge to complete this thesis. All respect to the Holy Prophet Muhammad ﷺ, who is the last messenger and whose life is a perfect role model for the whole mankind.

First and foremost, I would like to express my deepest gratitude to my supervisors, Prof. Jian-Guo Dai and Prof. You Dong, for their invaluable guidance, continuous encouragement, and constructive feedback throughout my PhD journey. Their expertise and mentorship have been instrumental in shaping both my academic and professional development. Studying under their supervision is a great honour, and I will forever cherish this experience. I am also sincerely thankful to Dr. Mingfeng Kai for his supervision and guidance on the molecular dynamics simulation work, and to Dr. Muhammad Riaz Ahmad for his constant support, discussions, and encouragement during my research. I also acknowledge the support of my group members, who trained me for many experiments, and Dr. Das for his advice and guidance in completion of experimental work of my PhD thesis (Chapter 6).

I would also like to extend my heartfelt thanks to Prof. Hegoi Manzano, who hosted me as a visiting fellow for six months at the University of the Basque Country (UPV/EHU). His supervision and insightful discussions greatly enriched my research experience in MD simulation, and his constant support and encouragement were invaluable throughout my stay. I am equally grateful to Dr. Eduardo Duque-Redondo for his collaboration and valuable contributions, as well as to other colleagues in Prof. Hegoi's group, whose support and hospitality made my stay both productive and enjoyable.

My sincere appreciation also goes to the Department of Civil and Environmental Engineering, The Hong Kong Polytechnic University, the Head of Department, and the staff of the General Office (GO), Finance Office (FO), Research Office (RO), and Gradate School (GS) for their kind assistance and administrative support. I am truly honoured to have been awarded the PolyU Presidential PhD Fellowship, which enabled me to pursue this research, and I am also grateful for the additional funding that supported my six-month exchange abroad.

I would like to thank my friends in Hong Kong who stood by me during my PhD journey. Special thanks to Dr. Naeem Shahzad for his discussions, guidance, and encouragement, as well as to Dr. Majid Nazeer, Muhammad Waqas, Dr. Imran Mehmood, Dr. Husnain Tansar (USA), Dr. Ghazanfar Ali Anwar (USA), Abdullah, Dr. Abasal Hussain, Hassan Qasim and Gomal Amin for their companionship and support.

I remain grateful to my teachers from both my bachelor's and master's studies, whose guidance laid the foundation for my academic career. I wish to particularly acknowledge my master's supervisor, Prof. Moon-Young Kim (SKKU), and my bachelor's supervisor, Prof. Muhammad Yaqoob (UET Taxila), for their mentorship and encouragement.

I would also like to thank my close friends from Pakistan, especially Khuram Shahzad (XEN Irrigation), Qaisar Abbas (SDO Highway), Mudassar Shah (SDO Highway), Rizwan Khan (SDO Irrigation), Zeshan Akbar (Lecturer, The Superior University Lahore), Rana Dilawar (XEN Public Health), Zahid Abbas, and Zeshan Liaqut for their friendship and support. My appreciation also extends to my friends in Spain for the warm welcome and memorable experiences during my exchange period. I am especially thankful to Dr. Rizwan Ishaq, Dr. Muhammad Zahid Khan, Dr. Ubaidullah, Dr. Irfan Ahmad, Zain Ul Abideen, Dr. Muhammad Asif, and Mukhtar Ahmad for their kindness and companionship.

I owe special thanks to my school teachers who worked tirelessly to guide, support, and encourage me in my early years of education. In particular, I would like to remember and thank Sir Muhammad Riaz, Sir Mubarak Ali, Sir Muhammad Amin, Sir Muhammad Zafar, Sir Qurban Ali, Sir Farooq Ahmad, Sir Nasir Abbas (Faran Model college Jhang), Sir Abdul Jabbar (Faran Model college Jhang), and Sir Asif Mehmood (Faran Model college Jhang) for grooming me and instilling in me the value of hard work.

Finally, I would like to express my deepest gratitude to my parents for their constant prayers, love, and unwavering support throughout my life. Their sacrifices and encouragement have been the foundation of all my achievements, and I sincerely pray for their good health, happiness, and long life. I am also thankful to my sisters and their families for their love, kindness, and encouragement during this journey. My heartfelt thanks also go to my brothers, Sajid Ali (Pakistan Navy), Amir Sohail, Muhammad Mudassir, and Muhammad Asif, who have always stood by me with their advice, support, and encouragement. I would like to dedicate this thesis to my parents, brothers, and sisters in recognition of their endless love and support. I also extend my gratitude to all my relatives and cousins, who have remembered me in their prayers and offered moral support along the way.

Above all, I am profoundly grateful to my wife, whose love, patience, and encouragement have been my greatest source of strength. She stood by me through every challenge of this journey, offering constant support and understanding. Her sacrifices and unwavering belief in me made this PhD possible, and I dedicate this achievement to her with heartfelt gratitude.

TABLE OF CONTENTS

LIST OF FIGURES

LIST OF TABLES

Chapter 1. Introduction

1.1 Background and Significance

Concrete is the most widely used material in the construction industry (Han et al., 2015). Its production consumes 16.6×109 m^3 of freshwater annually, accounting for approximately 18% of annual industrial water consumption worldwide (Miller et al., 2018). This amount roughly corresponds to the annual domestic consumption of 150 million United States citizens. It is projected that by 2050, nearly 75% of the global water demand for concrete production will arise in regions that are expected to face significant water stress (Miller et al., 2018). Against this backdrop, preparing concrete with seawater instead of traditional freshwater offers a potentially sustainable option, particularly for marine and offshore structures. However, the use of seawater in concrete introduces significant amounts of aggressive ions, which can significantly modify the hydration process and alter the microstructural characteristics of concrete (Zhao et al., 2021). These aggressive seawater ions significantly affects both the mechanical properties and durability of seawater concrete (Chang, 2017). Numerous researchers have investigated the effect of seawater on the mechanical properties of concrete, discovering that the use of seawater tends to increase early compressive strength while decreasing setting time (Wegian, 2010, Xiao et al., 2017, Younis et al., 2018, Dhondy et al., 2019, Guo et al., 2020, Khatibmasjedi et al., 2020, Li et al., 2020, Ting et al., 2020, Wang et al., 2020b, Han et al., 2021a, Xie et al., 2022, Ebead et al., 2022a). Despite these mechanical advantages, limited knowledge is available regarding the durability of seawater-mixed concrete.

The durability issues of concrete are closely related to the transport behaviour of chloride and other aggressive ions within the cement matrix (Du et al., 2020, James et al., 2019, Ma

et al., 2020). Mass transport in porous concrete is a complex process involving a series of physical and chemical events, which are far from being fully understood (Cascudo et al., 2021). The ingress of aggressive ions from seawater not only alters the transport behaviour within cementitious matrices but also modifies the nature of hydration products. Reactions with chloride, sulphate, and magnesium ions can produce expansive products such as ettringite, gypsum, or Friedel's salt, while simultaneously promoting decalcification of calcium silicate hydrate (C-S-H). These processes can induce shrinkage or expansion stress, which may ultimately lead to surface cracking, compromising both the aesthetics and the load-carrying capacity of concrete structures. Consequently, evaluating these transport properties is essential for predicting the durability of the concrete structure. In coastal marine environments, cyclic exposure to wetting and drying conditions further contributes to the accelerated deterioration of cement-based materials, an area of substantial interest and ongoing experimental investigation (Ukpata et al., 2019, Cheng et al., 2020, Chen et al., 2022). During the drying process, the desorption of water leads to significant changes in the transport and mechanical characteristics of the material, concurrently inducing a decrease in volume (Yurtdas et al., 2006, Di Bella et al., 2017). The effects of salt solution evaporation within nanoscale pores (below 10 nm) on cement-based materials remain unclear. Moreover, the seawater cations such as Na^+, K^+, and, Mg^{2+}, whether present in pore solutions or introduced from external aggressive environments, significantly influence the hydration kinetics, mechanical properties, and durability of cement-based materials (Jawed and Skalny, 1978, Lindgård et al., 2012, Shi and Lothenbach, 2020, Tang et al., 2021, Liu et al., 2022a, Liu et al., 2022b, Tao et al., 2024, Liu et al., 2024). However, a fundamental understanding of how these seawater cations interact with C-S-H, and how they impact the nanoscale cohesion and mechanical properties of the C-S-H, remains limited.

The main constituent of hydrated cement paste is C-S-H gel, which possesses 60-70% volume fraction of cement paste (Lange et al., 1994). C-S-H has a porous structure with the pores taking approximately 25% of the total volume of C-S-H (Lange et al., 1994). The properties of hydrated cement paste, such as strength development, ionic transport, and volume change in hardened concrete, are significantly influenced by the different types of pores present in it. These voids consist of gel pores (5-100 Å diameter), capillary pores (100-1000 Å diameter), and air voids (Lange et al., 1994). Advanced characterization techniques such as atomic force microscopy and nanoindentation mapping offer significant insights into the microscale mechanical behaviour of C-S-H, particularly its elastic properties (Li et al., 2015b, Ashraf et al., 2016, Zha et al., 2018). However, these approaches are inadequate for investigating the mechanical properties at nanoscale due to constraints such as the dimensions of the indenter tip, which limit efficient probing of the C-S-H layer. To overcome these limitations, atomistic simulations serve as an essential complementary approach, enabling the investigation of cement hydration products at the nanoscale level.

Molecular dynamics (MD) simulations, a mature and powerful computational technique that models atomic-scale interactions using force field-based methods, provide a valuable tool for investigating fundamental atomic-scale processes in cement-based materials (Abdolhosseini Qomi et al., 2014b, Yu et al., 2022, Barbhuiya and Das, 2023, Abdolhosseini Qomi et al., 2021). Previous MD studies have investigated the transport behaviour of different salt solutions through nanopores within cement-based materials (Jiang et al., 2017, Zhang et al., 2017, Yang et al., 2018, Zhou et al., 2018, Hayat et al., 2024). These investigations have consistently shown the weak adsorption of Cl^- ions onto the C-S-H surface with low Ca/Si ratios, which is attributed to repulsive interactions

between the Cl^- and C-S-H surface (Pan et al., 2010, Duque-Redondo et al., 2018, Liu et al., 2020, Duque-Redondo et al., 2022a, Honorio et al., 2022). In contrast, strongly adsorbed cations (i.e., Na^+, Ca^{2+}, Mg^{2+}, K^+, and Cs^+) were found to enhance the adsorption of Cl^- ions by forming stable ionic pairs (Hou and Li, 2014, Zhou et al., 2016). MD simulations were used to calculate the diffusion coefficients of Cl^- ions and cations, determining that these coefficients depend on factors such as pore size, solution concentration, and the force field employed (Pan et al., 2010, Zehtab and Tarighat, 2016, Hou et al., 2017a, Li et al., 2017a, Liu et al., 2020, Duque-Redondo et al., 2021a, Duque-Redondo et al., 2021b). Additionally, atomistic simulations have extensively investigated the elastic and mechanical properties of C-S-H, analysing its response to tensile and shear stresses, as well as the influence of temperature, water content, or chemical replacements (Hou et al., 2014b, Fan and Yang, 2018, Liang, 2020, Hou et al., 2021, Sun et al., 2021a, Zhang et al., 2021b, Wang et al., 2024). Despite these advances, little attention has been paid to the role of pore size and temperature on NaCl solution transport and local structure within C-S-H nanopores. Even less is known about the desorption of confined NaCl solutions in C-S-H nanopore, where the interplay between nanostructure, water content, and evaporation dynamics is critical for predicting drying shrinkage in cement-based materials. Furthermore, nanoscale mechanisms governing the mechanical degradation of C-S-H in seawater environments remain poorly understood. Addressing these questions is essential for developing a complete atomistic picture of transport and degradation in seawater-mixed cementitious systems. Upscaling these atomistic insights with macroscale durability performance is vital, as nanoscale processes ultimately govern cracking, phase stability, and service life in concrete exposed to marine environments. This multiscale understanding will provide the foundation for predictive models and more durable

cementitious materials suitable for sustainable construction in water-scarce and coastal regions.

1.2 Research Aims and Objective

This thesis presents a comprehensive investigation at both the nanoscale and macroscale to understand the behaviour of seawater-mixed cementitious systems. At the nanoscale, MD simulations are used to investigate ion transport, confined water behaviour, and the degradation mechanisms of C-S-H. At the macroscale, experiments are conducted to assess the durability of seawater-mixed cement pastes exposed to chloride and sulphate solutions. The main objectives of the thesis are given below:

(1) To understand the transport behaviour of NaCl solutions in C-S-H nanopores using MD simulations, with emphasis on the impact of pore size and temperature on ion transport, clustering, and interfacial interactions.

(2) To investigate the desorption and evaporation of confined NaCl solutions in C-S-H pores under different thermodynamic conditions, and to determine the influence of pore shrinkage and Ca/Si ratio on structural evolution and ionic distribution.

(3) To examine nanoscale mechanisms governing the mechanical degradation of C-S-H in seawater environments. Specifically, the influence of seawater cations (Na^+, K^+, and Mg^{2+}) on nanoscale cohesion and mechanical properties of C-S-H as a function of ions chemistry and interfacial distance.

(4) To assess the long-term durability of seawater-mixed cement pastes subjected to chloride, sulphate, and combined chloride-sulfate attack, and characterise the resulting phase evolution, microstructural changes, and micromechanical properties.

1.3 Scope of thesis

This thesis consists of 7 chapters, and the overall structure of thesis is shown in Figure 1.1. Chapter 1 provides the general background of seawater-mixed concrete, describes the research motivations that drive this study and clearly specifies the purpose and objectives of the thesis. Chapter 2 provides an extensive review of the existing literature on the use of seawater in cementitious materials. This includes a discussion on the effects of seawater on hydration mechanisms, microstructural evolution, and mechanical properties, as well as its implications for long-term durability. In addition, the chapter examines the structural characteristics of C-S-H and summarizes the different models that have been developed to describe its nanostructure and morphology. Chapter 2 also describes computational methods, with a particular focus on MD simulations. It describes the theoretical basis of MD, the force fields used, and the modelling methods. Chapter 3 examines the transport of NaCl solutions in C-S-H nanopores, specifically the impact of pore size and temperature in controlling ion transport and interfacial interactions. Chapter 4 extends this work by focusing on the desorption and evaporation of confined NaCl solutions within C-S-H nanopore. In Chapter 5, we look at how cations like Na^+, K^+ and Mg^{2+} affect the mechanical degradation of C-S-H. Chapter 6 shifts the focus to the macroscale, presenting experimental investigations on the durability of seawater-mixed cement pastes exposed to chloride, sulfate, and combined chloride-sulfate attack. Finally, Chapter 7 summarises the overall findings of the research and makes recommendations for future research.

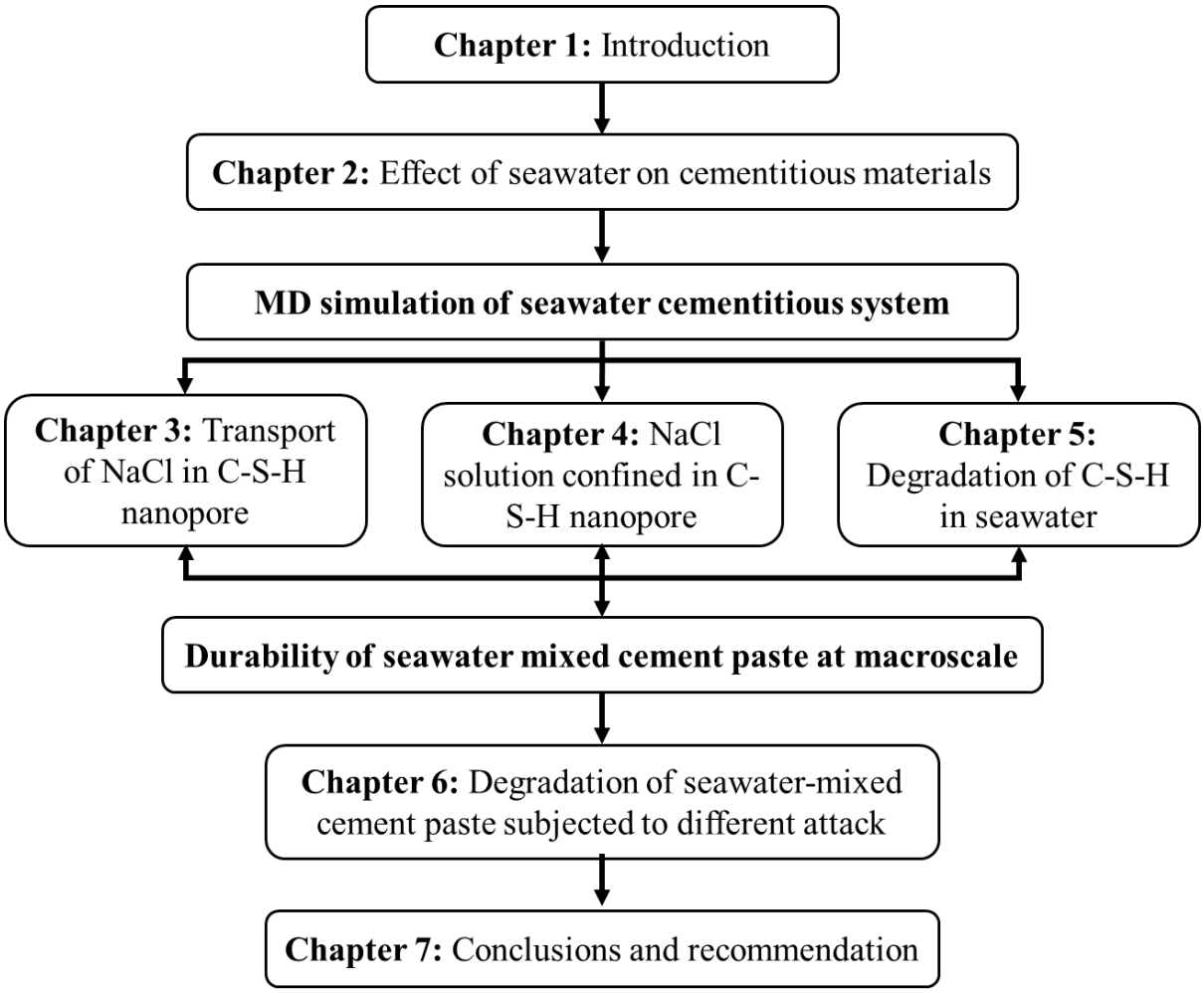

Figure 1.1. Framework of the dissertation.

Chapter 2. Literature Review

2.1 Introduction

Seawater-mixed concrete refers to concrete prepared by replacing seawater for the freshwater normally used in the mixing process. Concrete production annually consumes 16.6×10^9 m^3 of freshwater, which accounts for approximately 18% of annual industrial water consumption worldwide (Miller et al., 2018). This amount roughly corresponds to the annual domestic consumption of 150 million United States citizens. Miller et al., projected that by 2050, nearly 75% of the global water demand for concrete production will arise in regions that are expected to face significant water stress (Miller et al., 2018). Seawater-mixed concrete presents a potential alternative for marine and offshore applications, as it has been reported to achieve higher strength development compared with conventional freshwater concrete (Khatibmasjedi et al., 2020).

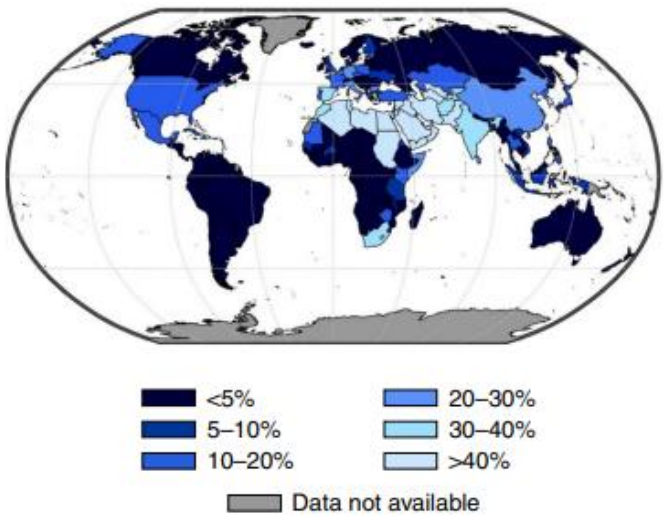

Figure 2.1. The ratio of water withdrawal to renewable water resources indicates water stress (Miller et al., 2018).

The use of seawater for mixing and curing concrete is not a novel concept, and the ancient Romans may have pioneered it by combining lime, volcanic ash, and zeolitic tuff with seawater to produce a matrix that demonstrated greater long-term stability compared with conventional concrete (Jackson et al., 2012, Jackson et al., 2013). The hydration products of Roman concrete differed substantially from those of modern cementitious systems, largely due to the influence of alkali cations present in both ash and seawater, as well as the high reaction temperatures involved. Furthermore, research has indicated that mixtures containing little or no Portland cement, but incorporating high-alumina natural pozzolans combined with seawater, could act as sustainable and durable analogues of Roman concretes (Oleson et al., 2006). Therefore, a deeper understanding of the chemistry and technology underlying both Roman concrete and seawater-mixed modern systems may therefore provide valuable guidance for designing more resilient and sustainable concrete today.

A significant difference between ancient and modern concrete lies in the use of steel reinforcement, which raises concerns about potential steel corrosion when using seawater (rich in chloride) in modern concrete. The chloride concentration in seawater is approximately 20,000 ppm, and its use in mixing can result in chloride concentrations between 0.5 and 1.5% by mass of cement, based on the mixture proportions (Montanari et al., 2019). For this reason, the application of seawater in reinforced concrete is generally discouraged due to the risk of premature steel corrosion. However, the use of seawater remains feasible for unreinforced concrete elements. Furthermore, recent advancements in non-corrosive reinforcement, such as fibre-reinforced polymers (FRP), have demonstrated that seawater-mixed concrete reinforced with FRP is a viable and durable alternative (Xiao et al., 2017).

(a) Installation of sensors on GFRP bars (b) Casting of SSC

(c) Bridge using GFRP reinforced SSC

Figure 2.2. Application of SCC (Xiao et al., 2017).

2.2 Effect of seawater on hydration reactions and microstructural development

2.2.1 Influence of seawater on hydration reactions

Several studies have reported that seawater accelerates the early hydration of cement, leading to a shorter induction period as well as an earlier and more pronounced heat evolution peak (Thomas et al., 2011, Li et al., 2020, Yaseen et al., 2020, Li et al., 2021, Zhao et al., 2021). When compared with cement paste prepared using freshwater, seawater-mixed cement paste has been shown to exhibit a 35-40% higher silicate peak, a 15-30% earlier occurrence of the silicate peak, a 5-10% increase in cumulative heat release at 3 days, and a similar level of heat release at 7 days (Wang et al., 2018, Li et al., 2021).

Figure 2.3 schematically illustrates the influence of seawater on cement hydration heat flow.

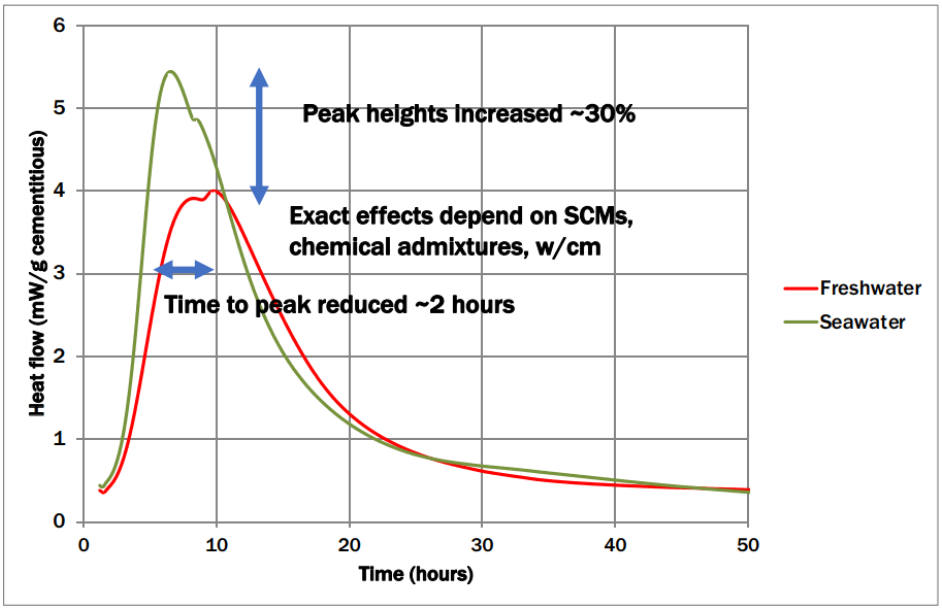

Figure 2.3. Influence of seawater on cement hydration heat flow (Ebead et al., 2022a).

The acceleration of tricalcium silicate (C_3S) hydration has been linked to the presence of multiple dissolved ions in seawater. Experimental investigations have consistently confirmed this enhanced reactivity (Sun et al., 2021b). The proposed mechanism suggests that calcium hydroxide formed during hydration interacts with seawater ions, raising the pore solution pH and promoting additional gypsum formation. In addition, the interaction of sodium hydroxide with salts in seawater generates extra calcium hydroxide, further contributing to the acceleration process (Yaseen et al., 2020).

$$3Ca(OH)_2 + 3Na_2SO_4 \rightarrow 3CaSO_4 + 6NaOH \quad (2.1)$$

$$CaCl_2 + 2NaOH \rightarrow Ca(OH)_2 + 2NaCl \quad (2.2)$$

2.2.2 Pore solution in seawater-mixed cement

Few studies have investigated the effects of seawater on the pore solution in cement pastes (Montanari et al., 2019). In seawater-mixed pastes, the concentrations of Na^+ (10 times) and Cl^- (1000 times) are significantly higher than in freshwater-mixed pastes as shown in Figure 2.4. K^+ concentrations remain unchanged, while OH concentrations increase slightly. Cl concentrations fall, specifically between 12 h and 3 days due to Cl binding and the possibility of Cl participation in hydration reactions (Sun et al., 2021b). Na and OH concentrations rise as hydration progresses as water is consumed. At 28 days, the chloride content of cement is 0.67% by mass of cement (Wang et al., 2018), which is high for the safe use of steel reinforcement. Pore solution analyses have been employed to estimate ionic uptake, indicating approximately 5 mg of chloride per gram of C-S-H and 2 mg of sodium per gram of C-S-H. Similar patterns have been observed in alite-salt systems with high water/binder ratios, where chloride concentration decreased by around 20% between 6 hours and 28 days, with majority of this reduction occurring within the first 24 hours (Sun et al., 2021b).

Incorporating seawater into cement paste increases pore solution pH by 0.15 units and ionic strength by nearly fourfold, due to increased Na^+ and Cl^- concentrations. This modification also reduces the electrical resistivity of the pore solution by about 50% (Montanari et al., 2019). Higher ionic concentrations may cause leaching when exposed to groundwater or rainfall; nevertheless, persistent seawater exposure can limit additional entry and leaching, thereby boosting long-term strength (Montanari et al., 2019, Khatibmasjedi et al., 2020). However, the greater alkalinity of seawater is likely to exacerbate alkali-silica interactions in seawater-mixed concrete.

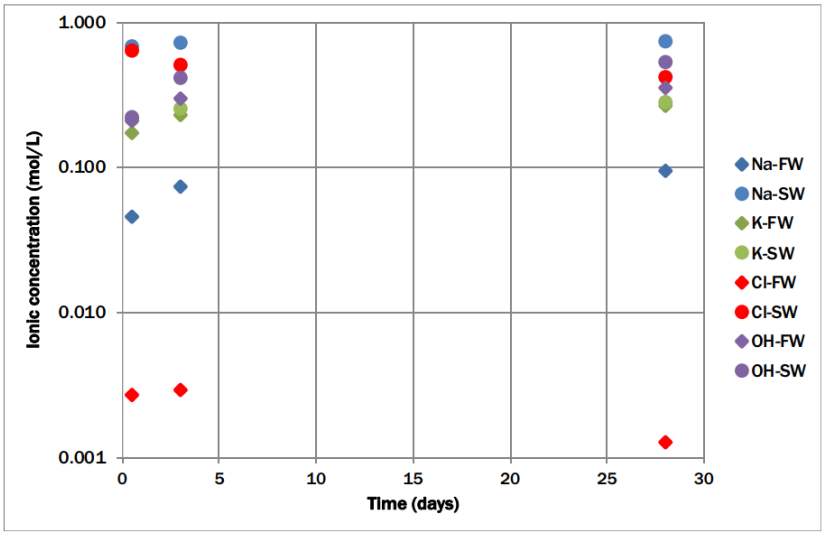

Figure 2.4. Ionic composition of pore solution in freshwater (FW) cement paste and seawater (SW) cement pastes (Ebead et al., 2022a).

2.2.3 Influence of seawater on microstructure

A range of quantitative techniques such as dynamic vapor sorption, mercury intrusion porosimetry, Brunauer, Emmons, and Teller (BET) theory, and nitrogen adsorption for specific surface area have been used to study pore size distributions in seawater-mixed cement pastes (Wang et al., 2018, Montanari et al., 2019, Li et al., 2020, Li et al., 2021). Seawater reduces porosity and refines pore sizes. The effect is most pronounced at early ages (within the first three days), when hydration progresses differently in seawater and freshwater systems, whereas the influence becomes less significant at later stages of hydration (Montanari et al., 2019, Khatibmasjedi et al., 2020, Li et al., 2021).

Seawater influences the pore characteristics of cement pastes by altering the morphology of the hydrates, leading to the development of nanocrystals closely integrated with the C-S-H matrix phases, which increases the BET surface areas. The formation of high Ca/Si C-S-H and Friedel's salt have also been proposed as causes of microstructure densification in seawater-mixed cement pastes (Li et al., 2018). Scanning electron microscopy (SEM) and

transmission electron microscopy (TEM) analyses have shown that seawater promotes the development of C-S-H with higher surface areas. Correspondingly, the BET surface area of seawater-mixed cement pastes was found to be nearly twice that of pastes prepared with freshwater (Wang et al., 2018, Li et al., 2021, Zhao et al., 2021). Several authors have observed a reduction in porosity and a refinement of pore structure (Wang et al., 2018, Montanari et al., 2019, Khatibmasjedi et al., 2020), both of which are indicative of microstructural densification. The formation of Friedel's salt has been identified by SEM and EDX (Wang et al., 2018, Li et al., 2020), while TGA results further confirm its presence at early stage, with the amount increasing by three days (Montanari et al., 2019).

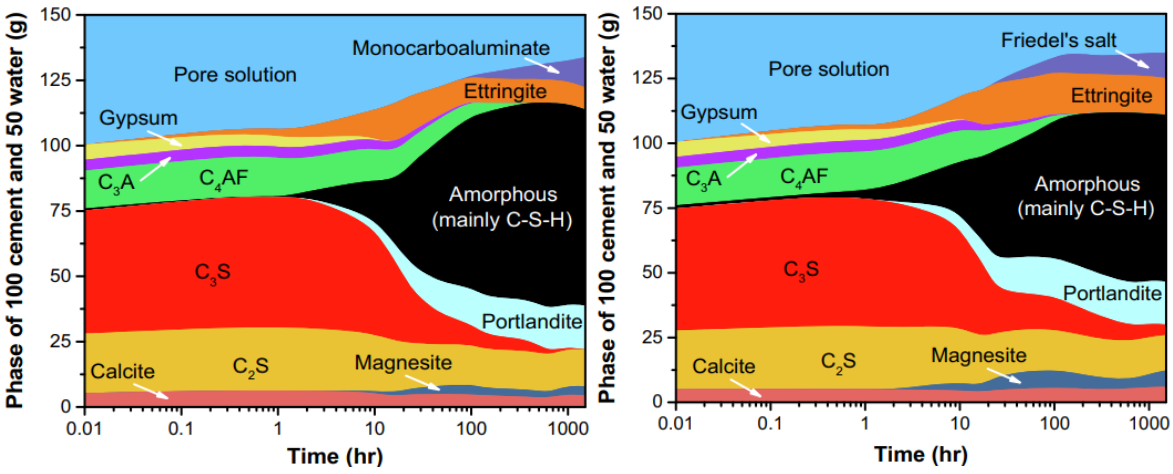

(a) OPC hydrated in distilled water (b) OPC hydrated in seawater

Figure 2.5. Phase evolution of hydrated OPC in seawater and distilled water (Li et al., 2020).

EDX analysis verifies the high concentrations of Na^+ and Cl^- ions in seawater concrete, as well as the chloride sorption in the C-S-H phase (Younis et al., 2018, Li et al., 2020). The amount of Friedel's salt formed in seawater-mixed concrete may vary based on conditions of curing and the application of SCMs at later ages (Wang et al., 2018, Montanari et al.,

2019, Li et al., 2020). In C_3S pastes containing seawater, crystal growth of calcium hydroxide with a hexagonal platelet morphology was observed (Yaseen et al., 2020). In seawater mixed pastes, the C-S-H gel typically develops as a dense cluster that extends outward from the grain surface and is interlinked with needle-shaped gypsum crystals. TEM observations of alite hydration in the presence of seawater ions reveal an increase in the average length of early-age C-S-H fibres, a feature associated with accelerated hydration. Complementary NMR analyses indicate a longer mean silicate chain length and a higher degree of polymerization at early ages, which may explain the development of these elongated fibres (Sun et al., 2021b). XRD, FTIR, and TGA collectively confirm that presence of seawater accelerates the formation of different hydration phases, promotes Friedel's salt formation, and changes in the nature of hydration products at early ages, but their influence appears to be less significant at later stages of hydration (Wang et al., 2018, Montanari et al., 2019, Li et al., 2020, Yaseen et al., 2020, Cai et al., 2021).

2.3 Fresh and hardened properties of SSC

2.3.1 Fresh properties

Extensive research on the fresh properties of seawater concrete and cement pastes indicates that seawater incorporation has only a limited effect, regardless of the mixture composition (Younis et al., 2018, Wang et al., 2020b). Density of seawater mixed concrete is slightly higher (2-3%) as compared to fresh water mixed concrete (Younis et al., 2018). Changes in the ionic composition and surface tension of seawater can alter the rheology and workability of cement paste, thereby altering its fresh properties (Wang et al., 2020b). Seawater is denser and more viscous than freshwater, resulting in a stiffer mixture and lower slump values (Younis et al., 2018). Due to the presence of ions that speed up the hydration process, the use of seawater can also result in reducing initial and final setting

times (Wang et al., 2018, Montanari et al., 2019). However, the use of superplasticizers has been shown to mitigate the influence of seawater on cement paste workability and to significantly improve its flow characteristics (Li et al., 2019).

2.3.2 Mechanical properties

Research on seawater concrete has predominantly focused on strength development and corrosion-related concerns. Results indicate that seawater can enhance early-age compressive strength by approximately 4-23%, primarily due to accelerated hydration, pore structure refinement, and the formation of hydrates with altered microstructural characteristics (Wegian, 2010, Xiao et al., 2017, Younis et al., 2018, Dhondy et al., 2019, Guo et al., 2020, Khatibmasjedi et al., 2020, Li et al., 2020, Ting et al., 2020, Wang et al., 2020b, Han et al., 2021a). Some long-term studies demonstrate comparable strengths, while others demonstrate slight decreases or increases (Khatibmasjedi et al., 2020). However, the long-term effect on mechanical properties is relatively negligible, as the seawater-induced hydration acceleration does not persist beyond three days. Under conventional curing conditions, such as storage in a fog room, seawater concrete may show a slight reduction in long-term strength compared with conventional concrete, primarily because of hydrate leaching. However, evidence suggests that in actual marine environments, its long-term performance can be superior, owing to the reduced ingress of seawater and lower leaching rate (Khatibmasjedi et al., 2020). Figure 2.6 depicts a schematic of the development of concrete's strength when mixed with seawater.

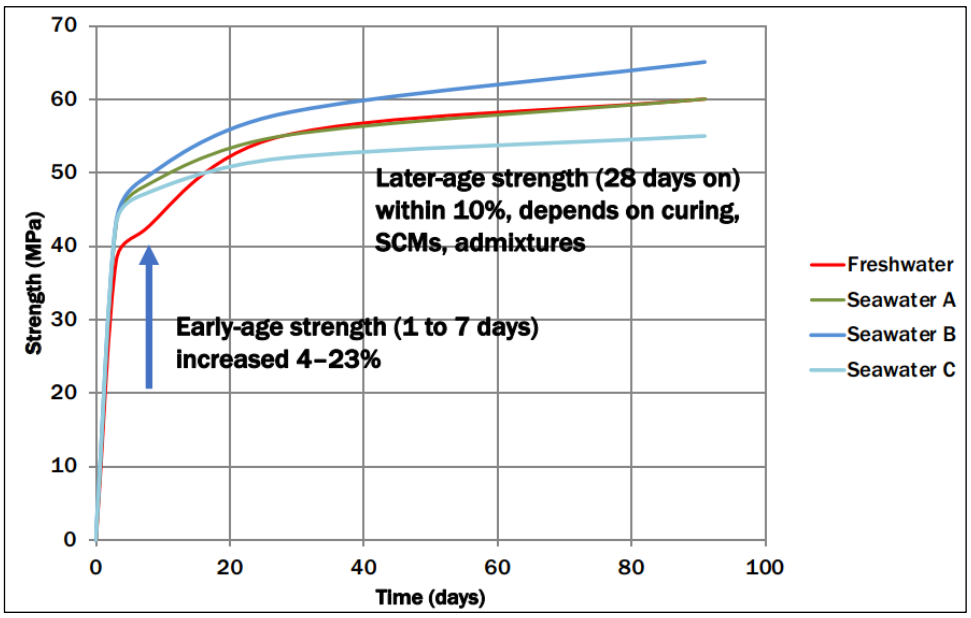

Figure 2.6. The impact of seawater on the early and late age compressive strength of concrete (Ebead et al., 2022a).

2.4 The durability of seawater mixed concrete

The durability of seawater concrete is affected directly or indirectly due to the modification of the microstructure. The following section compares the research on the durability of seawater concrete to that of freshwater concrete.

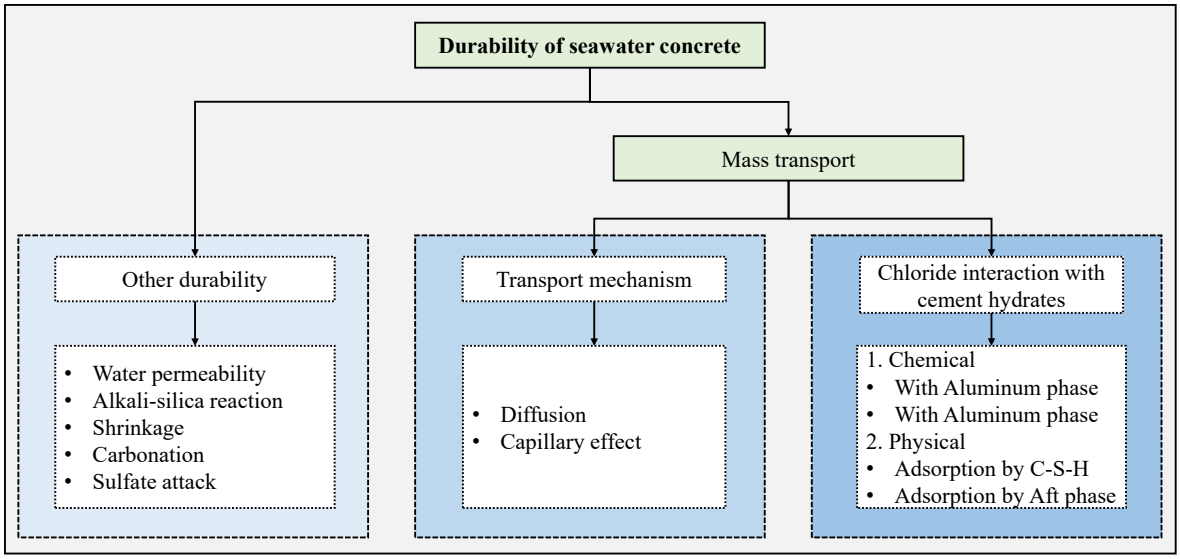

Figure 2.7. Schematic illustration for the durability of seawater-mixed concrete.

2.4.1 Mass transport

2.4.1.1 Mechanisms of chloride transport in cementitious materials

Since the 19th century, researchers have examined chloride transportation, a mass transport process (Middleman, 1997, Basmadjian, 2003). This phenomenon is relevant in a wide range of processes, such as diffusion, leaching, distillation, and drying making it a fundamental subject in multiple disciplines. Existing mass transport knowledge provides a solid foundation for comprehending chloride transport. Since the 1980s, the durability of concrete structures exposed to chloride-rich environments has been a major problem. This issue is largely related to the enormous marine infrastructure built in the 1940s, many of which began to deteriorate after decades of service, necessitating destruction. As a result, chloride transport in concrete has become a major focus of global research, leading to a constantly deeper understanding of the mechanisms driving this process. (Shi et al., 2019).

Chloride ions can infiltrate concrete in two primary ways: from the concrete ingredients themselves, known as internal chlorides, or from an external source such as seawater or de-icing salt, known as external chlorides (Yuan, 2009, Trejo et al., 2018). Limiting the chloride content of concrete raw materials makes it possible to limit the amount of internal chlorides. Managing chloride concentration in the environment is not possible. Durability of reinforced concrete in chloride environments depends significantly on chloride ion penetration and subsequent corrosion of embedded steel. Consequently, chloride transport in concrete is of considerable interest. Chloride transport is difficult to comprehend due to the intricate physical and chemical processes involved, despite the numerous studies conducted on the subject. According to the 2012 study by Tang and Nilsson, at least three variables contribute to this complexity (Luping et al., 2012).

- Concrete structures in marine environments are subject to highly variable environmental conditions. Although the chloride concentration in seawater remains relatively consistent across different regions, the extent of deterioration in concrete structures varies considerably depending on the exposure zone, including fully submerged, splash, marine fog and tidal environments. These zones vary in chloride concentration and water saturation. Consequently, the degree of concrete deterioration varies between sections.
- The complexity of concrete structures and their changing compositions over time is considerable. Modern concrete contains a variety of components, including cement, sand, mineral and chemical admixtures, and aggregates. Owing to this diversity of materials, the interactions among the different components are often complex, and the quality of the raw materials can vary significantly.
- In engineering applications, the movement of chloride ions occurs slowly and involves complex physical and chemical interactions via a variety of mechanisms. Current testing methods may not accurately represent the actual chloride ion transport process, as our understanding of these transport mechanisms remains incomplete. This is due to the difficult-to-replicate complex interaction of environmental factors such as temperature fluctuations, rainfall, and sunlight exposure.

From a physics perspective, the movement of matter can generally be classified into two main categories.

Transport by concentration gradients: According to the fundamental principles governing their transport, a driving potential induces the flow of mass, energy, and

electricity. Gradients can be represented in two general ways (Basmadjian, 2003). Gradients can take on a variety of forms. One is a situation in which the gradient changes in the same direction as the flow, as in diffusion or conduction. For example, ions or molecules diffuse into a matrix due to concentration variations, where the gradient changes with depth, resulting in a non-uniform pushing force. In contrast, there are circumstances where the driving gradient is constant regardless of flow direction. A common example is an applied electric field, in which the driving power is given as potential divided by distance. Under these conditions, when an electric field is given to a sample, its magnitude remains constant throughout the specimen's depth.

Non-gradient-driven transport: Capillary action, also known as capillary motion or wicking, is a distinct type of non-gradient-driven transport. Unlike most transport mechanisms, which rely on concentration or potential gradients, capillary action enables a liquid to travel through narrow spaces without external aid and even against gravity. This phenomenon results from intermolecular interactions between the liquid and solid surfaces. When the pore sizes are small enough, surface tension mixed with adhesion forces between the liquid and pore walls pulls the liquid into the pore. (Shi et al., 2019).

In close proximity to salt water, chloride conditions can be complex and severe for concrete structures. Based on their interaction with seawater, these structures can be divided into three exposure zones: immersed, tidal, and atmospheric. In the atmospheric zone, concrete is exposed to chloride-bearing fog, resulting in the typically unsaturated precipitation of chloride ions on the structure. The tidal zone subjects concrete to repeated wetting and drying cycles, accelerating chloride ingress and often causing severe deterioration. For structures in the immersed zone, where concrete remains fully saturated,

chloride primarily diffuses into concrete. Despite the high chloride concentration in seawater-immersed concrete, steel corrosion is uncommon due to the lack of oxygen.

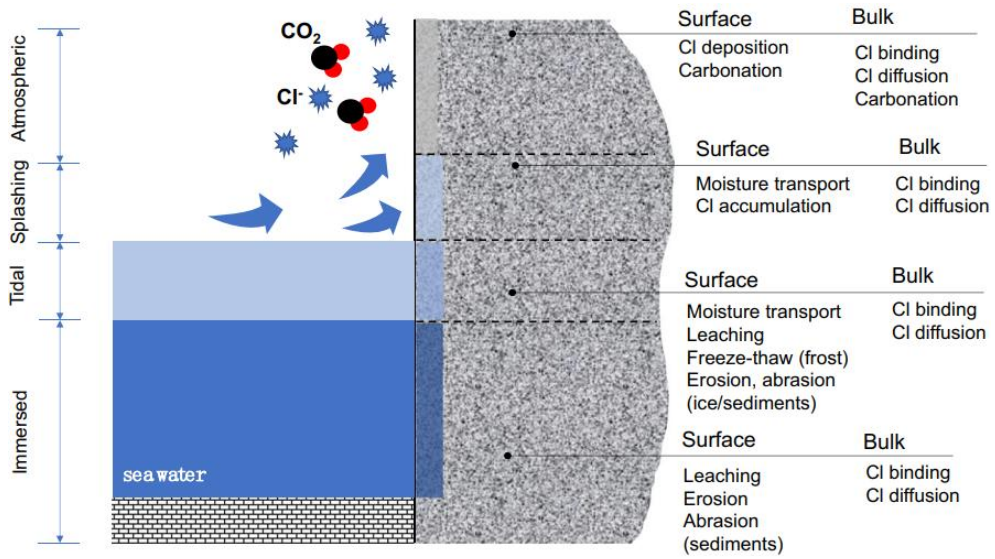

Figure 2.8. Durability of concrete in sea environments (Li et al., 2022).

2.4.1.2 Chemical interaction between chlorides and hydration products

Chloride binding is the process by which Cl^- from external solutions penetrate concrete and are then captured by hydration byproducts. This phenomenon has a significant impact on the durability of structures made from reinforced concrete. When analysing the movement of Cl^- within concrete, it is essential to account for Cl^- binding. Given that concrete is a porous material consisting of both liquid and solid constituents, mass transfer through the solid components is minimal compared to that within the pores. In saturated concrete, transport is predominantly determined by the movement of mass through the pore solution, whereas in unsaturated situations, suction takes precedence. The infiltration of Cl^- from external sources is one of the most crucial elements affecting the durability of reinforced concrete in most service situations (Shi et al., 2019).

The chemical binding of chlorides frequently results from the interaction of chlorides with C_3A or the AFm phase, forming Friedel's salt or a similar compound through a reaction with C_4AF. The adhesion of chloride ions to the C-S-H surfaces is responsible for the physical binding. In cementitious materials, Cl^- can be captured by a variety of hydration products, including C-S-H gel, Friedel's salt, HO-AFm, $Ca(OH)_2$, and SO_4-AFm, with varying Cl^- binding capacities observed across studies. The aluminum phase (C_3A and C_4FA) content typically governs Cl^- binding in in Cl^- containing systems. Cl^- binding is primarily due to the AFm phase's chemical binding and the C-S-H gel's physical adsorption when external chloride is introduced (Shi et al., 2019).

2.4.1.3 Physical adsorption of chlorides by hydration products

Adsorption of chlorides by C-S-H

Most studies found that Cl^- binding on the C-S-H's surface was the most crucial aspect of physical adsorption (Diamond, 1986, Ye et al., 2016, Shi et al., 2017). The structural properties of C-S-H before and after interaction with Cl^- were examined. The research revealed that Cl^- adsorption did not affect the structural characteristics of the C-S-H (Hirao et al., 2005). The relationship between Cl^- and C-S-H in aluminum-free systems was analysed. The research revealed that a higher w/c ratio of the C-S-H facilitated the interaction between the Cl^- and the gel (Zibara et al., 2008). Although the interaction of Cl^- with C-S-H is less pronounced than their binding with aluminum-bearing phases, the adsorption of chloride by C-S-H remains important because of the substantially larger volume of C-S-H compared to other hydration products.

It was found that most physically adsorbed Cl^- were attracted to the ion-exchange sites of C-S-H, and the majority of these interactions were reversible (Luping and Nilsson, 1993).

This indicates that the desorption of Cl^- from exchange sites may occur when the Cl^- concentration in the pore solution decreases. The Cl^- adsorbed on the surface of the C-S-H could move from one region to another in response to a concentration gradient but at a significantly slower rate than in the pore solution. The interaction between Cl^- and C-S-H was classified into three categories: within the chemical adsorption layer of the C-S-H, penetrating the interlayer of the C-S-H, and being strongly bound within the C-S-H lattice (Ramachandran, 1971). It was also found that the surface potential of C-S-H, which was typically influenced by the Ca/Si ratio of the C-S-H, could be positive with a high Ca/Si ratio (Monteiro et al., 1997). The positively charged surface of the C-S-H could then attract and adsorb anion ions from the pore solution.

Adsorption of chlorides by Aft phase

It is demonstrated that Cl^- could be adsorbed by the AFt phase, even at low chloride ion concentrations (Birnin-Yauri and Glasser, 1998). Nonetheless, experimental confirmation of this hypothesis is lacking. The Cl^- binding capacity of the AFt phase was investigated, and it was determined incapable of binding with chloride ions from external solutions (Hirao et al., 2005). In addition, the structure of the AFt phase was unaffected by exposure to a chloride solution. The Cl^- binding capacity of the AFt phase was discovered to be intermediate between that of Friedel's salt and C-S-H (Elakneswaran et al., 2009). Discrepancies in these studies, such as differences in Cl^- concentration and the reversibility of physical adsorption, may account for the divergent results. The AFt phase present in cement can transform into Friedel's salt when exposed to high concentrations of Cl^- (Hirao et al., 2005). The amount of AFt phase in cement is significantly less than that of C-S-H, so the AFt phase's Cl^- binding capacity can be largely disregarded.

2.4.1.4 Chloride penetration resistance

Multiple researchers have investigated the resistance of concrete to chloride penetration using the Rapid Chloride Penetration Test (RCPT) in accordance with the ASTM C1204 standard. This test measures the amount of electrical charge that successfully traverses the test sample. Seawater concrete typically shows less chloride permeability than freshwater concrete when exposed to external chloride, primarily due to the difference in chloride concentration gradients (Li et al., 2017b). Previous research has demonstrated that seawater concrete exposed to seawater has a lower Cl^- diffusion coefficient than freshwater concrete with a higher W/B (0.55) ratio (Mohammed et al., 2004). This difference, however, becomes negligible at lower W/B (0.45) ratios, presumably due to improvements in the concrete's microstructure that counteract seawater's effects on chloride penetration.

SCMs have a significant impact on the chloride diffusion coefficient of seawater concrete (N. Otsuki, 2014, Shi et al., 2015). In seawater concrete, substituting 70% of the cement with GGBS at a W/B ratio of 0.5 can reduce the chloride diffusion coefficient by 20% more than in freshwater concrete (N. Otsuki, 2014). Incorporating 30% FA had less of an effect on seawater concrete than on freshwater concrete due to the low C_3A content of FA, which reduces the hydration acceleration effects of seawater. Experiments revealed that the use of MK at concentrations ranging from 0% to 6% reduces chloride permeability in seawater concrete significantly more than in freshwater concrete (Li et al., 2015a, Shi et al., 2015). In accordance with ASTM C1204 standards, concrete containing 10% MK and 10% GGBS reduced the total charge passing through the concrete to a remarkably low level (Cheng et al., 2018).

In comparison to Natural Coarse Aggregate (NCA), the use of Recycled Concrete Aggregate (RCA) in seawater concrete significantly increased the electric flux (Etxeberria and Gonzalez-Corominas, 2017). The complex composition and high conductivity of the

pore solution may, however, affect the testing validity of ASTM C1202 for seawater concrete. It is important to note that only a limited number of studies have focused on durability aspects.

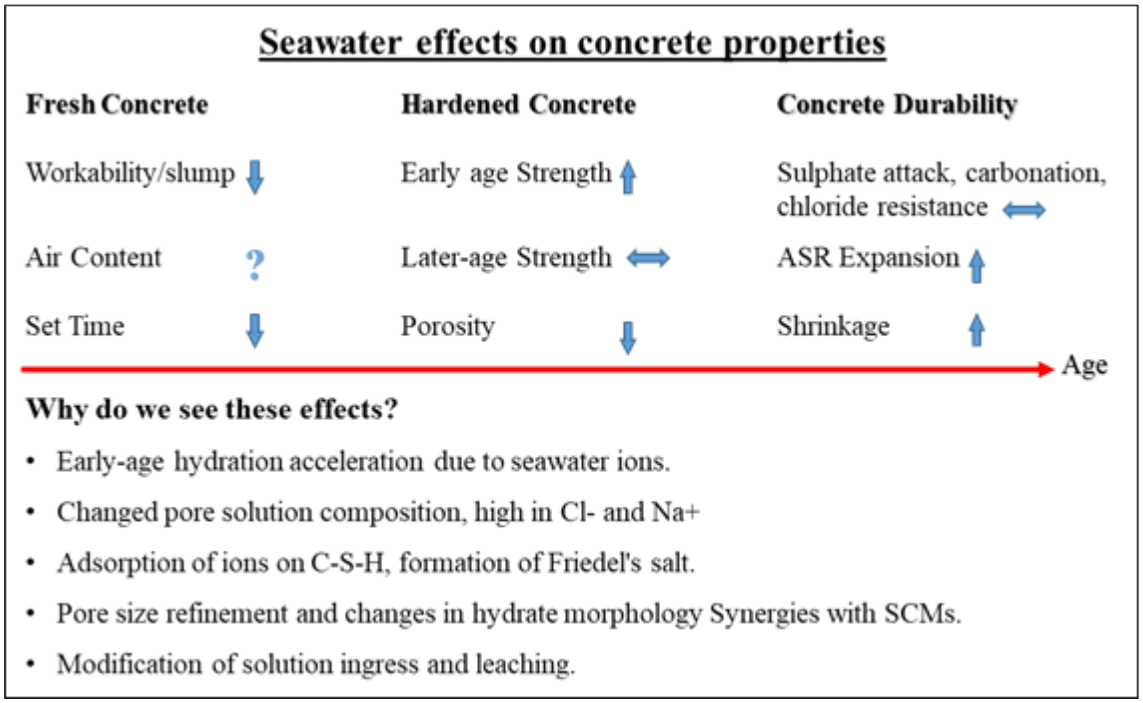

Figure 2.9. Micro- and macro-scale effects of seawater on concrete properties across different ages (Ebead et al., 2022b)

2.4.2 Other relevant durability

2.4.2.1 Water permeability

The permeability of seawater-based concrete is typically lower than that of conventional concrete (K. Katano, 2013, Etxeberria et al., 2016). It was found that the water penetration depth in seawater concrete was 25 mm, which is less than the 32.5 mm depth in freshwater concrete after a 7-day seawater curing (Abdel-Magid et al., 2016). Katano and colleagues (K. Katano, 2013) came to the same conclusion, observing that the coefficient of water permeability for seawater concrete was half that of freshwater concrete. They attributed

this improved impermeability to the increased formation of ettringite and Friedel's salt within the seawater concrete, which blocked pore pathways and improved the pore structure. In contrast, Zhang et al. (Zhang et al., 2013a) found that the SSSC's permeability was almost identical to that of conventional concrete. The disparate results are likely attributable to different water-to-binder (W/B) ratios and the seawater and sea-sand salinity levels utilized in the respective studies.

Supplementary Cementitious Materials (SCMs) such as Ground Granulated Blast-furnace Slag (GGBS) and chemical additives such as calcium nitrate are known to improve the impermeability of concrete by refining its pore structure (K. Katano, 2013, Etxeberria et al., 2016). As shown in Figure 2.10, concrete samples have a certain capacity for capillary absorption. A lower capillary absorption capacity corresponds to decreased water permeability, thereby increasing the permeation resistance of the concrete. GGBS significantly reduces seawater concrete's water absorption by increasing hydration products, gel materials, and decreasing the concrete's porosity. According to a study by Katano et al. [55], the addition of GGBS, Fly Ash (FA), and calcium nitrate reduced the water permeability of seawater concrete to approximately 1/70th that of freshwater concrete (K. Katano, 2013). In addition, it was reported that when Recycled Concrete Aggregate (RCA) is utilized, the increase in capillary absorption capacity in SSSC is less than in conventional concrete due to the combined effects of seawater and RCA (Etxeberria et al., 2016). The pozzolanic reaction between GGBS, which is high in calcium, and seawater, which is high in alkalinity, assists in mitigating the increased capillary absorption capacity resulting from using RCA (Yamamoto, 2017, Adiwijaya et al., 2017).

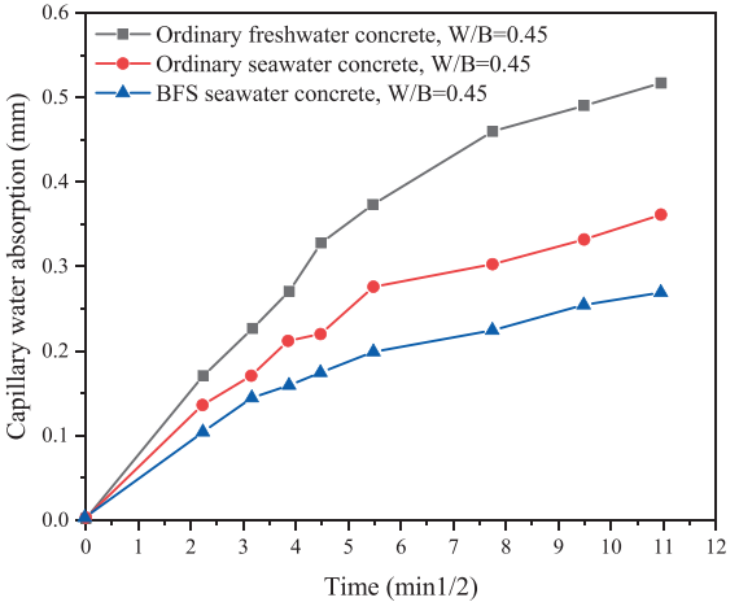

Figure 2.10. Capillary water absorption of different concrete mixtures (Zhao et al., 2021)

2.4.2.2 Carbonation resistance

In general, the carbonation resistance of concrete is evaluated using the phenolphthalein method (JIS-A-1152) or by monitoring the formation of calcium carbonate ($CaCO_3$) (N. Otsuki, 2014). Similar to other research on durability, studies on the carbonation of concrete containing seawater are scarce. The research of Otsuki et al. revealed that the carbonation resistance of seawater concrete during the first 16 weeks was comparable to that of freshwater concrete at carbon dioxide concentrations of 5% and 10% (N. Otsuki, 2014). Both under accelerated conditions (temperature of 20°C, relative humidity of 50%, and CO_2 concentration of 4%) and under natural indoor exposure conditions, seawater does not significantly influence the carbonation process (Carsana et al., 2019). However, Adiwijaya et al. presented an opposing view, suggesting that seawater actually increases the resistance of concrete to carbonation under both accelerated and natural conditions. This enhancement was observed in concretes with and without supplementary cementitious

materials (SCMs) such as fly ash and slag, and it was most pronounced when the concrete was air-cured (Adiwijaya and Hamada, 2017)..

The use of GGBS and FA can expedite the carbonation of SSC, with the carbonation rate anticipated to increase as the replacement ratio increases (N. Otsuki, 2014). As the substitution levels of GGBS (0-70%) and FA (0-30%) in seawater concrete increased, so did the carbonation rate (N. Otsuki, 2014). This phenomenon can be explained by the higher initial concentration of $Ca(OH)_2$ in seawater concrete compared to normal concrete. The additional hydration of GGBS and FA absorbs a substantial amount of $Ca(OH)_2$, thereby altering the alkaline environment of seawater concrete. This disruption promotes the formation of $CaCO_3$ and accelerates the decomposition of hydration products (Khan and Siddique, 2011, Gruyaert et al., 2013).

2.4.2.3 Alkali-silica reaction

In the literature, the issue of alkali-silica reaction (ASR) degradation in concrete containing seawater has not received much attention. Adiwijaya et al. (Adiwijaya et al., 2015, Adiwijaya and Hamada, 2017) examined the expansion behaviour of seawater and freshwater mixed concretes containing coarse reactive aggregates. Specimens were subjected to three different curing methods, water curing, seawater curing, and moisture curing, for 28 days and subsequently stored in a chamber at 40 ºC and 100% relative humidity for one year, during which their expansion was monitored. The results showed that, irrespective of the curing method, concretes mixed with seawater exhibited expansion, primarily attributed to their high alkali content. In contrast, freshwater-based concretes did not show expansion even after curing in seawater. This indicated that ASR did not occur when the concrete's inherent alkali content was low. It was possible to limit the expansion of seawater concrete by using SCMs such as fly ash and slag. Since seawater accelerates

cement hydration and increase the pore solution pH at later ages by roughly 0.15 units, an increase in ASR expansion can be expected. In seawater-mixed concrete containing reactive aggregates, increasing the use of SCMs compared to freshwater-mixed concrete is recommended, though additional research is required.

2.4.2.4 Shrinkage

In a comprehensive study, Khatibmasjedi et al. (Khatibmasjedi et al., 2019) examined the shrinkage behaviour of seawater concrete and mortar, considering both autogenous and drying shrinkage. They examined the drying shrinkage of mortars prepared with OPC and OPC blended with a 20% fly ash at w/b of 0.36 and 0.45. Seawater mixtures with a w/b of 0.45 exhibited greater drying shrinkage. The mortar containing seawater and fly ash exhibited the greatest drying shrinkage, most likely associated with their finer pore size distribution (Wang et al., 2018, Khatibmasjedi et al., 2019, Montanari et al., 2019) and changes in mass loss behaviour. Increases in the pH and viscosity of the pore solution may also contribute to the increased drying shrinkage. Younis et al. also observed a slight increase in drying shrinkage with the use of seawater at a w/cm ratio of 0.34 (Younis et al., 2018), while Olutoge and Modupeola noted an increase in the drying shrinkage of concrete with a w/cm ratio of 0.60 when seawater was used for mixing (Modupeola and Olutoge, 2014).

In the case of lightweight concretes, seawater reduced drying shrinkage, which is quite interesting (Cheng et al., 2018). These studies show that seawater accentuates the drying shrinkage of mixtures with a high w/cm ratio, but has no effect on mixtures with a low w/cm ratio. Both Khatibmasjedi et al. (Khatibmasjedi et al., 2019) and Li et al. (Li et al., 2018) observed greater autogenous shrinkage when seawater was used for mixing, possibly due to seawater enhancing cement hydration and perhaps stimulating the reaction of SCMs.

Despite concerns about increased shrinkage, seawater-mixed concrete may be suitable for high-humidity or fully saturated environments, where shrinkage may not be a significant concern. In situations where shrinkage is a major concern, the application of shrinkage-reducing admixtures or internal curing methods is recommended.

2.4.2.5 Sulfate attack resistance

Limited research has been conducted on the resistance of seawater-mixed concrete to sulfate attacks. Ting et al. investigated the SO_4^{-2} resistance of OPC concrete with a w/b of 0.32 when exposed to a 5% Na_2SO_4 solution for up to 90 days (Ting et al., 2020). They observed a significant decrease in compressive strength after 90 days. Swapping freshwater for seawater marginally mitigated the damage caused by sulfate attacks. Zhao et al. conducted a study on OPC concrete made with freshwater and admixed chlorides (3% NaCl), with a w/cm of 0.48 (Zhao et al., 2018). Although they did not study seawater-mixed concrete directly, they did examine concrete made with freshwater and admixed chlorides. After one year of exposure to 3%, 5%, and 10% sodium sulfate solutions, concrete samples with added chlorides exhibited greater volume expansion, mass loss, and a decrease in compressive strength compared to samples without Cl^-. The level of damage increased as solution concentration and exposure time increased.

In addition to differences in chloride concentrations, w/b, it appears that these two studies have produced contradictory findings. Even though the hydration products and microstructures of seawater-mixed concrete do not differ significantly with age, the system contains higher levels of free and bound alkali chloride and sulfate. In addition, Friedel's salt forms in C-S-H. To comprehend the behaviour of sulfate attack in seawater-mixed concrete, it is essential to understand how the ingressed sulfate is affected by the pre-existing chloride and sulfate.

2.5 C-S-H gel formation

Cement paste, a porous and multiphase material, undergoes hydration when combined with water. This reaction produces several chemical compounds, including C-S-H, ettringite $Ca(OH)_2$, and monosulfoaluminates. C-S-H constitutes approximately 50-70% of all fully hydrated products and is primarily responsible for determining the mechanical strength, durability, and shrinkage of cement-based materials (Richardson, 2008). Therefore, a comprehensive understanding and command of C-S-H gel are indispensable for the advancement of cementitious materials.

Due to the multilayered nature of concrete, however, its structure consists of different levels with varying length scales. On a macro scale (greater than 10^{-3} m), concrete appears to consist primarily of two parts: aggregate and cement matrix. At the micrometre scale, the cement paste structure becomes heterogeneous due to different hydration products and gel morphologies. At the sub-micrometre scale (<1 μm), the C-S-H gel appears as ellipsoid-shaped particles of varying densities. At the nanometre scale (less than 10^{-9}m), the spatial distribution and arrangement of calcium, silicon, and OH constitute the fundamental structure of C-S-H. However, despite its compositional, structural, and physical complexity, the current understanding of C-S-H gel, the principal binding phase in cement hydrates, remains incomplete (Allen et al., 2007).

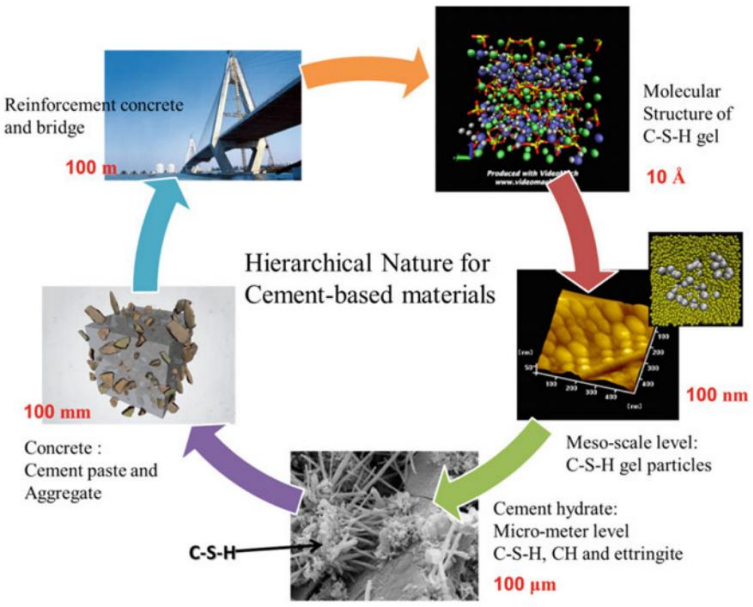

Figure 2.11. Structure of concrete (Hou, 2020b).

2.6 C-S-H gel characterization

2.6.1 Morphology

During cement hydration, the morphology of C-S-H gel at the micrometre scale can be classified into two types: inner products and outer products. As seen in Figure 2.12b, the inner products grow in close proximity to the cement grains, resulting in a relatively dense structure. It is composed of aggregated globular particles ranging in size from 4-6 nm, with pores typically smaller than 10 nm. In contrast, as illustrated in Figure 2.12c, the outer products forms in environments with less spatial limitations and more water availability, allowing the gel to expand into elongated, fibril-like morphologies with a high length-to-width ratio. This development pattern creates a more open structure, with significant porosity between the fibrils.

At the mesoscale (below 1 µm), atomic force microscopy (AFM) provides important insights into the structure of C-S-H. As illustrated in Figure 2.13, AFM images reveal the boundaries and packing orientations of ellipsoid-shaped C-S-H particles. Complementary

research, including nanoindentation tests, have validated granular mechanical behaviour of these particles (Constantinides and Ulm, 2007), whereas small-angle neutron scattering (SANS) measurements indicate the occurrence of nanoparticle aggregation (Allen et al., 2007), as shown in Figure 2.13. Despite these developments, the specific quantitative parameters surrounding the shape, size distribution, and packing arrangement of C-S-H particles remain unsolved, and the mechanism behind the production of the C-S-H colloidal structure is still an open subject. Advanced techniques like AFM, NMR, SANS, and SAXS have been used at the nanometre scale ($<10^{-9}$ m) to study the molecular structure of C-S-H. However, none of these methods can fully resolve the structure, and no single strategy has been able to produce a universally consistent model. Instead, each method adds complimentary information, revealing insights into distinct aspects of the structural and physical properties of C-S-H gel.

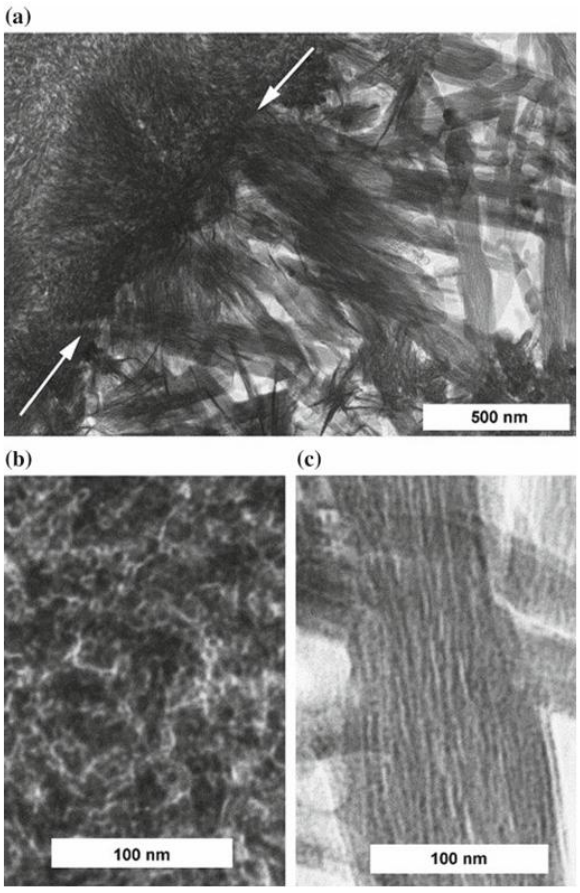

Figure 2.12. (a) Inner and outer prducts C-S-H in hardened C_3S paste. (b) Inner product C-S-H, (c) Outer product C-S-H (Groves, 1986a).

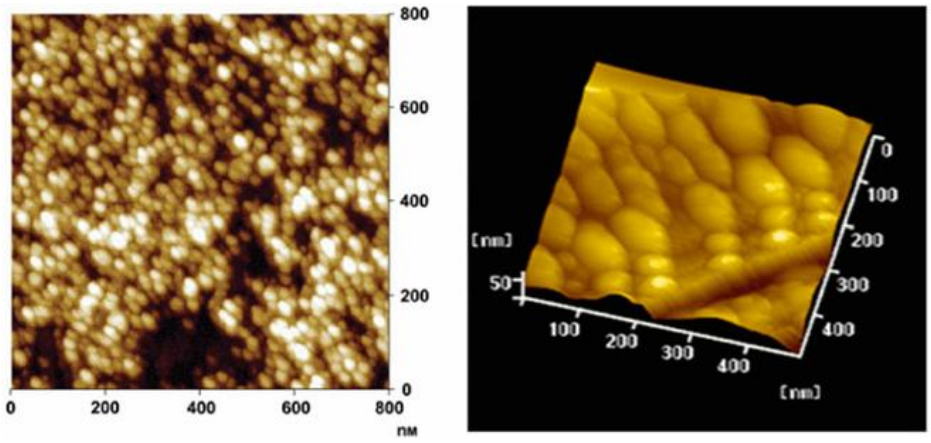

Figure 2.13. C-S-H particles from AFM (Nonat, 2004).

2.6.2 Calcium/Silicon (Ca/Si) ratios

Stoichiometry describes the quantitative relationships between reactants and products in a chemical reaction. However, the stoichiometry of C-S-H is not accurately defined. While the presence of Ca, Si, and H is known, their exact proportions are variable. The Ca/Si ratio is widely used to distinguish between different compositions, but it varies depending on the cement compositions (Taylor, 1997). This ratio frequently varies significantly within a single cement paste sample, typically ranging from 1.5 to 2.3 with an average value of 1.75, although in some cases, values may exceed 2.3 or fall below 1.2.

2.6.3 Water content

In hydrated cement paste, water is present in several distinct forms. One of the most widely accepted classifications was proposed by Sierra (Gmira, 2004), based on both structural and energetic considerations, though the boundaries between categories are not always clearly defined. The main types include:

a) Interlayer water: Located between the layers of C-S-H, it usually forms a monolayer stabilised by hydrogen bonding (Mehta and Monteiro, 2014). The loss of this water results in significant shrinkage of C-S-H.
b) Adsorbed water: Found on the surfaces of hydrated pores, kept in place by intermolecular forces that weaken with increasing distance from the surface.
c) Capillary water: Present the larger pores and voids, generally greater than 5 nm in size (Mehta and Monteiro, 2014).

2.6.4 Layer structure

C-S-H has a layered structure similar to the minerals tobermorite and jennite, with the key difference is the silicate chains arrangement. In C-S-H, the silicate tetrahedra (SiO_4) can form dimers, pentamers, and longer chains with the sequence 2, 5, 8, … (3n-1). NMR studies describe these silicate units using the notation Q^n, where Q^n represents the connectivity of tetrahedron:

Q^0: One unit SiO_4

Q^1: Two units SiO_4

Q^2: Three units SiO_4

During hydration, the proportion of Q^0 species decreases, while Q^1 and Q^2 units become more prominent. No evidence of higher connectivity such as Q^3 and Q^4 has been reported (Taylor, 1997). Figure 2.14 illustrates these different connectivity types, ranging from isolated tetrahedra (Q^0) to dimers (Q^1) and longer chain segments (Q^2). Within the first 24 hours of hydration, the fraction of Q^0 decreases alongside the growth of Q^1. At later stages, longer chains, primarily pentamers and octamers, appear consistent with the 3n-1 rule. Even after six months of hydration, dimers still account for nearly 40% of the silicate

chains. The average silicate chain length, defined as the mean number of tetrahedra in a chain, is typically calculated from the Q^2/ Q^1 ratio. As shown in Figure 2.15, the mean silicate chain length decreases with increasing Ca/Si ratio, indicating that higher Ca content promotes shorter silicate chains (Lagerblad et al., 2004).

$$Mean\ silicate\ chain = 2\left(1 + \frac{Q^2}{Q^1}\right) \qquad (2.14)$$

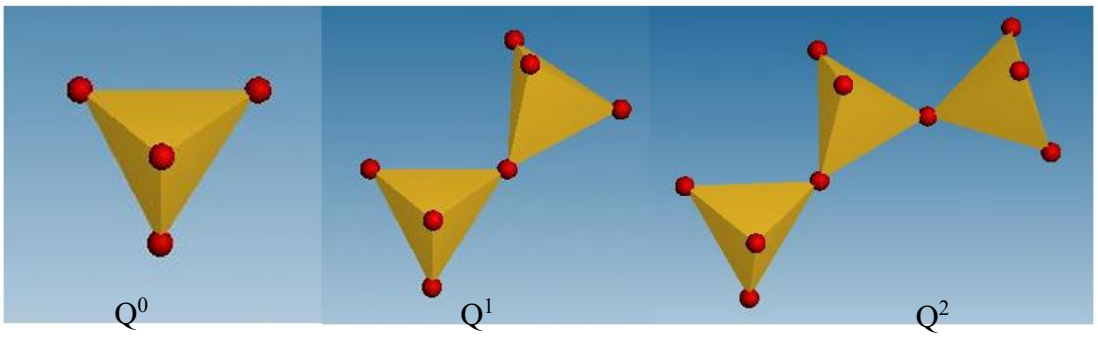

Figure 2.14. Connectivity of different SiO_4 tetrahedral (Arar, 2016).

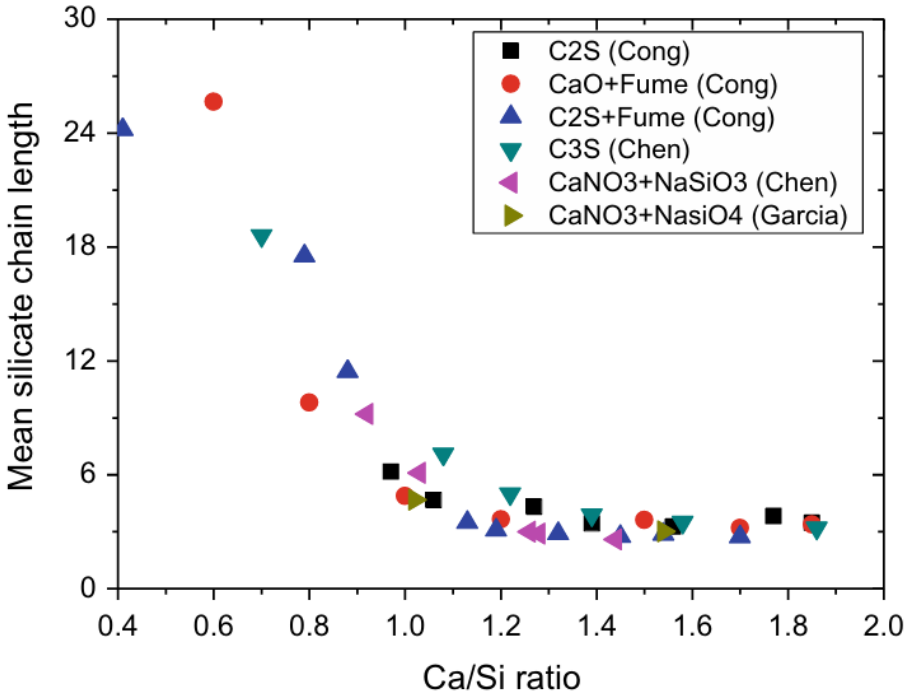

Figure 2.15. Length of silicate chain as a function of Ca/Si ratio (Hou, 2020a).

2.7 C-S-H Gel Mineral Analogues

At least thirty crystalline minerals have similarities to the composition of C-S-H gel (Richardson, 1999). TEM (Groves, 1986b) and XRD studies show that the C-S-H gel has layered characteristics similar to tobormorite (Hamid, 1981) and jennite(Bonaccorsi et al., 2004).

2.7.1 Tobermorite

Tobermorite, a naturally occurring C-S-H mineral, comes in three varieties: 14, 11, and 9 Å, which differ in basal spacing due to varying hydration degrees. Among these, the 11 Å tobermorite is characterized by a layered structure consisting of a central calcium sheet flanked by silicate chains. As shown in Figure 2.17, the Dreierketten chains are made up of two "paired" tetrahedrons that point towards the calcium sheet and one "bridging" tetrahedron that connects to the interlayer, forming a repetitive basic unit. These chains are not directly aligned but are offset by b/2. Calcium atoms and water molecules can live in interlayer zones.

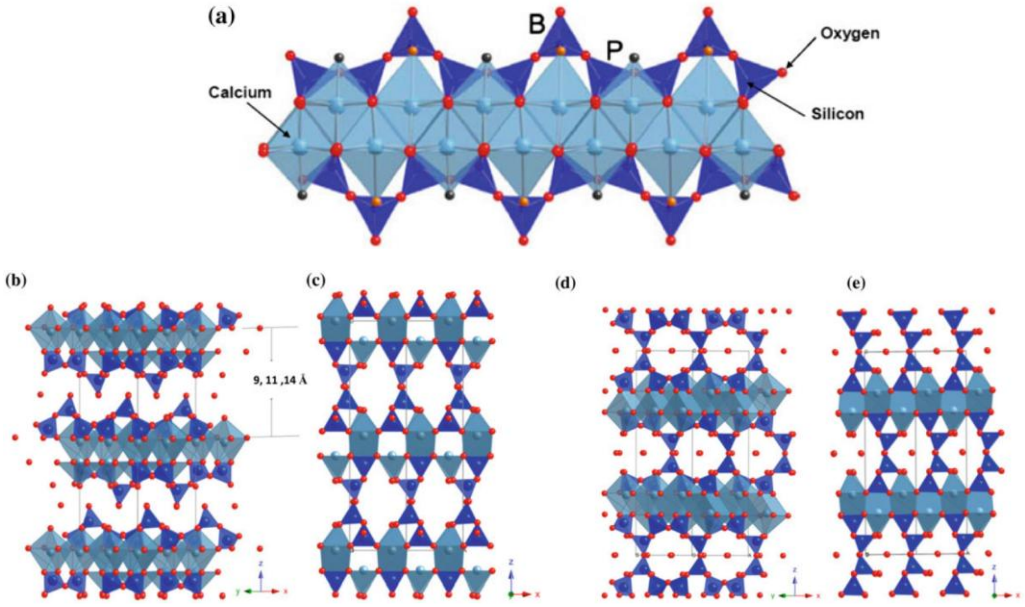

Figure 2.17. (a) A C-S-H layer representation shows a main Ca-O layer with silicate tetrahedrons attached on both sides. (b) tobermorite by Hamid 11 along (110), (c) along

(010) (Hamid, 1981), (d) tobermorite by Merlino along (110), and (e) along (010) (Merlino et al., 2001). The letters "P" and "B" stand for "paired" and "bridging" tetrahedrons, respectively.

The Hamid structure, which views tobermorite as separate layers (Hamid, 1981), and the Merlino structure (Merlino et al., 2001), which views tobermorite as chemically bonded layers, are the two distinct structures of the 11 tobermorite. Despite the fact that the structure of the calcium silicate backbone layer remains constant, the Hamid tobermorite can have three different Ca/Si ratios: 0.67, 0.83, and 1. The addition of calcium atoms in the interlayer region causes changes in the Ca/Si ratio. The protons in the hydroxyl groups must be eliminated to maintain electronic neutrality. The interlayer connection between the bridging tetrahedrons distinguishes the Hamid and Merlino structures.

2.7.2 Jennite

Jennite is a rare silicate mineral whose crystal structure was decoded by (Bonaccorsi et al., 2004) through single-crystal XRD data from a thin crystal. This structure, shown in Figure 2.18, is made up of three parts: a chain of edge-sharing calcium octahedrons, wollastonite-type silicate chains, and an extra calcium octahedron located on inversion centres. These ribbons connect to form a zigzag layer of calcium octahedrons that are also solidly linked by silicate chains. According to the hydrogen bonds connecting the H_2O molecules, jennite contains oxygen and hydroxyl anions. Jennite has the chemical formula $Ca_9Si_6O_{18}(OH)_6.8H_2O$. Jennite has a Ca/Si ratio of 1.5, which is higher than tobermorite and much closer to the average Ca/Si ratio in real hydrated cement.

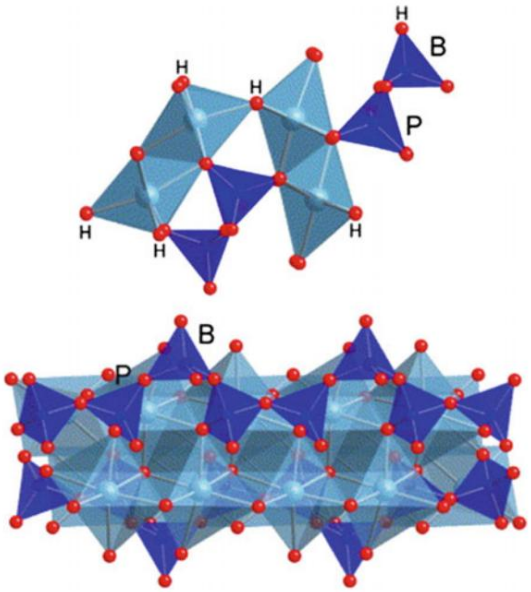

Figure 2.18. Jennite structure along (010) and (100) (Hou, 2020b).

2.8 Model of C-S-H gel

Over the years, numerous microstructural models have been developed to explain the nanoscale structure of C-S-H gel and the formation of gel pores. Among these, the models proposed by Powers and Brownyard, Feldman and Sereda, Wittmann, and Jennings and Tennis have been the most widely adopted and extensively studied.

2.8.1 Powers and Brownyard model

One of the earliest models describing the structure of cement gel was proposed by (Powers and Brownyard, 1947), based on their extensive investigations of water vapor sorption isotherms and chemically bound water in hardening cement pastes. C-S-H gel in this model is represented as layered particles consisting of 2-3 sheets. As shown in Figure 2.19, these layers are randomly arranged and held together primarily by surface forces, with strong ionic-covalent bonds providing additional linkage between adjacent particles. According to their findings, water in C-S-H gel can be classified into three main types: water of

constitution, gel water, and capillary water. Water of constitution refers to non-evaporable water, including crystallization water and hydroxyl groups such as Ca-OH, chemically bonded into the structure. Gel water consists of adsorbed water and water retained by surface interactions, occupying the space between hydrate layers. In contrast, capillary water refers to the free water present within the larger pores, not held by surface interactions.

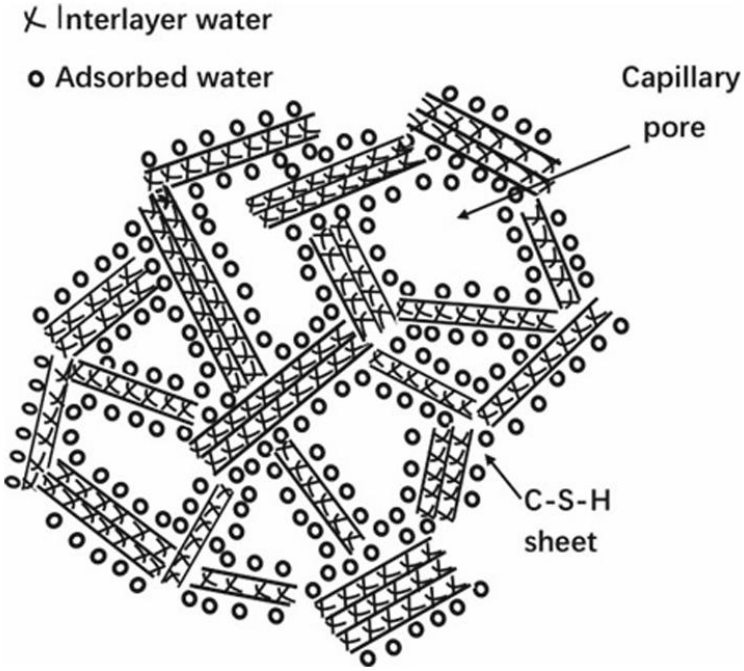

Figure 2.19. Illustration of Powers and Brownyard model for the C-S-H gel structure. (Powers and Brownyard, 1947).

2.8.2 Feldman and Sereda model

A model proposed by (Feldman and Sereda, 1968) that shares similarities with the Powers-Brownyard model but introduces several key differences. As shown in Figure 2.20, the C-S-H gel in their model is composed of irregularly arranged sheets, typically one to four molecular layers thick, which combine randomly to create interlayer spaces. Based on their gas sorption isotherm studies, they concluded that at low relative humidity, water

molecules penetrate these interlayer spaces and structurally bonded to C-S-H. Importantly, this water can enter and exit the structure, which contradicts the Powers-Brownyard interpretation of adsorption data. In this model, the bonding between layers happens via solid-solid interaction, having intermediate strength, stronger than VDW interactions but weaker than ionic-covalent bonds. These contacts form during the drying of cement paste and are disrupted when the material is rewetted. Feldman and Sereda emphasised that such interlayer bonding represents a unique type of chemical interaction, distinct from simple surface to surface forces between C-S-H sheets. Because water vapour adsorption can distort surface area measurements due to the reversible behaviour of interlayer water, they suggested that nitrogen adsorption provides a more reliable means of characterising pore surfaces compared to water adsorption techniques.

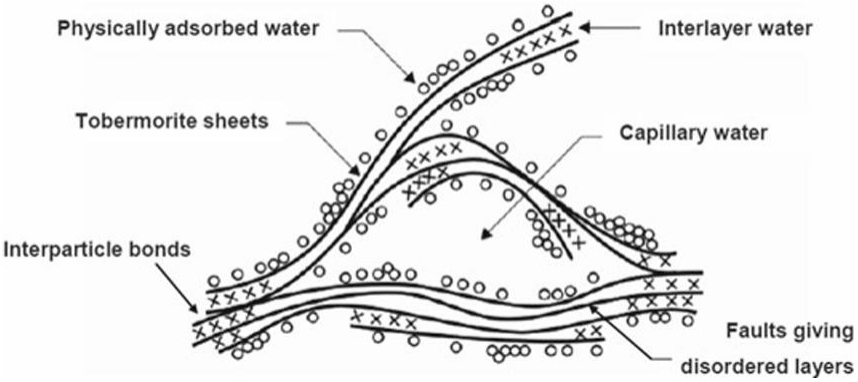

Figure 2.20. Illustration of Feldman and Sereda model for the C-S-H gel structure (Feldman and Sereda, 1968).

2.8.3 Munich model

The Munich model, developed by F. Wittmann in 1979, which was based on sorption measurements and described the C-S-H gel as a three-dimensional network of amorphous colloidal particles forming a xerogel structure (Figure 2.21) (Wittmann, 1979). The

Munich model describes C-S-H gel particles as being separated by thin films of strongly adsorbed water, which generate a repulsive swelling pressure that offsets the attractive VDW forces between solid surfaces. Although VDW interactions contribute to interparticle cohesion, the primary binding energy originates from stronger ionic-covalent bonds. The model further proposes that the disjoining pressure of water in capillary pores can induce swelling or shrinkage of the C-S-H gel, depending on the ambient relative humidity, particularly within the ranges associated with capillary condensation. Owing to these features, the Munich model has been extensively used to interpret the behaviour of hardened cement paste under different humidity conditions.

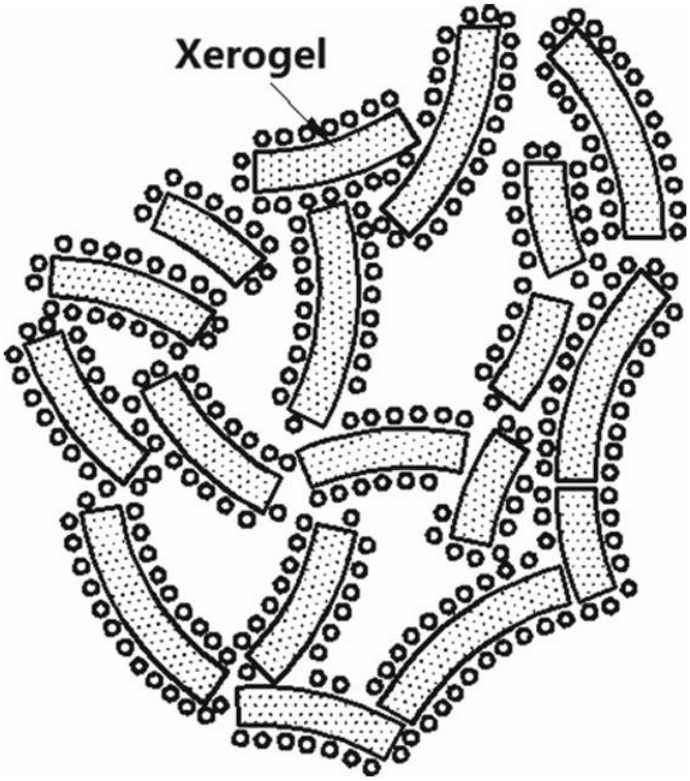

Figure 2.21. Schematic illustration of Wittmann's model for the C-S-H gel structure (Wittmann, 1979).

2.8.4 Jennings model

In contrast to earlier models, the Jennings model provides a more detailed description of C-S-H gel, particularly in terms of surface area, density, and water content (Jennings, 2000, Jennings, 2008). In this model, C-S-H is described as a collection of nanoscale colloidal particles. The fundamental building units are colloidal spheres with diameter of ~2.2 nm and a density of 2.8 g/cm^3. As illustrated in Figure 2.22, these spheres can aggregate into larger globules about ~5.6 nm in diameter. Depending on how efficiently these globules are packed, two distinct forms of C-S-H gel are produced: HD phase with about 24% porosity, and a LD phase with around 37% porosity. The HD phase corresponds to the compact inner products, while the LD phase represents the more porous outer products. This dual-phase concept helps reconcile conflicting observations from different measurement techniques. For example, although the HD phase has a high surface area to volume ratio, nitrogen adsorption methods often underestimate it, as nitrogen molecules are unable to access the narrow pores within HD regions. These two different phases of C-S-H also exhibit distinct mechanical properties. Ulm later carried out extensive nanoindentation studies on various cement pastes, and the observed bimodal distribution of elastic properties confirmed the coexistence of LD and HD phases of C-S-H gel (Constantinides and Ulm, 2004). According to Ulm, the packing density of these phases are approximately 74% and 64%, which corresponds to the theoretical limits of close packed spheres and random packing of spheres, respectively.

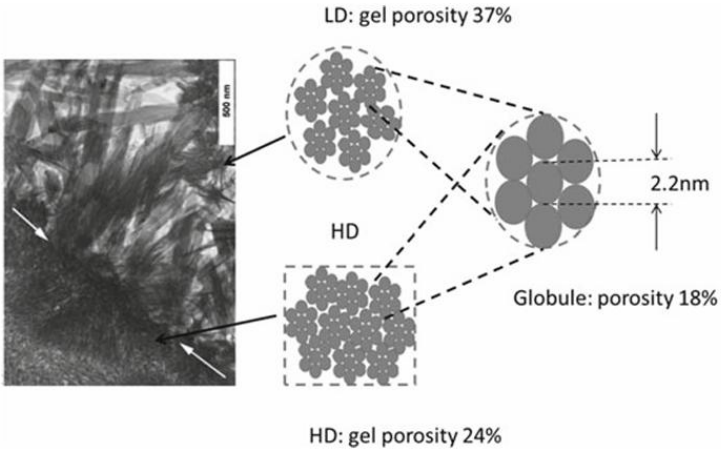

Figure 2.22. Schematic illustration of CM-I model (Hou, 2020a).

To improve the description of the C-S-H building blocks, Jennings incorporated insights from the layered molecular structures of tobermorite and jennite, leading to a modification of the original model. Using results from SANS and SAXS experiments (Allen et al., 2007), the density of the globules was 2.604 g/cm^3, with an average chemical composition of approximately C1.7SH1.8. As shown in Figure 2.23, Jennings proposed that C-S-H is better represented as an arrangement of brick-like globules with an approximate cross-sectional dimension of 5 nm, rather than as spherical colloidal particles. Based on the relative humidity, these globules can exist in four states: fully saturated with a monolayer of water, partially saturated, saturated without monolayer water, and a dried state where most water has evaporated. When these globules are packed together, they form three types of voids: intra-globule pores, small gel pores, and large gel pores.

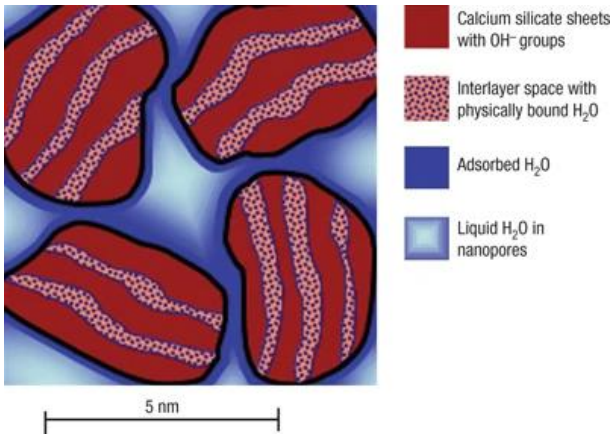

Figure 2.23. Schematic illustration of CM-II model (Allen et al., 2007).

2.9 Atomic structure model of C-S-H

The molecular structure of C-S-H gel has been thoroughly studied by researchers in both physics and chemistry. As explained previously, C-S-H is characterised by its layered morphology, structural similarities to tobermorite, and the distribution of silicate chains. These characteristics have been determined from a range of experimental techniques, including XRD, NMR, and TEM analyses (Groves, 1986a, Chen et al., 2004, Grangeon et al., 2013).

Bernal et al. first proposed the dreierkette-based structural model for C-S-H (Bernal et al., 1952). Through crystallographic studies, they indicated that the hydration product of C_3S resembles the C-S-H formed in dilute suspensions, consisting of a layer, fibrous structure closely related to 11 Å tobermorite. Later, Taylor and Howison (Taylor and Howison, 1956) suggested that the typical Ca/Si ratio of ~0.8 in tobermorite could be increased by removing the bridging tetrahedra and substituting them with Ca atoms, a characteristic that has been incorporated into several different tobermorite-derived models for C-S-H (Cong and Kirkpatrick, 1996b, Kantro et al., 1962, Cong and Kirkpatrick, 1996a, Grutzeck, 1999). To account for the variability in composition, it has also been proposed that the layers of

C-S-H are separated by an interlayer region capable of keeping H_2O, Ca^{2+}, and OH^- ions. In addition, some researchers proposed structural similarities between C-S-H and jennite (Viehland et al., 1997). In jennite, roughly half of the oxygen atoms originate from the central Ca-O groups within the C-S-H layer, where they are shared with OH groups, but in tobermorite, all oxygen atoms are linked through infinite parallel silicate chains.

Taylor claimed that C-S-H in cement paste has a disordered layered structure, which represents a combination of structural features from 14 Å tobermorite and jennite (Taylor, 1986). As shown in Figure 2.24, this hybrid interpretation offers a theoretical explanation for the comparatively high Ca/Si ratios found in cement paste (1.7-2.0). Specifically, during the early stages of hydration, dimeric 14 Å tobermorite exhibited a Ca/Si ratio of about 1.25, whereas jennite-type structures showed a higher ratio of approximately 2.25. In addition, the water to calcium ratio of C-S-H at 11% relative humidity lies between the values associated with these two structural representations.

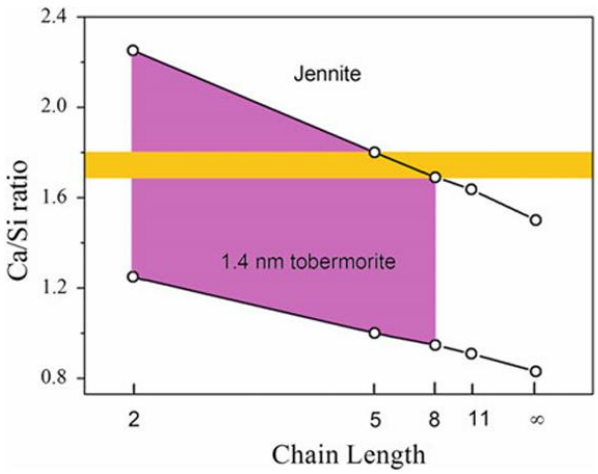

Figure 2.24. Relationship between Ca/Si ratio and silicate chain length as interpreted from tobermorite and jennite based structural models (Taylor, 1986).

Richardson and Groves (Richardson, 2004) suggested a dual classification approach to better define the chemistry of C-S-H by distinguishing between tobermorite/jennite (T/J)

and tobermorite/calcium hydroxide (T/CH) models. In the T/CH model, C-S-H is regarded as a solid solution with tobermorite layers containing calcium hydroxide between them. In contrast, the T/J method views C-S-H as a collection of tobermorite-like structure interspersed with jennite domains. Taylor has remarked that both approaches miss essential elements, such as distinguishing between intralayer and interlayer Ca^{2+}, and accounting for the influence of water content under varied drying conditions. Nonetheless, the T/CH framework has proven effective in describing hydrated KOH-activated metakaolin-Portland cement systems, while conventional water-hydrated Portland cement pastes can only be partially interpreted using either the T/J or T/CH models.

2.9.1 Molecular simulation-based models of C-S-H

While the modified tobermorite and jennite models have some similarities to the C-S-H gel, they do not perfectly mimic the structure and morphology of the real C-S-H. These theoretical models fail to comprehensively capture key physical characteristics, including density, silicate chain distribution, Ca/Si ratio, and water content. For instance, notable discrepancies exist between mineral analogues and C-S-H gel: tobermorite typically exhibits a Ca/Si ratio of 0.82 with a density of 2.19 g/cm^3, whereas C-S-H gel shows higher values, with an average Ca/Si ratio of 1.74 and a density of about 2.6 g/cm^3. Using molecular simulation, a "realistic model" of the C-S-H gel's chemical composition as the fundamental properties has been developed (Pellenq et al., 2009). This coherent molecular model, which takes into account the properties of the C-S-H gel from multiple experiments, illustrates how CaO, SiO_2, and H_2O interact to form a defective silica chain morphology, in accordance with realistic density and chemical composition values for an average C-S-H phase. As depicted in Figure 2.25, the model with a chemical composition of $(CaO)_{1.65}(SiO_2)(H_2O)_{1.75}$ proposes that the structure of the C-S-H gel consists of both glass-

like short-range order and crystalline features similar to those of the mineral tobermorite. Experimentally validated, the model also predicts several essential structural characteristics and fundamental properties, such as the rigidity and strength of a real cement paste system.

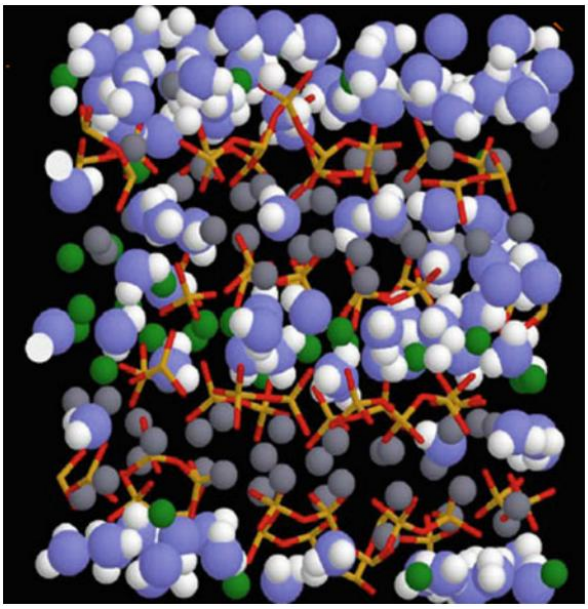

Figure 2.25. A realistic C-S-H model (Pellenq et al., 2009).

The so called "realistic model" represented the first effort to describe nanoscale cement structure using molecular simulation, providing a connection between experimental observations and theoretical models. Based on this foundation, subsequent studies have extensively explored thermodynamic, reactive, dynamic, and mechanical properties, offering molecular-level insights that help bridge nanoscale structural features with macroscale experimental findings (Manzano et al., 2013, Manzano et al., 2012a, Bonnaud et al., 2012a). Nonetheless, this model has certain limitations: the silicate chain backbone, hydroxyl groups, and the local structure of calcium octahedrons require further development to accurately represent the molecular structure of the C-S-H gel.

2.10 Elastic and mechanical properties of C-S-H at nanoscale

Among the various topics investigated using atomistic simulations, the evaluation of the elastic and mechanical behaviour of C-S-H has received considerable attention. After establishing reliable structural models of C-S-H, researchers have been able to systematically examine its response to different loading conditions, including tensile and shear deformations. These simulations have also enabled the study of how factors such as temperature, moisture content, and chemical substitutions influence mechanical performance. Although only key developments are summarized here, numerous additional studies have recently contributed to this rapidly growing area of research (Fan and Yang, 2018, Liang, 2020, Zhang et al., 2021b).

One of the earliest atomistic investigations into the elastic behaviour of the principal hydration phases in Portland cement paste was reported by Manzano et al. (Manzano et al., 2009). In their study, classical force-field simulations combined with a core-shell modelling strategy were employed to estimate the mechanical properties of these phases. The calculated elastic stiffness coefficients were used to determine the bulk and shear moduli through the Hill averaging scheme, from which the corresponding Young's modulus and Poisson's ratio were obtained under the assumption of isotropic behaviour. An early structural representation of C-S-H was adopted, based on crystalline analogues such as tobermorite and jennite with varying silicate chain lengths, including dimeric, pentameric, and octameric configurations. The results demonstrated that the mechanical stiffness of C-S-H strongly depends on silicate polymerization, with shorter chains leading to reduced elastic properties. This dependence was nonlinear, with a pronounced increase in stiffness observed during the transition from short dimeric units to longer pentameric chains, primarily due to the formation of additional bridging tetrahedra. Pellenq et al. (Pellenq et al., 2009) developed a molecular model of C-S-H and evaluated its elastic

behaviour using atomistic simulations. The predicted elastic moduli were slightly higher than those of crystalline tobermorite (Manzano et al., 2009, Shahsavari et al., 2009), which was attributed to the denser and more disordered nature of their C-S-H structure. Beyond linear elasticity, they also estimated the rupture strength (approximately 3 GPa) and the indentation modulus.

Shahsavari et al. (Shahsavari et al., 2011) later evaluated the performance of commonly used force fields for C-S-H, including the core-shell model and ClayFF, by comparing their predicted elastic properties with quantum chemistry calculations (Shahsavari et al., 2009). Their results showed that the core-shell approach provided more accurate mechanical predictions, whereas ClayFF tended to underestimate stiffness (Shahsavari et al., 2011). To improve both accuracy and efficiency, they developed a modified force field (CSH-FF) based on ClayFF (Cygan et al., 2004). This new parameterization reproduced elastic properties comparable to higher-level methods while significantly reducing computational cost, making it more suitable for large-scale simulations. Bonnaud et al. (Bonnaud et al., 2013) investigated how temperature influences the mechanical behaviour of C-S-H using a defective molecular structure model (Pellenq et al., 2009). Their simulations showed that the elastic moduli (bulk, shear, and Young's) increased with temperature, which was attributed to water loss that enhances interparticle cohesion by reducing the screening effect of interlayer water. They also estimated indentation moduli for low-density and high-density C-S-H phases. While the predictions for the low-density phase were consistent with experiments, the high-density values were overestimated, likely due to simplified assumptions regarding packing changes and the limitations of modelling a single grain without fully accounting for the porous network. In 2014, Qomi et al. (Abdolhosseini Qomi et al., 2014b) examined how variations in the Ca/Si ratio affect the mechanical

behaviour of C-S-H using an extended version of the previously developed molecular model (Pellenq et al., 2009). Their simulations showed that increasing the Ca/Si ratio reduced the indentation modulus of the dense C-S-H phase, which was attributed to the formation of more defective and less stiff atomic structures. A similar decrease was observed for hardness. Analysis of the ratio between indentation modulus and hardness revealed a peak near Ca/Si=1.5, suggesting that this composition corresponds to the lowest elastic strain tolerance of the material. Hou et al. (Hou et al., 2018c) later extended the investigation of C-S-H mechanical behaviour by examining the influence of water ingress under tensile loading. Using a reactive force field (ReaxFF) together with a Pellenq-type structural model at Ca/Si=1.1, they simulated the interaction between mechanical deformation and water uptake. Molecular configurations generated at different strain levels were equilibrated to control water content, followed by reactive molecular dynamics to capture water-solid interactions. Their results indicated the existence of a critical strain below which water penetration is negligible, corresponding to the elastic regime. Beyond this limit, deformation created nanoscale cavities that facilitated water adsorption, and in regions with broken silicate bonds, confined water could dissociate and form hydroxyl groups.

The shear behaviour of C-S-H has also been widely examined to better understand creep mechanisms in cementitious materials. Early atomistic studies compared the shear response of tobermorite and model C-S-H structures and demonstrated that interlayer water strongly influences mechanical behaviour, including yield strength, stress evolution, and post-yield softening (Pellenq et al., 2009, Manzano et al., 2013). Under shear loading, deformation was found to concentrate in water-rich regions, where water reduces electrostatic interactions between adjacent layers and facilitates sliding. This lubricating effect of

confined water was shown to promote interlayer slip, supporting its important role in creep and drying shrinkage (Maruyama et al., 2019, Suwanmaneechot et al., 2020). Subsequent simulations (Manzano et al., 2013) using different deformation approaches reported consistent shear strengths of approximately 3 GPa and similar sliding mechanisms between C-S-H layers. More recent work (Morshedifard et al., 2018) employed advanced loading strategies to investigate time-dependent deformation and showed that increasing interlayer water content shifts the response from predominantly viscoelastic to logarithmic creep, although the analysis remained limited to non-aging behaviour due to computational constraints.

Table 2.1. Bulk modulus (K), Young's modulus (E), shear modulus (G), indentation modulus (M_s), and Poisson's ratio (ν) of single particle of C-S-H.

Phase	Ca/Si	K (GPa)	E (GPa)	G (GPa)	M_s (GPa)	ν	Ref.
T. 11Å	0.67	66.65	82.82	32.03	90.59	0.29	(Shahsavari et al., 2009)
T. 11Å	1.0	53.6	91.62	37.7	96.06	0.22	(Shahsavari et al., 2011)
T. 14Å	0.83	35.9	51.90	20.61	55.64	0.26	(Shahsavari et al., 2009)
T. 14Å	0.83	42.4	50.05	19.2	55.12	0.30	(Shahsavari et al., 2011)
T. 14Å	0.83	44.2	56.2	21.8	61.3	0.29	(Manzano et al., 2013)
C-S-H	1.65	49	55-68	23	65	0.3	(Pellenq et al., 2009)
C-S-H	1.65	50.5	56.92	21.69	63.07	0.31	(Shahsavari et al., 2011)
C-S-H	1.65	48.3	63.6	24.8	69	0.28	(Manzano et al., 2013)
C-S-H	0.7-2.3	18	19-28	9.7	-	0.25	(Richardson, 2004, Constantinides and Ulm,

							2004)

2.11 MD simulation of water and ions transport in C-S-H gel pore

2.11.1 Confined water in C-S-H gel pore

Over the past decade, molecular simulations have become an effective tool for investigating the behaviour of water confined within the bulk and dense nanostructure of C-S-H. These studies have provided important insights into how nanoscale water influences key processes such as creep, shrinkage, ion transport, and freeze-thaw response. Consequently, the dynamics of confined water are closely linked to both the mechanical performance and mass transport properties of cementitious materials. For the extremely confined interlayer regions of C-S-H (typically below 1 nm), molecular simulations have shown that water exhibits markedly restricted mobility and altered structural organization (Pan et al., 2010). Under such strongly hydrophilic confinement, interlayer water behaves in a glass-like manner even at room temperature, with significantly reduced diffusion and molecular rearrangement. Subsequent studies (Manzano et al., 2013, Zhou et al., 2016, Jiang et al., 2017) confirmed these suppressed dynamics across different interaction models and further demonstrated that confined water can act as a lubricant during shear deformation, thereby influencing long-term relaxation and creep behaviour of C-S-H. In addition, the amount of interlayer water was found to control the time-dependent mechanical response, governing transitions between viscoelastic and logarithmic creep regimes (Morshedifard et al., 2018). Variations in Ca/Si ratio were also shown to modify both the structure and dynamics of confined water, affecting hydrogen bonding, density,

and molecular motion, which becomes quasi-two-dimensional and resembles that of supercooled or glassy states (Abdolhosseini Qomi et al., 2014b, Zehtab and Tarighat, 2016).

Beyond the interlayer region, at length scales greater than approximately 1 nm, the C-S-H phase contains gel pores with characteristic widths ranging from about 1 to 10 nm (Hou and Li, 2014). These nanoscale pores are commonly represented in simulations using "slit pore" models. Using this approach, Bonnaud et al. (Bonnaud et al., 2012a, Bonnaud et al., 2013) examined pores close to the lower bound of this range (~1 nm) under different relative humidity (RH) conditions and temperatures. At ambient temperature, their results indicated that the cohesion between adjacent C-S-H particles is primarily governed by calcium-mediated interactions, while the presence of water reduces interparticle attraction by screening these forces. Consequently, increasing relative humidity, which corresponds to higher water content, leads to a reduction in overall cohesion within the material (Bonnaud et al., 2012a). When temperature was increased, progressive water desorption from the interparticle space was observed between 373-473 K (Bonnaud et al., 2013), consistent with experimental findings (Hou et al., 2018a). The removal of water caused particle densification and shrinkage, which in turn enhanced the mechanical properties of the material, showing reasonable agreement with experimental measurements (DeJong and Ulm, 2007). Calculated pore pressures revealed the existence of a transition temperature around ~385 K, below which interparticle cohesion increased and above which cohesion decreased. This behaviour qualitatively matches experimental observations, including reported peaks in hardness (~473 K) (DeJong and Ulm, 2007) and macroscale compressive strength (~473-573 K) (Ulm et al., 1999). In addition, Bonnaud et al. reported temperature-dependent transitions in thermodynamic and structural properties such as potential energy

and water density at low and intermediate temperatures, which were associated with liquid–liquid transformations of confined water (Bonnaud et al., 2016). Analysis of translational mean square displacement data suggested a glass transition near ~170 K. Above this simulated glass transition temperature, water mobility followed Arrhenius behaviour, with activation energies in the range of 27-41 kJ/mol for temperatures below 180-195 K, values that agree well with recent experimental measurements (~41 kJ/mol) (Cerveny et al., 2011, Monasterio et al., 2013).

The behaviour of water confined within larger gel pores has also been examined by Hou et al. (Hou et al., 2015, Li et al., 2017a), who focused on saturated pores with widths of approximately 4.5 and 6 nm. In their simulations, the solid framework was represented using a Pellenq-type C-S-H structural model. Their results showed that water molecules located near the pore surfaces exhibited significantly reduced mobility, whereas those situated toward the centre of the pore gradually recovered bulk-like characteristics, including mass density and self-diffusion coefficients, particularly for pores around 4.5 nm in width (Hou et al., 2015, Li et al., 2017a). The reduced diffusivity near the interfaces was attributed to strong interactions between water and the C-S-H surface, specifically hydrogen bonding with oxygen atoms of the silicate chains and the influence of calcium ions that form hydration shells close to the pore wall. These surface interactions effectively restrict molecular motion in the interfacial region. Similar behaviour was reported by Duque-Redondo et al. (Duque-Redondo et al., 2021a), who evaluated the variation of the water self-diffusion coefficient as a function of distance from the C-S-H surface. Their findings revealed a comparable trend, with diffusion progressively increasing from the interface toward the pore centre and approaching bulk values in pores of about 5 nm.

More recently, Honorio and Abahri (Honorio and Abahri, 2019) investigated water transport within nanoporous tobermorite (1.1 nm), which is commonly employed as a structural analogue for C-S-H. Their study considered pores with widths of approximately 0.8, 4.2, and 8 nm. Using non-equilibrium molecular dynamics simulations, a constant external force was applied to the fluid parallel to the pore walls to induce flow. For pores wider than about 4 nm, the resulting behaviour followed classical Poiseuille-type flow characteristics. Under these conditions, the velocity distributions along both in-plane directions were nearly identical, indicating that the atomic-scale surface roughness of the tobermorite substrate had only a minor influence on water transport. The simulated flow profiles were accurately described by continuum hydrodynamic theory when incorporating a slip length of roughly 0.265 nm. These findings suggest that, for sufficiently large mesopores (greater than ~4 nm and extending to tens of nanometres), water transport can be reasonably approximated using the Navier-Stokes framework.

2.11.2 Ion transport in C-S-H gel pore

Ion transport within C-S-H gel plays a fundamental role in determining the durability and long-term performance of cementitious materials. In particular, the migration of chloride ions and their interactions with C-S-H surfaces have attracted significant attention, as chloride ingress is a primary cause of steel reinforcement corrosion in concrete structures. Beyond structural durability, ionic mobility in C-S-H has also been investigated for applications such as the containment and immobilization of radionuclides in cement-based barriers. It should be noted that diffusion coefficients obtained from atomistic simulations correspond to transport occurring within nanopores typically ranging from approximately 1 to 6 nm in size. Consequently, directly extrapolating these values to bulk-scale diffusivity is challenging, since macroscopic transport behaviour is additionally influenced by factors

such as pore size distribution, connectivity, tortuosity, multiphase composition, and chemical gradients. Therefore, atomistic modelling should be regarded as a complementary approach that provides insight into fundamental nanoscale mechanisms, helping to distinguish intrinsic diffusion processes within confined pores from transport phenomena observed at larger structural scales.

Early molecular simulations of cement-solution interfaces were carried out by Kalinichev et al. (Kalinichev and Kirkpatrick, 2002), who investigated the behaviour of chloride-bearing aqueous systems confined within nanoscale pores of cement hydration phases. Their study examined the structural arrangement and dynamic properties of Cl^-, Na^+, and Cs^+ ions in nanopores formed by portlandite, ettringite, and 0.9 nm tobermorite, the latter serving as a representative model for C-S-H. Based on the degree of interaction between ions and the solid surface, the aqueous species were classified into three categories. The first group consists of inner-sphere complexes, where ions directly coordinate with surface atoms. The second group comprises outer-sphere complexes, in which ions remain separated from the surface by a single layer of water molecules. The third group includes fully solvated ions located either within the diffuse layer or in the central region of the pore, where they are separated from the surface by multiple hydration layers and exhibit behaviour similar to bulk solution species. Their simulations showed that alkali cations, particularly Na^+ and Cs^+, exhibit a clear tendency to accumulate near the solid surface, indicating favourable interactions with the hydration products. In contrast, chloride ions did not form inner-sphere surface complexes adjacent to the tobermorite interface. Kalinichev et al. (Kalinichev and Kirkpatrick, 2002) proposed that the affinity of C-S-H for chloride may be even weaker than that observed for tobermorite. This is because the silicate chains in tobermorite are largely hydrogen-saturated, whereas realistic C-S-H

structures are typically more deprotonated under higher pH and elevated Ca/Si conditions. Such surface deprotonation can generate electrostatic repulsion, thereby reducing the likelihood of chloride adsorption at the solid-liquid interface.

2.11.2.1 Chloride adsorption

Later atomistic investigations (Pan et al., 2010, Hou and Li, 2014, Zehtab and Tarighat, 2016, Zhou et al., 2016, Hou et al., 2018a, Wang et al., 2019, Liu et al., 2020, Duque-Redondo et al., 2021c), despite employing different structural models and computational approaches, reported broadly consistent trends. In general, chloride ions exhibit weak affinity toward C-S-H surfaces because electrostatic repulsion limits direct adsorption (Pan et al., 2010, Hou and Li, 2014, Wang et al., 2019, Liu et al., 2020, Duque-Redondo et al., 2021c). However, these studies emphasized that cations strongly bound to the pore surfaces as inner-sphere complexes can indirectly enhance chloride retention. Such adsorbed cations promote the formation of stable ionic pairs, enabling chloride to associate with the surface as outer-sphere complexes (Hou and Li, 2014, Zhou et al., 2016), which aligns with experimental observations (Yu and Kirkpatrick, 2001, Kirkpatrick et al., 2001). Liu et al. (Liu et al., 2020) further demonstrated that surface chemistry plays a critical role, showing that chloride adsorption reaches a maximum at a Ca/Si ratio of approximately 1.2, coinciding with enhanced cation uptake, as also reported in related experimental and computational works (Zhou et al., 2018, Duque-Redondo et al., 2021b). Reported chloride self-diffusivity values vary considerably among studies because they depend strongly on model selection, pore dimensions, ionic associations, solution concentration, and force-field parameters; therefore, direct numerical comparison is challenging. For example, Zehtab et al. (Zehtab and Tarighat, 2016) estimated chloride diffusion coefficients of ~0.71 x 10^{-9} m^2/s, comparable in magnitude to experimentally derived values (~0.11 x 10^{-9} m^2/s

(Pivonka et al., 2004)), and largely independent of the accompanying cation species. In contrast, Liu et al. (Liu et al., 2020) observed lower chloride mobility in $CaCl_2$ and $BaCl_2$ systems compared with NaCl and KCl solutions. Such discrepancies may arise from concentration-dependent effects. Supporting this interpretation, Wang et al. (Wang et al., 2019) reported that increasing ionic concentration reduces chloride diffusivity. Additional factors also influence transport behaviour; for instance, Hou et al. (Hou et al., 2018a) showed that sulfate ions can significantly hinder NaCl mobility by strongly interacting with surface Ca^{2+} and immobilizing sodium ions within the pore solution.

2.11.2.2 Mobility of cations

The transport behaviour of cations within C-S-H nanopores has also been widely examined using MD simulations. Pan et al. (Pan et al., 2010) showed that Na^+ ions located close to the C-S-H surface, corresponding to inner-sphere surface complexes, exhibit diffusion rates approximately one order of magnitude lower than those positioned slightly farther from the surface (~0.1 nm). Comparable trends were reported by Duque-Redondo et al. (Duque-Redondo et al., 2018, Duque-Redondo et al., 2021a, Duque-Redondo et al., 2021b, Duque-Redondo et al., 2021c), who observed that the self-diffusivity of adsorbed Cs^+, Ca^{2+}, and Na^+ ions can be up to two orders of magnitude smaller than that of ions residing in the pore centre. Time autocorrelation analyses indicated that inner-sphere complexes have longer residence times than outer-sphere species, reflecting their stronger interactions with the C-S-H surface. Moreover, the bonding lifetimes between silicate oxygen atoms and Cs^+ were shorter than those for Na^+ and Ca^{2+}, likely due to differences in ionic radius and effective charge.

Consistent findings were reported by Jiang et al. (Jiang et al., 2017), who showed that the smaller hydration shells of Na^+ and K^+ ions, compared with Cs^+, enable easier penetration

into surface cavities and stronger coordination with silicate oxygen atoms, thereby reducing their mobility, following the trend $D_{Na} < D_K < D_{CS}$. Duque-Redondo et al. (Duque-Redondo et al., 2021c) further examined the influence of Ca/Si and Si/Al ratios, as well as the role of counterions (Cl^-, OH^-, or SO_4^{-2}), on cation dynamics. Higher Ca/Si and Si/Al ratios were associated with fewer available adsorption sites, resulting in a greater fraction of Cs^+ ions remaining solvated in the pore interior rather than bound to the surface (Duque-Redondo et al., 2021a, Duque-Redondo et al., 2021b). Sulfate ions were found to form $CaSO_4$ ion pairs, which can extract Ca^{2+} from the C-S-H surface and subsequently alter the distribution and adsorption of other cations. Using ReaxFF, Hou et al. (Hou et al., 2017a) investigated the mobility of Ca^{2+}, Na^+, Al^{3+}, and Mg^{2+} within the interlayer region. Their results showed that water molecules surrounding Al^{3+}, and Mg^{2+} exhibit longer residence times than those around Na^+ and Ca^{2+}, and the calculated diffusion coefficients followed the order $D_{Na} > D_{Ca} > D_{Al} > D_{Mg}$. However, these results should be interpreted cautiously, as the ReaxFF parameters for Mg, Al, and Na combined with Ca/Si/O/H systems have not yet been fully validated.

2.12 Computational methods

Molecular modelling is a computational technique that simulates and studies the behaviour of molecules in order to predict their structural, kinetic, and physicochemical properties at the atomic scale. This technique has applications in different fields, including chemical engineering, materials science, and applied physics. At the core of molecular modelling lies atomic simulation, which is achieved by solving mathematical formulations that describe the motion and interactions of electrons and nuclei. These formulations are typically addressed through two main frameworks: quantum mechanics and classical mechanics. In quantum mechanics, the system is described by Schrödinger's equation,

which mathematically characterises atoms and molecules. This equation can be handled in two ways: the ab-initio method, which derives structural properties entirely from first-principles quantum computations, and the semi-empirical method, which includes experimental data to simplify calculations. While ab-initio simulations provide highly accurate electronic descriptions, they demand significant computational resources, especially for medium-sized systems containing hundreds of atoms. In contrast, semi-empirical models reduce computational cost by integrating empirical parameters into the mathematical framework, making them more efficient but slightly less rigorous. In contrast, the classical mechanics approach represents atomic interactions using force fields with specified parameters rather than electronic structure. This approach enables the efficient simulation of large systems with thousands of atoms. Although it does not capture electronic properties directly, it offers a practical balance between computational efficiency and the ability to describe large-scale molecular and material behaviour, without the need for input from quantum calculations.

2.13 Molecular mechanics

This approach applies the principles of classical mechanics to represent molecular systems. Rooted in Newton's second law, it defines particle motion and the forces that act on them. In molecular mechanics, two main assumptions are made:

- Atoms are modelled as particles characterised by a specified radius (commonly the VDW radius), a defined polarizability, and a fixed partial charge, usually obtained using either experimental data or quantum calculations.
- Bonded interactions are modelled as elastic springs, where the equilibrium distance reflects the experimentally determined or theoretically calculated bond length. The interactions are defined exclusively in terms of atomic locations,

with the surrounding electrons assumed to have an energetically favourable distribution. These interactions are formally described by simple analytical functions, often known as 'potential functions' or 'force fields' (Leach, 2001).

In molecular mechanics, the total energy of a system is calculated as the sum of its interatomic interactions. The functional forms that describe covalent and non-covalent interactions are chosen to reflect the underlying physical behaviour of the system. Their parameters are generally calibrated against ab-initio calculations or experimental measurements. The following section reviews the most often utilised potential functions for cement and cement-based materials that are relevant to both atomic bonding and non-bonded interactions. The total energy of a molecular system can be expressed as the sum of the following energy contributions:

Total Energy = Bond stretching energy + Angle bending energy + Torsional rotation energy + Out-of-plane bending energy + non-bonded interactions energy

2.13.1 Potential functions

2.13.1.1 Bond stretching energy

To simplify calculations, bond stretching energy is commonly calculated using the harmonic oscillator model, which includes small vibrations around the equilibrium bond length. Although higher-order expansions based on a Taylor series can provide more detailed descriptions, they are rarely used in large systems due to their complexity. The Morse potential is considered one of the most accurate representations of bond stretching; yet it requires three parameters, making it computationally demanding when applied to systems with large number of atoms. In practice, most chemical bonds undergo only minor deviations from their equilibrium lengths, making the harmonic oscillator-formulated

through Hook's law, a practical and efficient choice for energy evaluation. Figure 2.26 depicts the bond stretching energy and equation 2.15 is Hooke's law equation to calculate the energy.

$$E_{stretch} = \frac{1}{2} K_b (r - r_o)^2 \qquad (2.15)$$

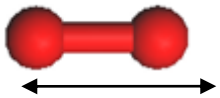

Figure 2.26. Bond stretching.

In this approach, the bond stiffness constant (K_b), the equilibrium bond length (r_o), and the instantaneous bond length (r) after vibration are used to compute the bond stretching energy.

2.13.1.2 Angle bending energy

The Figure 2.27 depicts the bending energy associated with three atoms connected in series, which occurs when the bond angle deviates from the equilibrium value. This energy is typically less than that required for bond stretching or compression, as angular distortions are easier to accommodate. A Taylor series expansion with higher-order terms can provide a more accurate representation, although this increases computational cost dramatically. In practice, the harmonic form based on Hooke's law is often used.

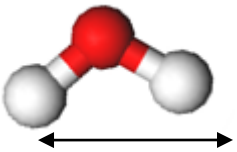

Figure 2.27. Angle bending energy.

$$E_{bending} = \frac{1}{2} K_\theta (\theta - \theta_o)^2 \qquad (2.16)$$

Where K_θ is the bond-angle force constant, θ is the instantaneous bond angle, and θ_o is the equilibrium bond angle.

2.13.1.3 Torsional rotation energy

In molecular mechanics, torsional and non-bonded interactions frequently account for the largest deviations in total energy. Torsional energy arises by the rotation of four sequentially bonded atoms whose dihedral angle deviates from their preferred equilibrium locations. To capture this behaviour, torsional energy is often represented by a simple periodic function:

$$E_{Torsion} = \sum_{n=1}^{\infty} \frac{1}{2} E_n(cosn\varphi - \theta) \quad (2.17)$$

Where E_n is the barrier height for the torsional rotation, n denotes the periodicity (number of repeating energy barriers within 360°), φ is the torsion (dihedral) angle, and θ is the phase shift. This functional form enables the modelling of staggered and eclipsed conformations, with lower energy corresponding to stable staggered arrangements and higher energy corresponding to eclipsed configurations.

2.13.1.4 Out of plane bending energy

Out of plane bending is treated differently from in plane bending. In this case, three atoms remain aligned inside a single plane, while a fourth is displaced, resulting in an angle w relative to the plane. The related energy is typically represented by a harmonic potential of the form:

$$E_{out\ of\ plane\ bending} = \frac{1}{2} K_\theta\ (w)^2 \quad (2.18)$$

Here, K_θ represents the out of plane force constant, and w denotes the angular displacement from the reference plane.

2.13.1.5 Non-bonded interactions energy

Atoms can interact with each other through non-bonded interaction that are not bonded directly. These interactions occur across space and are mostly determined by the distance between particles. In molecular simulations, such non-bonded interactions are often classed as two types: electrostatic forces and van der Waals forces.

$$E_{non\ bonded} = E_{electrostatic} + E_{VDW} \qquad (2.19)$$

2.13.1.6 Electrostatic interactions

When atoms differ in electronegativity, the electron cloud is distributed unevenly, leading to partial charges on the atoms. These partial charges give rise to electrostatic forces between them. The electrostatic interaction between two atoms i and j carrying partial charges can be determined using Coulomb's law as given below (Cygan et al., 2021):

$$E_{electrostatic} = \frac{e^2}{4\pi\epsilon_o} \sum_{i \neq j} \frac{q_i q_j}{r_{ij}} \qquad (2.20)$$

Here, e denotes the elementary charge of an electron, q_i and q_j represent the partial atomic charges obtained from quantum mechanical calculations, r_{ij} is the separation distance between atoms i and j, and ϵ_o is the dielectric constant of vacuum, with a value of 8.85419 $\times 10^{-12}$ F/m.

2.13.1.7 Van der Waals interactions

Van der Waals interactions, like electrostatic forces, arise from temporary dipoles formed between atoms or molecules. Individually, these forces are small; yet, because they occur simultaneously across many atoms, their combined influence can be significant. Van der Waals forces act over short distances, and their energy decreases rapidly as atoms separate

according to the $^{1}/_{r^{6}}$ relationship. The interaction energy has two opposing components: an attractive term and a repulsive term. When atoms are brought very close together, repulsion dominates, resulting in a significant increase in energy due to electron cloud overlap (Pauli exclusion principle). Attraction, on the other hand, results from instantaneous dipoles caused by changes in electron density. The most generally used mathematical formulation that captures both the attractive and repulsive contributions is the Lennard-Jones potential (L-J) or 6-12, as represented in equation (2.21) (Cygan et al., 2021).

$$E_{VDW} = \sum_{i \neq j} 4\varepsilon_{ij} \left[\left(\frac{\sigma_{ij}}{r_{ij}} \right)^{12} - \left(\frac{\sigma_{ij}}{r_{ij}} \right)^{6} \right] \quad (2.21)$$

In this expression, ε_{ij} represents the depth of the potential well, while σ_{ij} corresponds to the distance at which the interaction energy becomes zero. Both ε_{ij} and σ_{ij} are typically used as adjustable parameters to describe the interaction between atoms i and j.

2.13.2 Force field used

In molecular mechanics and molecular dynamics simulations, a force field refers to the mathematical framework and associated parameters used to calculate the potential energy of an atomic system. It forms the foundation of material characterization within these methods. Several force fields, including ClayFF, CSHFF, and ReaxFF, have been employed in literature to model calcium silicate phases and other cement hydration products. ClayFF is used in this study to simulate cement hydration products.

ClayFF was selected in this study due to its proven reliability and flexibility in modelling hydrated mineral systems and solid-liquid interfaces relevant to cementitious materials. Unlike more specialized force fields such as CSHFF, ClayFF provides transferable and

well-validated parameters for a wide range of ions commonly present in seawater and cement pore solutions, including Na^+, K^+, Mg^{2+}, Ca^{2+}, and Cl^-, enabling consistent simulation of multi-ionic environments. Previous studies have demonstrated that ClayFF reproduces structural, thermodynamic, and transport properties of C-S-H and confined water in good agreement with experimental observations and higher-level simulations (Honorio et al., 2025). Compared to reactive force fields such as ReaxFF, ClayFF offers significantly lower computational cost while maintaining sufficient accuracy for studying ion transport, adsorption, and interfacial phenomena at the nanoscale. These advantages make ClayFF particularly suitable for systematic investigations of seawater ion transport and interaction with C-S-H over extended simulation times and varying pore conditions.

2.13.2.1 ClayFF

ClayFF is a widely used force field designed for molecular simulations of hydrated crystalline materials and their interactions with aqueous phases (Cygan et al., 2004). It describes metal-oxygen bonding through an ionic-covalent framework, making it particularly effective for hydrated systems. This force field has been successfully applied to model the structures of oxides and hydroxides, the adsorption of aqueous species on their surfaces, and the dynamics of water and ions within layered interlayers (Kirkpatrick et al., 2005, Cygan et al., 2009). Although ClayFF was not originally parameterized for cementitious systems, numerous studies on phases such as CH, AFm (hydrated calcium aluminates), and tobermorite have demonstrated its suitability for simulating calcium silicate systems with reliable accuracy.

In ClayFF, water molecules are described using the flexible Simple Point Charge (SPC) model (Berendsen et al., 1987). The covalent O-H bonds are represented through a harmonic potential function, as defined in Eq. 2.15. Because this functional form

effectively accounts for the various contributions to bond energy, Coulombic interactions within the bonded group are typically excluded. In addition to bond stretching, the intramolecular H-O-H angle is modelled using a three-body harmonic potential, as defined in Eq. 2.16 in the previous section. Atoms in the ClayFF framework are considered as point charges with full translational freedom. Interactions between metal and atoms are described using the combination of the 12-6 LJ potential and Coulombic forces. The total energy of the system is thus produced by adding two contributions; the electrostatic term, which accounts for Coulomb interactions among partial atomic charges, and the LJ term, which represents short-range VDW dispersion effects as defined in Eqs. (2.20) and (2.21).

2.14 Molecular dynamics

Molecular dynamics (MD) is a computational technique that models the motion of atoms and molecules while accounting for their interactions (Frenkel and Smit, 2023). By numerically integrating Newton's equations of motion, MD generates trajectories that describe how the positions and velocities of particles evolve within the system over time.

$$\frac{d^2x_i}{dt^2} = \frac{F_{xi}}{m_i} \quad (2.22)$$

Here, F_{xi} represents the force on a particle arising from interatomic interactions, m_i is the mass of particle, and xi denotes the atomic coordinates. The primary goal of MD is to compute the forces between particles and calculate the energy of the system. Beyond that, MD allows for the calculation of average macroscopic properties, which can be compared to experimental data or used to investigate situations that are difficult to replicate experimentally. At a given temperature, atoms are allocated initial random velocities, which cause changes in their locations and trajectories. Using the specified potential (force field), the forces acting on these atoms at revised places are then calculated as:

$$F_i = \frac{dE(r_i)}{dr_i(t)} = \nabla E(r_i) \quad (2.23)$$

Here, E denotes the potential energy derived from classical mechanics, and r_i represents the position of the atoms. When velocities are assigned to a group of molecules, the system is initially displaced from thermodynamic equilibrium but gradually relaxes to a stable condition over time. Once equilibrium is achieved, macroscopic properties of the system can be evaluated. The force calculations are carried out in a sequence of very small-time increments (typically on the order of 1 fs). At each step, the forces, updated positions, and velocities of atoms are computed, generating a trajectory from which equilibrium behaviour and average properties of the system can be determined.

2.14.1 Solution for equation of motion (algorithms)

The force acting on a particle changes depending on its position or the positions of neighbouring particles. Because the motions of each particle are linked, the system becomes a complex many-body problem that cannot be addressed analytically. To overcome this, the equation of motions is approximated and numerically solved using finite difference methods. A number of algorithms have been developed to numerically integrate Newton's equations of motion and compute atomic trajectories in MD simulations. The goal of these methods is to maintain both numerical stability and accuracy throughout the simulation. One of the earliest and most widely adopted approaches was introduced by Verlet (Verlet, 1968), which is derived through the following procedure:

By applying a Taylor series expansion to both the forward and backward time positions and keeping terms up to the third order.

$$\boldsymbol{r}(t + \Delta t) = \boldsymbol{r}(t) + v(t)\Delta t + \frac{1}{2!}\boldsymbol{a}(t)\Delta t^2 + \frac{1}{3!}\frac{d^3\boldsymbol{r}(t)}{dt^3} \quad (2.24)$$

$$\boldsymbol{r}(t-\Delta t) = \boldsymbol{r}(t) - v(t)\Delta t + \frac{1}{2!}\boldsymbol{a}(t)\Delta t^2 - \frac{1}{3!}\frac{d^3\boldsymbol{r}(t)}{dt^3} \qquad (2.25)$$

After adding Eq. (2.24) and (2.25), the final expression for the position $t + \Delta t$ is given below:

$$\boldsymbol{r}(t+\Delta t) = 2\boldsymbol{r}(t) - \boldsymbol{r}(t-\Delta t) + \boldsymbol{a}(t)\Delta t^2 \qquad (2.26)$$

It is important to note that velocities are not explicitly included in the time evolution within the Verlet algorithm. However, since velocities are necessary for calculating kinetic energy, they are obtained indirectly by estimating them from the change in particle positions over a time interval of $2\Delta t$ as follows:

$$v(t) = \frac{\boldsymbol{r}(t+\Delta t) - \boldsymbol{r}(t-\Delta t)}{2\Delta t} \qquad (2.27)$$

The Verlet algorithm is straightforward and efficient, requiring just a single force calculation at each timestep. It provides good accuracy, with small error, as higher-order terms beyond the fourth are neglected in the expansion.

2.14.2 Periodic boundary conditions

In MD simulations, atoms located at the boundaries of the simulation box experience less neighbouring interactions compared to atoms in the interior, resulting in surface forces that differ from those in the bulk. This discrepancy prevents the system from accurately representing real material behaviour, regardless of box size. To address this limitation, periodic boundary conditions (PBC) are applied. Under PBC, the simulation box is theoretically repeated infinitely in all Cartesian directions. As particles move within the primary cell, their images in the surrounding replicas move correspondingly. Furthermore, when a particle exits through one face of the box, it simultaneously re-enters through the

opposite face with the same velocity. This approach preserves the total number of particles and ensures that system density remains constant throughout the simulation.

2.14.3 Cutoff distance

The number of atomic interactions increases because of eliminating boundary conditions that must be considered, which in turn slows down computational performance. To address this, a cut-off distance is introduced: only interactions within the specified range are calculated, while those beyond it are neglected. For accuracy, the chosen cut-off distance must be less than half of the simulation box length.

2.14.4 Ensembles

The purpose of molecular modelling is to estimate macroscopic properties such as pressure, energy, and volume by simulating the behaviour of atoms and molecules at the microscopic scale. Through the framework of statistical mechanics, these bulk properties can be derived from the collective behaviour of individual particles. At the macroscopic level, a system is described by variables including temperature (T), pressure (P), volume (V), and the number of particles (N). In contrast, at the microscopic level, the state of the system is described by the atomic positions and their momenta, which collectively define coordinates within a multidimensional phase space. An ensemble represents a collection of possible systems that share the same macroscopic properties but differ in their microscopic configurations. Various types of ensembles can be employed in MD simulations, depending on the physical conditions being studied.

- Microcanonical ensemble (NVE): keeps the number of atoms, volume, and energy constant.

- Canonical ensemble (NVT): maintains constant number of atoms, volume, and temperature through thermostats such as Nose-Hoover.
- Isothermal-isobaric ensemble (NPT): allows both temperature and pressure control, often used to equilibrate systems under realistic conditions.

2.14.5 Analysis of MD Trajectories

A MD simulation normally has two stages: the equilibration run and the production run. Property analysis occurs during the production stage, when the relationship between atomic properties and trajectory data is determined. Common methods for this purpose include the RDF, MSD, TCF, and uniaxial tension tests, all of which provide useful insights into molecular structure of the material, dynamic behaviour, and mechanical response.

2.14.5.1 Radial distribution function (RDF) analysis

RDF defines the probability of finding a particle at a certain distance from another particle. This function can evaluate the local configuration and degree of order of ions and adjacent water molecules in different systems. The general expression to calculate the RDF is given below:

$$g(r) = \frac{dN/N}{dV/V} = \frac{V}{N}\frac{\langle N(r,\Delta r)\rangle}{4\pi r^2 \Delta r} \quad (2.28)$$

Where r denotes the radial distance, $N(r, \Delta r)$ represents the number of atoms present in a shell volume of $4\pi r^2 \Delta r$ between r and Δr, and the bracket denotes the time average.

2.14.5.2 Mean square displacement (MSD) analysis

MSD is a crucial metric for characterizing the transport rate of molecules or ions in a system, the following equation can be used to calculate the MSD:

$$\text{MSD} = \langle \Delta \boldsymbol{r}^2(t) \rangle = \sum_{i=1}^{N} |\boldsymbol{r_i}(t) - \boldsymbol{r_i}(0)|^2 = \langle |\boldsymbol{r_i}(t) - \boldsymbol{r_i}(0)|^2 \rangle \quad (2.29)$$

Where $\boldsymbol{r_i}(t)$ denotes the position of the atom $\boldsymbol{i}$ at time $\boldsymbol{t}$ while $\boldsymbol{r_i}(0)$ represents its initial position at the beginning of the simulation.

2.15 Chapter summary

This chapter emphasize the growing global demand for concrete and the corresponding freshwater use, highlighting the potential of seawater as an alternative mixing water. The historical usage of seawater in Roman concrete was briefly discussed, followed by modern concerns about steel reinforcement corrosion due to chloride ions. The effects of seawater on hydration were discussed, showing its impact on reaction kinetics, pore solution composition, and microstructural evolution. Studies on the fresh and hardened properties of seawater-mixed concrete were also discussed, with a focus on workability, setting time, density, and compressive strength. Using seawater as mixing water can reduce the durability of both plain and reinforced concrete. Although limited research has been conducted on the durability of seawater-mixed concrete, more research is required to comprehend their behaviour. The chapter also explored C-S-H, the main hydration product responsible for strength and durability in cement systems. The properties of C-S-H gel have been examined using a wide range of experimental techniques, providing insights into its Ca/Si ratio, density, silicate chain connectivity, and water states. Taken together, these studies indicate that C-S-H is composed of disordered, glass-like layers that share certain structural features with mineral analogues such as tobermorite and jennite. While each experimental method provides valuable information, a complete structural model of C-S-H requires integrating these findings. However, because of the compositional heterogeneity and hierarchical character of C-S-H, experimental methods are constrained by instrumental accuracy, scale limits, and material purity. To complement these efforts, theoretical models

have been developed at both the colloidal and molecular levels. Many rely on crystalline minerals, such as tobermorite, jennite, and portlandite, or their disordered combinations to explain particular structural aspects. Still, the nanoscale structure of C-S-H remains unresolved, with challenges arising from inconsistencies in reported Ca/Si ratios, silicate chain lengths, densities, and its inherently disordered layered configuration.

Molecular simulation provides a bridge between theory and experiment. Simulations can be used to test theoretical models and compare their predictions to experimental data in order to assess their validity. At the same time, because experimental approaches alone cannot fully capture the underlying molecular structure of C-S-H, computational simulations are critical for interpreting findings and revealing structural and dynamic behaviour at the atomic scale.

This chapter also discusses the molecular computation methodologies and concepts typically used in literature. There are two basic approaches: molecular modelling using quantum mechanics and molecular modelling using classical (molecular) mechanics. The ab-initio methodology, which solves the Schrödinger equation, is one of the most used quantum-based methodologies. While this approach and its variations produce extremely accurate representations of electrical states, they are computationally demanding and time-consuming. In contrast, molecular mechanics treats atoms as masses connected by springs, which allows for more efficient calculation of the potential energy of the system. The choice of force field is an important factor in this approach since it affects the accuracy and dependability of the outcomes. Molecular modelling using the ClayFF force field enables the identification of atomic configurations corresponding to minimum energy states, where any deviation increases energy of the system. MD extends this analysis by simulating the time evolution of atomic interactions and trajectories. The Verlet algorithm is typically

employed to numerically integrate Newton's equations of motion, providing a link between microscopic atomic behaviour and macroscopic material properties. From such simulations, properties like, elastic constants, RDF, and MSD can be determined.

Chapter 3. Transport of NaCl solution in C-S-H

3.1 Introduction

Mass transport in porous concrete is a complex process involving a series of physical and chemical events. As reviewed in Chapter 2, Concrete durability issues and the associated steel corrosion are directly related to the transport behaviours of NaCl (Du et al., 2020, James et al., 2019, Ma et al., 2020). The primary binding phase in concrete is C-S-H gel, which possesses 60-70% volume fraction of cement paste (Lange et al., 1994). C-S-H is a porous structure with the pores taking approximately 25% of the total volume of C-S-H (Lange et al., 1994). The properties of hydrated cement paste, such as strength development, ionic transport, and volume change in hardened concrete, are significantly influenced by the different types of pores present in it. These voids consist of gel pores (5-100 Å diameter), capillary pores (100-1000 Å diameter), and air voids (Lange et al., 1994). When exposed to an aqueous environment, these pores with different sizes can serve as capillary routes for the transport of water and ions, and the pore size plays a dominant role in the transport behaviours of water and ions (Pack et al., 2010). In the past decades, numerous experimental and simulation studies have been conducted on the capillary adsorption or ionic diffusion of salty solution in the pore channel of C-S-H (Zhou et al., 2016, Zhou et al., 2018). For example, Yang et al. (Yang et al., 2019b) proposed a multiscale model for the diffusion of ions in cement paste, which incorporates the lattice Boltzmann method and a modified Nernst Planck equation to account for the steric and ion-ion correlation effects. They found that the effective diffusivity of chloride ions is comparable to that of tritiated water (HTO) and higher than that of sodium ions, which is due to electrical double-layer effects near charged C-S-H surfaces.

In practical applications, cement-based materials often experience temperature fluctuations. These fluctuations can occur due to weather changes, seasonal changes, or diurnal temperature variations. Previously, researchers developed macroscopic models to examine the effect of temperature on chloride diffusion and moisture. Samson and Marchand (Samson and Marchand, 2007) developed a numerical model that considers the impact of temperature on the dynamic and chemical reactions of cementitious materials. The findings indicated that temperature had a comparable effect on diffusion across different materials. Furthermore, a multi-ionic transport model was able to accurately replicate chloride profiles. Isteita and Xi (Isteita and Xi, 2017) conducted experiments to study the effect of temperature gradients on chloride penetration in concrete with varying water-cement ratios and found that the penetration process of chloride increases significantly with temperature gradient. Bai et al. (Bai et al., 2020) developed an analytical model that utilized the Laplace and inverse Laplace transformations to calculate the chloride concentration profiles in cementitious materials under the influence of temperature and ionic concentration gradients. Results showed that moisture and chloride transfer in concrete are positively correlated with temperature gradients. Despite much experimental and numerical work, the exact mechanisms, especially from a micro/nanoscale, remain elusive and cannot be fully elucidated.

Molecular dynamics (MD), a force field-based numerical calculation method, is a mature tool to investigate atomic-scale processes in cement-based materials (Abdolhosseini Qomi et al., 2014a, Kai et al., 2023d, Luo et al., 2023a, Luo et al., 2022, Li et al., 2023). In addition, the atomic-level information can further be used to bridge the material performance at larger scales via multiscale simulation, like machine-learning interatomic potentials (MLIPs)-based method (Vu-Bac et al., 2015, Mortazavi et al., 2021). Previously,

MD studies have been carried out to study the transport process of different salt (e.g., NaCl, Na_2SO_4, and CsCl) solutions in various pores in cement-based materials (Jiang et al., 2017, Zhang et al., 2017, Hou et al., 2018a, Hou and Li, 2018, Hou et al., 2018b, Yang et al., 2018, Zhou et al., 2018, Hou et al., 2019, Xie and Luo, 2023). Numerous studies consistently demonstrate the weak adsorption of Cl^- ions on the surface of C-S-H due to repulsive interactions (Pan et al., 2010, Hou and Li, 2014, Zehtab and Tarighat, 2016, Duque-Redondo et al., 2018, Wang et al., 2019, Liu et al., 2020, Duque-Redondo et al., 2021c, Duque-Redondo et al., 2022a). Highly adsorbed cations enhance chloride ions' adsorption by establishing stable ionic pairs (Hou and Li, 2014, Zhou et al., 2016). MD was used to compute the Cl^- and cation diffusion coefficients, and it was discovered that the coefficient is dependent on pore size, concentration, and force field (Pan et al., 2010, Hou and Li, 2014, Bonnaud et al., 2016, Zehtab and Tarighat, 2016, Hou et al., 2017a, Li et al., 2017a, Duque-Redondo et al., 2018, Wang et al., 2019, Liu et al., 2020, Duque-Redondo et al., 2021a, Duque-Redondo et al., 2021b). The effects of ultra-confined water in C-S-H on the mechanical properties were investigated by Sun et al. (Sun et al., 2021a). The results indicated that nano-pore size affected water distribution and chemical interactions and increasing water content weakened the cohesion and brittleness of C-S-H. Liu et al. (Liu et al., 2021) utilized MD simulations to examine the mechanism of transporting multiple ions in unsaturated gel nanopores C-S-H. The impact of the electrical double layer and percolation effect on ion transport was observed through changing parameters such as pore size and initial saturations. Hamadouche et al. (Ait Hamadouche et al., 2023) used MD simulations to investigate C-S-H's frequency-dependent dielectric response in the 0-1000 GHz range. They discovered anisotropic and pore size-dependent responses and developed homogenization models for non-destructive testing of cement-based materials. Honorio et al. (Honorio et al., 2022) used MD simulations to examine the

water diffusion and transition from glassy to Fickean-dominated dynamics in C-S-H with varying pore sizes. They proposed an expression to capture the pore size and temperature dependence of water self-diffusion in C-S-H. T. Honorio (Honorio, 2024) reported Non-Equilibrium MD simulations of water confined in C-S-H nanopores of varying sizes, with a focus on permeability, boundary conditions, and viscosity. The study emphasized the significance of slip boundary conditions and confinement-dependent viscosity in accurately measuring water permeability in C-S-H gel.

In addition, Wang et al. (Wang et al., 2020a) studied the effect of temperature on the transport behaviours of sodium sulfate solution (1mol/L) in the C-S-H nano-pores. They observed that as the temperature increased, the transport rate of sodium and sulfate ions decreased due to the weakening of the hydration shells of sodium and sulfate ions and the precipitation of calcium sulfate. Wen et al. (Wen et al., 2022) investigated the effect of temperature on the transport behaviours of sodium chloride (NaCl) and sodium sulfate solution in calcium aluminate silicate hydrate (C-A-S-H) nano-pores. They found that while water transport increases with temperature, ion movement decreases due to cluster formation and necking. Xiang-peng et al. (Xiang-peng et al., 2023) investigated the adsorption of Cl^- ions by C-S-H at various temperatures and pH levels. The study used experiments, thermodynamic calculations, and MD simulations to show that temperature, pH, and Ca^{2+} concentration all influence Cl- adsorption capacity. Hu et al. (Hu et al., 2024) used MD simulation to investigate the transport of water and Cl^- ions in the gel pores of C-S-H at different temperatures. The study discovered that the dynamic properties of water and ions are highly dependent on temperature. All those prior studies have investigated the transport of NaCl solutions in C-S-H, more focusing on dynamic properties. However, to

the best of our knowledge, limited work has yet investigated the effect of pore size and temperature on the NaCl solution transport and local structure in C-S-H nano-pores.

The primary objective of this paper is to investigate the effect of pore size and temperature on the transport behaviours of NaCl solution in Tobermorite (a representative C-S-H model) pores using the MD method. The C-S-H nanochannels were created to represent C-S-H pores by splitting two parallel C-S-H layers. The distance between the two C-S-H layers varied from 35, 65, to 95 Å, and the system temperature was set at 275-350 K. The mean square displacement (MSD) was used to investigate the influences of temperature and gel pore size on the diffusion characteristics of NaCl solution in the C-S-H nanochannels. The dynamic contact angle was used to evaluate the hydrophilicity of the C-S-H layer under the influence of temperature and pore size. In addition, atomic intensity diagrams, interfacial bonding at the solid-liquid interface, and radial distribution function (RDF) plots were used to examine the ion distribution and local structure evolution in the C-S-H nanochannels.

3.2 Methodology

3.2.1 Model Construction

The capillary transport model for the penetration of NaCl solution into the C-S-H nanochannel is illustrated in Figure 3.1. It comprises two main components: the C-S-H nanochannel and the 1 mol/L NaCl solution. A higher salt concentration is used in this study to eliminate individual ions' random impact and make the results more reliable. The C-S-H nanochannel is composed of two parallel C-S-H sheets with a thickness of approximately 23 Å. It was created by cleaving the tobermorite-11Å crystal along the [001] direction. Tobermorite-11Å crystal was used because it has a similar layered structure and

chemical composition to realistic C-S-H (Kai et al., 2022). To investigate the effect of pore size on the transport behaviours of NaCl solution in C-S-H gel, the splitting distance between two parallel C-S-H sheets was set to 35, 65, and 95 Å. These pore sizes were selected because the gel pore size ranges from 5-100Å which is long enough to get stable results.

The 1 mol/L NaCl solutions were prepared by packing water molecules, Na^+ ions, and Cl^- ions (number ratio = 55.5: 1: 1) into the simulation boxes with a pre-defined 1 g/cm^3 density. The box size along the *x* and *y* directions were constant, equal to 39 Å and 200 Å, respectively, and along the *z* direction, the box size was equal to the sum of the pore size and thickness of the two C-S-H sheets. After packing, the NaCl solutions were placed at the entrance (left side) 10 Å away from the C-S-H nanochannel. To prevent water molecules and ions from random escape during the thermodynamics process before penetration, vacuum spaces of 50 Å and 70 Å were set on the left and right sides of the simulation box in the *y* direction.

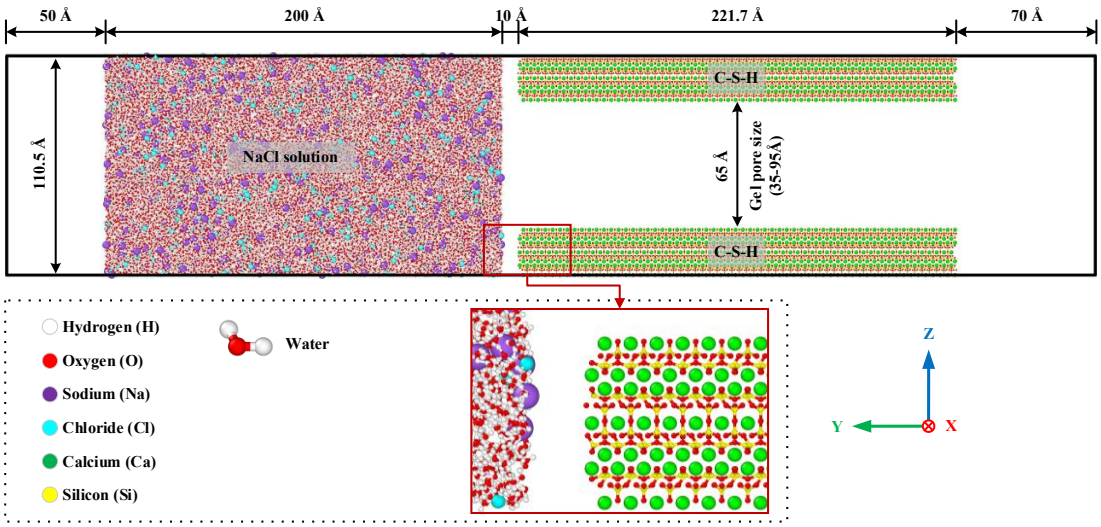

Figure 3.1. Transport model of NaCl solution in the C-S-H channel with a pore size of 65 Å.

3.2.2 Force Field and Molecular Dynamic Procedure

The selection of an appropriate force field is of utmost importance in MD simulations, as it has a substantial influence on the accuracy and reliability of the obtained results. The ClayFF force field (Cygan et al., 2004), developed based on a detailed analysis of experimental X-ray diffraction data and density functional theory (DFT) calculations, was validated to be accurate for the simulation of C-S-H systems and their interfaces with aqueous solutions. Previous studies have extensively used this force field to simulate clay, bulk and confined solutions, and the solution-clay interfaces (Hou et al., 2018b, Zhang et al., 2017, Zhou et al., 2018, Zhou et al., 2016). In addition, the ClayFF force field can successfully simulate the mass transport of water and ions in cement hydrates at the molecular level (Hou et al., 2017b, Yang et al., 2019a). This study used the arithmetic mixing rule to calculate the interatomic interactions, utilizing the Lennard-Jones function and the Coulomb formula. The cut-off distance for the interatomic interactions was set to 12 Å, and the particle-particle particle-mesh (PPPM) algorithm was used to consider the long-range Coulombic interactions.

The methodology used in this study is illustrated in Figure 3.2. All simulations were carried out using LAMMPS (Plimpton, 1995, Jam et al., 2022, Noori et al., 2021), a large-scale atomic/molecular massively parallel simulator. Initially, the C-S-H sheets and NaCl solution were thermodynamically relaxed under the canonical ensemble (NVT) at 300 K for 500 ps to obtain a well-equilibrated C-S-H structure and NaCl solution. The Nose-Hoover thermostat was used to keep the system temperature constant (Hou et al., 2022). An invisible wall was placed between the solution and the C-S-H gel pore to prevent water and ions from entering the channel at this stage. After the relaxation, the transport process of NaCl solution into the C-S-H nanochannels was simulated at 300 K for 4000 ps. The

invisible wall was removed to allow free penetration of the NaCl solution into the C-S-H nanochannels. The NVT ensemble was used during the transport process, and the time step was 1 fs. To investigate the temperature effect, the relaxed system with a pore size of 65 Å was further set to 275-350 K. The Verlet algorithm was employed to compute the trajectory of atoms during the simulation. The periodic boundary conditions were used in all directions and two invisible walls were placed perpendicular to the y-direction to avoid the random escape of the solution (Yu et al., 2019, Hou et al., 2018a, Yang et al., 2019a).

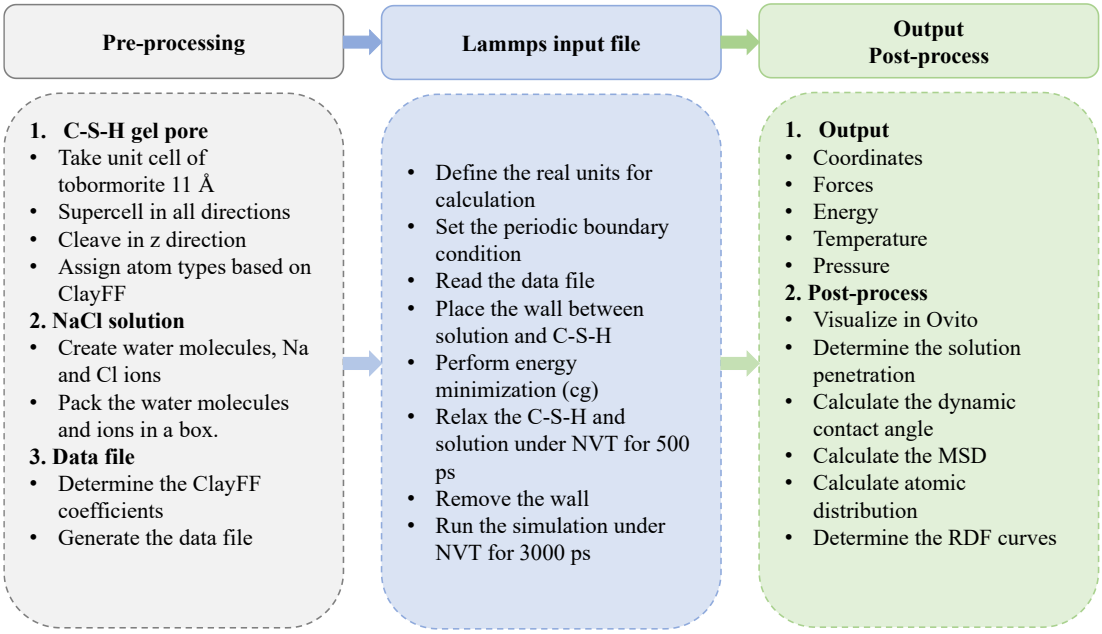

Figure 3.2. Illustration of NaCl solution transport in C-S-H gel using MD simulation.

3.3 Results and Analysis

3.3.1 The effect of pore size

3.3.1.1 NaCl solution transport in C-S-H nanochannel

Figure 3.3 illustrates the process of NaCl solution penetration into the C-S-H nanochannels with different sizes at 300 K. During the penetration process, the NaCl solution gradually penetrated the nanochannels with different sizes. The advanced solution front exhibited a

meniscus shape, a typical capillary adsorption characteristic. The contact angle between the advancing solution and the C-S-H substrate was less than 90°, indicating the hydrophilic nature of the surface. As water molecules preferred to transport near the hydrophilic surface and moved relatively slowly in the centre of the nanochannel, the contact angle gradually decreased during the penetration process, which aligns with previous research (Hou et al., 2020) and can be explained through molecular kinetic theory (Berg, 1993). In addition, it was observed that with the increase in penetration time, the ions in solutions were gradually filtered by the C-S-H nanochannel. For example, in Figure 4.3(a), at 500 ps, the ions in solutions were randomly distributed within the channel, whereas at 3000 ps, only a handful of ions further penetrated into a deeper distance in the nanochannel. This phenomenon indicates that the nanochannel has a filtration effect on the ions during the penetration process.

Comparing Figures 3.3(a) and 3.3(b) revealed that the NaCl solution penetrated into the C-S-H nanochannels with larger sizes faster than those with smaller sizes. For example, the penetration process in the C-S-H nanochannel with a size of 95 Å was completed after 3000 ps, while that with a size of 35 Å was only 174 Å. This phenomenon was consistent with the freshwater penetration process in pores with different sizes, which was due to the fact that smaller pore size provides less space for the solution to transport. In addition, for larger pore size (Figure 3.3b), more ions in solutions were observed to penetrate into the C-S-H nanochannel together with water molecules, indicating that with the increase of pore size, the filtration effect disappeared gradually. The potential mechanism can be as follows: In the case of a small pore, the volume of the penetrated solution and the total number of ions are also small, while the pore surfaces exert a strong attraction on the ions from the solution (as indicated by the following MSD data, Figure 3.4), leading to the

purification of the penetrated solution (the filtration phenomenon). On the other hand, for a large pore, both the volume of the penetrated solution and the total number of ions are significant. But its pores surfaces exhibit a weak attraction on the ions from the solution, particularly in the middle regions (as indicated by the following MSD data, Figure 3.4). Consequently, the filtration effect gradually diminishes for larger pores.

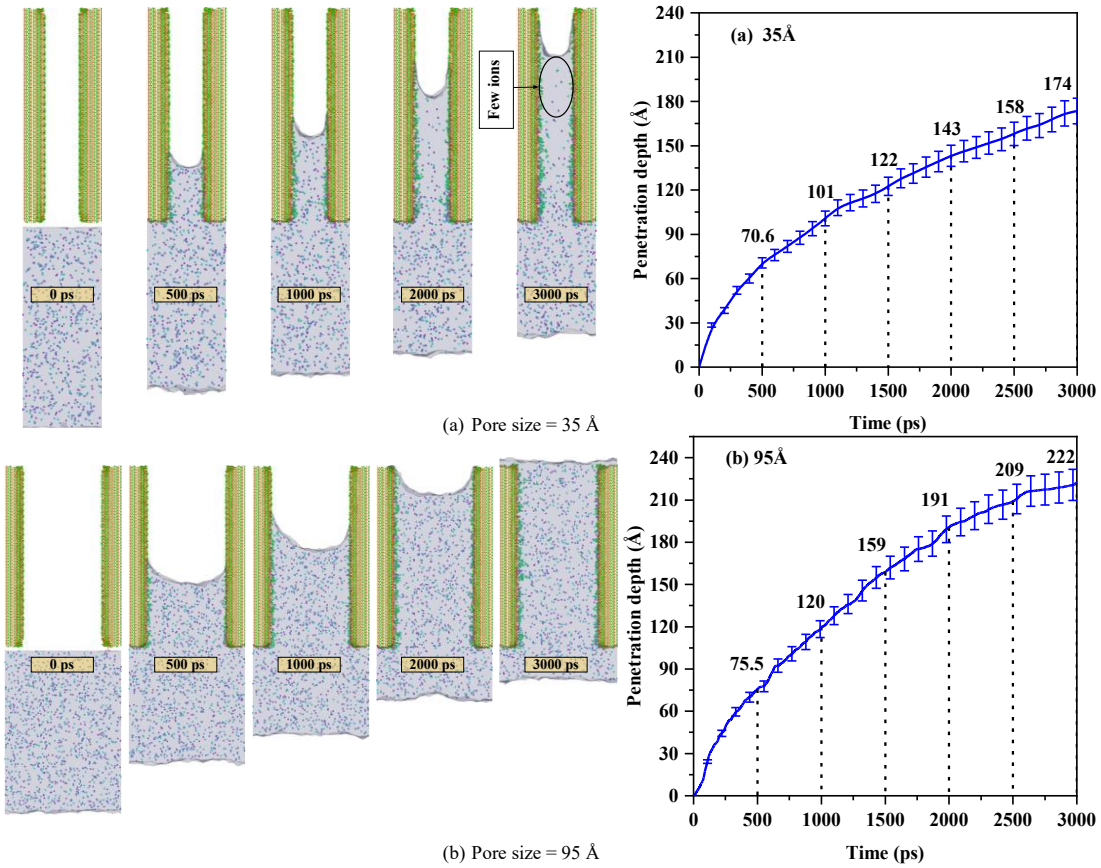

Figure 3.3. Snapshots of the penetration process and recorded penetration depth of NaCl solution in C-S-H nanochannels with (a) pore size = 35 Å and (b) pore size = 95 Å.

3.3.1.2 Mean square displacement (MSD) analysis

MSD is a crucial metric for characterizing the transport rate of molecules or ions in a system (Luo et al., 2023b, Kai et al., 2020, Tang et al., 2019b). In this work, the following

equation was used to calculate the MSD along the *y*-axis of water molecules and ions in the C-S-H nanochannels:

$$\text{MSD} = \langle \Delta \boldsymbol{y}^2(t) \rangle = \sum_{i=1}^{N} |\boldsymbol{y_i}(t) - \boldsymbol{y_i}(0)|^2 = \langle |\boldsymbol{y_i}(t) - \boldsymbol{y_i}(0)|^2 \rangle \quad (3.1)$$

where $\boldsymbol{y_i}(t)$ denotes the position of the atom $\boldsymbol{i}$ at time $\boldsymbol{t}$ along the y-axis while $\boldsymbol{y_i}(0)$ represents its initial position along the y-axis at the beginning of the simulation.

Figure 3.4(a) displays the MSD curves of water molecules and ions in the C-S-H nanochannels in three sizes (35, 65, and 95 Å). For all cases, the MSD values followed the sequence: water > Cl^- > Na^+, consistent with earlier findings (Zhang et al., 2017, Zhou et al., 2016). Comparing Figures 3.4 (a1-a3) revealed that the MSD of water molecules and ions was dependent on the pore size and increased as the pore size increased. In addition, the difference among the MSD curves of water, Na^+, and Cl^- became smaller when the pore size increased, and the curves were nearly identical when the pore size reached 95 Å. It agreed with the findings from Figure 3.3 that the filtration effect disappeared gradually with the increasing pore size.

The diffusion coefficients were calculated based on the recorded MSD data within the time range from 3 ns to 4 ns, following the method in Ref (Kai et al., 2023c). Figure 3.4(b) shows the calculated diffusion coefficient of the penetrated solution within the nanochannels along the *z*-direction. The obtained results are in good agreement with the existing literature (Zehtab and Tarighat, 2016, Zhou et al., 2016, Liu et al., 2020), with minor differences due to the use of different models, solution concentrations, and pore sizes. Across all cases, the diffusion coefficient of the solution increased when the solution was gradually away from the C-S-H surface, reaching its maximum in the middle region of the nanochannels. This is because the confinement on the solution caused by the adsorption

of C-S-H was strong near the C-S-H surface and became weaker and weaker when approaching the middle region of the nanochannels. Comparing Figures 3.4(b1-b3) revealed that a larger pore size could induce a faster diffusion of the penetrated solution, indicating that the increase in pore size can effectively weaken the confinement on the penetrated solution, no matter near the C-S-H surface or in the middle region of the nanochannels.

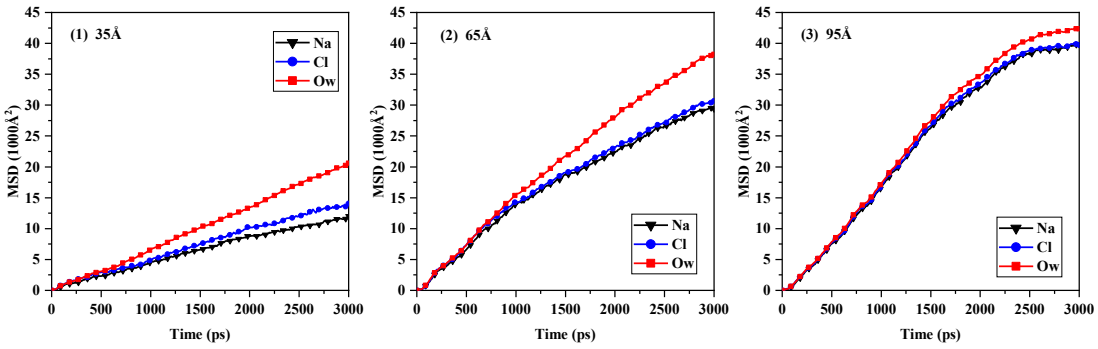

(a) MSD of water and ions in the C-S-H nanochannels

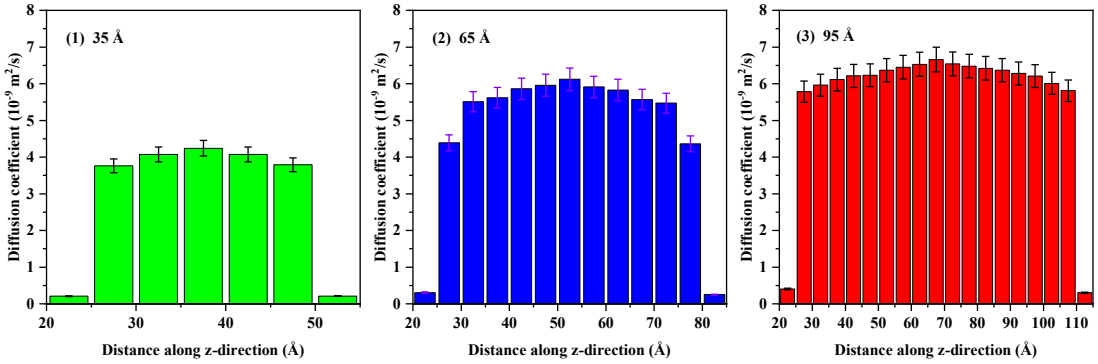

(b) Diffusion coefficient of solution in the C-S-H nanochannels

Figure 3.4. (a) MSD of water molecules and ions in the C-S-H nanochannel with pore size = 35, 65, and 95 Å; (b) Diffusion coefficient of water molecules and ions in the C-S-H nanochannel with pore size = 35, 65, and 95 Å.

The diffusion coefficient was calculated by the myopic algorithm recording the atomic diffusion within the time range from 3 ns to 4 ns, which was used to compare the difference between the diffusion rates at different regions.

3.3.1.3 Dynamic contact angle

The dynamic contact angle refers to the technique that measures the contact angle during movement, which can describe how the liquid spreads or retracts on a solid surface over time (Hou et al., 2020, Hou et al., 2018b). In this work, the dynamic contact angle of the NaCl solution on the C-S-H surface during the penetration process was calculated, as shown in Figure 3.5.

For all cases, the solutions were initially placed at the entrance of the nanochannel, yielding a dynamic contact angle of 90°. As the penetration process began, the dynamic contact angle decreased quickly because the NaCl solution at the entrance climbed along the C-S-H surface owing to the solid-liquid interactions (first stage). As a result, the shape of the penetrating solution changed from a roughly flat surface to a concave meniscus, resulting in a significant decrease in the dynamic contact angle. However, it should be noted that at this stage, the NaCl solution almost did not penetrate in the middle region of the nanochannel. Subsequently, the dynamic contact angle increased a little as the solution in the centre of the meniscus started to move into the nanochannel faster than that near the C-S-H surface, resulting in an increase in dynamic contact angle (second stage). This stage stayed for a short period, after which the dynamic contact decreased gradually again as it was a stable penetration process at this stage (third stage). The evolution of the dynamic contact angle was in line with that observed by A et al. (A et al., 2022), who measured the dynamic contact angle of the freshwater-penetrated nanochannels. By comparing Figures 3.5(a-c), it can be observed that the pore size had a limited effect on the dynamic contact

angle at the first stage because the evolution of the dynamic contact angle at this stage originated from the NaCl solution at the entrance climbing along the C-S-H surface, which was the same for all the cases. However, the larger pore size indicated a longer second stage, indicating that a longer time was needed to reach the stable penetration process for the transport model with a larger pore size. Besides, the dynamic contact angle at the third stage increased as the pore size increased, indicating a more curved meniscus. According to the Young-Laplace equation, the curvature of the meniscus in a nanochannel is inversely proportional to its radius (Liu and Cao, 2016), which agrees with the current findings.

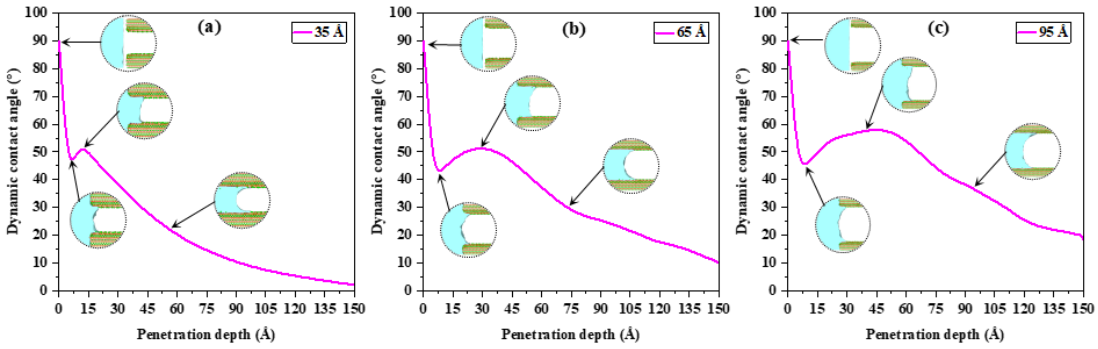

Figure 3.5. The dynamic contact angle of the NaCl solution on the C-S-H gel surface with different gel pore sizes over the penetration depth (a) 35 Å, (b) 65 Å, (c) 95 Å.

3.3.1.4 The atomic intensity curve

Atomic intensity curves can evaluate the distribution of molecules or ions in the C-S-H nanochannels (Hou et al., 2018a). Figure 3.6(a) shows the atomic intensity curves of Na^+ and Cl^- in the C-S-H nanochannels along the z-axis after the penetration process. A peak for Na^+, close to the C-S-H surface, was observed for all the cases, indicating that the Na^+ ions were attracted to the C-S-H surface because the abundant O on the C-S-H structure provided the coordination sites for Na^+. The adsorption of Na^+ led to the surface being positively charged, and thus a peak for Cl^- appeared at the outer side near the peak for Na^+,

as previously found in Ref. (Hou and Li, 2014, Zhou et al., 2016). Therefore, it can be concluded that double layers of ions (one layer of Na^+ on the inner side and one layer of Cl^- on the outer side) were adsorbed on the C-S-H surfaces, which agreed with the phenomenon observed in Ref. (Kai et al., 2023a). By comparing Figures 3.6(a1-a3), it can be found that the atomic intensity of Na^+ and Cl^- in the middle region of the nanochannel became higher with the increase in pore size, which was in agreement with the filtration phenomena of the transport models with different pore sizes (Figure 3.3). As a result, the peak intensity for Na^+ and Cl^- near the C-S-H surface became larger when the pore size increased from 35 Å to 65 Å. However, the peak intensity for Na^+ and Cl^- only increased slightly when the pore size increased from 65 Å to 95 Å. It indicated that the O on the C-S-H structure was almost fully coordinated by Na^+ when the pore size reached 65 Å, and thus the limited Na^+ could be further adsorbed by the C-S-H surface with the further increase in pore size. Figure 3.6(b) shows the snapshots of Na^+ and Cl^- on the C-S-H surface. Obviously, there were double layers of ions adsorbed on the C-S-H surface, and more ions were adsorbed with the increase in pore size. This mechanism emphasizes the relationship between pore size, filtration effect, ion penetration, and surface adsorption, resulting in a better understanding of the observed trends.

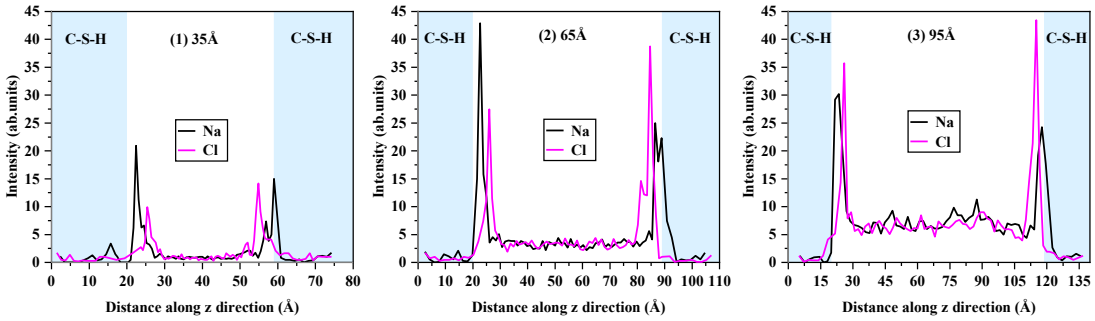

(a) Atomic intensity distribution

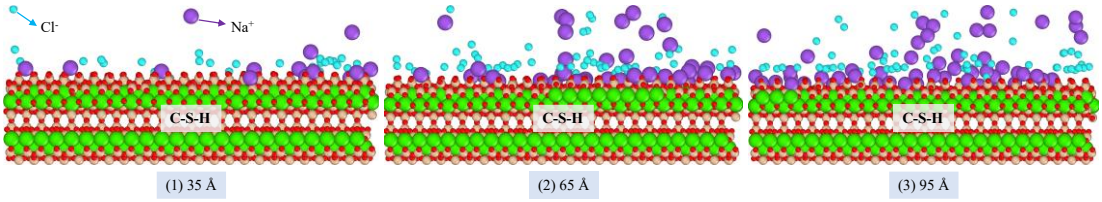

(b) Snapshots of Na^+ and Cl^- on the C-S-H surface

Figure 3.6. (a) Atomic intensity distribution of Na^+ and Cl^- inside the C-S-H nanochannel with different sizes; (b) Snapshots of Na^+ and Cl^- on the C-S-H surface of transport models with different pore sizes.

3.3.1.5 The interfacial bonding

There exist four types of interfacial bonding between the penetrated solution and C-S-H sheets, including ionic bonding Na-O_s (O_s: oxygen of C-S-H), Ca-Cl, Ca-O_w (O_w: oxygen of water), and hydrogen bonding H_w-O_s (H_w: hydrogen of water). The interfacial bond numbers were calculated after the penetration process in C-S-H nanochannels with different pore sizes, as shown in Figure 3.7(a). With the increase in pore size, there was an observed increase in the bond number of Na-O_s and Ca-Cl. This could be attributed to the larger number of ions (Na^+ and Cl^-) that penetrated the nanochannel as the pore size increases. As the pore size increases, so does the release of Ca ions from the C-S-H surface. This Na-Ca ion exchange increases the concentration of Ca ions in the solution, facilitating the formation of Ca-Cl bonds due to the strong affinity between Cl ions and Ca ions. However, the bond number of Ca-O_w and H_w-O_s exhibited a negative correlation with the pore size, which was because the existence of Na^+ and Cl^- on the C-S-H surfaces occupied the spaces, and thus the number of water molecules on the surface was reduced.

Along with the formation of the interfacial bonding after the penetration of NaCl solutions, it was observed that a few Ca^{2+} were dissociated from the C-S-H surface, as depicted in Figure 3.7(b). The number of dissociated Ca^{2+} were 10, 13, and 15 for the three cases with

the pore size = 35, 65, and 95 Å, proving that the increase in pore size caused more Ca^{2+} dissociation. This phenomenon could be attributed to the fact that the adsorption of Na^{+} on the C-S-H surface occupied, to some extent, the coordination sites of the exposed O on the C-S-H surface, which was originally occupied by Ca^{2+}. A similar phenomenon was observed in Ref. (Kai et al., 2023a), which studied the solid-liquid interfacial characteristics between C-S-H and NaCl solutions and named this phenomenon "Na-Ca" cation exchange.

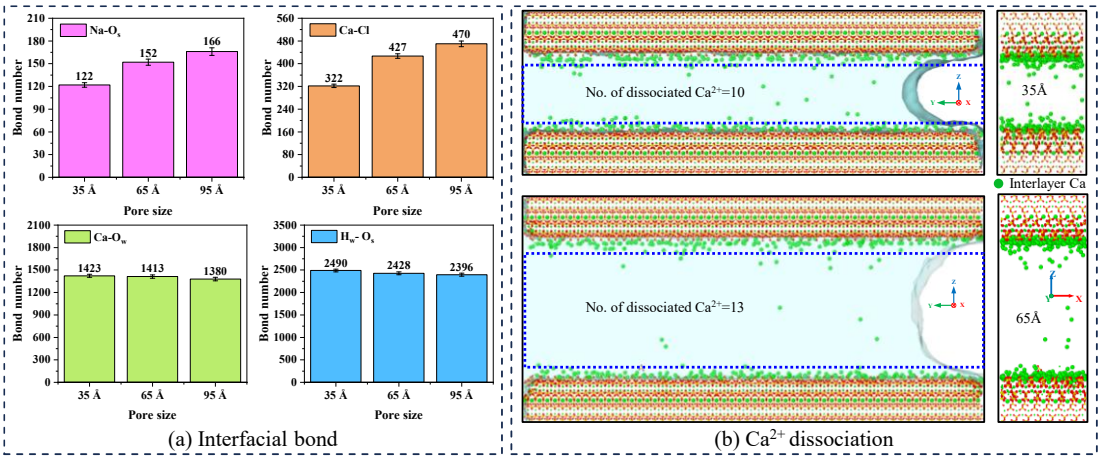

Figure 3.7. (a) Interfacial bond Na-Os, Ca-Cl, Ca-Ow, and Hw-Os between NaCl solution and C-S-H with different pore sizes at 300 K; (b) Dissociation of Ca^{2+} from the C-S-H surface at a pore size of 35 Å and 65 Å.

Note: The H_W-O_S bond is defined when the distance between these two atoms is less than 2.5 Å, according to the method proposed by Matsumoto (Matsumoto, 2007). Ca-O_W bond is determined when the distance between calcium-oxygen is less than 3.0 Å, according to the method proposed by Hou et al. (Hou et al., 2014a, Kai et al., 2023a).

3.3.1.6 Radial distribution function (RDF) analysis

RDF defines the probability of finding a particle at a certain distance from another particle (Kai et al., 2019). This function can evaluate the local configuration and degree of order of

ions and adjacent water molecules in different systems. The general expression to calculate the RDF is given below:

$$g(r) = \frac{dN/N}{dV/V} = \frac{V}{N}\frac{\langle N(r,\Delta r)\rangle}{4\pi r^2 \Delta r} \tag{3.2}$$

where r denotes the radial distance, $N(r, \Delta r)$ represents the number of atoms present in a shell volume of $4\pi r^2 \Delta r$ between r and Δr, and the bracket denotes the time average.

Figure 3.8 displays the RDF curves for Na-O_w, Cl-O_w, and Na-Cl pairs in the penetrated solutions in different pores (the atoms at the interlayer are not considered). For each pair, the peaks in RDF curves were located at the same position. For example, the first peak in RDF curves for Na-O_w, Cl-O_w, and Na-Cl pairs in all cases was located at ~ 2.4 Å, ~3.2 Å and ~ 2.9 Å, respectively. These values closely agreed with the experimental measurements obtained through X-ray and neutron diffraction (Pálinkás et al., 1980). However, the intensity of all the peaks in RDF curves decreased with the increase in pore size, indicating that the probability of finding a pairing ion in close proximity to a central atom was in negatively correlation with the pore size. The possible reason for this phenomenon could be attributed to the fact that larger pore size caused faster penetration in the C-S-H nanochannel, and thus the molecules and ions were more strongly fluctuated in the penetrated solution (as indicated in Figure 3.4a), leading to a less probability for the pairs in the solutions to find each other. In addition, the coordination number (CN) of Na^+ and Cl^- was determined by counting the number of nearest neighbours within the first peak of the corresponding RDF curve, as labelled in Figure 3.8. Obviously, the CN of Na^+ and Cl^- decreased with the increase in pore size, demonstrating that the coordination probability of them was reduced by increasing the pore size.

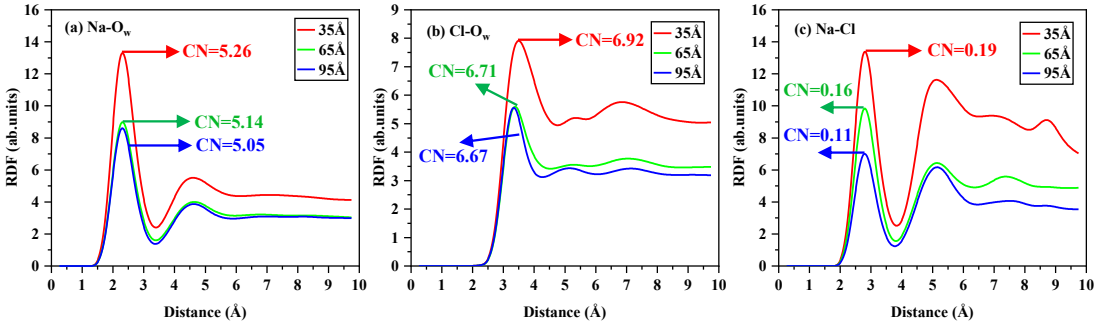

Figure 3.8. Radial distribution function of (a) Na-Ow, (b) Cl-Ow, and (d) Na-Cl.

Note: Ow and Os represent oxygen in water molecules and oxygen in silicate chain, respectively

3.3.2 The effect of temperature

3.3.2.1 NaCl solution transport in C-S-H nanochannel

Figure 3.9 illustrates the penetration process of NaCl solution into the C-S-H nanochannels (35 Å and 65 Å) at different temperatures (275 K and 350 K). It can be observed that the penetration rate of NaCl solution into the C-S-H nanochannels increased significantly at higher temperatures. The C-S-H nanochannel with pore size of 35 Å had a penetration depth of 149 Å at 275 K, which increased to 221 Å at 350 K after a simulation time of 3000 ps. On the other hand, the C-S-H nanochannel with pore size of 65 Å had penetration depths of 142 Å and 215 Å at 275 K and 350 K, respectively, after a simulation time of 2000 ps. These findings suggest that higher temperatures promote deeper penetration depths in both nanochannels. This was due to the increased kinetic energy of the molecules at higher temperatures, which facilitated their entry into the nanochannel.

In addition to affecting the penetration rate, the temperature impacted the filtration effect of C-S-H nanochannels on the ions in the NaCl solution. In the 35 Å C-S-H nanochannel (Figure 3.9a), there were a few ions (i.e., Na^+ and Cl^-) at 275 K, while almost no ions

existed in the 35 Å C-S-H nanochannel at 350 K. In the 65 Å C-S-H nanochannel (Figure 3.9b), the ions penetrated freely into the nanochannel at 275 K, indicating no obvious filtration effect. But when the temperature rised up to 350 K, the ions in the nanochannel became less, proving that the 65 Å nanochannel had a filtration effect at the higher temperatures.

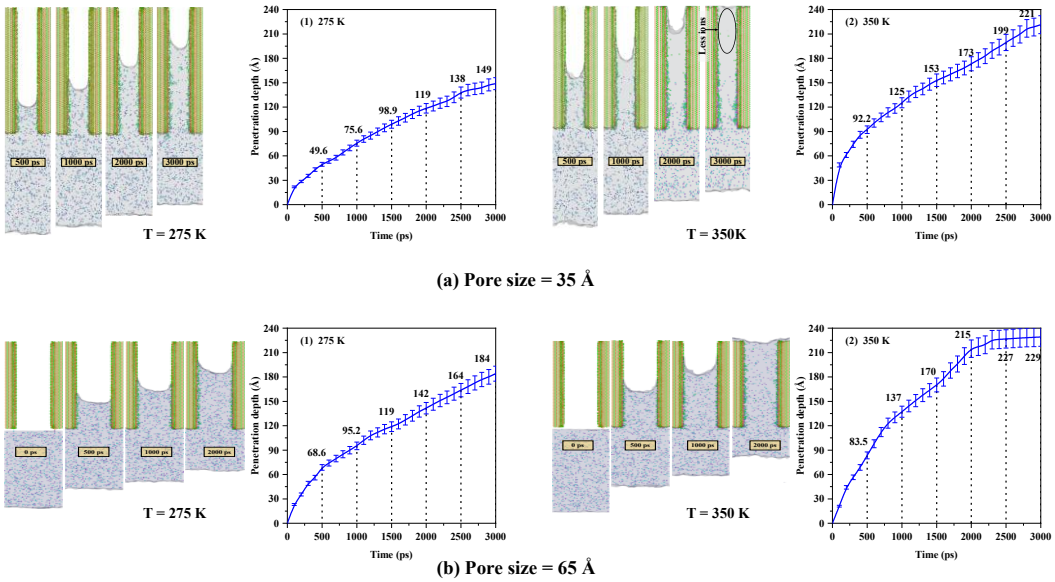

Figure 3.9. Transport process of NaCl solution in the 35 Å and 65 Å C-S-H nanochannels at 275 K and 350 K.

3.3.2.2 MSD analysis

Figure 3.10(a) displays the MSD curves of water molecules and ions in the 65 Å C-S-H nanochannels at various temperatures at 275-350 K. Comparing Figures 3.10(a1-a6) revealed that the MSD of water molecules and ions increased as the temperature increased, attributed to that higher temperature enabled the ions and water to move more freely through the channel by overcoming energy barriers. This observation aligned with findings from experimental studies (Touil et al., Shao et al., 2016). In addition, as the temperature increased, the MSD values of water increased relative to those of Na^+ and Cl^- ions,

indicating that water penetrated the solution faster than the ions. In other words, at higher temperatures, the ions in the solution were filtrated, which corresponded to the filtration phenomenon observed in Figure 3.9(b).

Figure 3.10(b) illustrates the diffusion coefficient of the penetrated solution within the 65 Å nanochannel along the *z*-direction at different temperatures (275 K, 325 K, and 350 K). Across all cases, the diffusion coefficient gradually increased with distance along the *z*-direction, reaching its maximum in the middle region of the nanochannel, which is a typical diffusion characteristic of solutions in a nanochannel. Comparing Figures 3.10(b1-b3) revealed that a higher temperature could induce a faster diffusion of the penetrated solution, irrespective of near the C-S-H surface or in the middle region of the nanochannel. This is due to the increased kinetic energy of the penetrated solution at a higher temperature, which improves diffusion across the nanochannel.

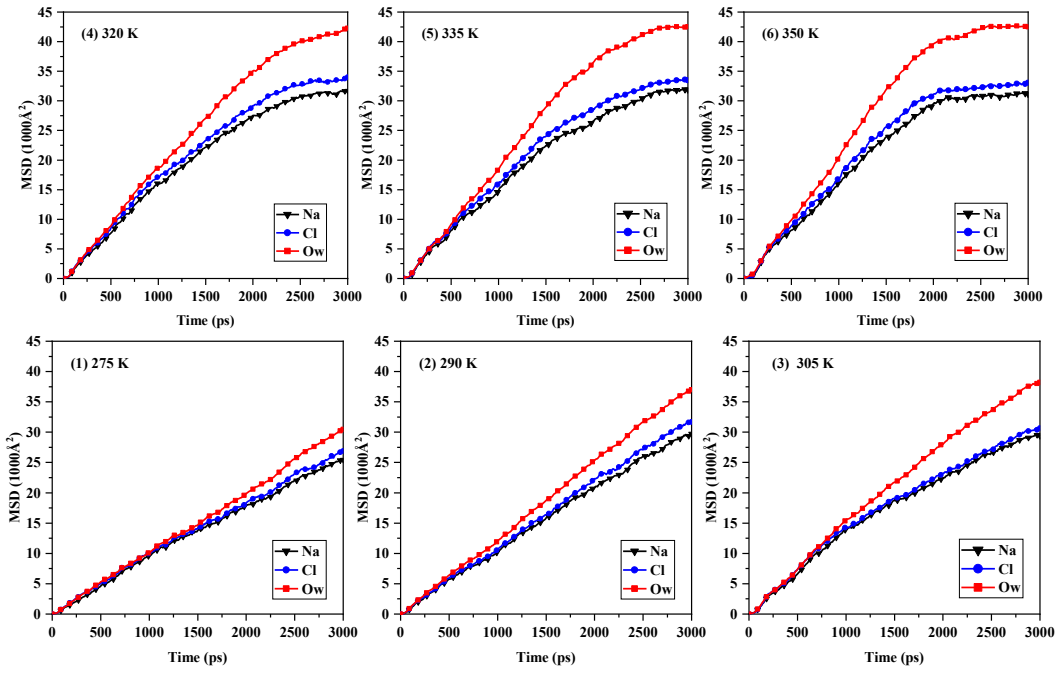

(a) MSD at various temperatures.

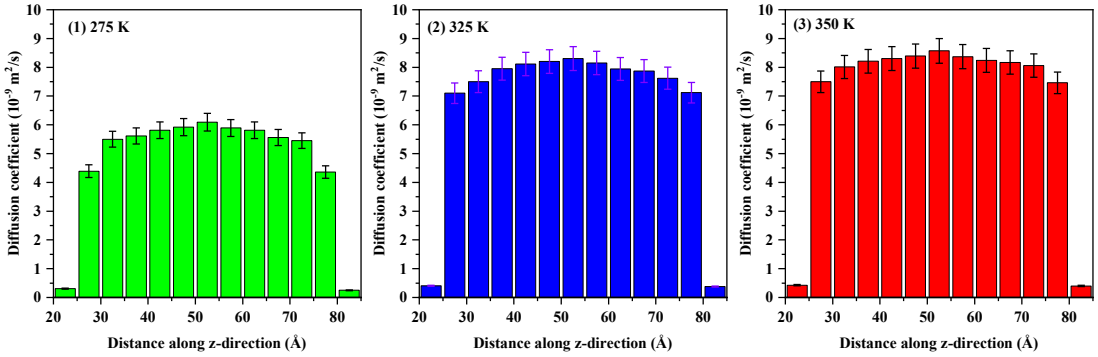

(b) Diffusion coefficient along the z-direction.

Figure 3.10. (a) MSD of water molecules and ions in the 65 Å C-S-H nanochannel at temperature = 275, 325, and 350 K; (b) Diffusion coefficient of water molecules and ions in the 65 Å C-S-H nanochannel at temperature = 275, 325 and 350 K.

3.3.2.3 Dynamic contact angle

Figure 3.11 shows the dynamic contact angle of the NaCl solution with the C-S-H surface during the penetration process at three different temperatures (275, 325, and 350 K). The dynamic contact angle underwent three stages for all cases, as discussed in Section 3.3.1.3. By comparing Figures 3.11(a), (b), and (c), it can be observed that the temperature had a significant effect on the dynamic contact angle at different stages. In the first stage, the dynamic contact angle experienced a faster drop during this stage at a higher temperature. It indicated that high temperature could accelerate the climbing of NaCl solution along the C-S-H surface at the entrance of the nanochannel. In the second stage, with the increase in temperature, the duration of this stage became longer, which stated that a longer penetration time was needed to reach the stable penetration process. At the third stage, the NaCl solution penetrated into the nanochannel stably, and a higher temperature accelerated the drop of dynamic contact angle at this stage. Overall, high temperature facilitated better wetting of the C-S-H surface and reduced the contact angle between the solution and the

surface. In other words, the hydrophilicity of the C-S-H surface increased with the temperature rise. This was consistent with the behaviour observed in previous studies (Bera et al., 2012, Hou et al., 2020, A et al., 2022).

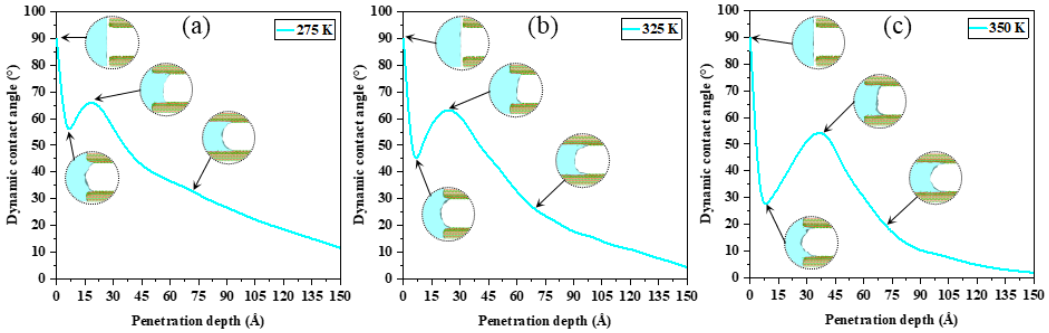

Figure 3.11. The dynamic contact angle of the NaCl solution on the C-S-H surface during the penetration process at different temperatures: (a) 275 K, (b) 325 K, and (c) 350 K.

3.3.2.4 The atomic intensity curve

Figure 3.12(a) shows the atomic intensity curves of Na^+ and Cl^- in the 65 Å C-S-H nanochannels along the *z*-axis after the penetration process at three different temperatures (275 K, 325 K, and 350 K). In the middle region, the atomic intensity of Na^+ and Cl^- became smaller with the increase in temperature. It stated that less Na^+ and Cl^- were penetrated into the C-S-H nanochannel at higher temperatures, agreeing with the filtration phenomenon observed in Figure 3.9(b) at higher temperatures. Near the C-S-H surface, the peaks for both Na^+ and Cl^- ions became sharper as the temperature increased, suggesting better adsorption by the C-S-H surface (Wen et al., 2022). This was because elevated temperatures reduced the hydration layer surrounding the ions, thus increasing their interaction with the C-S-H substrate. It is also worth noting that the peak intensity of Cl^- ions was closer to the interface at high temperatures than at low temperatures. Figure 3.12(b) shows the snapshots of Na^+ and Cl^- on the C-S-H surface. It can be observed that

the double layer of ions was adsorbed on the C-S-H surface, and more ions were adsorbed at higher temperatures, which agreed with the findings in Figure 3.12(a).

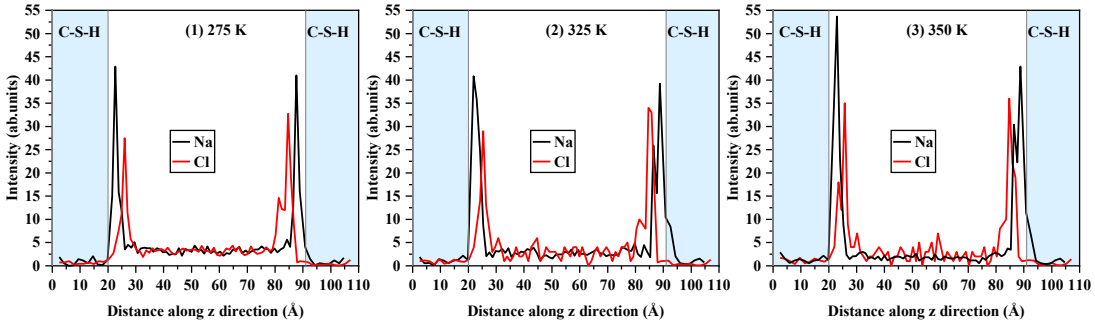

(a) Atomic intensity distribution

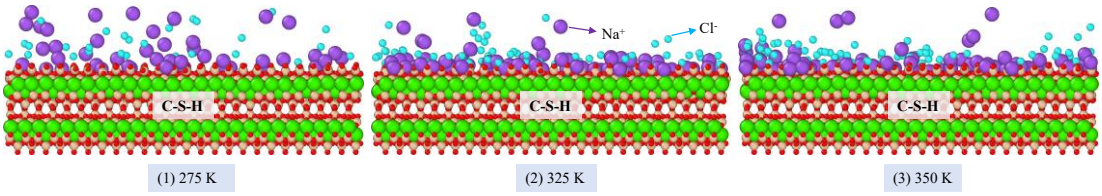

(b) Snapshots of Na^+ and Cl^- on the C-S-H surface

Figure 3.12. (a) Atomic intensity distribution of Na+ and Cl^- inside the C-S-H nanochannel at different temperatures; (b) Snapshots of Na+ and Cl^- on the C-S-H surface of transport models at different temperatures.

3.3.2.5 The interfacial bonding

The evolution of the interfacial bond numbers, including ionic and hydrogen bonding, was calculated after the penetration process in the 65 Å C-S-H nanochannel at different temperatures (275K-350K), as shown in Figure 3.13(a). As the temperature increased, the bond number of Na-O_s and Ca-Cl increased due to the adsorption of Na^+ and Cl^- on the C-S-H surfaces. However, the bond number of Ca-O_w and H_w-O_s exhibited a negative correlation with the temperature, which was because the number of water molecules on the

surface was reduced due to the existence of more Na^+ and Cl^- on the C-S-H surfaces, as explained in Section 3.3.1.5.

Along with the formation of the interfacial bonding after the penetration of NaCl solutions into the C-S-H nanochannel, it was observed that a few Ca^{2+} were dissociated from the C-S-H surface, as depicted in Figure 3.13(b). Temperature variations significantly influenced the dissociation of Ca^{2+}. The number of dissociated Ca^{2+} ions were 4, 17, and 19 for the three cases at temperatures = 275, 325, and 350 K, proving that the increase in temperature caused more Ca^{2+} dissociation. The temperature increased the kinetic energy of Ca^{2+} in C-S-H and decreased the reaction barrier, which facilitated the escape of Ca^{2+} from the geometrical and chemical constraints of silicate chains (Wang et al., 2020a). This phenomenon could also be attributed to the fact that the adsorption of more Na^+ on the C-S-H surface at higher temperatures caused more dissociation of Ca^{2+} ions from the surface (so-called "Na-Ca" cation exchange) (Kai et al., 2023a).

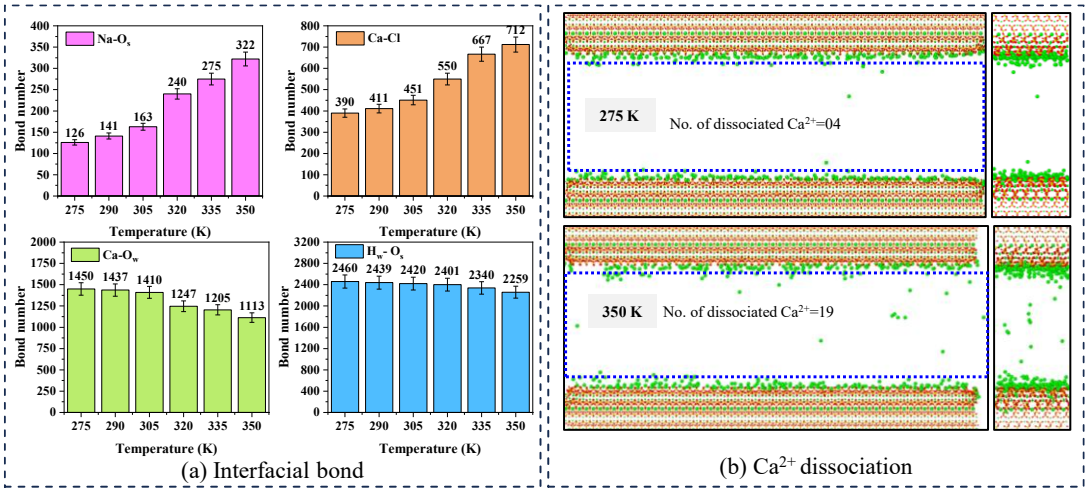

Figure 3.13. (a) Interfacial bond Na-Os, Ca-Cl, Ca-Ow, and Hw-Os of C-S-H gel with a gel pore size of 65 Å at 275-350 K. (b) Dissociation of Ca^{2+} from the C-S-H surface at a temperature of 275 K and 350 K.

3.3.2.6 RDF analysis

Figure 3.14 displays the RDF curves for Na-O_w, Cl-O_w, and Na-Cl pairs in the penetrated solutions at different temperatures (275, 325, and 350 K). The peak intensity in the RDF curves for Na-O_w and Cl-O_w pairs decreased with the increase in temperature, as depicted in Figure 3.14(a) and (b). This suggested that the likelihood of ions being located near water molecules decreased at higher temperatures. The reason for this phenomenon could be attributed to the fact that higher temperatures caused faster penetration of NaCl solution in the C-S-H nanochannel, and the molecules and ions in the penetrated solution were more strongly fluctuated, leading to a less probability for the pairs in the solution to find each other. However, the peak intensity in the RDF curves for the Na-Cl pair increased with the increase in temperature, as depicted in Figure 3.14(c) (Wen et al., 2022). It indicated that ions are more likely to be present near each other and the surface at elevated temperatures. In addition, the CN of Na^+ and Cl^- was determined by counting the nearest neighbors within the first peak of the corresponding RDF curve, as labelled in Figure 3.14 (Pálinkás et al., 1980, Hou et al., 2018b). The CN of Na^+ and Cl^- around water molecules decreased from 5.26 to 5.05 and from 6.74 to 6.62, respectively, with the increase in temperature, demonstrating that their coordination probability was reduced by increasing the temperature. However, the CN of Na^+ with Cl^- increased from 0.16 to 0.19 with temperature, as shown in Figure 3.14(c), indicating that the coordination probability of ion-ion was increased by increasing the temperature.

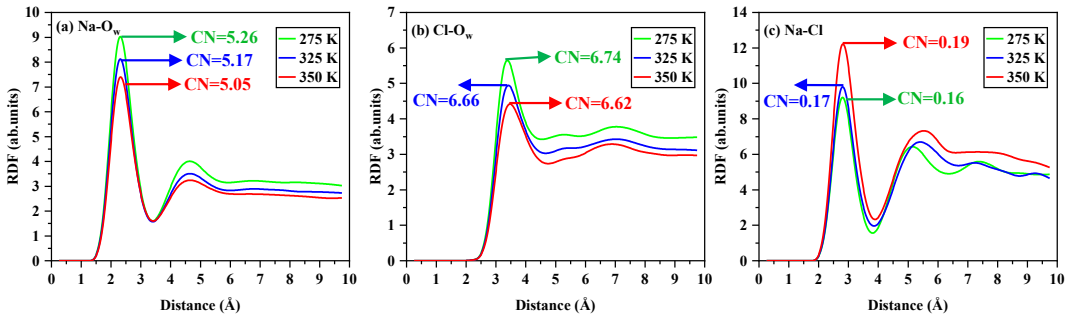

Figure 3.14. Radial distribution function of (a) Na-Ow, (b) Cl-Ow, and (c) Na-Cl at different temperatures (275, 325, and 350 K).

3.4 Summary

The transport of water and ions in the porous C-S-H gel plays a significant role in determining the concrete durability. This MD study has examined the effects of pore size and temperature, two important factors, on the transport of NaCl solution in the C-S-H nanochannels. The key findings are as follows:

(1) During ingress, the advancing solution front exhibited a meniscus-like shape, consistent with hydrophilic wetting and confined imbibition. Increasing pore size and temperature accelerated the overall penetration rate, reflecting reduced confinement resistance in larger pores and enhanced molecular mobility at higher temperature.

(2) In the smallest nanochannels, ions were retarded relative to water, leading to a confinement-controlled "filtration" behaviour (selective exclusion/retardation of ions rather than true membrane filtration). This effect weakened as pore size increased, whereas higher temperature tended to enhance ion-surface/ion-ion interactions and made the ion retardation more evident under strong confinement.

(3) Transport was spatially heterogeneous across the pore: motion in the pore centre was faster than near the C–S–H surface due to strong interfacial interactions and

hydration constraints close to the wall. Both increased pore size and higher temperature accelerated transport in all regions, but the near-surface region remained the most restricted.

(4) After penetration, ions reorganized at the interface and formed a stable interfacial double layer, with Na^+ enriched closer to the C-S-H surface and Cl^- preferentially located outside that layer. Larger pores and higher temperatures promoted stronger interfacial adsorption and more pronounced ion accumulation, indicating enhanced ion–surface association and interfacial restructuring.

(5) Ca^{2+} dissolution from the C-S-H surface was accelerated at larger pore sizes and higher temperatures, which correlated with increased Na^+ adsorption and interfacial exchange processes. In addition, larger pore size and elevated temperature reduced the extent of ion hydration constraints, implying more dynamic fluctuations and more frequent rearrangements in the confined NaCl solution.

These results identify nanoscale mechanisms that are difficult to isolate at larger scales, including (i) wetting/imbibition-like ingress with a meniscus-shaped front in hydrophilic confinement, (ii) confinement-driven selective ion retardation ("filtration") relative to water, (iii) near-surface versus pore-centre transport heterogeneity, (iv) formation of a stable interfacial ionic double layer, and (v) ion-induced Ca^{2+} dissolution and interfacial exchange. These coupled processes jointly control NaCl solution ingress under the studied conditions and help explain why transport in C-S-H nanopores cannot be fully captured by simplified continuum descriptions. In particular, classical flow models such as Lucas-Washburn-type approaches treat the liquid as a continuum and typically do not account for interfacial ion layering, selective ion retardation, or ion-specific surface interactions that emerge under nanoconfinement. Therefore, the findings provide mechanistic insight that

can support improved interpretation of durability-related mass transport and inform multiscale modelling of concrete exposed to saline environments

Chapter 4. NaCl solution confined in C-S-H nanopore

4.1 Introduction

Building on the findings from Chapter 3, which investigated the transport behaviour of NaCl solutions in C-S-H nanopores at different pore sizes and temperatures, it is also critical to investigate how these confined solutions evolve during drying. While transport determines ion ingress and redistribution inside saturated pores, desorption is the next stage in which water loss affects local structure, ionic distribution, and interfacial stability. Understanding this transition from transport to desorption is critical for getting the complete nanoscale picture of fluid behaviour in C-S-H and its implications for durability. Experimental studies on the sorption characteristics, drying shrinkage, strength, and elastic modulus of hardened cement paste have demonstrated that C-S-H exhibits a gel-like or colloidal nature, and its behaviour is strongly dependent on the surrounding water molecules (Scherer, 1999, Jennings, 2008). Studies have shown that increased relative humidity (RH) leads to reduced strength and elastic properties of cement-based materials, observed across higher (10–90%) and lower (10–40%) RH ranges through various measurement techniques at different scales (Burlion et al., 2005, Di Bella et al., 2016). Foundational studies by Wittmann (Wittmann, 1973) found that the Young's modulus of hardened cement paste changed during the initial drying process. As RH decreased from 90% to 40%, the Young's modulus decreased and reached a minimum at around 40% RH. However, as the humidity further decreased from 40% to 11%, the Young's modulus then increased. Wittmann attributed the increase between 40% and 11% RH to the decrease in surface free energy of the C-S-H gel, while the decrease from 90% to 40% RH was attributed to the disjoining pressure of the adsorbed water molecules. Despite varying RH

intervals, the weakening of material properties with increasing RH was consistently observed in more recent studies (Pimienta et al., 2014, Di Bella et al., 2016). Feldman and Sereda (Feldman and Sereda, 1968) proposed a model where the C-S-H gel layers rearrange during the initial desorption process, driven by capillary tension or surface's free energy, leading to a decrease in external surface area and irreversible shrinkage. A more recent study also concluded that the shrinkage observed during the initial desorption was irreversible due to the collapse of small pores (Maruyama et al., 2014).

Shrinkage in OPC is a significant issue caused by water loss from the nanopores of cement paste during drying. The challenge is further complicated when using seawater for concrete mixing, as the salts can alter the hydration process and affect shrinkage behaviour (Zhao et al., 2021, Ebead et al., 2022a). Khatibmasjedi et al. (Khatibmasjedi et al., 2019) investigated the drying shrinkage behaviour of cement mortars, with water-to-cement (*w*/*c*) ratios of 0.36 and 0.45. Their findings showed that at the lower *w*/*c* ratio of 0.36, the drying shrinkage was only marginally impacted by the use of seawater as the mixing water. However, at the higher *w*/*c* ratio of 0.45, the seawater mixtures exhibited notably greater drying shrinkage compared to the freshwater mixtures. Modupeola and Olutoge (Modupeola and Olutoge, 2014) found that concrete with a *w*/*c* ratio of 0.60 exhibited increased drying shrinkage when seawater was used as the mixing water, compared to using fresh water. The study by Younis et al. (Younis et al., 2018) revealed that the drying shrinkage of concrete made with seawater was consistently greater than that of concrete made with fresh water. The complexity of shrinkage and sorption experiments in cement-based materials, along with the intricate nature of the materials themselves, can make it difficult to distinguish the contributions of the many physical processes involved (Bisschop and Wittel, 2011, Gartner et al., 2017). In this regard, independent simulations modelling

these processes can offer valuable insights (Abdolhosseini Qomi et al., 2021). Additionally, surface adsorption and disjoining pressure effects, being nanometre-scale phenomena involving intermolecular interactions, can be advantageously studied through molecular simulations.

MD simulations in materials science offer promising insights into the nanoscale processes governing this phenomenon. Yang et al. (Yang et al., 2023) used MD simulations to investigate the crystallization of NaCl within the nanopores of C-S-H gels. They found that NaCl crystallization occurs in a two-stage process of nucleation and crystallization. Cations, particularly Na^+ ions, are adsorbed by the negatively charged C-S-H surface, with sorption behaviour modulated by both surface chemistry and pH-dependent charge development. Regarding water sorption, several studies have used MD to explore the effect of pore width, temperature, and Ca/Si ratio on the sorption, water structure, and mechanical properties (Bonnaud et al., 2013, Manzano et al., 2012b, Bonnaud et al., 2012b). Masoero et al. (Masoero et al., 2018) examined the impact of the nanostructure of C-S-H gel in hydrating cement paste on humidity and water content. The study highlighted limitations in current hydration models that do not account for this nanostructure, leading to the use of sorption isotherms and self-desiccation as inputs rather than predicted outcomes. The study by Masara et al. (Masara et al., 2023) found that the Kelvin-Cohan equations can effectively model sorption processes in larger C-S-H interlayer pores, but these equations do not apply at smaller pore sizes where only adsorbed water films are present. Hou et al. (Hou et al., 2014a) examined the structural, dynamic, and mechanical properties of C-S-H gels at different water contents. The findings indicated that higher water content induces a transition in C-S-H from an amorphous to a layered configuration, which significantly compromises tensile strength and stiffness due to the weakening of chemical bonding.

Bonnaud et al. (Bonnaud et al., 2016) found that properties such as density, diffusivity, and hydrogen bonding in nanoconfined water were notably influenced by temperature changes. For example, as temperature rises, density decreases and diffusivity increases. Additionally, they found that phase transitions in nanoconfined water differed from bulk water behaviour due to confinement, a critical factor for understanding the durability of cementitious materials under thermal stress. Honorio et al. (Honorio et al., 2023) found that the thermal desorption of water from C-S-H is driven by the thermal expansion of water and the transition from liquid to vapour phase. Additionally, water molecules far from the C-S-H surface desorb more easily. However, important questions remain unanswered (or, at least, poorly understood) regarding the desorption of NaCl solution confined in C-S-H gel pores. There is a lack of MD research on the desorption of water from NaCl solutions within the nanopores of cement-based materials. Understanding the interplay between the C-S-H nanostructure, water content, and the evaporation dynamics of NaCl solution is crucial for predicting and mitigating drying shrinkage in cement-based materials.

The primary objective of this study is to conduct a comprehensive investigation into the desorption of water from the NaCl solution confined in a C-S-H gel pore with a size of 3.5 nm under various conditions and compositions using MD. The study examines the impact of several key factors, including the presence of seawater with a 1M NaCl solution, varying Ca/Si ratios in the C-S-H structure ranging from 1.2 to 2.0, and the effect of fixed (NVT) versus shrinking (NPT) pores. By exploring these multifaceted parameters, the study seeks to gain deeper insights into the fundamental mechanisms governing water desorption and the resulting implications for drying shrinkage in cement-based materials. The findings from this study contribute valuable knowledge towards predicting and

mitigating drying shrinkage, a critical issue affecting the long-term performance and integrity of cement-based construction materials.

4.2 Methods and models

4.2.1 Computational model

The C-S-H gel represents the major hydration product in cementitious materials, and its structure is characterised by a highly disordered and imperfect atomic arrangement that can be described as a defective tobermorite (Richardson, 2004, Zhang et al., 2012, Pellenq et al., 2009). The fundamental structure comprises silicate chains connected to calcium oxide sheets, which constitute the primary binding phase within the hydrated cement paste. The C-S-H model used in this study is composed of two parts: the solid C-S-H layers and a nanopore of 3.5 nm filled with a 1M NaCl solution. The C-S-H structural models employed in this work were generated using the pyCSH Python code (Casar et al., 2024), an automated tool developed for creating atomic-level models of C-S-H based on the brick model (Mohamed et al., 2018). In this approach, each brick represents a fundamental structural unit of the C-S-H, which can be combined in different configurations to generate models with varying compositions. Five distinct models were created to represent Ca/Si ratios ranging from 1.2 to 2.0 to capture the compositional variability in C-S-H gel. For further details on the structural generation procedure, structural characterisation, and Ca/Si control are provided in the Supplementary Information (S.I.), along with the scripts used to generate the different models (Figures A1.1–A1.3) to ensure reproducibility.

An example of a generated C-S-H model with a Ca/Si ratio of 1.6 is shown in Figure 4.1. The initial system size consisted of 6 bricks along the *x*-direction, 6 bricks along the y-direction, and 3 bricks along the z-direction. The monoclinic C-S-H structural models

generated using the pyCSH code (see Figure 4.1(a)) were subsequently transformed into an orthogonal structure (see Figure 4.1(b)) to optimise the performance of the simulations since it reduces computational complexity and facilitates data processing. The final dimensions of the C-S-H models were x = 4.04 nm, y = 3.73 nm, and z = 4.20 nm. Then, a nanopore of 3.5 nm was created in the orthogonal models by cleaving the C-S-H structure along the [001] direction, as shown in Figure 4.1(c). This nanopore was designed to mimic the confined spaces within the C-S-H structure where ionic transport takes place, as used in previous studies (Hou et al., 2018a, Yang et al., 2019a). The choice of a 3.5 nm nanopore corresponds to the predominant pore size observed in C-S-H when the cement hydration degree reaches approximately 80% (Masoero et al., 2018), which is the typical cement hydration degree in reinforced concrete structures during their service life.

Once the nanopore was created, it was filled with a NaCl solution. To achieve this, the volume of the C-S-H nanopore (x = 4.04 nm, y = 3.73 nm, z = 3.5 nm) was calculated, and the corresponding number of molecules to simulate a 1M solution with a density of approximately 1.0 g/cm^3 was determined. This required 1699 water molecules, 32 Na^+, and 32 Cl^-, which were placed in random positions within the pore using the Packmol package (Martínez et al., 2009), ensuring an even initial distribution, as shown in Figure 4.1(d). This study uses a slightly higher salt concentration to reduce the variable effects of individual ions, hence improving the reliability of the results (Yang et al., 2019a). Three-dimensional periodic boundary conditions (PBC) were applied to minimise the impact of system size limitations.

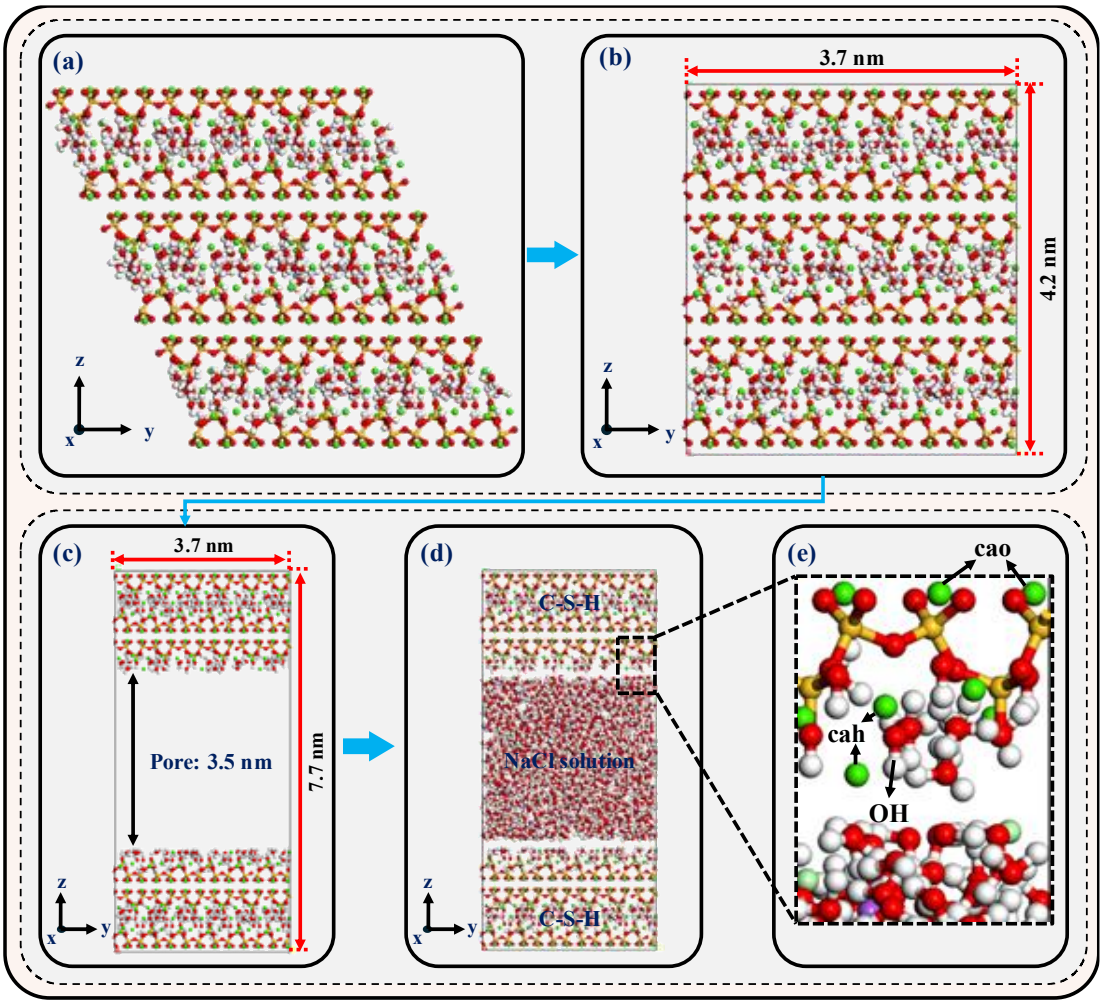

Figure 4.1. Model construction process for the C-S-H models with a nanopore of 3.5 nm: (a) Initial 6x6x3 monoclinic C-S-H model with Ca/Si = 1.6, (b) Transformation into an orthorhombic C-S-H model, (c) Creation of a 3.5 nm nanopore, (d) Insertion of a 1M NaCl solution into the nanopore, (e) A zoomed-in view of the pore wall region.

cao is intralayer calcium, cah is interlayer calcium, and OH is hydroxide (Note: Na^+, Cl^-, and Ca^{2+} ions are represented as purple, light blue, and green balls, while O, H, and Si atoms are shown as red, white, and yellow balls.)

4.2.2 Computational procedure

For this study, the ClayFF force field (Cygan et al., 2004) was selected based on its proven reliability in modelling C-S-H systems and their interactions with aqueous solutions (Zhou

et al., 2016, Hou et al., 2018b). It has been applied extensively to simulate clay materials, bulk and confined solutions, solution-clay interfaces (Zhou et al., 2018, Zhou et al., 2016, Zhang et al., 2017, Hou et al., 2018b), and to the adsorption of anions and cations on hydroxyl surfaces (Kalinichev et al., 2007, Dongshuai et al., 2016). ClayFF forcefield was employed in this study to realistically model the interactions between the C-S-H gel pore surfaces and the NaCl solution during the evaporation process. ClayFF parameters for all the species used in this study are provided in Table A1.1 of the Appendix 1.

The methodology followed in this study is summarized in Figure 4.2 and explained as follows. MD simulations were performed using the LAMMPS (Large-scale Atomic/Molecular Massively Parallel Simulator) software package (Plimpton, 1995). A Verlet algorithm was employed to integrate the trajectories with a time step of 1 fs. For the interatomic interactions, an arithmetic mixing approach was utilized to compute both the Lennard-Jones potential and the Coulomb formula for electrostatic interactions. A cutoff distance of 8 Å was applied for the short-range interactions, while the long-range Coulombic effects were treated using the particle-particle particle-mesh (PPPM) algorithm. The initial C-S-H gel pore models with the confined NaCl solution were first subjected to energy minimization using the conjugate gradient method. The equilibration of the models was performed in two steps using the NPT ensemble, allowing the system to relax and reach a stable configuration. In the first step, the system was gradually heated from 10K to 298K under the NPT ensemble (Tdamp = 100 fs, and P = 1 atm) for 0.5 ns. This controlled temperature ramp ensured a smooth relaxation of the system. In the second step, further equilibration was carried out under the NPT ensemble at room conditions (T = 298 K, P = 1 atm) for 20 ns, with a timestep of 1 fs. The Nosé-Hoover thermostat was used to keep the temperature constant. The trajectory output during equilibration was recorded every 50 ps.

Once the system is equilibrated, both canonical (NVT) and isothermal-isobaric (NPT) ensembles were employed to investigate the evaporation process by randomly deleting water molecules from the NaCl solution. The LAMMPS "fix evaporate" command was employed to randomly delete one water molecule from the simulation at intervals of 58 ps. In the first scenario, the NVT ensemble was used, and the size of the C-S-H pores was assumed to remain constant during the simulation, reflecting the microstructural constraints of the material. This allows for a more controlled analysis of the desorption of water molecules within the static nanopore environment. In the second scenario, the NPT ensemble was employed, allowing the nanopores to shrink during desiccation. This setup simulates conditions where drying induces pore contraction, enabling the study of the impact of pore shrinkage in the transport of NaCl ions and water molecules within the C-S-H structure. For both NVT and NPT ensembles, simulations were run for 100 ns at 298 K, with the evaporation of the water molecules from the NaCl solution set at a rate of one water molecule every 58 ps. This rate ensures that, by the end of the 100 ns simulations, all water molecules from the solution have been removed. The trajectory output during evaporation was recorded every 200 ps for data analysis.

TRAVIS (Trajectory Analyzer and Visualizer) (Brehm and Kirchner, 2011, Brehm et al., 2020) was used to postprocess all the trajectory files. The radial distribution function (RDF) represents the probability of finding a pair of particles at a specific distance from one another and is valuable for analysing the structural characteristics of the simulated system. It provides insights into the degree of structural ordering and the spatial correlation between ions and atoms by examining the size, width, and relative positions of the RDF peaks. The definition of RDF is given below:

$$g_{ab}(r) = \frac{V}{N_a \cdot N_b} \sum_{i=1}^{N_a} \sum_{j=i+1}^{N_b} \left\langle \delta\left(r - \left|\vec{r}_i(t) - \vec{r}_j(t)\right|\right)\right\rangle_t \quad (4.1)$$

where $\vec{r_i}$ and $\vec{r_j}$ represent the position vectors of the i-th and the j-th particles, respectively. The δ function equals 1 in the interval $[-w, w]$ (where w is the bin width) and 0 otherwise (Brehm and Kirchner, 2011).

The atomic density profiles were used to evaluate the spatial distribution of molecules or ions within the nanopore, thereby enhancing the understanding of the pore interface structure. Atomic density profiles represent the average count of atoms located within a distance range of z ± Δz/2 from a reference plane (Brehm and Kirchner, 2011):

$$\rho(z) = \langle \frac{1}{\sqrt{2\pi\Delta z}} \sum_i exp\left(-\frac{(z-z_i)^2}{2\Delta z}\right) \rangle \quad (4.2)$$

where z_i denotes the position of particle i, and the summation includes all particles located at a distance $z \pm \Delta z/2$ from the reference plane. Examining the ion density distribution on the pore surface can reveal the chemical and physical interactions between the C-S-H gel surface and the ions, indirectly suggesting the distribution of ion nucleation sites. OVITO (Stukowski, 2010) was used to visualise the resulting trajectories.

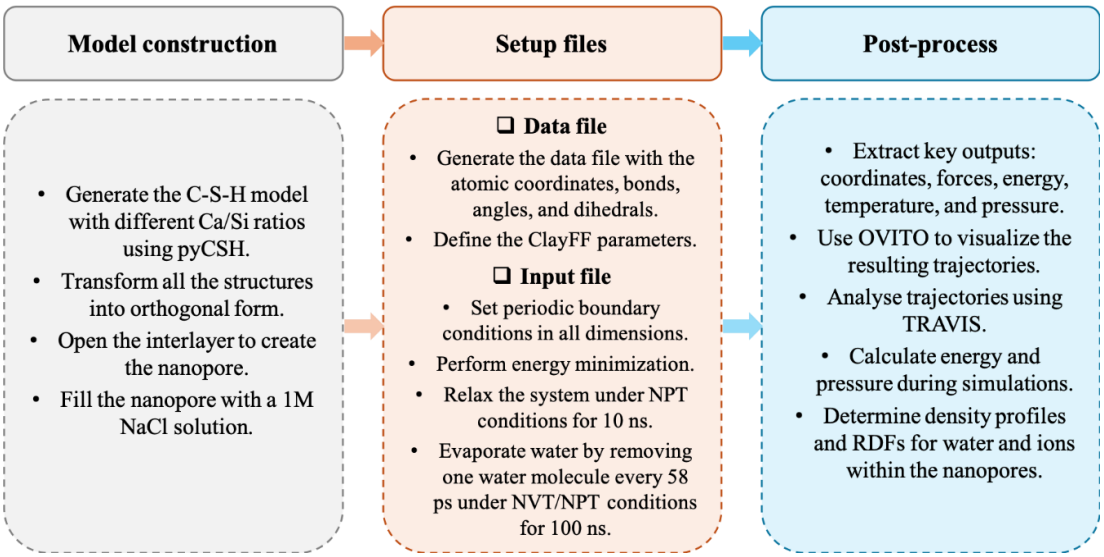

Figure 4.2. Workflow for modelling and simulating C-S-H systems.

4.3 Results and discussion

In this section, we present the results of our study on the water desorption process from the confined nanopores of C-S-H. Firstly, we highlight the importance of the equilibration step, as it plays a critical role in setting the initial conditions for accurate desorption simulations. Subsequently, we present the results obtained under both NVT and NPT ensembles to explore the underlying mechanisms of water desorption, considering various Ca/Si ratios (1.2, 1.4, 1.6, 1.8, and 2.0). Interestingly, the results for different Ca/Si ratios show remarkable similarities. Therefore, the Ca/Si ratio of 1.6 was selected as the base case for a more detailed explanation and exploration of the desorption phenomenon.

4.3.1 Equilibration stage

During the equilibration, the delta energy (ΔE) of the system is subject to significant fluctuations as the particles adjust to the initial conditions and interaction forces, as illustrated in Figure 4.3. Over time, the energy stabilises, indicating that the system has reached a state of equilibrium (Bagheri et al., 2018). The stabilisation of these fundamental system properties is essential to ensure that the simulation has reached a thermodynamically balanced condition, thereby enabling a reliable analysis of the characteristics of the system. Further insight into the equilibration process can be gained from the density profiles of the Cl^- ions during the equilibration, as shown in Figure 4.4. At the beginning of the equilibration, Cl^- ions are randomly distributed throughout the nanopore. However, as the simulation progresses, the ions begin to localise, forming distinct peaks near the C-S-H surface along the z-axis. These peaks indicate that the ions are finding energetically favourable positions, driven by the interactions with the C-S-H surface and the surrounding water molecules. After 10 ns, the density profile shows a more stable ion distribution near the surface, suggesting that the system is approaching equilibrium. The density profile in Figure 4.4 is not symmetrical near the two surfaces due

to differences in surface charge distribution and adsorption state between the two exposed C-S-H interfaces.

It is important to note that previous studies on water and ions in nanopores have reported equilibration times considerably shorter than 10 ns, so the thermodynamic equilibrium might not always be reached under such conditions (Kalinichev et al., 2007, Pan et al., 2010, Zehtab and Tarighat, 2016, Li et al., 2017a, Barbhuiya and Das, 2023). This can lead to problems that undermine the reliability of the results, as the studied properties may not accurately reflect the true equilibrium state. For instance, as shown in Figure 4.4, ions require sufficient time to settle into stable positions within the nanopore. If the simulation time for equilibration is not enough, the resulting ion distribution could be misrepresented, potentially leading to incorrect conclusions about how the ions interact with the surface. Additionally, insufficient equilibration time can also affect the accuracy of transport and diffusion measurements (Duque-Redondo et al., 2022a). Ions and water molecules that have not fully equilibrated may exhibit artificially high or low diffusion rates, deviating from their true equilibrium behaviour. Proper equilibration ensures that transport properties, like diffusion coefficients, are measured under equilibrium conditions, yielding more reliable and accurate results.

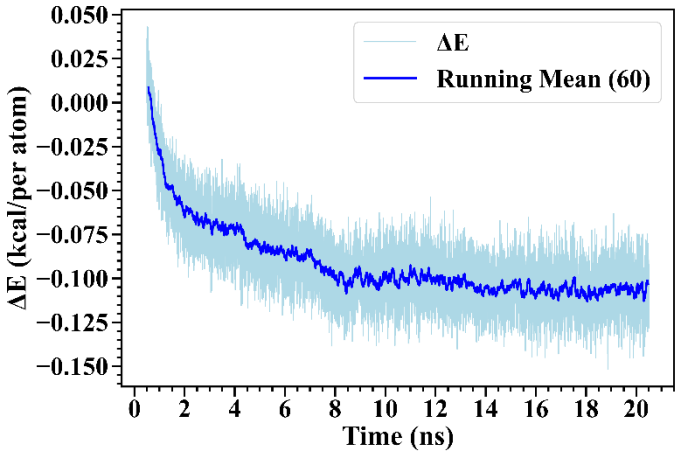

Figure 4.3. Evolution of the mean energy fluctuation (ΔE) per atom during the equilibration process over 20 ns.

The dark blue line represents the running average of ΔE, while light blue lines represent the ΔE values for every step. Note that the shown ΔE begins at 0.5 ns, as the first 0.5 ns corresponds to the initial equilibration step with the temperature ramp from 10 to 298 K, which is not included in the plot. (Note: The total energy (potential energy + kinetic energy) was divided by the total number of atoms to calculate the energy per atom, and ΔE was determined as the difference between the initial and final energy values.

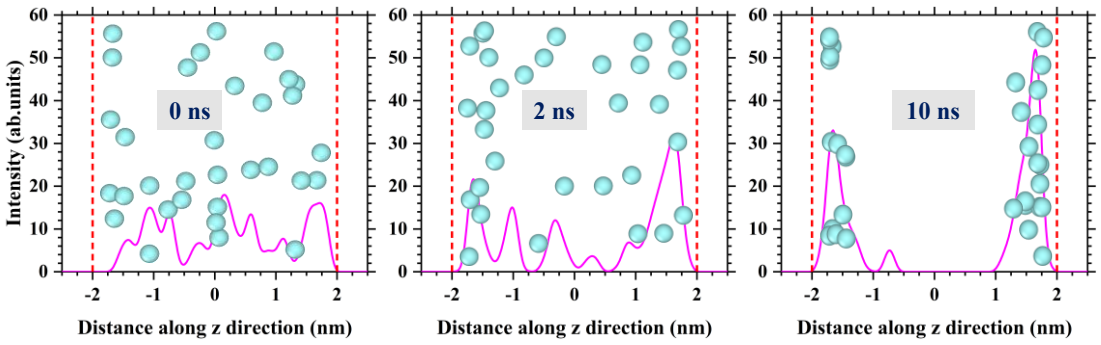

Figure 4.4. The continuous pink lines correspond to the density profiles of Cl- ions with the C-S-H gel pore at different times (0–10 ns) during the equilibration, while the red dashed lines represent the position of the C-S-H surface along the z-axis.

Note that the centre of the pore is set at a distance z = 0 nm. The blue balls represent the spatial distribution of Cl^- ions in the xz plane.

4.3.2 Constant volume: pore fixed

This section presents the evaporation of an aqueous solution confined within the C-S-H nanopore with a Ca/Si ratio of 1.6, conducted under NVT ensemble conditions. We first investigate the pressure and energy profiles to comprehend the thermodynamic changes occurring in the system during evaporation. Subsequently, we analyse the density profiles

of water and ions to elucidate the spatial distribution and behaviour of water and ions during the evaporation process. Finally, we examine RDFs of Na-Cl and Ca-Cl ions, which clarify the interactions and configurations of ions in the solution during evaporation.

4.3.2.1 Pressure and energy profile

The total pressure profile and normalised energy of the system are presented in Figure 4.5 as a function of the amount of water evaporated during the MD simulations. Six specific points along the pressure profile, denoted by encircled markers, were identified to conduct a more detailed examination of the behaviour of the system at critical stages during the evaporation process, including the initial pressure decline, the subsequent pressure rise, the stable pressure plateau, and the final decrease in pressure. The details of these specific points are provided in Table 4.1. Independent 5 ns simulations were performed at these six specific points along the trajectory for a more in-depth analysis. At these key points, the structural properties of water and ions (density profile and RDF) inside the nanopore were determined.

During the initial stage of the evaporation (points 1–2), the internal pressure of the system decreases significantly, reaching approximately -1500 atm. At this stage of evaporation, the nanopore is saturated with water and, consequently, the disjoining pressure is relatively low or balanced (Honorio, 2019). The negative pressure observed in the confined system indicates that it is under tension, a consequence of the nanoscale confinement and the cohesive interactions among the water molecules, which resist phase separation. These negative pressures are indicative of metastable liquid states, where the high energy barrier required for phase separation in nanopores suppresses cavitation (Caupin and Herbert, 2006, Israelachvili, 2011). As evaporation progresses and the water density in the nanopore decreases, the disjoining pressure begins to rise. The increasing pressure can be explained

by the densification of the residual confined liquid and the enhanced hydration forces between water molecules and the nanopore surfaces. In confinement, water molecules typically organise into structured layers adjacent to hydrophilic surfaces, leading to repulsive hydration forces that increase pressure. Furthermore, the increasing concentration of dissolved ions within the nanopore likely contributes to the osmotic pressure through ion crowding effects (Israelachvili, 2011). In the final stages of evaporation (point 6), only a few water molecules remain in the nanopore, and the pressure decreases again. The final decrease in pressure can be attributed to the reduction in confined liquid volume, which minimised the effects of hydration and osmotic forces. At this point, the system transitioned to a vapour-predominant state, with the remaining water molecules exerting minor pressure on the nanopore surfaces.

These findings offer valuable insights into the behaviour of confined aqueous solutions during evaporation. The observed extreme pressures, ranging from -1500 atm to 1500 atm, highlight the significant impact of nanoscale confinement, where surface forces, hydration interactions, and capillary effects supersede bulk thermodynamic properties. These nanoscale phenomena have crucial implications for understanding the behaviour of water and ions in cement-based materials, where confinement within nanopores profoundly influences material properties and transport mechanisms (Abdolhosseini Qomi et al., 2021, Israelachvili, 2011).

Figure 4.5(b) shows the evolution of the energy per atom as a function of the number of evaporated water molecules, illustrating how the system's energy changes during water removal in a confined nanopore environment. At each evaporation step (every 58 ps), a water molecule is removed from the nanopore, and the total energy of the system is recorded. To account for the energy contribution of the removed molecule, the energy of a

single water molecule in bulk water is added to the system's total energy. The resulting energy is then normalized by the total number of atoms, which remains constant throughout the process, to obtain the energy per atom. Initially, when the system is fully hydrated, the total energy is lower due to stabilizing interactions between water molecules and the C-S-H structure, as well as solvation effects on the Na^+, Cl^-, and Ca^{2+} ions. As evaporation progresses, the energy increases, reflecting the loss of these stabilizing interactions and the growing influence of direct ion-ion and ion-surface interactions. The approximately linear increase suggests that the energy cost of removing each water molecule remains relatively constant, possibly because the remaining water molecules still provide similar stabilization at each step. Finally, as the system transitions toward a nearly dry state, stronger direct electrostatic interactions between ions and the nanopore surface may further increase the system's energy, as fewer water molecules remain to mediate and screen these interactions.

To quantify the energetic cost of water removal from the C-S-H nanopore, we computed the total energy difference between the fully hydrated system (0 ns) and the final state after evaporation (100 ns). This total energy change was divided by the number of evaporated water molecules (1699) to estimate an average dehydration energy of −13.97 kcal/mol per water molecule. This energy reflects the overall energetic cost of water removal from the C-S-H nanopore environment, including the breaking of hydrogen bonds between water molecules, the disruption of water–ion interactions (especially with Na^+, Cl^-, and Ca^{2+}), and the detachment of water from the C-S-H surface. Although this is a global average and does not distinguish between individual mechanisms, it provides a useful quantitative estimate of the energetic barrier associated with drying at the molecular scale.

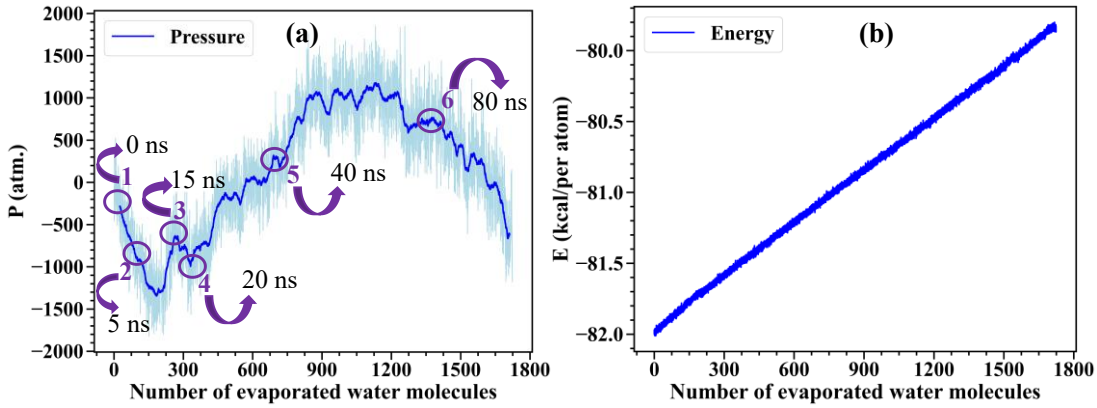

Figure 4.5. (a) Pressure profile at different water contents evaporated under NVT ensemble during the evaporation. (b) Normalised energy of the system as a function of water molecules evaporated under the NVT ensemble during the evaporation.

Table 4.1. Number of evaporated and remaining water molecules within the nanopore at the six selected points in Figure 4.5(a).

Encircled points	**1**	**2**	**3**	**4**	**5**	**6**
Time at the six points (ns)	0	5	15	20	40	80
Water molecules evaporated	0	86	258	344	689	1379
Remaining water molecules in the nanopore	1699	1613	1441	1355	1010	320

4.3.2.2 Water desorption process

A visual representation of the water evaporation process in the C-S-H gel pore at six specific time intervals (0, 5, 15, 20, 40, and 80 ns) is provided in Figure 4.6. At 0 ns, the nanopore is fully saturated with water molecules, which are uniformly distributed throughout both the centre of the nanopore and in the proximity of the C-S-H surfaces. As evaporation begins (5 and 15 ns), a decrease in water density is observed primarily in the bulk region. At 20 ns, a more pronounced change is observed, characterised by the formation of a cavitation in the centre of the nanopore. This highlights that the central

region of the nanopore experiences a more accelerated loss of water compared to the areas near the C-S-H surfaces. The snapshot at 40 ns illustrates a further progression of the evaporation process, with a clearly visible cavitation in the middle region of the nanopore. Cavitation in C-S-H gel pores typically occurs homogeneously in the central region of nanopores (Masara et al., 2024). This observation suggests that water in the bulk region is more easily removed than water near the C-S-H surfaces, likely due to the strong electrostatic interactions between water molecules and the charged surface of the C-S-H (Honorio et al., 2023). At 80 ns, the evaporation process is nearly complete, leaving only thin layers of water concentrated along the C-S-H surfaces, while the middle region of the nanopore is almost entirely devoid of water. This final stage represents a significant transition, with the remaining water confined to areas adjacent to the surfaces, reflecting the stronger interactions in these regions and the difficulty of removing surface-bound water.

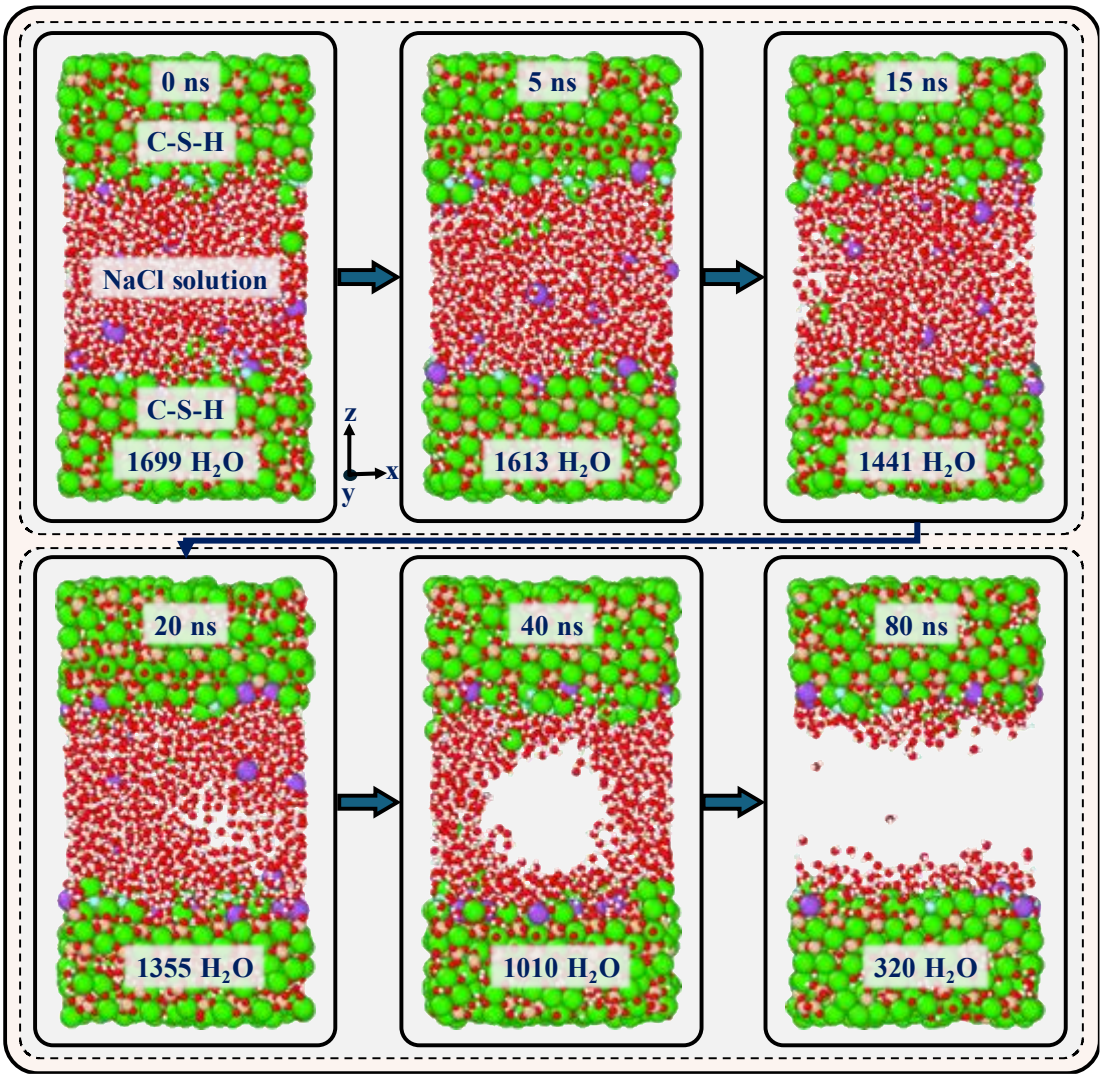

Figure 4.6. Snapshots of the evaporation process under the NVT ensemble at different stages (0, 5, 15, 20, 40, and 80 ns, corresponding to 1699, 1613, 1441, 1355, 1010, and 320 remaining water molecules within the nanopore, respectively).

Refer to Table 4.1 for full details. Na^+, Cl^-, and Ca^{2+} ions are shown as purple, light blue, and green balls, respectively; O, H, and Si atoms are represented as red, white, and light brown balls.

4.3.2.3 Density Profile of Water

Figure 4.7 depicts the evolution of the water density profile along the *z*-direction at six distinct simulation times (0, 5, 15, 20, 40, and 80 ns) during the water desorption process.

The shaded area represents the C-S-H layer determined by the density profiles of Si, as shown in the Appendix 1. (Figure A1.4). Water peaks observed in those areas correspond to water from other interlayers. At 0 ns, the density profile indicates that water is uniformly distributed throughout the nanopore, indicating a saturated system (Yang et al., 2018, Hou et al., 2017a). As evaporation begins (5 ns), a decrease in water density is observed, particularly in the middle region of the nanopore. At 15 and 20 ns, the decrease in water density becomes more pronounced, and a clear density gradient emerges. The water density in the middle region is significantly reduced compared to the regions closer to the C-S-H surfaces (Honorio et al., 2023). This also shows the formation of cavitation in the bulk region as explained in the previous section. This gradient highlights the stronger hydrophilic interactions between water molecules and the C-S-H surfaces, which hinder the escape of water from the surface region (Hayat et al., 2024, Kai et al., 2023a). As evaporation continues (40 ns), the density gradient becomes even steeper, with the central region showing a near-complete depletion of water molecules. At 80 ns, the density profile exhibits a notable change. While the majority of the nanopore is empty of water, a well-defined peak in water density remains very close to the C-S-H surfaces. This residual water corresponds to interlayer water tightly bound to the C-S-H surfaces (320 water molecules in total), which was not removed during the simulations.

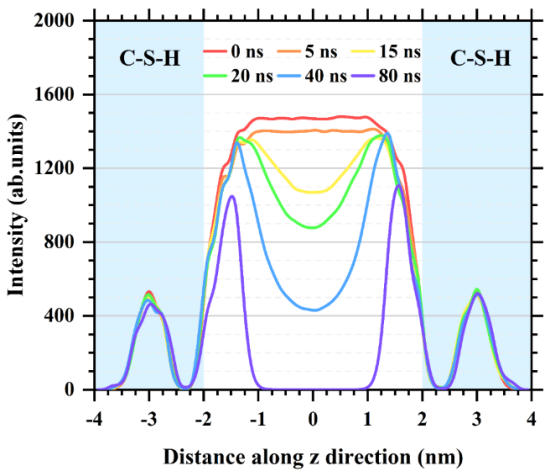

Figure 4.7. Density profiles of water molecules (including both Ow and Hw) within the C-S-H gel pore at different stages of evaporation under the NVT ensemble

(0, 5, 15, 20, 40, and 80 ns, corresponding to 1699, 1613, 1441, 1355, 1010, and 320 remaining water molecules, respectively). The 0 nm value corresponds to the pore centre along the z-axis, and the blueish-shaded areas represent the C-S-H layers.

It is worth noting that, unlike in some previous studies (Tang et al., 2019a, Sun et al., 2021a) where 2-3 distinct water layers were observed near solid surfaces, our results show only a single dominant peak close to the interface. This desorption may arise from averaging over both Ow and Hw, which may slightly smoothen fine structural features in the density profile, but also from the high ionic strength (1 M NaCl) and strong ion-surface interactions that can disrupt typical water layering by modifying the interfacial structure, especially as evaporation progresses and ion concentration increases.

4.3.2.4 Density Profile of Na and Cl ions

The density profiles presented in Figure 4.8(a) depict the distribution of Na^+ and Cl^- ions along the *z*-axis of the C-S-H gel pore at different times during the water desorption process, ranging from 0 to 80 ns. These profiles demonstrate the dynamic redistribution of ions as water is evaporated. The peaks for Na^+ ions consistently appear closer to the C-S-H surface than the peaks for Cl^- ions (Hou et al., 2018b, Liu et al., 2020). This indicates that Na^+ ions are attracted to the negatively charged C-S-H surface, while Cl^- ions are coordinated to both Ca^{2+} and Na^+ on the surface, as observed in previous studies (Hou and Li, 2014, Yang et al., 2023). As a result, an electric double layer of ions forms near the C-S-H surfaces, a phenomenon already reported in the literature (Kai et al., 2023a).

During the initial stages of evaporation (5–20 ns), the ions gradually migrate towards the nanopore surfaces as water evaporates, reducing their concentration in the centre of the nanopore, while increasing at the C-S-H surfaces, as can be seen both in the density profiles (Figure 4.8(a)) and in the corresponding snapshots of the nanopores (Figure 4.8(b2-b4)). At 40 ns, this pattern becomes more pronounced, with the density profiles displaying distinct peaks next to the C-S-H surfaces and a nearly flat profile in the middle region. At this stage, the majority of Na^+ and Cl^- ions are clustered along the surfaces, whereas the middle region of the nanopore has been significantly depleted of these ions (see Figure 4.8(b5)) (Yang et al., 2023). At 80 ns, the density profiles only display sharp peaks near the nanopore surfaces, indicating that all Na^+ and Cl^- ions have concentrated along the surfaces, while the centre of the nanopore is completely devoid of these ions (see Figure 4.8(b6)). This redistribution is prompted by the continuous evaporation process, which reduces the availability of water for ion solvation, particularly in the middle region of the nanopore. Nevertheless, it should be noted that the spatial arrangement of the Ca^{2+} ions was not significantly influenced by the loss of water, as can be seen in Appendix 1. (Figure A1.5 and Figure A1.7), because they remain near the C-S-H surface due to their strong interactions with it throughout the simulation. The results indicate that a more compact EDL is formed with evaporation.

The ion accumulation at the C-S-H surface, driven by water evaporation, is a critical precursor to salt crystallization. As evaporation progresses, the ionic concentration within the nanopore increases, eventually surpassing the solubility limit of NaCl and $CaCl_2$. This might trigger the formation of salt crystals, nucleating at the C-S-H surface where ion concentration is highest (Yang et al., 2023). The subsequent growth of these crystals within the confined nanopore space can generate significant internal stresses, potentially

compromising the mechanical strength and long-term durability of the material (Charola, 2000, Lubelli et al., 2010).

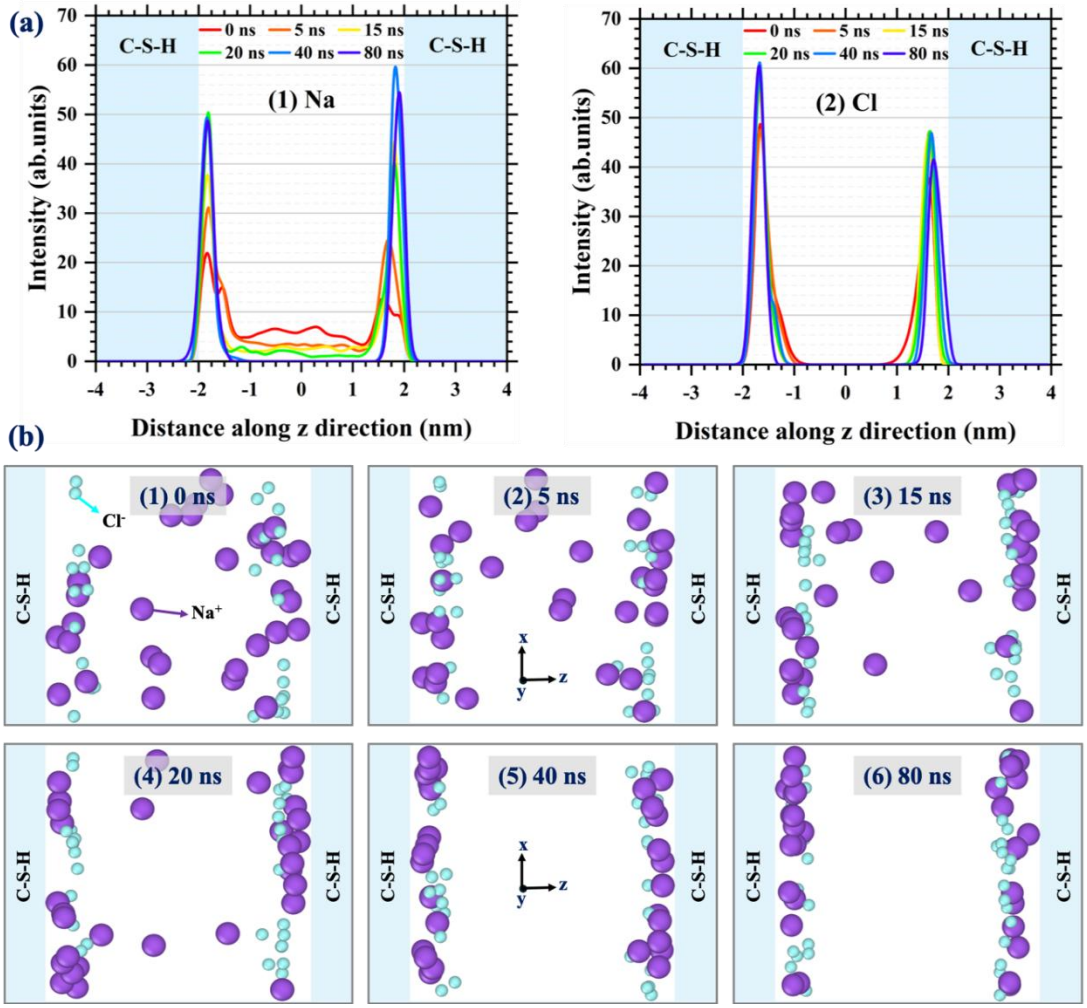

Figure 4.8. (a) Evolution of the density profiles of (1) Na+ and (2) Cl- ions during the evaporation process under the NVT ensemble. (b) Snapshots of Na+ and Cl- ion distributions within the gel pore at different stages

(0, 5, 15, 20, 40, and 80 ns, corresponding to 1699, 1613, 1441, 1355, 1010, and 320 remaining water molecules, respectively). The bluish-shaded areas indicate the regions occupied by the C-S-H surfaces, while Na^+ and Cl^- ions are illustrated as purple and light blue balls.

4.3.2.5 RDF Analysis

Figure 4.9(a) depicts the RDF analysis of Na-Cl and Ca-Cl in the C-S-H gel pore at different stages of the water evaporation. At the initial stage (0 ns), the first peaks of Na-Cl and Ca-Cl are located at 2.8 and 2.7 Å, respectively. These values are consistent with the average Na–Cl and Ca–Cl distances reported in the literature from X-ray and neutron diffraction experiments (Pálinkás et al., 1980, Hou et al., 2018b, Ohtomo and Arakawa, 2006). As the evaporation begins and progresses (5–20 ns), the first peak for Na-Cl increases in intensity and broadens slightly, as shown in Figure 4.9(a). The increase in peak intensity suggests a higher probability of Na^+ and Cl^- ions being nearby as water is removed. This behaviour is likely due to the reduced amount of water available for hydration, which promotes closer interactions between the ions, rather than changes in confinement, as the pore size remains constant. The broadening of the peak indicates a growing variability in Na-Cl distances within the first coordination shell, possibly due to the reduced hydration environment. In contrast, the peak for Ca-Cl pairs remains unchanged in intensity, with only minor broadening during the same evaporation interval, as shown in Figure 4.9(a). This suggests that the spatial arrangement of Ca^{2+} and Cl^- ions is relatively stable despite the reduction in water content due to evaporation. The slight broadening of the peak indicates a small increase in variability of the distances between the Ca^{2+} and Cl^- ions, but the strong electrostatic interactions between these ions maintain their pairing in a relatively organised manner throughout this phase. At 80 ns, the first RDF peak of Na-Cl reaches its maximum height and broadens further. This behaviour indicates that Na^+ and Cl^- ions are more likely to be nearby as the system approaches a near-dry state, likely due to the reduced water content. The broader peak reflects increased variability in ion-ion distances, suggesting a less organised spatial arrangement. For Ca-Cl pairs at 80 ns, the RDF peak still exhibits a well-defined peak, with only minimal reduction in intensity

and slight broadening. This broadening suggests the strong ionic interactions between Ca^{2+} and Cl^- are resilient, even under near-dry conditions.

The high intensity and consistent peak position at ~2.7 Å confirm that the Ca-Cl ionic interactions are stable, even as the system approaches a near-dry state (Zhou et al., 2018). This resilience can be attributed to the higher ionic charge density of Ca^{2+} compared to Na^+, which results from its divalent charge (+2) and smaller ionic radius. These characteristics facilitate stronger electrostatic interactions with Cl^- ions, even as water content decreases significantly. As evaporation progresses, the second peak for Na-Cl pairs shows a noticeable reduction, whereas the second peak for Ca-Cl pairs remains mostly unaffected by evaporation, indicating stronger long-range interactions for Ca^{2+} and Cl^-.

The coordination number (CN) quantifies the number of neighbouring ions surrounding a central ion within a specified distance and is calculated by integrating the radial distribution function. To determine the CN for the first coordination shell, the integration is performed up to the first minimum of the RDF, which marks the boundary of the shell where ions are directly coordinated. In this way, this metric can quantify the average number of ions (e.g., Cl^-) coordinated with a central ion (e.g., Na^+ or Ca^{2+}) and is, therefore, a direct indicator of local ionic interactions. However, when the RDF is integrated over larger distances (beyond the first minimum), the CN reflects the cumulative number of ions surrounding the central ion, including those in outer coordination shells or loosely associated clusters. This broader integration provides a measure of the overall ionic environment around the central ion. In this study, we have focused on the CN for the first coordination shell for Na-Cl and Ca-Cl ion pairs within the C-S-H gel pore under the NVT ensemble, as depicted in the inset of Figure 4.9(b). The study found that the CN of these ion pairs grew during the evaporation process, with the Ca-Cl pair increasing from 2.8 Cl^-

per Ca^{2+} at 0 ns to around 3.3 Cl^- per Ca^{2+} at 80 ns (Zhou et al., 2016, Deng and He, 2021). As the water content reduced, the solution volume decreased and ionic concentration increased, resulting in a modest rise in apparent coordination that likely reflects statistical crowding rather than enhanced ion-ion bonding. As the ions became more proximate, their ability to form ion pairs increased, leading to a higher coordination number. This trend directly reflects the enhanced ionic interactions that occur as evaporation progresses within the C-S-H gel pore. The RDF of Ca^{2+} ions with water molecules can be seen in Appendix. (Figure A1.6).

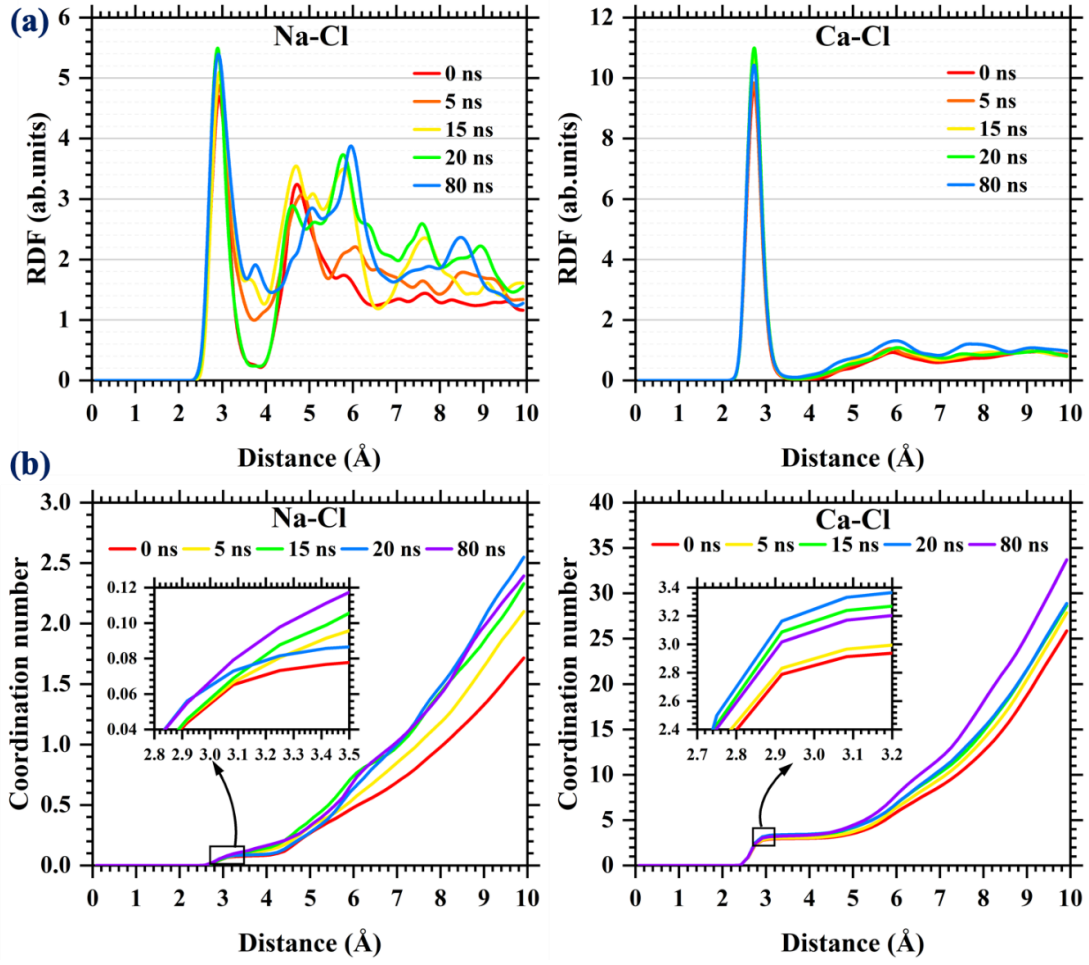

Figure 4.9. (a) Radial distribution functions (RDFs) and (b) the corresponding coordination numbers (CNs) for Na-Cl (left) and Ca-Cl (right) pairs within the C-S-H gel pore at different stages of the evaporation under the NVT ensemble.

Although this study did not explicitly simulate the nucleation and growth of NaCl crystals, the observed increase in the coordination number and the enhancement of the first RDF peak for Na^+–Cl^- pairs under decreasing water content suggest a progressive strengthening of ion-ion interactions. These microscopic changes point to the potential formation of pre-nucleation clusters, which are widely considered as precursors to crystallization. Therefore, the evolution of the local ionic environment revealed by the CN and RDF analysis offers valuable microscopic insight into the early-stage physicochemical conditions that may govern salt crystallization within C-S-H nanopores.

4.3.3 Constant pressure: pore shrinkage

This section investigates the evaporation dynamics of an aqueous NaCl solution confined within a C-S-H nanopore with a Ca/Si ratio of 1.6, conducted under the NPT ensemble. The spatial distribution and behaviour of water and ions are examined through density profiles. Additionally, the radial distribution functions of Na-Cl and Ca-Cl ions are analysed to elucidate the interactions and configurations of the ions during the evaporation process.

4.3.3.1 Evaporation process

Figure 4.10 depicts a series of snapshots showing the evaporation process within the C-S-H gel pore under the NPT ensemble at different time intervals (0, 5, 15, 20, 40, and 80 ns) during the evaporation. At 0 ns, the nanopore is completely saturated with water, displaying a uniform distribution of water molecules and Na^+ ions throughout the C-S-H gel pore. As the evaporation process begins (5–20 ns), a significant reduction in the water content within the nanopore is observed. Water begins to evaporate from the nanopore. This results in a visible decrease in the pore volume as the C-S-H layers begin to adjust to

the reduced water availability, and the nanopore exhibits initial signs of shrinkage. By 40 and 80 ns, the nanopore has undergone significant shrinkage compared to its initial state at 0 ns. The continued evaporation of water leads to a further decrease in the pore volume, confining the remaining water molecules to thin layers near the C-S-H surfaces. As a result, the ions are drawn closer together, concentrating near the remaining water at the surface. This shrinkage of the nanopore facilitates a more compact arrangement of the ions in the proximity of the C-S-H surfaces. Notably, despite the substantial shrinkage, the C-S-H structure remains intact at this stage, demonstrating its mechanical stability under these conditions.

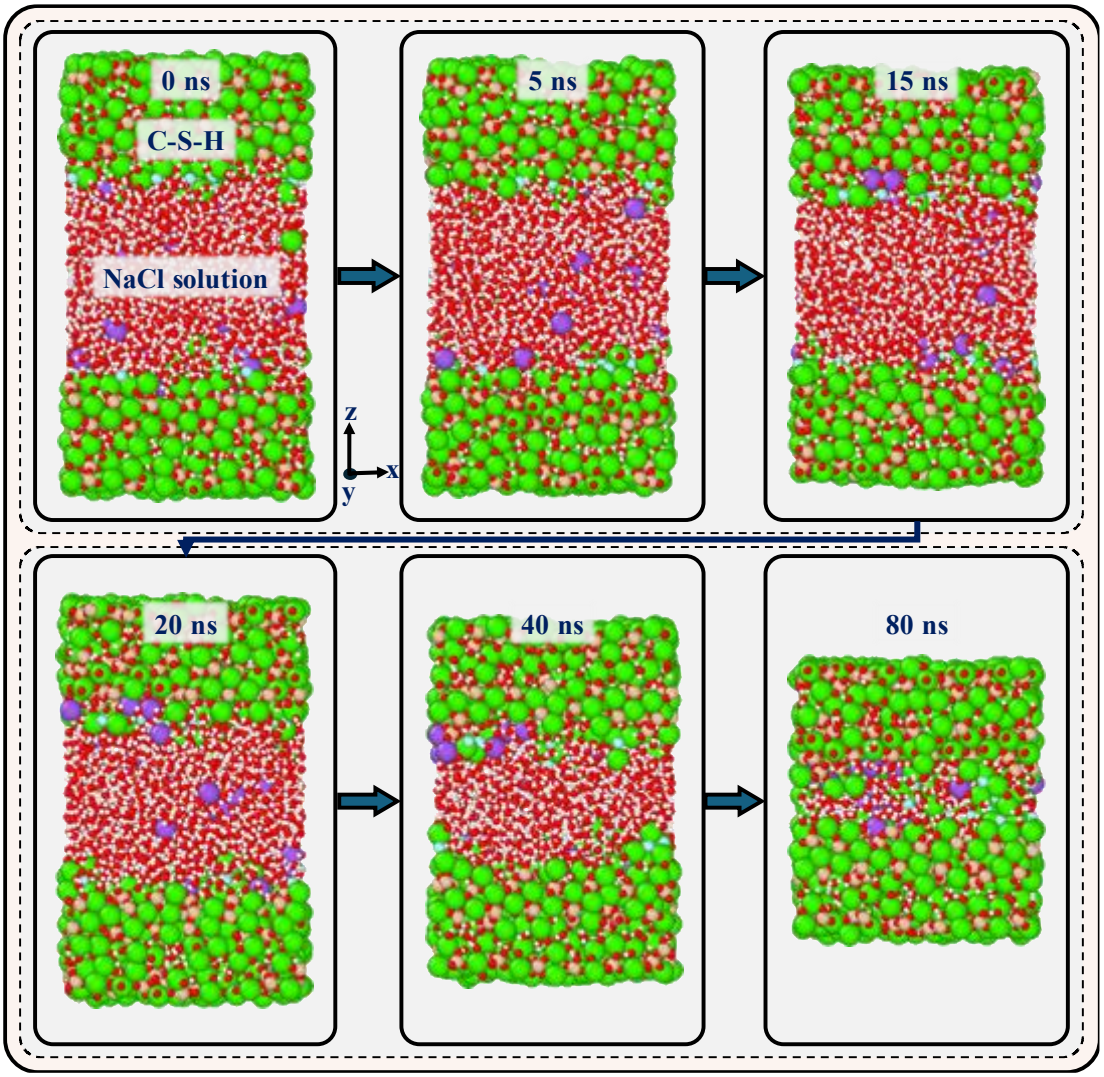

Figure 4.10. Snapshots of the C-S-H nanopore with the NaCl solution at different stages of evaporation under the NPT ensemble.

(0, 5, 15, 20, 40, and 80 ns, corresponding to 1699, 1613, 1441, 1355, 1010, and 320 remaining water molecules, respectively). Views are shown along the xz plane. The colour code for the different atoms is the same as in Figure 4.6.

4.3.3.2 Density profile of water

The water density profiles provide insights into the distribution of water molecules within the C-S-H nanopore. Accordingly, Figure 4.11 shows their evolution at different time intervals (0, 5, 15, 20, 40, and 80 ns) during the evaporation process. Initially, at 0 ns, the water density profile is relatively flat in the nanopore, indicating a uniform distribution of water molecules in the fully hydrated nanopore. During the early stages of evaporation (5–20 ns), water remains evenly distributed in the central region as the plateau in the density profiles is kept. However, as evaporation progresses, there is a reduction in pore size (shrinkage) while maintaining this uniform distribution under the NPT ensemble. At 40 ns, the water density profile maintains a shape similar to earlier phases; however, the pore size has significantly reduced at this stage. At 80 ns, the water density profile reveals a continuous shrinkage of the nanopore. The decrease in water density is observed at this stage. Although water distribution remains along the C-S-H surfaces, the reduced density indicates the near-dry state of the nanopore at this advanced stage of the evaporation process.

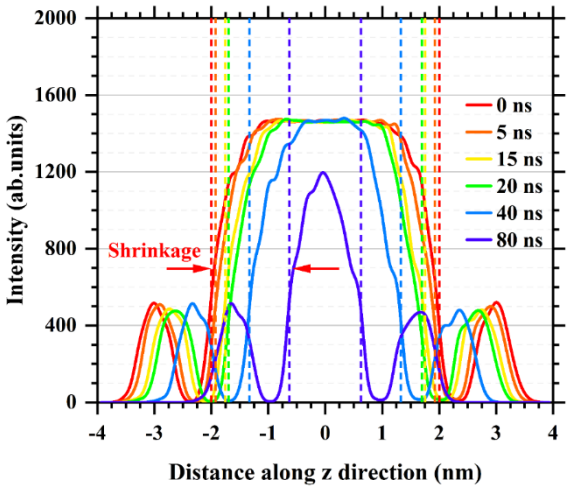

Figure 4.11. Density profiles of water within the C-S-H gel pore at different stages of evaporation under the NPT ensemble.

(0, 5, 15, 20, 40, and 80 ns, corresponding to 1699, 1613, 1441, 1355, 1010, and 320 remaining water molecules, respectively). Note that boundaries of the gel pore change over time; dashed lines in the same colour as each density profile indicate the corresponding nanopore boundary at each evaporation stage.

4.3.3.3 Density profile of ions

The spatial distribution of Na^+ and Cl^- ions in the C-S-H gel pore at different times (0, 5, 15, 20, 40, and 80 ns) during the water evaporation process under the NPT ensemble is shown in Figure 5.12. At 0 ns, the density profiles of the Na^+ ions (Figure 4.12(a)) show that the majority of Na^+ ions are located near the surface while few exist in the central region of the nanopore. However, all the Cl^- ions are adsorbed near the C-S-H surface (see Figure 4.12(b1)) at this stage. During the initial stages of evaporation, specifically from 5 to 20 ns, the ion density profiles exhibit minimal changes, apart from the reduction in pore size, which causes the position of the main peak to adjust accordingly, suggesting that the ionic distribution is not significantly impacted by the desorption of water molecules.

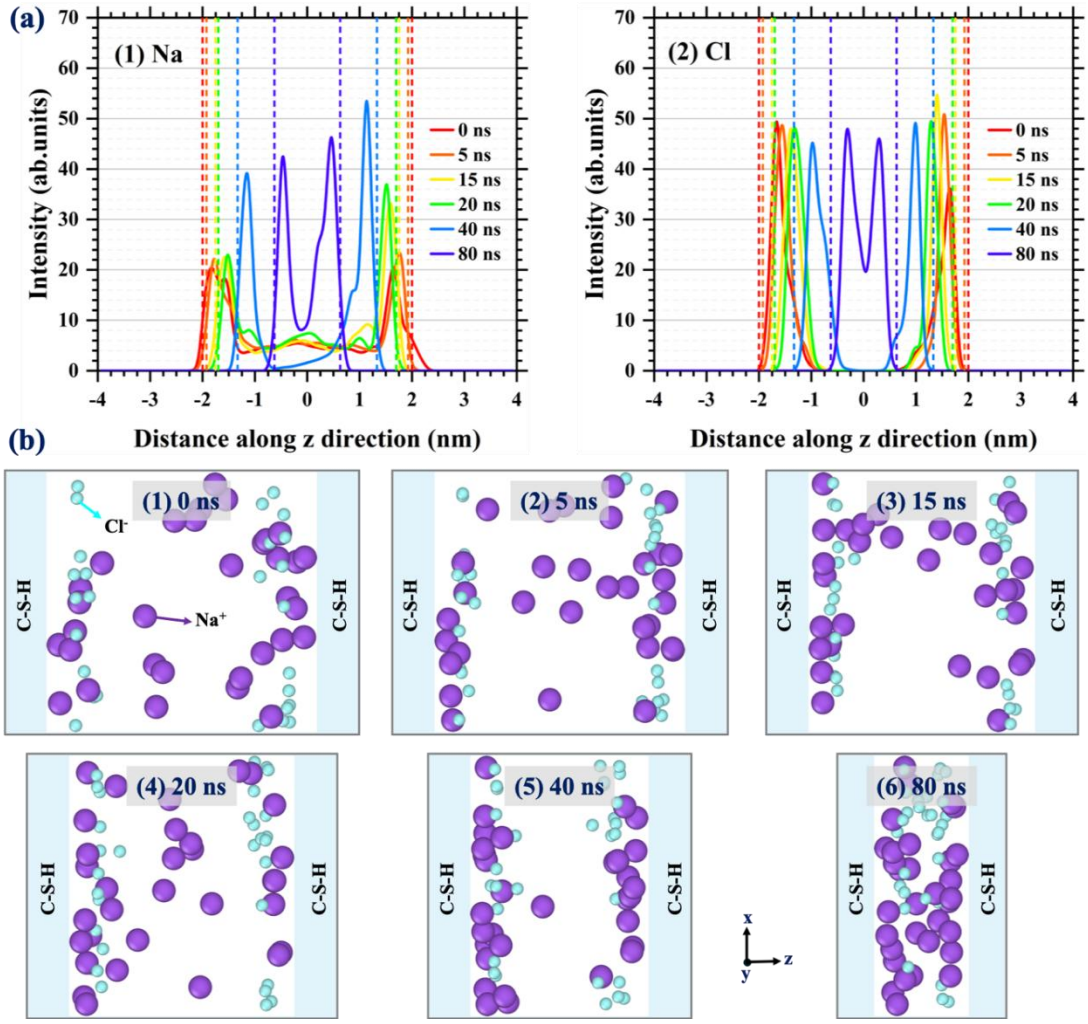

Figure 4.12. (a) Density profiles of (1) Na+ and (2) Cl- ions, and (b) snapshots of their spatial distribution within the C-S-H gel pore at different stages of evaporation under the NPT ensemble

(0, 5, 15, 20, 40, and 80 ns, corresponding to 1699, 1613, 1441, 1355, 1010, and 320 remaining water molecules, respectively). Views are shown in the xz plane. The bluish-shaded areas indicate the regions occupied by the C-S-H surfaces, while Na^+ and Cl^- ions are illustrated as purple and light blue balls.

The ions maintain a consistent distribution inside the nanopore, with very slight movements toward the nanopore surfaces (see Figures 4.12(b2) and (b4)), indicating that sufficient hydration is maintained during these early phases of the evaporation process. At

40 ns, the density profiles show a pronounced redistribution of the ions, with their concentration being very high near the surfaces of the C-S-H gel pore. The middle region of the nanopore becomes depleted of ions. The pronounced peaks in the density profiles at this point highlight the strong electrostatic interactions between the ions and the C-S-H surfaces, which efficiently attract and retain the ionic species. At 80 ns, the density profiles reveal that the ions are primarily concentrated near the nanopore surfaces, suggesting a nearly dried state in the middle region of the nanopore. The continuous decrease in the width of the density profile indicates a gradual reduction in nanopore size. This contraction of the nanopore leads to a more concentrated ionic distribution localised to the surface regions.

4.3.3.4 RDF analysis

The RDFs of Na-Cl and Ca-Cl ion pairs in the C-S-H gel pore during the evaporation under the NPT ensemble are shown in Figure 4.13(a). At the initial stage (0 ns), the RDF peaks for Na-Cl and Ca-Cl pairs are positioned at 2.8 Å and 2.7 Å, respectively, which are consistent with previously reported values (Hou et al., 2018b). As the evaporation continues (0–40 ns), the RDF peaks for Na-Cl pairs exhibit a reduction in intensity and a broadening of the first peak. This behaviour indicates a less organised spatial arrangement of Na-Cl pairs, driven by the continuous loss of water. In contrast, the RDF peaks for Ca-Cl pairs remain relatively consistent in both position and peak shape over the same period (0–40 ns). This suggests that the local structure of Ca^{2+} and Cl^- ion pairs is largely preserved during this phase. At 80 ns, significant changes are observed in the RDFs. The first peaks for both Na-Cl and Ca-Cl pairs decrease sharply in intensity and broaden, reflecting increased disorder in the spatial arrangement of Cl^- ions around Na^+ and Ca^{2+}. The nearly dry state of the nanopore reduces water-mediated ordering, leading to greater

variability in ion-ion distances, which contributes to the overall broadening of the RDF peaks.

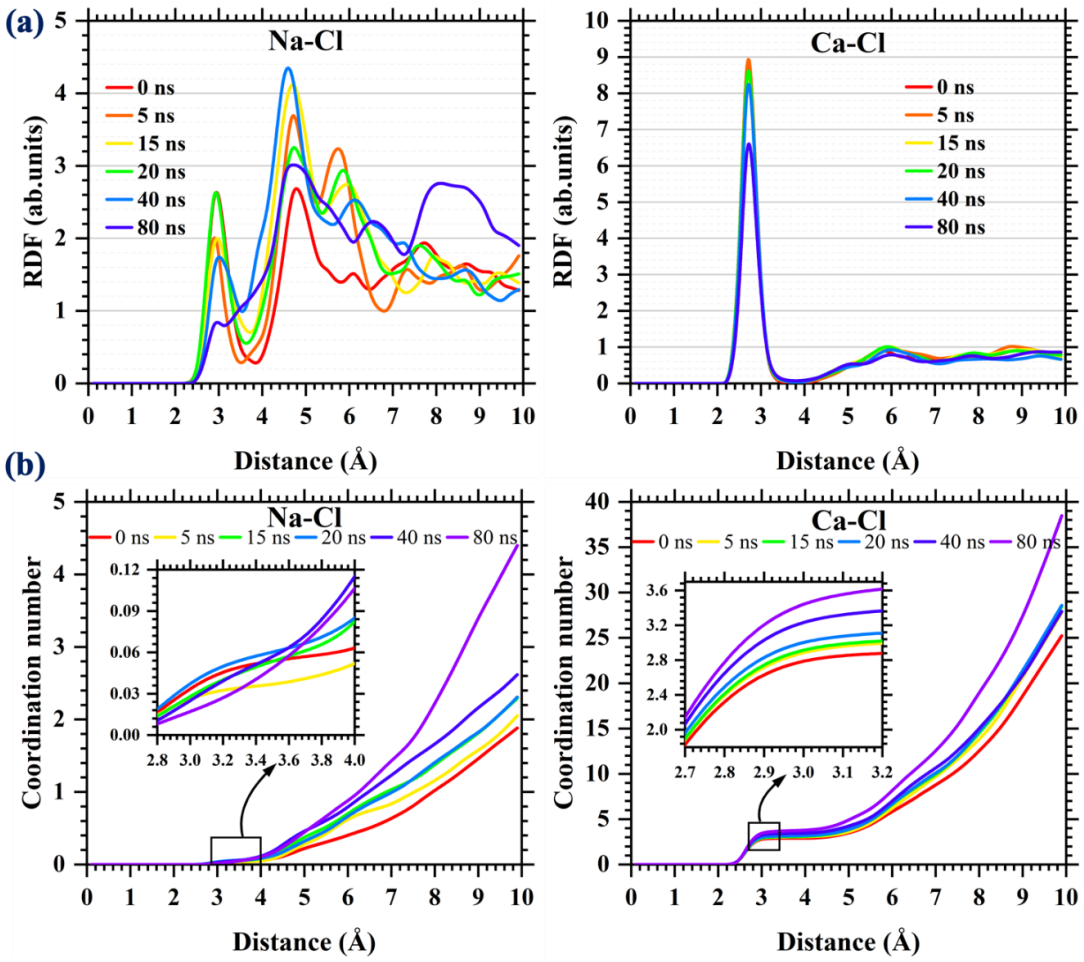

Figure 4.13. (a) Radial distribution functions (RDFs) of Na-Cl (left) and Ca-Cl (right) pairs within the C-S-H gel pore at different stages of evaporation under the NPT ensemble. (b) Corresponding coordination numbers (CNs) for each ion pair as a function of evaporation stage.

The corresponding coordination numbers for the Na-Cl and Ca-Cl pairs within the gel pore are shown in Figure 4.13(b). The analysis revealed distinct trends for the two ion pairs during the evaporation process. For Na-Cl pairs, the CN remained relatively constant at shorter distances throughout the different stages of evaporation; however, at larger

distances, the CN increased significantly with evaporation, specifically at 80 ns. Conversely, for Ca-Cl pairs, the CN increased with evaporation, rising from approximately 2.7 Cl^- per Ca^{2+} at 0 ns to around 3.6 Cl^- per Ca^{2+} at 80 ns, similar to values observed in the literature. This suggests that, as the nanopore shrinks, the ions are drawn closer together, likely due to the reduction in pore volume and available water molecules. The increased confinement appears to enhance the coordination of Cl^- ions around Ca^{2+}

4.3.4 Influence of the Ca/Si ratio

The influence of the Ca/Si ratio on the evaporation behaviour of an aqueous solution confined within C-S-H gel pores is examined. The results under NVT ensemble conditions are presented in this section, while the impact of Ca/Si ratios on evaporation behaviour under NPT conditions is detailed in the Appendix 1. (Figure A1.8–A1.10).

4.3.4.1 Constant volume: pore fixed

This section examines the effect of the Ca/Si ratio on the evaporation behaviour of an aqueous solution contained within C-S-H gel pores under NVT ensemble conditions. Pressure profiles are initially used to examine the impact of the Ca/Si ratio on evaporation behaviour. Subsequently, the density profiles of water and ions for different Ca/Si ratios were examined.

4.3.4.2 Pressure profiles

Figure 4.14 depicts the pressure variations within the C-S-H gel pore as water is progressively evaporated under the NVT ensemble for different Ca/Si ratios, ranging from 1.2 to 2.0. Across all examined Ca/Si ratios, the pressure initially decreases as the water begins to evaporate, reflecting the release of internal stress in the fully hydrated nanopore. As the evaporation process continues, the pressure starts to increase, indicating growing

confinement and stronger interactions between the remaining water molecules, ions, and the C-S-H surfaces. The patterns of the pressure profiles at different Ca/Si ratios are not substantially altered, suggesting that the Ca/Si ratio does not significantly impact the overall pressure trends during evaporation. The similar shape of the pressure curves across all ratios underscores a consistent evaporation behaviour regardless of the specific Ca/Si ratio.

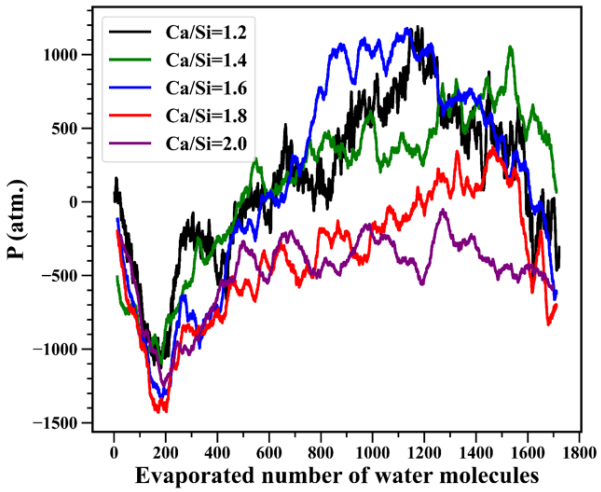

Figure 4.14. Pressure profile at different water content evaporated under NVT ensemble during the evaporation with different Ca/Si ratios.

Note that the pressure profiles at the beginning are slightly different because these are determined by taking the running average for 300 steps.

4.3.4.3 Density profiles

Figure 4.15 depicts the water density profiles in C-S-H gel pores at varying Ca/Si ratios during the evaporation process. Due to the minimal differences observed between the density profiles, only those for Ca/Si ratios of 1.2, 1.6, and 2.0 are presented for clarity. For all examined Ca/Si ratios, water molecules tend to aggregate near the nanopore surfaces, forming distinct peaks in the density profile, while the middle region of the nanopore

exhibits lower water density. As evaporation progresses, the water density in the middle region of the nanopore decreases, resulting in a density gradient, and the observed peaks become less pronounced. The water density profiles show little variation across different Ca/Si ratios. The general trend of water accumulation near the nanopore surface is consistent, suggesting the Ca/Si ratio has a limited impact on the water density distribution during evaporation.

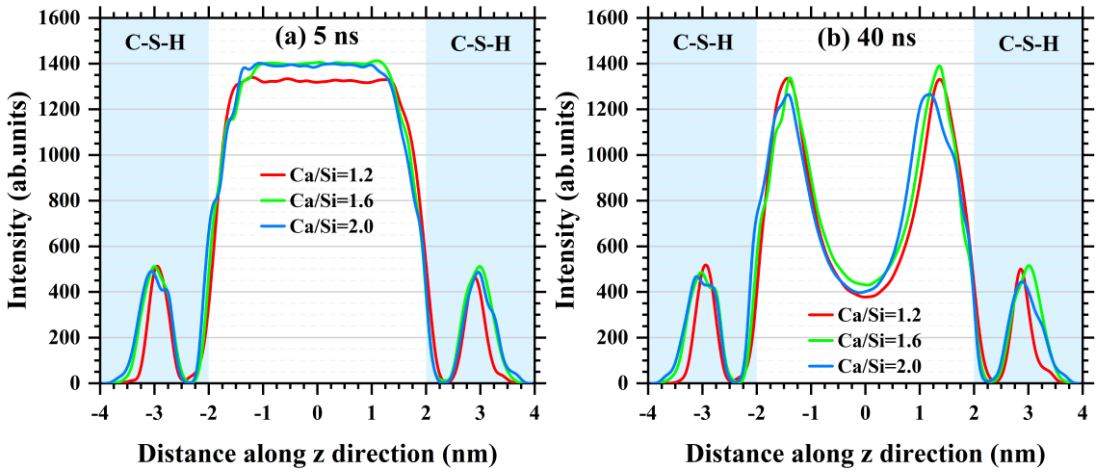

Figure 4.15. Density profiles of water within the C-S-H gel pore with different Ca/Si ratios during evaporation under the NVT ensemble at (a) 5ns and (b) 40 ns.

Figure 4.16 depicts the Na^+ and Cl^- ions density profiles in the C-S-H gel pore during the evaporation process at different Ca/Si ratios (1.2, 1.6, and 2.0). At the initial stage of evaporation, the density profiles of Na^+ exhibit more prominent peaks at lower Ca/Si ratios. This can be attributed to the varying concentrations of Ca^{2+} ions present on the C-S-H surface at different Ca/Si ratios. At lower Ca/Si ratios (e.g., 1.2), there is less Ca^{2+} on the surface, reducing the repulsive interactions experienced by Na^+ ions, allowing them to accumulate closer to the C-S-H surface. As a result, the Na^+ density profile shows a sharper peak under these conditions. Conversely, the Cl^- ion density profile shows a higher peak at higher Ca/Si ratios (e.g., 2.0). This is due to the stronger electrostatic interactions

between the Ca-Cl pairs when higher Ca^{2+} is present on the surface. As the evaporation progresses (5–20 ns), both Na^{+} and Cl^{-} ions migrate closer to the C-S-H surface, and their density profiles become similar. At the later stages of evaporation (40 ns), the distinct peaks in the ion density profiles are no longer significantly influenced by the Ca/Si ratio. This suggests that, as the water content decreases, the ions stabilise near the pore surface, and the impact of the Ca/Si ratio on their distribution becomes negligible. Both types of ions tend to localise near the C-S-H surfaces, regardless of the Ca/Si ratio in the nearly dehydrated state.

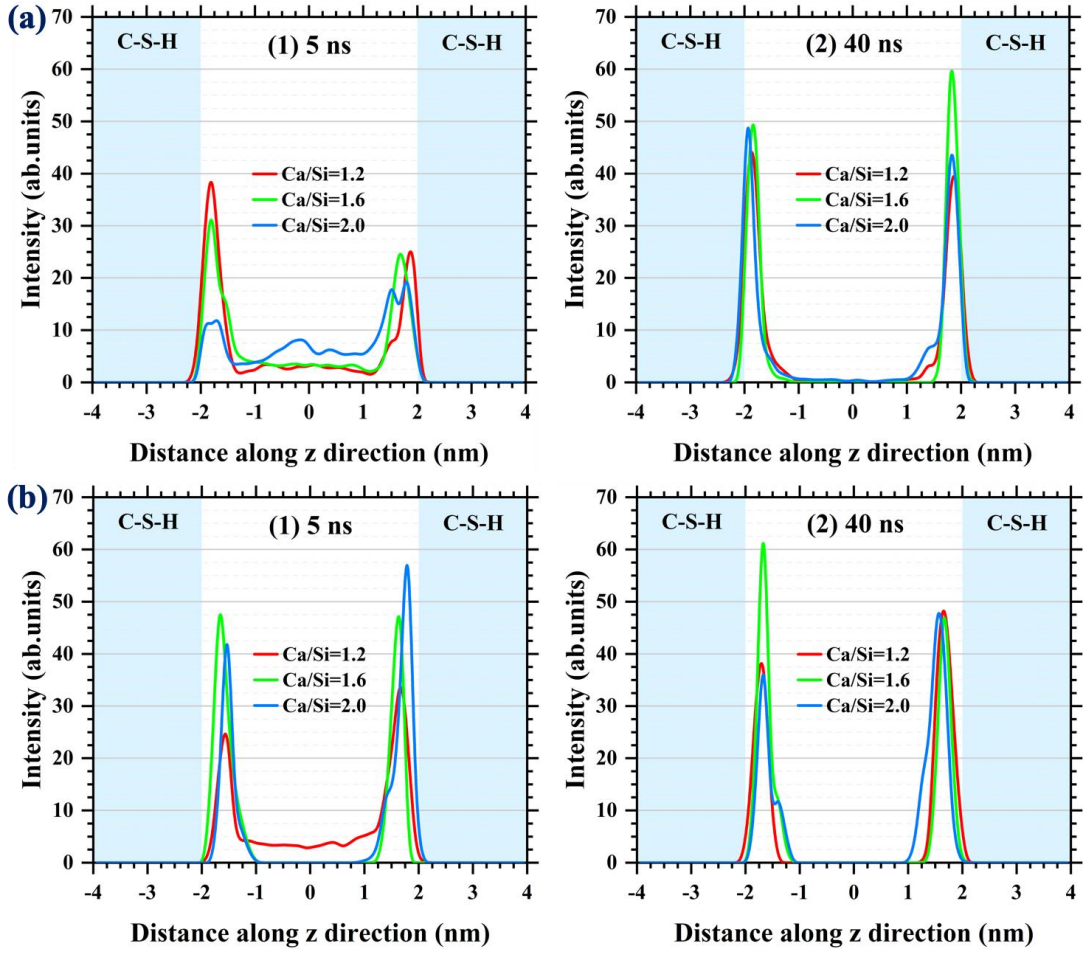

Figure 4.16. Density profiles of (a) Na+ and (b) Cl- ions within the C-S-H gel pore with different Ca/Si ratios during evaporation at (1) 5 ns and (2) 40 ns.

4.4 Summary

This study provides atomic-scale insights into the evaporation of water from NaCl solutions confined within C-S-H nanopores, revealing fundamental mechanisms that govern drying processes in cementitious materials. Through molecular dynamics simulations, it was observed that, under NVT conditions, where the pore size remains fixed, evaporation occurs preferentially from the central region of the nanopore. This leads to a density gradient within the confined water phase, progressively concentrating ions near the C-S-H surface. As the system loses water, Na^+ and Cl^- ions migrate towards the pore walls, forming a double ionic layer that alters the local ionic distribution. This redistribution could play a key role in the initial stages of salt precipitation, potentially influencing long-term degradation mechanisms such as crystallisation-induced damage in cementitious structures.

In contrast, when the system is allowed to relax under NPT conditions, the nanopore undergoes significant shrinkage, dynamically adapting its size as water evaporates. Despite this contraction, the C-S-H structure remains stable, suggesting that nanopores in cementitious materials can accommodate drying-induced stresses without collapsing. However, even under NPT conditions, ion migration towards the C-S-H surface persists, reinforcing the idea that drying significantly modifies the physicochemical environment within nanopores. This could later affect ionic transport and crystallisation dynamics, potentially leading to structural alterations in larger-scale cementitious systems.

Additionally, the study found that variations in the Ca/Si ratio (1.2–2.0) have a negligible impact on the overall evaporation behaviour. This indicates that water desorption mechanisms within C-S-H nanopores are largely independent of the Ca/Si ratio within this range. These findings advance our understanding of water transport and ion redistribution

in confined cementitious environments, which are fundamental to predicting durability issues such as drying shrinkage and salt-induced damage. By providing a detailed molecular perspective on the drying process, this work contributes to the development of more accurate models for concrete deterioration and highlights the importance of considering nanoscale confinement effects when assessing long-term performance.

Chapter 5. Degradation of C-S-H in seawater

5.1 Introduction

Based on Chapters 3 and 4, it was observed that seawater cation can adsorb on the C-S-H surface and replace interlayer Ca ions. These seawater cations, whether present in pore solutions or introduced from external aggressive environments, significantly influence the hydration kinetics, mechanical properties, and durability of cement-based materials (Jawed and Skalny, 1978, Lindgård et al., 2012, Shi and Lothenbach, 2020, Tang et al., 2021, Liu et al., 2022a, Liu et al., 2022b, Tao et al., 2024, Liu et al., 2024). However, a fundamental understanding of how incorporated Na^+, K^+, and Mg^{2+}ions impact the mechanical properties of the C-S-H, as well as the underlying mechanisms governing their effect on strength, remains limited. Therefore, this study investigates the effects of Na^+, K^+, and Mg^{2+}incorporation on the nanoscale cohesion and mechanical properties of C-S-H.

C-S-H possesses a multiscale hierarchical structure (Cuesta et al., 2018): at the microscale, it consists of randomly packed particle clusters (globules) of varying densities, interspersed with gel pores. At the nanoscale, each globule is made up of layered C-S-H (C-S-H_{layer}) units, which serve as the fundamental building blocks (Jennings, 2008). The C-S-H layers are bound together by molecular interactions that determine the macroscopic strength of the material (Constantinides and Ulm, 2007, Vandamme and Ulm, 2009). Mechanical stress in C-S-H arises from external loading, capillary forces in partially saturated pores, and crystallisation pressures resulting from chemical processes. These stresses produce a non-uniform stress distribution at the nanometre scale, where time-dependent relaxation determines creep deformation and viscous response of the material, critical factors in its long-term mechanical degradation (Bažant et al., 1997). Simulations using nanoparticles

have demonstrated that the collective rearrangement of multiple C-S-H units at the 10–50 nm scale leads to stress relaxation and creep strain consistent with experimental observations, thereby supporting key assumptions in macroscopic models (Ioannidou et al., 2017, Liu et al., 2019, Masoero and Di Luzio, 2020). The interfacial cohesiveness between adjacent C-S-H nano-units drives these mesoscale rearrangements (Manzano et al., 2013, Morshedifard et al., 2018, Haist et al., 2021). Studies indicate that creep in cementitious materials may result from interlayer sliding among adjacent C-S-H particles (Alizadeh et al., 2010, Suwanmaneechot et al., 2020). These findings demonstrate the lubricating role of interlayer water, indicating that water-rich interlayers facilitate C-S-H sliding and reduce the creep modulus (Geng et al., 2018, Maruyama et al., 2019, Suwanmaneechot et al., 2020, Gardner et al., 2021). Additionally, research has demonstrated that ions are primarily adsorbed by C-S-H (Chappex and Scrivener, 2012), and this cohesion can be altered through cation exchange, such as Na^+, K^+, or Mg^{2+} replacing Ca^{2+} in the C-S-H layer (Sugiyama, 2008, Sánchez‐Herrero et al., 2016, Sánchez‐Herrero et al., 2017). These alterations can modify molecular interactions, influencing the mechanical characteristics of C-S-H. Therefore, a comprehensive understanding of the interaction of Na^+, K^+, and Mg^{2+} with C-S-H is crucial for understanding and enhancing the performance of cementitious materials.

Na^+ and K^+ ions are common alkalis present in cementitious materials. Their interaction with C-S-H can affect alkali balance, the kinetics of cement hydration, and alkali-silica reaction (ASR) (Puertas et al., 2004, Yan et al., 2022). The uptake of alkali ions into C-S-H is either by surface adsorption or interlayer incorporation, with both mechanisms influenced by charge imbalance. These ions influence the structure and behaviour of C-S-H, potentially modifying the interlayer bonding environment and altering the basal spacing.

X-ray diffraction (XRD) results demonstrate that alkali ions reduce the average basal spacing of C-S-H, particularly at low Ca/Si ratios (Bach et al., 2013, L'Hôpital et al., 2016). A possible explanation is that alkali ions replace Ca^{2+} ions in the C-S-H interlayer, altering the local bonding environment and reducing the interlayer spacing. Nonetheless, the specific mechanisms behind this process are still not well understood. However, Yan et al. (Yan et al., 2022) observed an increase in interlayer distance upon the introduction of alkali ions, which they attributed to decreased interlayer forces resulting from the removal of Ca^{2+} ions from the interlayer of C-S-H. The different effects of alkali ions on the interlayer spacing of C-S-H can be attributed to several factors. At lower concentrations, alkali ions promote charge compensation within the interlayer, resulting in a reduced interlayer distance. Conversely, at higher concentrations, increased ionic strength can induce electrostatic repulsion, leading to interlayer expansion. Additionally, the introduction of alkali ions reduces silicate polymerisation, resulting in shorter mean silicate chain lengths compared to alkali-free C-S-H (Myers et al., 2015, Garg et al., 2019). Regarding mechanical properties, Mendoza et al. (Mendoza et al., 2015) found that alkali ions increase the elastic modulus of C-S-H via electrostatic interaction between positively charged alkali cations and the negatively charged C-S-H surface, resulting in a denser microstructure. In contrast to alkali ions, the incorporation of Mg^{2+} ions into the C-S-H structure is not yet fully understood. Research indicates that up to 3.5% of Mg^{2+} may be incorporated into C-S-H via reversible ion exchange at broken bonds or outer surface, as well as through an irreversible reaction with calcium silicates (Shrivastava et al., 1991). Tang et al. (Tang and Chen, 2020, Tang et al., 2021) examined a $CaO–SiO_2–MgO–H_2O$ system at high temperatures and found that Mg^{2+} can link silicate tetrahedra in C-S-H, resulting in the formation of a new phase termed as calcium magnesium silicate hydrate (C-M-S-H). This finding aligns with observations of increased polymerisation and a non-

homogeneous distribution of Mg, Ca, and Si. Furthermore, FTIR studies have also indicated that the incorporation of Mg increases polymerisation and promotes cross-linking between silicate chains (Mostafa et al., 2009).

Advanced characterisation techniques such as atomic force microscopy and nanoindentation mapping offer significant insights into the microscale mechanical behaviour of C-S-H, particularly its elastic properties (Li et al., 2015b, Ashraf et al., 2016, Zha et al., 2018). However, these approaches are inadequate for investigating mechanical properties at nanoscale due to constraints such as the dimensions of the indenter tip, which limit efficient probing of the C-S-H layer. To overcome these limitations, atomistic simulations serve as an essential complementary approach, enabling the investigation of cement hydration products at the nanoscale level.

Atomistic simulations have extensively investigated the elastic and mechanical properties of C-S-H, analysing its response to tensile and shear stresses, as well as the influence of temperature, water content, or chemical replacements (Hou et al., 2014b, Fan and Yang, 2018, Liang, 2020, Hou et al., 2021, Sun et al., 2021a, Zhang et al., 2021b, Wang et al., 2024). Tobermorite, a layered clay mineral analogous to C-S-H gel, has been studied for its resistance to shear deformation (Dupuis et al., 2021). In siliceous tobermorite, shear stress relaxation occurs via interlayer sliding, much like in C-S-H. Furthermore, it was found that when aluminium substitutes silicon into the structure, stress relaxation occurs in the intralayer via rearrangement of the CaO layer, a mechanism similar to that observed in C-A-S-H (Gardner et al., 2021). Manzano et al. (Manzano et al., 2013) employed atomistic simulations to compute the shear strength of a bulk C-S-H model (Ca/Si=1.65) and its crystalline analogue, 14 Å tobermorite. Under quasistatic shear strain, the C-S-H gel exhibited better ductility compared to tobermorite, a phenomenon the authors ascribed to

the disordered atomic structure of C-S-H. Morshedifard et al. (Morshedifard et al., 2018) investigated the long-term relaxation of C-S-H using quasistatic cyclic loading, characterised by affine shear displacements and enthalpy minimisation. They found that the non-affine strain was concentrated in the interlayer water region. They increased water content and interlayer spacing, finding a significant transition in the creep compliance (C) at approximately 0.1 nm interfacial distance: C remained constant (solid-like behaviour) below this threshold, while it decreased linearly beyond it. Duque-Redondo et al. (Duque-Redondo et al., 2022b) demonstrated that the shear strength of C-S-H diminishes significantly with increasing interfacial distance, becoming negligible beyond 0.3 nm as water mobility increases. Stress dissipates via stick-slip interlayer sliding while C-S-H layers remain rigid. They concluded that the water mobility directly determines the shear strength, with increasing flow dramatically reducing cohesion.

The influence of various ions on the structure and mechanical properties of C-S-H has been thoroughly investigated at the atomic level (Dufresne et al., 2018, Yaphary et al., 2020, Hou et al., 2021, Kai et al., 2021, Santos Rego et al., 2022, Kai et al., 2023b, Gao et al., 2025, Kai et al., 2023a). Dufresne et al. (Dufresne et al., 2018) investigated cation (Na^+ and K^+) adsorption in the C-S-H layer, finding that the elastic modulus is reduced by approximately 5% when loaded perpendicular to the C-S-H layer, while inducing a volumetric expansion of around 0.25%. Kai et al. (Kai et al., 2023a) found that seawater Na^+ substitutes interlayer Ca^{2+} in C-S-H, thereby enhancing interlayer bonding and improving fracture resistance. Rego et al. (Santos Rego et al., 2022), using DFT calculations, demonstrated that the replacement of Ca^{2+} by Mg^{2+} in C-S-H reduces lattice parameters (due to the smaller radius of Mg^{2+}) while enhancing chemical bonding (due to the greater electronegativity of Mg^{2+}), ultimately resulting in increased bulk, Young's, and

shear moduli. Yaphary et al. (Yaphary et al., 2020) investigated Na^+/Ca^{2+} exchange in C-S-H and found that Na^+ incorporation resulted in a 0.6% volumetric expansion due to increased interlayer spacing; however, no notable alterations in strength or moduli were observed. Gao et al. (Gao et al., 2025) investigated the incorporation of K^+ ions in C-S-H and found that K^+ decreases basal spacing (11.85 to 11.31 Å) while establishing K–O bonds. They reported that partial substitution (50%) improved tensile modulus (from 23.1 to 30.6 GPa) and strength (from 1.15 to 1.28 GPa), whereas complete replacement reduced fracture strain (from 0.51 to 0.21) and energy (from 6.12 to 3.70 J/m^2) due to diminished K–O bond strength. However, the information available in the literature regarding the effect of different ions is limited to the elastic modulus and tensile strength of the C-S-H layer. The influence of different seawater ions on the shear and tensile strength of the C-S-H as a function of interfacial distance, as well as the underlying atomistic mechanisms governing its mechanical response, remains poorly understood.

Therefore, in this work, we use non-equilibrium MD simulations at room conditions to study how different seawater ions (Na^+, K^+, and Mg^{2+}), and their concentrations (cation/Si=0.1-0.3), affect interlayer cohesion between adjacent C-S-H layers under shear strain. We further examine their impact on the mechanical properties of C-S-H under tensile loading. Specifically, we seek to elucidate how seawater ions affect the shear cohesion of C-S-H gel across varying interfacial distances, a critical factor governing mesoscale rearrangements that determine the mechanical degradation of cementitious materials. We apply shear strain at a rate of 10^{-8} fs^{-1} in the xz plane (perpendicular to the interface) and tensile strain at the same rate along the z-direction (normal to the C-S-H layer), considering interfacial distances ranging from bulk interfacial space to 1 nm. We define the bulk interfacial space as representing perfect particle contact, hereafter referred

to as the 'perfect contact' interface. The results demonstrate that both shear and tensile strength peak when adjacent C-S-H layers maintain perfect contact, following the cation order: $Ca^{2+} \approx Mg^{2+} > Na^{+} > K^{+}$. These mechanical properties decrease sharply with even minimal increases in interfacial distance. These findings suggest that both the composition of the interlayer solution and ion diffusivity are the primary factors governing shear strength and cohesion in C-S-H gels.

5.2 Computational methods

5.2.1 Model construction

The initial C-S-H structural models were produced in this work using the pyCSH Python tool (Casar et al., 2024), which automates the generation of atomic-scale C-S-H models based on the brick model (Mohamed et al., 2018). For further details, the model construction process is described in Chapter 4. Figure 5.1 shows a sample C-S-H model with a Ca/Si ratio of 1.6. The initial configuration comprised six bricks in the x-direction, six in the y-direction, and three in the z-direction. Using the pyCSH Python tool, monoclinic C-S-H models were generated (illustrated in Figure 5.1(a)) and then converted into an orthogonal structure (shown in Figure 5.1(b)) to enhance simulation efficiency by simplifying computational demands and streamlining data analysis. The resulting C-S-H model dimensions were x = 4.04 nm, y = 3.73 nm, z = 4.20 nm, $\alpha = 90°$, $\beta = 90°$, and $\gamma = 90°$. The created C-S-H supercell consists of three intra- and interlayers, as shown in Figure 5.1(b).

Previous studies have demonstrated that seawater cations (Na^{+}, K^{+}, Mg^{2+}) are primarily adsorbed into the C-S-H layers by replacing interlayer Ca^{2+} (Sugiyama, 2008, Dufresne et al., 2018, Yan et al., 2022, Liu et al., 2024). Semi-grand canonical Monte Carlo

simulations have shown that two monovalent cations (Na^+/K^+) can be adsorbed in the C-S-H interlayer for each substituted Ca^{2+} (Dufresne et al., 2018).

In this study, we systematically replaced interlayer Ca^{2+} ions to investigate the effects of seawater cations on C-S-H gel, maintaining charge neutrality by substituting each Ca^{2+} with either (i) two monovalent cations (Na^+ or K^+), or (ii) one divalent cation (Mg^{2+}). The substitution ratios explored were Na/Si=0.1–0.3 for CSH_Na, K/Si=0.1–0.3 for CSH_K, and Mg/Si=0.1–0.3 for CSH_Mg, selected to represent typical ion concentrations in seawater-exposed cementitious environments. Figure 5.1(c) illustrates a representative configuration of C-S-H _Na (Na/Si=0.3) under perfect contact conditions. Full details of the ion quantities and substitution schemes are provided in Table A2.1 of the Appendix 2 (A2) to ensure reproducibility of the simulations.

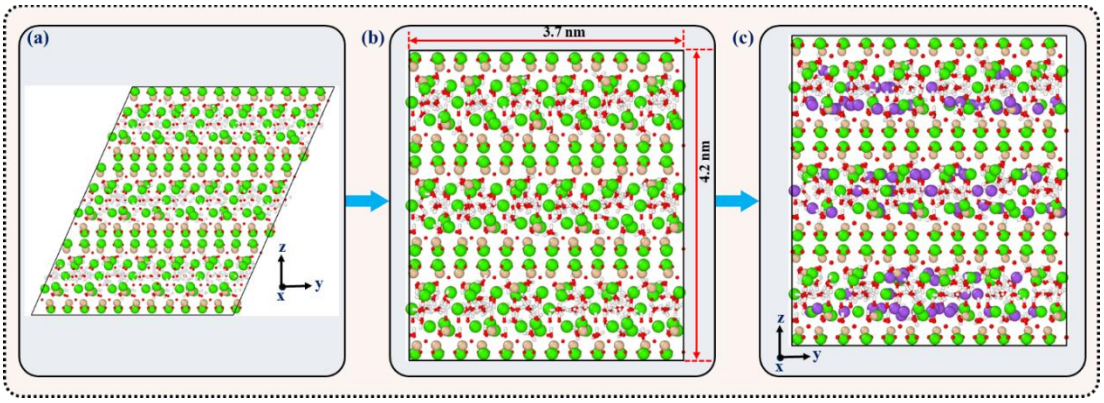

Figure 5.1. Model construction process for the initial C-S-H model with perfect contact: (a) initial 6 x 6 x 3 monoclinic C-S-H model with Ca/Si = 1.6, (b) transformation into an orthorhombic C-S-H model, (c) C-S-H_Na model with sodium-exchange cations.

Na^+, and Ca^{2+} ions are represented as purple, and green balls, while O, H, and Si atoms are illustrated as red, white, and light brown balls respectively.

Following model construction derived from the starting structure generated with pyCSH, where the generated structure represents the perfect contact interface, the interfacial distance was systematically increased up to 1 nm to investigate the effects of separation and water content on mechanical behaviour. For the perfect contact interface configuration, the interlayer spacing is approximately 0.5 nm. Systems with expanded pores are referred to by their additional (relative) interfacial distance rather than their total interlayer spacing. Specifically, the C-S-H structure was cleaved along the z-direction at the centre of the perfect contact interface to create controlled interlayer spaces. These spaces were subsequently hydrated with water molecules according to the excess water content per surface area as a function of interfacial distance specified in reference (Duque-Redondo et al., 2022b). The hydrated systems were then equilibrated in the isothermal-isobaric (NPT) ensemble under room conditions (298 K, 1 atm) to determine the equilibrated interfacial distances. We defined the nominal interfacial distance (d=0 nm) as the perfect contact interface, corresponding to the initial z-box dimension (z_0). Upon expanding the interface to a dimension z_1 in the z-direction and hydrating it, the nominal interfacial distance is calculated as $d=z_1-z_0$, representing the imposed expansion. Subsequent equilibration yielded an equilibrated dimension z_2; thus, all results presented correspond to the equilibrated interfacial distance ($d=z_2-z_0$).

5.2.2 Simulation details

In this study, ClayFF (Cygan et al., 2004) was used to simulate the interactions between C-S-H gel pore surfaces and different seawater ions. This force field has been thoroughly validated for simulating C-S-H systems and their interfacial interactions with aqueous environments (Dufresne et al., 2018, Hou et al., 2014b, Honorio et al., 2025). It has been widely used to model clay materials, bulk and confined solutions, and solution-clay

interfaces (Zhou et al., 2016, Zhang et al., 2017, Hou et al., 2018b, Zhou et al., 2018, Hayat et al., 2024), as well as the adsorption of anions and cations on hydroxyl surfaces (Kalinichev et al., 2007, Dongshuai et al., 2016).

All MD simulations in this study were performed using the LAMMPS (Large-scale Atomic/Molecular Massively Parallel Simulator) software package (Plimpton, 1995). The trajectories were integrated with a time step of 1 fs using the Verlet algorithm. Interatomic interactions were calculated using arithmetic mixing rules for both Lennard-Jones and Coulombic electrostatic potentials. Short-range interactions were truncated at 10 Å, while long-range electrostatics were computed with the particle-particle particle-mesh (PPPM) method. The initial configurations of all the interface models were first subjected to energy minimisation using the conjugate gradient method. The equilibration was performed in two stages under the isothermal-isobaric (NPT) ensemble conditions until the water density in the interlayer space became constant. In the first stage, the system was gradually heated from 10 K to 298 K over 0.5 ns in the NPT ensemble (Tdamp = 100 fs, and P = 1 atm). This controlled temperature ramp allowed the system to relax progressively. In the second stage, the system underwent further equilibration in the NPT ensemble at room conditions (T = 298 K, P = 1 atm) for 10 ns, with a timestep of 1 fs. The Nosé-Hoover thermostat was employed to maintain a steady temperature.

Shear and tensile deformations were performed on the equilibrated system by applying simple shear strain in the xz plane (perpendicular to the interface) and tensile strain along the z-direction (normal to the C-S-H layer), respectively. Various strain rates, ranging from 10^{-6} to 10^{-8} fs^{-1}, were evaluated and the results showed that strain rates exceeding 10^{-8} fs^{-1} did not allow sufficient time for molecular relaxation during deformation, as illustrated in Figure A2.1 (Appendix 2), leading to an overestimation of the calculated stresses.

Therefore, a strain rate of 10^{-8} fs^{-1} was used for both shear and tensile deformation. Shear deformations were performed in the canonical (NVT) ensemble at room temperature (298K), while tensile deformations were performed in the NPT ensemble at room conditions (T = 298 K, P = 1 atm). All simulations used a timestep of 1 fs and were run for 40 ns to achieve a total strain of 0.40 under both shear and tensile deformation.

All reported results in this study represent the averages from four independent simulations, each initiated with different initial velocities. TRAVIS (Trajectory Analyser and Visualiser) (Brehm and Kirchner, 2011, Brehm et al., 2020) and OVITO (Stukowski, 2010) programs were used for the analysis of the MD trajectories.

5.3 Results and discussion

5.3.1 Characterisation of interlayer space

First, we investigated the influence of nanoconfinement on the arrangement of water molecules within the interlayer space. Figure 5.2(a) depicts the density profiles of water molecules, including both O_w and H_w, along the z-axis for the configuration with perfect contact and additional interfacial distances of 0.08, 0.48, and 0.76 nm. In all cases, two small peaks in local water density are observed near the C-S-H surfaces, indicating an accumulation of ultra-confined water molecules and a structured orientation at the interface. This structured arrangement of water suggests that C-S-H exhibits hydrophilic properties, contrasting with the hydrophobic nature of cationic clays (Greenwell et al., 2006, Morrow et al., 2013, Masoumi et al., 2017, Duque-Redondo et al., 2019). Furthermore, the distribution of water in the interlayer space depends strongly on the interfacial distance. At distances less than 0.08 nm, water molecules are highly confined, and their density profile exhibits two peaks close to the substrate surfaces. When the interfacial distance increases

to 0.48 nm, the two initial peaks remain, while an additional peak emerges between them. At a distance of 0.76 nm, the water distribution displays a more ordered arrangement, characterised by a total of four distinct peaks, as shown in Figure 5.2(a). These results indicate that the transition from a configuration with two water layers to three water layers occurs at an interfacial distance of approximately 0.32 nm, while a further transition to four layers takes place at around 0.75 nm. This behaviour is consistent with observations reported in the previous studies (Duque-Redondo et al., 2022b).

Figure 5.2(b) presents a quantitative analysis of the total excess water present in the interlayer space as a function of additional interfacial distance. The term "excess" is used because, even when the C-S-H layers are in perfect contact (defined here as an interfacial distance of zero), some water molecules remain confined within the interlayer region. Therefore, Figure 5.2(b) illustrates the difference in water content between a given additional interfacial distance and the water content at perfect contact. The results indicate that the excess water content increases linearly with additional interfacial distance. The slope of this linear relationship (Figure 5.2(b)) represents the number of water molecules per unit volume, corresponding to the average water density in the interlayer space. This indicates that the average density of water within the interlayer remains constant as the separation between layers increases.

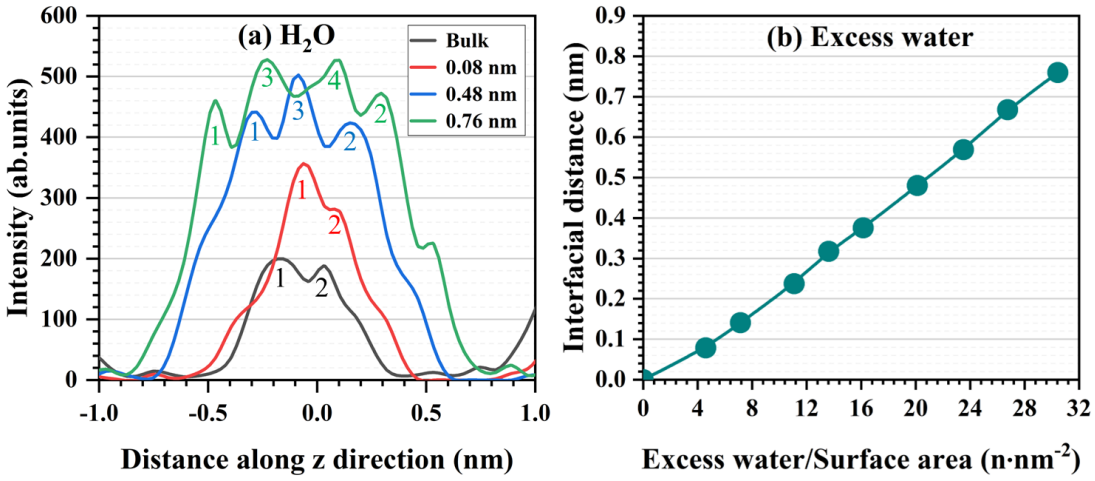

Figure 5.2. (a) Density profile of water molecules for perfect contact and an additional interfacial distance of 0.08, 0.48, and 0.76 nm. (b) Excess water content per unit surface area as a function of additional interfacial distance.

Figure 5.3(a) shows the volumetric expansion of the C-S-H systems after 10 ns of equilibration. Four C-S-H compositions are examined: C-S-H with Ca^{2+} (CSH), and versions where interlayer Ca^{2+} is partially substituted by Mg^{2+} (CSH_Mg), Na^{+} (CSH_Na), or K^{+} (CSH_K), with a cation/Si ratio of 0.3. Volume expansion is observed in monovalent cations substituted systems regarding the pure C-S-H, with the amount of expansion exhibiting the following trend: CSH_K (6.02%) > CSH_Na (1.18%). While decrease in volume is observed in the CSH_Mg (-1.72%) system in comparison with pure C-S-H system due to its smaller ionic radius. Previous atomistic simulations indicated that a volume expansion occurs due to the partial substitution of Ca^{2+} ions with monovalent cations (Dufresne et al., 2018, Yaphary et al., 2020), but a reduction in volume is noted with the partial replacement of Ca^{2+} ions by Mg^{2+} (Santos Rego et al., 2022). Similarly, Drame et al. (Dramé et al., 2007) observed swelling in hydrated cement and C-S-H upon exposure to aqueous salt solutions.

Figure 5.3(b) shows the dimensional changes along the perpendicular (z) direction for all the systems at perfect contact. An increase in length along the z-direction is observed with partial substitution of monovalent cations; however, a decrease in z length is observed with partial substitution of Mg^{2+} ions, following the same order as volumetric expansion. These results suggest that the presence of monovalent seawater cations in the interlayer of C-S-H increases the interlayer thickness while Mg^{2+} decreases it.

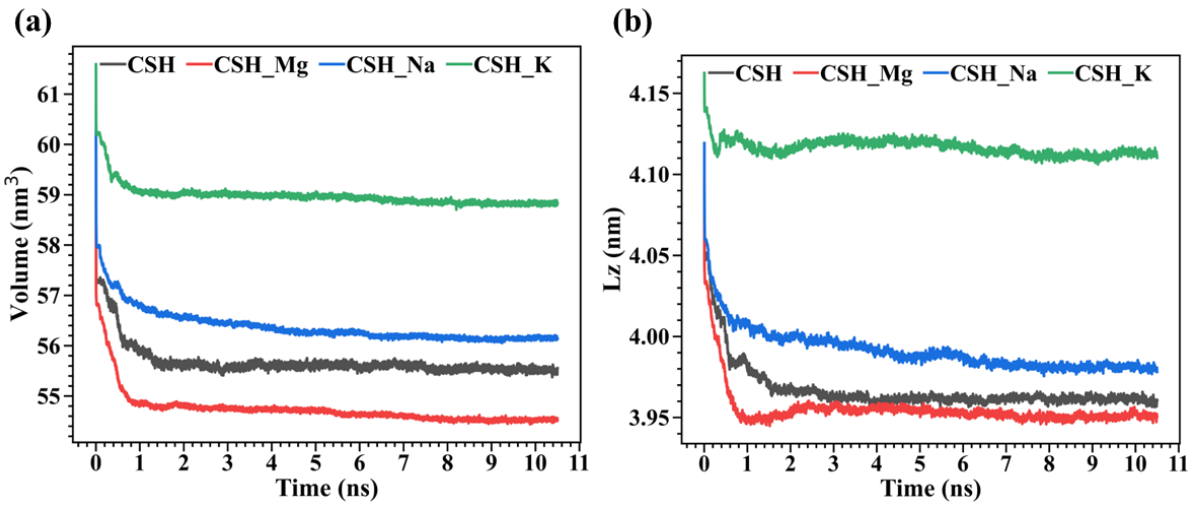

Figure 5.3. Evolution over time of (a) the simulation box volume and (b) the box length along the perpendicular (z) direction for the different C-S-H systems with perfect contact.

5.3.2 Interfacial shear strength

5.3.2.1 Stress-strain curve

Figure 5.4 depicts the stress-strain curve under shear deformation in the xz direction for systems with perfect contact and with an additional interfacial expansion of 0.08 nm. Four C-S-H compositions are examined: CSH, CSH_Mg, CSH_Na, and CSH_K, with a cation/Si ratio of 0.3. For all the cases, the shear stress shows a linear correlation with the shear strain during the initial (elastic) loading phase. Upon reaching peak stress, the shear stress exhibits oscillations, fluctuating around an average value as the strain continues to

increase. Under perfect contact conditions, the pure C-S-H system exhibits the highest shear strength, reaching its peak stress of 0.90 GPa at approximately 0.11 strain. The computed shear strength in this study is significantly higher than the macroscopic shear strength (0.33 GPa) observed in cement paste (Ulm et al., 2007). This discrepancy arises due to strength-controlling defects at larger mesoscopic scales in experimental samples. However, the computed strength value aligns with those calculated in prior bulk C-S-H simulations reported in the literature (0.72 GPa) (Duque-Redondo et al., 2022b). The CSH_Mg system displays a peak stress approximately equal to that of pure CSH, indicating that the mechanical integrity is maintained upon the partial substitution of Ca^{2+} by Mg^{2+}. In contrast, the partial substitution by monovalent cations leads to a decrease in shear resistance. Specifically, CSH_Na shows intermediate stress values, while CSH_K consistently exhibits the lowest stress across all strain levels. The overall performance order is: CSH ≈ CSH_Mg > CSH_Na > CSH_K. This trend becomes even more pronounced at an additional interfacial expansion of 0.08 nm (Figure 5.4(b)). Both C-S-H and CSH_Mg exhibit significant resistance to stress, with CSH_Mg closely resembling pure C-S-H. CSH_Na shows a more notable decrease in shear stress compared to the previous systems, while CSH_K displays the most significant reduction in performance, exhibiting the lowest shear stress values throughout the analysed strain range.

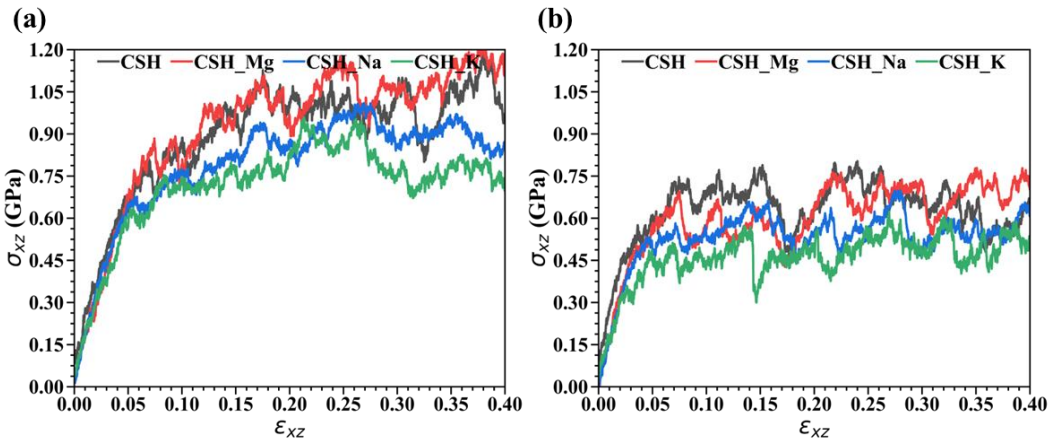

Figure 5.4. Stress-strain curves under shear deformation in the xz direction for (a) the perfect contact configuration and (b) with an additional interfacial expansion of 0.08 nm. In all cases, substituted C-S-H systems have a seawater cation/Si ratio of 0.3.

Shear strength

Figure 5.5(a) shows the shear strength as a function of additional interfacial distance for the systems with and without partial replacement by seawater ions. For all cases, shear strength decreases sharply as the interfacial distance increases; a trend consistent with previous observations (Duque-Redondo et al., 2022b). This behaviour arises because greater interfacial distances accommodate additional water layers between the C-S-H surfaces, resulting in reduced shear cohesion. Among the systems examined, pure C-S-H exhibits the highest shear strength, closely followed by CSH_Mg. The system with Na^+ substitution (CSH_Na) shows lower shear strength than these two, while the K^+-substituted system (CSH_K) displays the weakest performance with the lowest shear strength. The differences in shear strength between the systems are more pronounced at small interfacial distances, but become negligible beyond an additional interfacial distance of approximately 0.32 nm, where three layers of water are accommodated within the interlayer space. Shear strength with cation/Si=0.1 as a function of additional interfacial distance is shown in Figure A2.2 (Appendix 2), which shows similar behaviour as discussed above.

Figure 5.5(b) illustrates the shear modulus for all systems, derived from the slope of the stress-strain curves in the elastic regime, as a function of additional interfacial distance. Pure C-S-H exhibits the highest shear modulus at 16.8 GPa, which aligns well with previous results of 17.7 GPa (Honorio et al., 2025). Partial replacement of Ca^{2+} by seawater ions significantly reduces the shear modulus. Additionally, the shear modulus also decreases as the interfacial distance increases. This suggests that the partial

replacement by seawater ions diminishes both shear strength and shear modulus. The observed degradation patterns in shear strength and modulus highlight the combined influence of cation chemistry and interfacial distance on the nanoscale shear behaviour of C-S-H. To further investigate the mechanisms underlying these trends, Figure 5.6 examines the stress relaxation processes during shear deformations in C-S-H.

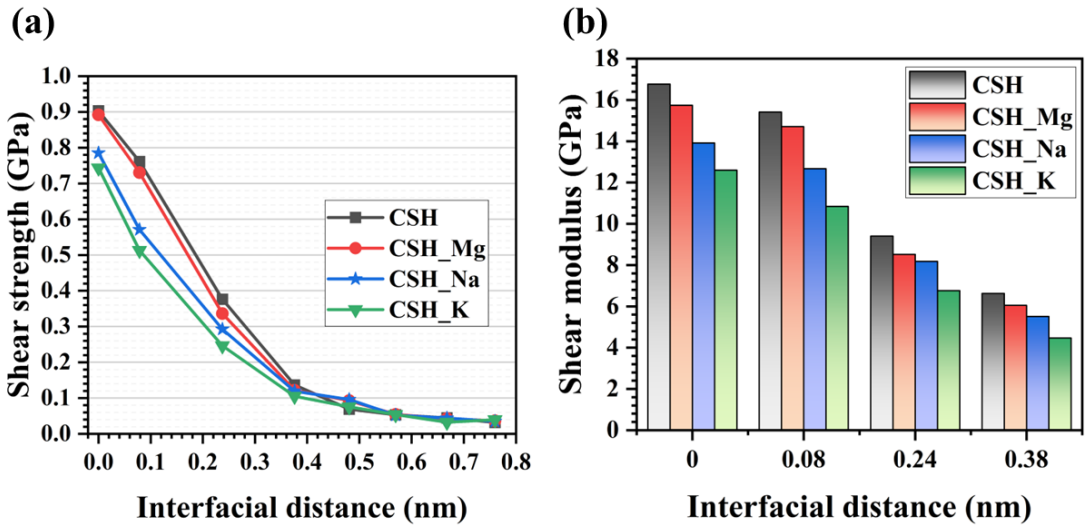

Figure 5.5. (a) Shear strength and (b) shear modulus as a function of additional interfacial distance for C-S-H with and without seawater ions with cation/Si=0.3.

5.3.2.2 Local strain plots

The spatial distribution of local shear strain in C-S-H samples subjected to shear deformation is shown in Figure 5.6. These distributions reveal localised structural adjustments that facilitate stress relaxation. At perfect contact or with small additional interfacial expansion (0.08 nm), all structural elements, including interlayer water molecules, as well as Ca and Si atoms in the C-S-H solid layers, undergo significant local deformations, collectively contributing to stress relaxation mechanisms. However, as the interfacial distance increases, stress relaxation primarily occurs through deformations in the interlayer space containing water, with local strain concentrated in this region, thereby

preserving the structural integrity of the solid C-S-H layers. Deforming the C-S-H layers themselves would require significantly more energy, as it could distort or break Si–O covalent bonds within the silicate chains, compared to overcoming the cohesive electrostatic and dispersive forces in the interlayer space. Consequently, when the interlayer space contains sufficient water, the C-S-H layers can slide over each other, facilitating stress relaxation under shear loading. In this scenario, both interfacial distance and water content determine the cohesion and mechanical behaviour. This observation aligns with the plastic deformation phenomena observed by Gardner et al. (Gardner et al., 2021). Raman spectroscopy investigations have shown that, for non-crosslinked C-S-H materials, similar to the model employed in this study, relaxation processes involve silicate chains sliding through a water-filled interlayer. Similar stick-slip relaxation mechanisms have also been described in C-S-H and other layered materials (Bhushan et al., 1995, Hantal et al., 2014, Duque-Redondo et al., 2014). In this study, the local shear strain distributions are shown only for pure C-S-H, without partial replacement of cations, as the stress relaxation behaviour was found to be consistent across all cases examined.

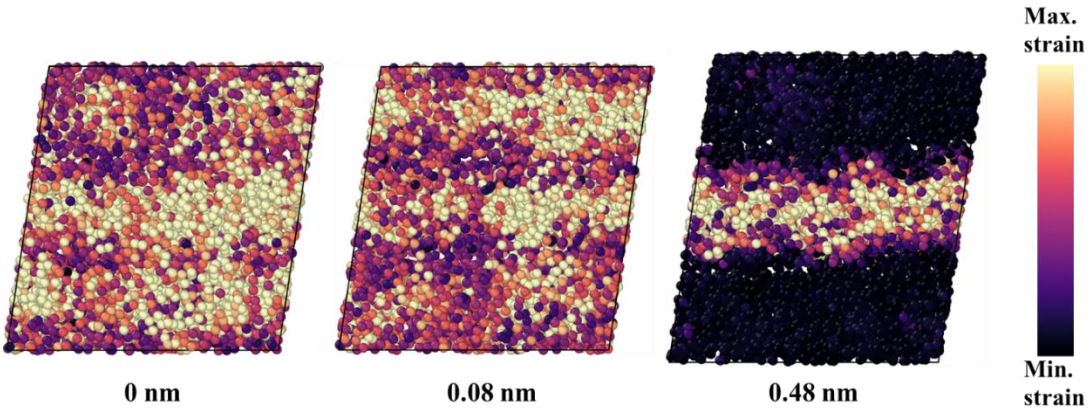

Figure 5.6. Normalized spatial distribution of local shear strain at 15% average shear strain for C-S-H systems with additional interfacial expansions of 0 nm (perfect contact), 0.08 nm, and 0.48 nm.

5.3.2.3 H-bond network

Prior research indicates that the hydrogen bond network likely plays a key role in the cohesion of layered composites (Duque-Redondo et al., 2014, Hou et al., 2014b, Fan and Yang, 2018). To assess the potential effect of hydrogen bonding on the cohesion of C-S-H systems, the average number of hydrogen bonds was computed for all cases, with and without partial replacement of Ca^{2+} by seawater cations. Figure 5.7 presents a linear Sankey diagram generated using TRAVIS (Brehm et al., 2020), illustrating hydrogen bond donors on the left and acceptors on the right. Three types of hydrogen bond donors are shown: water H, hydroxyl H, and total water and hydroxyl H. The three acceptors include water O, hydroxyl O, and O from the silicate surface. The values in the figure represent the average hydrogen bond count for each donor/acceptor. In pure C-S-H, the hydrogen bond network exhibits significant connectivity, with water molecules forming strong links between the silicate layers. This configuration results in a maximum average of hydrogen bonds per donor/acceptor, signifying improved cohesion and mechanical strength. The H-bond network of CSH_Mg closely resembles that of pure C-S-H. Due to the smaller ionic radius and equal charge to Ca^{2+}, Mg^{2+} can be incorporated into the interlayer structure, causing minimal disruption to the existing hydrogen bond network. This intact H-bond network explains why CSH_Mg maintains shear strength comparable to that of pure C-S-H. In contrast, systems incorporating monovalent cations show differences in their H-bond arrangements. Compared to pure C-S-H and CSH_Mg, the CSH_Na system exhibits reduced H-bond interconnectivity. This may be attributed to the lower charge density of Na^{+}, which limits its effectiveness in polarising water molecules and stabilising silicate–water interfaces (Liu et al., 2025). The CSH_K system has the weakest H-bond network, with the lowest average number of hydrogen bonds per donor/acceptor pair. The large

ionic radius of K^+ induces steric hindrance and reduces electrostatic interactions, leading to a less cohesive interlayer structure. This H-bond arrangement is consistent with the mechanical performance of this system, since CSH_K consistently demonstrates the lowest shear strength. The hydrogen bond network was also assessed at larger interfacial distances; however, no significant variation was seen with the increase in interfacial distance, as illustrated in Figure A2.3 (Appendix 2).

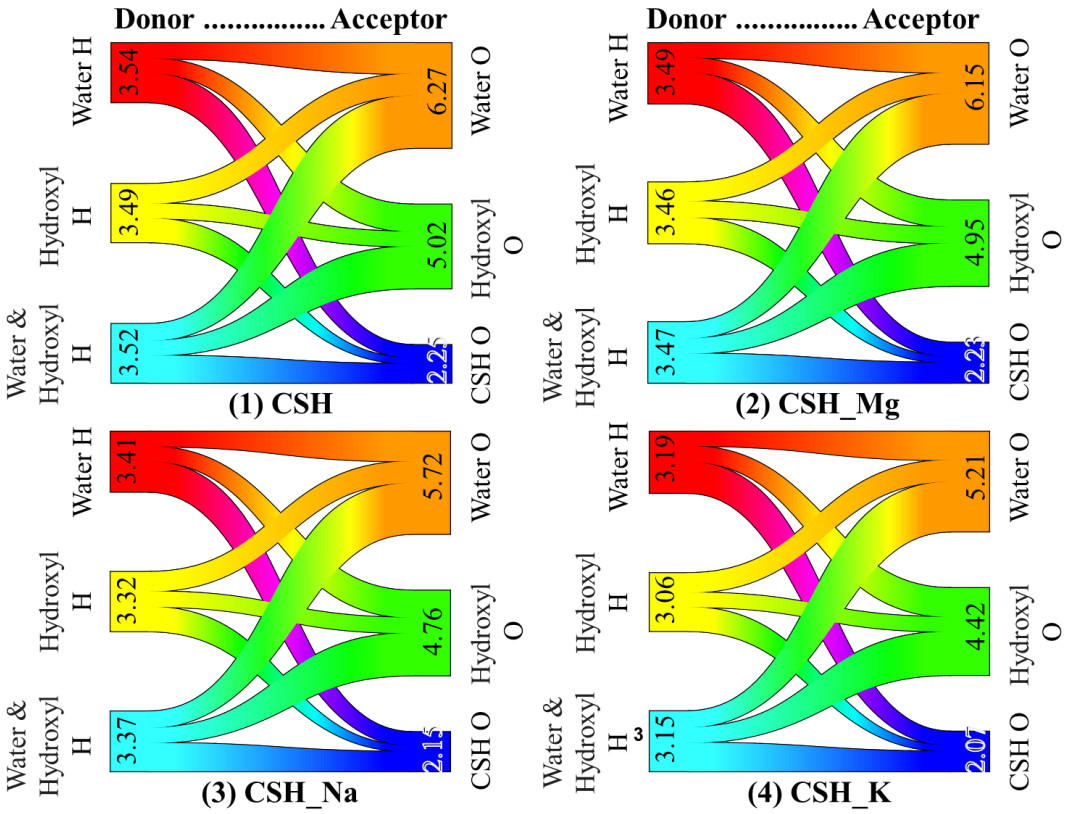

Figure 5.7. Linear Sankey diagram illustrating the hydrogen bonding topology in systems with an additional interfacial expansion of 0.08 nm.

5.3.2.4 Density profile of cations

Figure 5.8 shows the density profile of cations (Mg^{2+}, Na^+, and K^+) along the z-direction in the systems with additional interfacial expansions of 0.08, 0.48, and 0.76 nm. The cation distribution patterns revealed in these profiles are directly related to their bonding

behaviour and align with the shear strength trends observed in the previous section. For small additional interfacial expansions, density profiles show distinct adsorption behaviours for the three cations. Mg^{2+} ions exhibit clear density peaks close to the silicate surfaces, indicating strong adsorption onto the C-S-H sheets. Additionally, Mg^{2+} ions occupy positions similar to those of interlayer Ca^{2+} ions, as shown in Figure A2.4 (Appendix 2). This behaviour arises from the high charge density and small ionic radius of Mg^{2+}, which enables strong electrostatic interactions with the negatively charged silicate layers. On the other hand, Na^{+} ions have a more diffuse distribution, characteristic of monovalent cations with moderate charge density, while K^{+} ions are distributed most uniformly throughout the interlayer space, lacking notable surface adsorption peaks due to their large ionic radius and lower charge density that reduces electrostatic attraction to the silicate surfaces. The observed variations in cation distribution directly correlate with the differences in shear strength for those systems. As the interfacial distance increases, the distribution of all cations becomes more uniform; however, the inherent adsorption behaviours remain distinct.

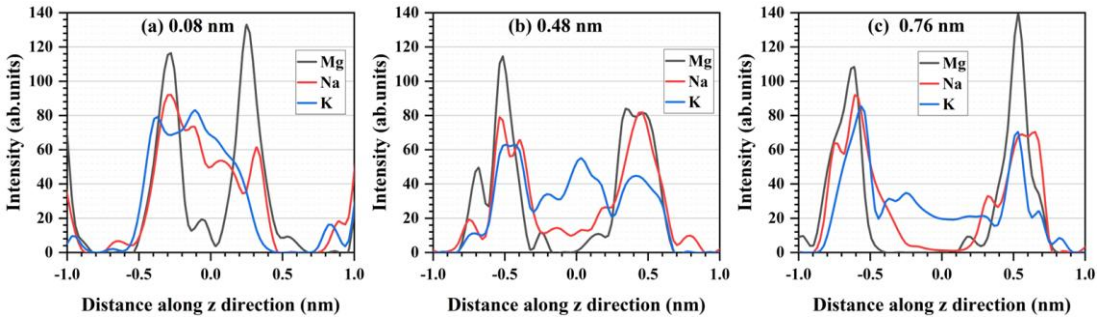

Figure 5.8. Density profile of seawater cations along the z-direction in the interlayer space at additional interfacial expansions of (a) 0.08, (b) 0.48, and (c) 0.78 nm.

5.3.2.5 Diffusion coefficients

Shear cohesion is significantly influenced by the mobility of water molecules in the interlayer space (Duque-Redondo et al., 2022b). To investigate this effect, we calculated the diffusion coefficients of water molecules and cations in the interlayer space as a function of additional interfacial distance, as shown in Figure 6.9. When the additional interfacial expansion is below 0.32 nm, water mobility is considerably restricted, resulting in very low diffusion coefficients. However, beyond this point, the behaviour of the system changes significantly due to the formation of a trilayer water structure. The diffusion coefficient increases linearly with further expansion of the interlayer distance, suggesting a transition towards behaviour more akin to that of bulk water. This transition occurs because water in the central region of the interlayer is far enough from the silicate surfaces to avoid their strong electrostatic influence, resulting in increased molecular mobility. The observed increase in diffusivity beyond 0.32 nm aligns with the sharp decrease in cohesion and shear strength seen in Figure 5.5, suggesting that the transition from bound to mobile water molecules weakens interlayer bonding at the nanoscale. Such behaviour has also been reported in previous studies on C-S-H (Duque-Redondo et al., 2022b) and in clay minerals (Duque-Redondo et al., 2019), suggesting it could be a common characteristic of layered materials containing confined water.

Figure 5.9(b) depicts the diffusion coefficients of cations (Mg^{2+}, Na^{+}, and K^{+}) as a function of additional interfacial distance, revealing ion-specific trends that directly correlate with their observed shear strength performance. Across all interfacial distances, the diffusion coefficients of cations follow the order: $K^{+} > Na^{+} > Mg^{2+}$, consistent with previous findings (Li and Merz, 2022). K^{+} ions exhibit the highest diffusion coefficients due to their weak adsorption to silicate surfaces, which facilitates their mobility in the interlayer space. This high mobility is associated with the reduced shear strength performance observed in

CSH_K. Na^+ ions display intermediate mobility, consistent with the moderate reduction in shear strength. In contrast, Mg^{2+} ions exhibit the lowest diffusion coefficients. This is due to their strong adsorption to the surface and resulting limited mobility, reflecting their strong adsorption to the silicate surfaces and restricted mobility. This limited movement enables Mg^{2+} to effectively bridge C-S-H layers, explaining why CSH_Mg maintains shear strength comparable to that of pure C-S-H systems. As the interfacial distance increases, the diffusion coefficients of all cations rise, indicating a reduction in the effects of confinement. Nevertheless, the relative order of these coefficients remains consistent across all examined interfacial distances.

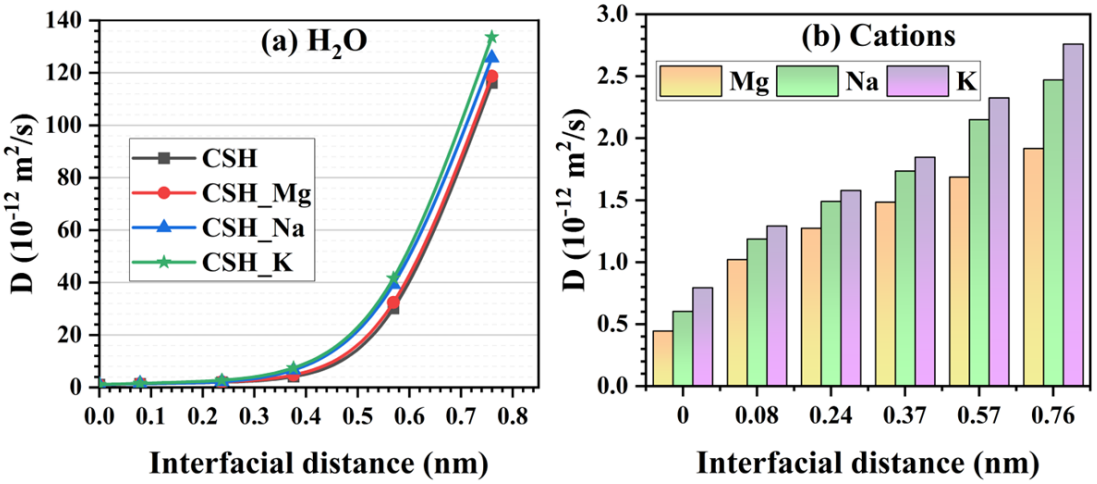

Figure 5.9. Average diffusion coefficient of (a) water molecules and (b) seawater cations as a function of additional interfacial expansion distances.

5.3.3 Uniaxial tension loading

5.3.3.1 Stress-strain curves

Figure 5.10 shows the stress-strain curves for all the systems under uniaxial tensile loading in the z-direction for the perfect contact configuration and for an additional interfacial expansion of 0.08 nm. During the initial loading phase (elastic region), all systems display

linear elastic behaviour. Tensile strength is defined as the maximum stress achieved, while Young's modulus corresponds to the slope of the stress-strain curve in the elastic regime, and the fracture strain is the strain at which stress falls to zero. Both tensile strength and fracture strain show considerable differences depending on cation substitution. The pure C-S-H system exhibits the best mechanical performance, reaching a maximum tensile strength of 2.51 GPa and the highest fracture strain of 0.46. These values are consistent with previous simulations on C-S-H (Zhu et al., 2023). This behaviour indicates the preservation of the atomic bond network within the original C-S-H structure. When Ca^{2+} is partially substituted, a clear decline in mechanical properties is observed, following the order: CSH_Mg > CSH_Na > CSH_K, for both tensile strength and fracture strain. CSH_Mg retains considerable tensile strength, although lower than that of pure C-S-H, as Mg^{2+} has a similar charge, but smaller ionic size compared to Ca^{2+}, allowing it to partially compensate for Ca^{2+} removal. CSH_Na exhibits a more pronounced reduction in strength, as the monovalent Na^{+} is less effective at forming ionic bridges between the silicate layers. CSH_K shows the weakest performance, with the large ionic radius of K^{+} causing significant disruption of the atomic bonding network. The reduction in fracture strain follows the same cation-dependent trend, suggesting that systems with cation replacement exhibit increased brittleness. Overall, these results indicate that cation substitution weakens the structural integrity of C-S-H and reduces its capacity for plastic deformation to accommodate tensile strain.

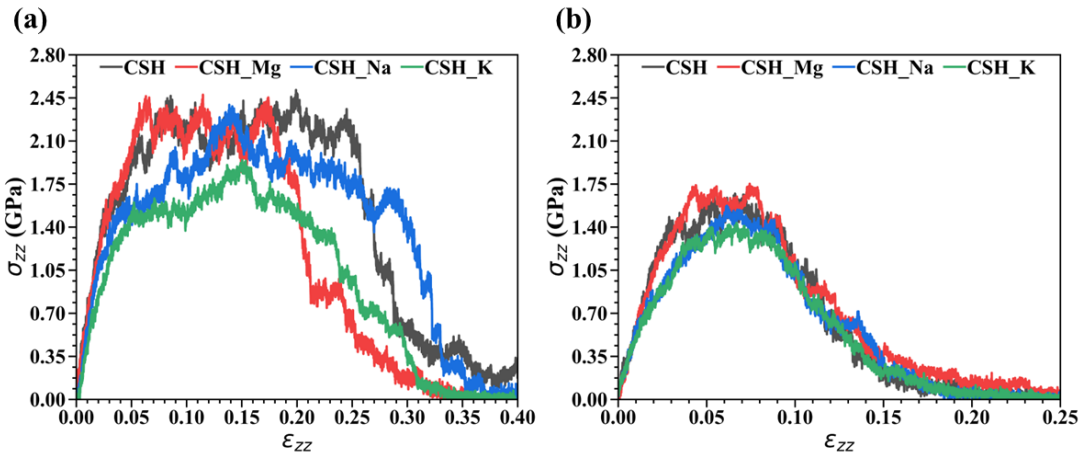

Figure 5.10. Stress-strain curves under uniaxial tensile loading in the z-direction for (a) perfect contact configuration and for (b) an additional interfacial expansion of 0.08 nm. Results are shown for pure C-S-H and substituted C-S-H with a cation/Si ratio of 0.3.

5.3.3.2 Tensile strength and Young's modulus

The mechanical performance parameters, including tensile strength and Young's modulus as a function of additional interfacial distances, shown in Figure 5.11, were derived from the stress-strain curves from Figure 5.10. Across all interfacial distances, the pure C-S-H system exhibits the highest tensile strength. Partial replacement of interlayer Ca^{2+} by other cations leads to a decrease in tensile strength, following the order: CSH $\approx$ CSH_Mg > CSH_Na > CSH_K. Notably, CSH_Mg closely follows pure C-S-H, highlighting the significant influence of cation chemistry on the mechanical properties of C-S-H. The decline in tensile strength is most pronounced when the interfacial distance is small, where the type of cation significantly affects the interlayer bonding. As the interfacial distance increases, these differences diminish, leading to similar tensile strengths across all systems. The observed tensile strength patterns align with previous shear strength results, supporting the idea that cation substitutions and interfacial distances affect both shear and tensile mechanical characteristics in a similar manner.

Figure 5.11(b) illustrates the evolution of Young's modulus as a function of additional interfacial distance for all the systems. The results show that pure C-S-H exhibits the highest stiffness, 60.7 GPa, consistent with previously reported values (55–68 GPa) (Pellenq et al., 2009, Duque-Redondo et al., 2022a). Partial replacement of interlayer Ca^{2+} with other cations leads to a corresponding decrease in Young's modulus, following the same order observed for tensile strength: CSH ≈ CSH_Mg > CSH_Na > CSH_K. For all systems, Young's modulus decreases significantly as the interfacial distance increases. Overall, substitution with seawater cations reduces strength, stiffness, and ductility across all the interfacial distances examined. The failure mechanisms under tensile loading are shown in Figure A2.5 (Appendix 2).

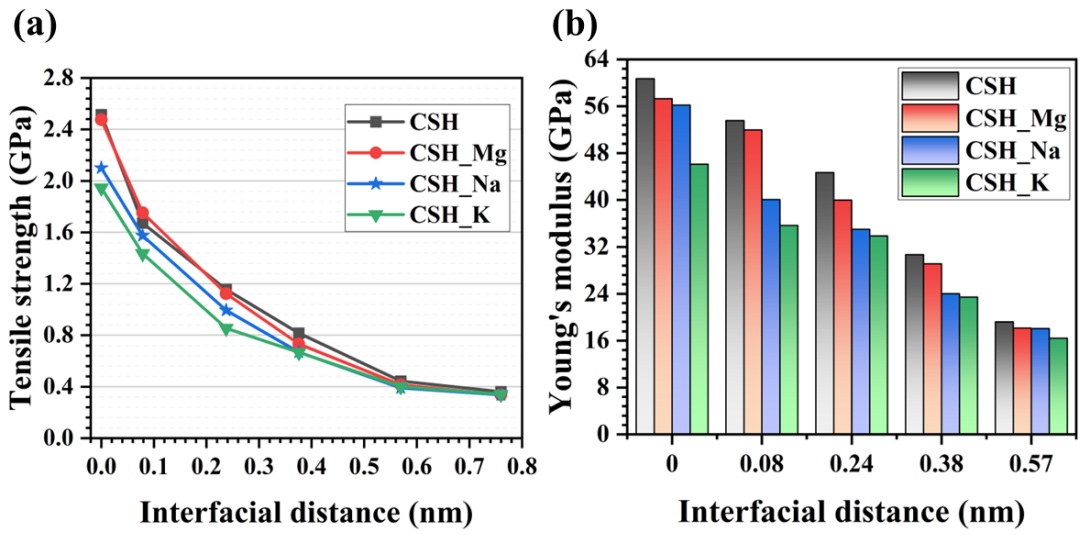

Figure 5.11. (a) Tensile strength and (b) Young's modulus as a function of additional interfacial expansion for pure and substituted C-S-H systems with a cation/Si ratio of 0.3.

5.3.4 Atomic-scale results in context

To contextualise the differences in atomic-scale shear moduli among the various C-S-H systems, we roughly evaluate the macroscopic impact of porosity using the self-consistent (SC) micro-mechanical model (Kröner, 1971). The aim is to evaluate if the impact of the

decalcification is significant compared to other factors, porosity in this case. Within the SC framework, the C-S-H gel is represented as a composite material comprising a solid phase (porosity-free C-S-H) with voids filled with water. The mechanical properties of C-S-H gel are derived from the mechanical properties of the solid phase and certain packing factors (η), which are related to the porosity (φ) of gel, represented by the equation η=1-φ. The shear modulus ($G_{C\text{-}S\text{-}H}$) and bulk modulus ($K_{C\text{-}S\text{-}H}$) of the C-S-H gel can be described as follows (Constantinides and Ulm, 2007, Manzano et al., 2009, Jennings et al., 2007):

$$\frac{G_{C-S-H}}{G_0} = \frac{1}{2} - \frac{5}{4}(1-\eta) - \frac{3}{16}r_0(2+\eta) + \frac{1}{16}\sqrt{144(1-r_0) - 480\eta + 400\eta^2 + 408r_0\eta - 120r_0\eta^2 + 9r_0^2(2+\eta)^2} \quad (5.1)$$

$$\frac{K_{C-S-H}}{K_0} = \frac{4\eta G/G_0}{4G/G_0 + 3(1-\eta)r_0} \quad (5.2)$$

where G_0 and K_0 are the intrinsic (porosity-free) shear and bulk modulus of C-S-H, and r_0 is defined as the ratio of K_0/G_0. K_0= 30 GPa was obtained from reference (Manzano et al., 2009), while G_0 corresponds to the shear modulus of the solid C-S-H phase, as determined through atomic-scale simulations in section 6.3.2.

Figure 5.12 illustrates how the shear modulus decreases with increasing porosity for CSH, CSH_Mg, CSH_Na, and CSH_K. Although the intrinsic (porosity-free) moduli differ significantly between the systems, these differences progressively diminish as porosity increases. At moderate porosity levels (e.g., φ > 0.25), the curves for different C-S-H systems are below the bulk values for CSH_K. Furthermore, the reduction produced by an additional 5% increase in porosity (from 25% to 30%). This clearly highlights that, at the macroscale, porosity exerts a stronger control on mechanical response than the atomic-scale stiffness differences introduced by cation substitution. This indicates that while atomic-scale substitutions influence the local stiffness, their effect on the overall mechanical response of the porous gel becomes less critical in highly porous regimes, and

CH consumption due to pH reduction, important for Mg but less for alkalis, should be considered for a broader view.

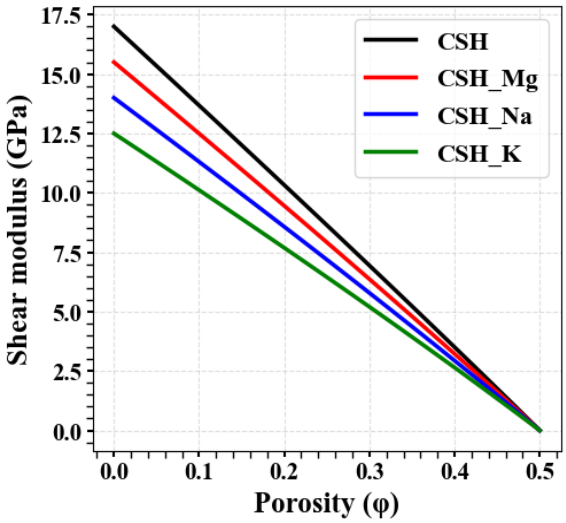

Figure 5.12. Micromechanical prediction of the shear modulus as a function of porosity for all the systems.

5.4 Summary

This study employed molecular dynamics simulations to investigate the shear and tensile properties of C-S-H at the nanoscale, considering the influence of both interfacial distance and partial substitution of Ca^{2+} by seawater ions (Mg^{2+}, Na^{+}, and K^{+}). The results demonstrate that, under constant shear strain and at perfect interface, the pure C-S-H system has the highest shear strength, reaching a maximum of 0.90 GPa at approximately 0.11 strain. The partial substitution with seawater cations results in a reduction of shear strength, following the order: CSH $\approx$ CSH_Mg > CSH_Na > CSH_K. As the interfacial distance increases, all systems show a sharp decline in shear strength, with a complete loss of cohesion beyond an expansion of 0.32 nm, attributed to the transition of water in the interlayer from a bilayer to a trilayer configuration.

The distribution of local shear strain demonstrates that stress relaxation is limited to the interlayer space, while the C-S-H layers remain rigid, confirming a stick-slip relaxation mechanism. This mechanism is consistent across all systems, regardless of cation substitution, indicating that the fundamental relaxation process is preserved.

The reduction in shear strength coincides with the increased mobility of water at interfacial expansions above 0.32 nm. Calculations of water diffusion coefficients within the interlayer space suggest that increased water mobility directly results in reduced shear strength. These findings confirm that the shear cohesion of C-S-H is significantly influenced by the mobility of interlayer water, as higher mobility reduces cohesive forces when water molecules are allowed to flow freely.

In tensile loading tests, the pure C-S-H system consistently outperforms cation-substituted systems in terms of mechanical properties, including tensile strength, stiffness, and ductility, following the order: CSH $\approx$ CSH_Mg > CSH_Na > CSH_K. The correlation between shear and tensile responses highlights the significant impact of cation substitution and interfacial distance on the mechanical behaviour of C-S-H systems. These findings provide a nanoscale understanding that can be leveraged to optimise cementitious materials, particularly in applications where interfacial cohesion and water-induced degradation are critical, such as in marine environments.

Finally, micromechanical modelling demonstrates that porosity progressively governs the macroscopic mechanical response of C-S-H gels, reducing the influence of atomic-scale differences between systems as porosity increases. At moderate-to-high porosity, the mechanical performance converges regardless of cation substitution, indicating that porosity dominates the mechanical behaviour at larger scales.

Chapter 6. Durability of seawater mixed cement paste

6.1 Introduction

Chapters 3-5 focused on the nanoscale, elucidating the role of seawater ions in transport, desorption, and the mechanical strength of C-S-H; nevertheless, the chapter 6 focuses on the durability of seawater mixed cement paste at macroscale. The durability of concrete is a crucial factor governing structural service life and must be carefully considered when evaluating the practical use of seawater-mixed concrete. The chemical interaction between seawater and cementitious materials is complex due to the presence of multiple aggressive ions in seawater, such as chloride, sulphate, magnesium, and carbonate (Song et al., 2021, De Weerdt et al., 2014a). Chloride ions are generally considered less aggressive than sulphate because the compounds they form are non-expansive. When cementitious materials are exposed to chloride-rich environments, chlorides either exist as free chlorides in the pore solution or in combination with different hydration products, thereby influencing their diffusion in concrete (Gallucci and Scrivener, 2007, Hayat et al., 2024). The chlorides chemically react with aluminate phases such as monosulphates to produce Friedel's salt (Eq. (1)) or the mixed chloro-sulphate AFm phase known as Kuzel's salt (Eq. (2)). In addition, chloride can be physically adsorbed onto C-S-H surfaces (Frias et al., 2013, De Weerdt et al., 2014a). Kalinichev et al. (Kalinichev and Kirkpatrick, 2002) showed that Cl^- can adsorb onto the surfaces of Friedel's salt, portlandite (CH), and C-S-H, indicating that multiple phases participate in chloride retention. Changes in the morphology of CH caused by chloride exposure have been reported to influence transport properties and reduce material stability (Galmarini et al., 2011). Additionally, studies have

shown that divalent cations exhibit a stronger chloride-binding capacity on cement surfaces compared with monovalent cations (Zhu et al., 2012).

$$C_3A+Ca(OH)_2+2Cl^-+10H_2O \rightarrow C_3A.CaCl_2.10H_2O\ (\text{Friedel's salt})+2OH^- \quad (6.1)$$

$$C_3A+0.5Ca(OH)_2+0.5CaSO_4+2Cl^-+10H_2O \rightarrow C_3A.(CaCl_2)_{0.5}.(CaSO_4)_{0.5}.10H_2O\ (\text{Kuzel's salt}) \quad (6.2)$$

Sulphate attack induces multiple degradation processes in cement paste, including CH decomposition, C-S-H decalcification, and gypsum formation, all of which compromise concrete durability. Zhang et al. (Zhang et al., 2013b) reported that cement concrete is highly vulnerable to sulphate attack, with the strength retention ratio declining to zero after two years of exposure. This degradation is ascribed to the formation of expansive products such as gypsum and ettringite, which disrupt the microstructure. As these products accumulate, they generate internal stresses and cracking, creating pathways for further ingress of aggressive ions (Gu et al., 2022). Moreover, the severity of sulphate attack depends on the specific type of sulphate involved. The impacts of Na_2SO_4 and K_2SO_4 on concrete are largely analogous, as both yield gypsum and ettringite as the major degradation products. Conversely, $MgSO_4$ is more deleterious, as Mg^{2+} interacts with CH to form brucite, hence reducing the pore solution pH and facilitating the leaching of Ca^{2+} from C-S-H. This mechanism promotes formation of M-S-H gel and additional gypsum, resulting in increased degradation. Interestingly, some investigations indicate that the incorporation of seawater can improve sulphate resistance by modifying the microstructure and decreasing C_3A content, thus mitigating expansion responses (Zhao et al., 2021, Han et al., 2021b). Han et al. (Han et al., 2021b) and Ting et al. (Ting et al., 2020) found that seawater-mixed OPC and high-ferrite Portland cement (HFPC) showed less damage from

sulphate attack compared with freshwater concrete. Du et al. (Du et al., 2022) demonstrated that incorporation of 0.1-1.0% NaCl significantly enhanced the sulphate resistance of OPC exposed to 10% Na_2SO_4 solution. Harrison (Harrison, 1990) confirmed that NaCl or $CaCl_2$ generally had negligible or favourable effects on sulphate resistance over long-term exposure, although $CaCl_2$ reduced sulphate resistance in some cases under severe sulphate conditions. The beneficial effects are ascribed to the refinement of pore structure by Friedel's salt (Han et al., 2021b), the reaction of chloride with C_3A and portlandite which reduces ettringite and gypsum formation (Han et al., 2021b), the restriction of sulphate ingress that limits ettringite and Glauber's salt crystallization (Du et al., 2022), and the increased solubility of ettringite in chloride-bearing pore solutions (Corner and Rippstain, 1985), which lowers expansion stresses. Cai et al. (Cai et al., 2025) investigated cement pastes mixed with seawater and deionised water, subjected to 50 g/L Na_2SO_4 for 450 days. Their findings reveal that seawater mixing reduced Ca leaching, mass loss, dimensional changes, and gypsum-induced cracking, while enhancing phase stability and maintaining higher compressive strength, thereby indicating improved sulphate resistance

Conversely, Zhao et al. (Zhao et al., 2018) found that the addition of 3, 5, and 10 wt% NaCl to concrete, when cured under standard conditions (20 °C, RH>95%) for 18 hours and subsequently immersed in sulphate solution for one year, resulted in increased expansion and mass loss, as well as reduced compressive strength relative to concrete without NaCl. When chloride-containing concrete is exposed to a sulphate solution, bound chlorides may be released as free chloride due to sulphate attack (Zhang et al., 2021a). Friedel's salt is especially susceptible to transformation into ettringite in the presence of sulphates, particularly Na_2SO_4 (Yang et al., 2019c). Moreover, sulphate ions compete with

chloride ions for adsorption sites on C-S-H, thereby reducing the amount of physically bound chloride (Cao et al., 2020). Zhao et al. (Zhao et al., 2023) investigated seawater-mixed cement paste subjected to sulphate attack and found that sulphates destabilise chloride-binding phases, such as Friedel's salt, resulting in the desorption of bound chloride as free chloride. The literature reports both the positive and negative effects of sulphate attack on seawater-mixed cement paste. Nonetheless, the influence of chloride, sulphate, and combined chloride-sulphate attack on seawater-mixed cement paste, including the distinct roles of various cations, are still not fully understood, and the associated phase evolution mechanisms require further investigation.

The aim of this study is to systematically assess the long-term impacts of chloride, sulphate, and combined chloride-sulphate attacks on seawater-mixed cement paste. Cement pastes made with seawater were subjected to a one-year exposure to 5% chloride (NaCl, KCl, $CaCl_2$, and $MgCl_2$), 5 % sulphate (Na_2SO_4, K_2SO_4, $CaSO_4$, and $MgSO_4$), and a mixed solution of 5% chlorides and 5% sulphates ($NaCl+Na_2SO_4$, $KCl+K_2SO_4$, $CaCl_2+CaSO_4$, and $MgCl_2+MgSO_4$). Following exposure, changes in mineralogical composition, microstructure, elemental distribution, and micromechanical characteristics were thoroughly evaluated using X-ray diffractometer (XRD), Fourier transform infrared (FTIR), thermogravimetric analysis (TGA), Energy dispersive spectroscopy (EDS), and nanoindentation. This study aims to explain the degradation mechanisms of seawater-based cementitious materials under combined chloride and sulphate exposures through the integration of phase analysis, microstructural characterisation, and micromechanical properties.

6.2 Experimental program

6.2.1 Raw material

This study used synthetic seawater prepared in accordance with ASTM D1141-98 specifications (Standard, 2013). Analytical-grade chemical reagents were used to synthesise artificial seawater, with the specific salts and concentration detailed in Table 6.1. Deionised water was utilised to prepare the chemical solutions. Cement used in this study is Ordinary Portland Cement (OPC) with grade 52.5, supplied by Gammon Construction Limited. X-ray fluorescence spectroscopy was used to analyse the chemical composition of the OPC, and the results are detailed in Table 6.2.

Table 6.1. The concentration of salt in synthetic seater (g/L).

NaCl	$MgCl_2.6H_2O$	Na_2SO_4	$CaCl_2$	KCl
24.530	5.200	4.090	1.160	0.695

Table 6.2. Chemical composition of cement by XRF (wt. %)

CaO	SiO_2	Al_2O_3	Fe_2O_3	MgO	K_2O	TiO_2	MnO	SO_3	P_2O_5	SrO
70.3	15.3	4.35	3.74	0.85	0.66	0.34	0.05	4.1	0.14	0.11

6.2.2 Cement paste preparation

All the cement paste were prepared with a water to cement (w/c) ratio of 0.4. Seawater (SW water) was utilised as mixing water to evaluate and examine the impact of seawater ions on the characteristics of cement paste. Following mixing, the fresh cement paste was cast into plastic cylinders with a nominal diameter of 50 mm and a height of 100 mm. The surface of the samples was then covered with plastic film for 24 hours to prevent water

loss. The specimens were demoulded after 24 hours and then preserved in sealed plastic bags for curing up to 90 days in a 95% humidity chamber at 23.0 ± 2.0 °C to ensure sufficient hydration.

6.2.3 Sample preparation for exposure

After a curing period of 91 days, the demoulded paste specimens were sliced into about 2 mm thick slices, as shown in Fig. 6.1 for subsequent exposure. These slices were taken from the middle portion of the cement paste cylinder to avoid the influence of segregation. The slices were initially dried for 72 hours in a vacuum desiccator containing silica gel at ambient temperature. Each slice was then placed in a plastic container and supported by small plastic grid as shown in Fig. 6.1. 60 ml of each exposure solution was added in the container by pipette. A reference sample was also prepared, and it was exposed to the same amount of DI water. The plastic containers were sealed with lids and parafilm and stored at room temperature, with the internal solutions being swirled after 14 days. Duplicate samples were prepared for each exposure condition. After a one year of exposure period, the samples were presumed to have reached equilibrium with the exposed solution, as established by prior research (Chen and Ye, 2022, Chen and Ye, 2023).

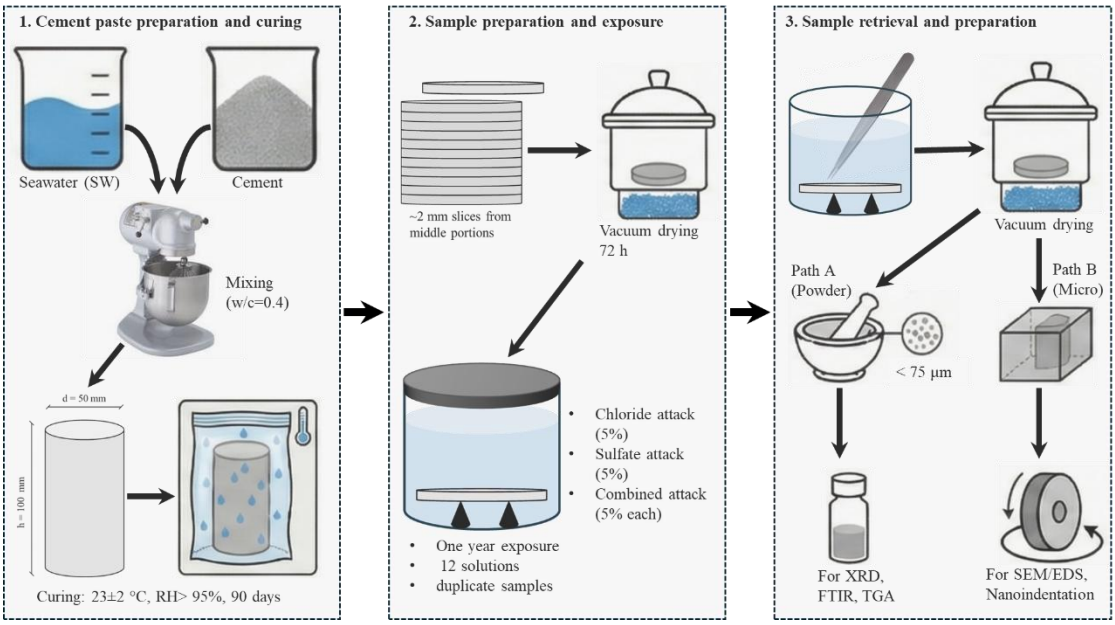

Figure 6.1. Schematic of experimental methodology for seawater mixed cement paste subjected to chloride, sulphate, and combined chloride-sulphate attack.

6.2.4 Exposure conditions

Three exposure conditions were designed, which consist of 12 different exposure solutions to study the chloride, sulphate and combined attack on seawater mixed cement paste. The details of the exposure condition are given below:

Scenario I aims to investigate the influence of chloride attack on the seawater mixed cement paste. Four solutions were designed for chloride attack which are NaCl, KCl, $CaCl_2$, and $MgCl_2$. We used a chloride concentration of 5% by weight for all the cases. The solutions were prepared by regent grade NaCl, KCl, $CaCl_2$, and $MgCl_2$.

Scenario II aims to investigate the influence of sulphate attack on the seawater mixed cement paste. Four solutions were designed for sulphate attack which are Na_2SO_4, K_2SO_4, $CaSO_4$, and $MgSO_4$. A sulphate concentration of 5% by weight was utilised in this study.

The type of sulphate is more important than the molar mass of sulphate (Yang et al., 2019c). The solutions were prepared by regent grade Na_2SO_4, K_2SO_4, $CaSO_4$, and $MgSO_4$.

Scenario III aims to investigate the influence of combined chloride and sulphate attack on the seawater mixed cement paste. Four solutions were designed for the combined attack which are NaCl + Na_2SO_4, KCl + K_2SO_4, $CaCl_2$ + $CaSO_4$, and $MgCl_2$+ $MgSO_4$. A concentration of each chloride and sulphate of 5% by weight was utilised.

Table 6.3. All the exposure solutions used in this study.

Solution	Name	Concentration (wt. %)
NaCl	NC	5%
KCl	KC	5%
$CaCl_2$	CC	5%
$MgCl_2$	MC	5%
Na_2SO_4	NS	5%
K_2SO_4	KS	5%
$CaSO_4$	CS	5%
$MgSO_4$	MS	5%
NaCl + Na_2SO_4	NCS	5% NaCl + 5 % Na_2SO_4

$KCl + K_2SO_4$	KCS	5% KCl + 5 % K_2SO_4
$CaCl_2 + CaSO_4$	CCS	5% $CaCl_2$ + 5 % $CaSO_4$
$MgCl_2 + MgSO_4$	MCS	5% $MgCl_2$ + 5 % $MgSO_4$

6.2.5 Analysis after exposure

After 1 year of exposure, the slices were extracted from the exposure solutions using tweezers. Subsequently, the surfaces of the slices were rinsed with a small amount of DI water and carefully cleaned using abrasive paper. Finally, the slices were dried in a vacuum desiccator at 40 ºC for a minimum of 3 days before undergoing further analyses using nanoindentation and SEM. Some part of slices was crushed into small fragments, and gently ground into dried powders until the particle sizes were less than 75 μm and stored under vacuum for later investigation using XRD, FTIR, and TGA analysis techniques.

X-ray diffraction instrument (XRD, Rigaku SmartLab, 9 kW, Cu Kα radiation source) was used to identify the minerals in the powder sample. The scans were carried out from 5° to 65° (2θ) with a step size of 0.02° and a speed of 2° per minute.

The Fourier transform infrared (FTIR) analysis was conducted utilising a Thermo Scientific IS10 spectrometer with the KBr pellet method, spanning the wavenumber range of 400-4000 cm^{-1}. Approximately 1 mg of sample powder was thoroughly mixed with 100 mg of IR-grade KBr and ground again to achieve homogeneity. The mixture was subsequently compressed into slender pellets for measurement. The measurements were taken with a resolution of 4 cm^{-1}, and each spectrum was obtained by averaging 32 scans.

Following to data collection, spectral deconvolution was executed utilising a Voigt function in Fityk (Wojdyr, 2010).

For TGA analysis, about 20 mg of each dry powder was put in an aluminium pan and analysed using a Rigaku Thermoplus EVO2. The samples were subjected to heating from 25 °C to 1000 °C at a rate of 10 °C/min, and the mass loss was recorded. Nitrogen as a protective gas at a flow rate of 50 ml/min was used during the measurement. The various hydration phases were subsequently determined according to the mass loss observed within particular temperature ranges.

For nanoindentation, a small part of the dried slices after one year of exposure in designated solutions was cut from the central portion. The samples were embedded in epoxy resin and allowed to harden at 30 °C. Subsequently, the resin-impregnated samples were prepared by grinding and polishing, using SiC sanding paper (600 and 1200 grit) and polishing cloths/agents (9, 3, and 0.05 μm), respectively. Ethanol was used as a lubricant where necessary. Each polishing step was lasted for 30 minutes to achieve the smooth surface. The surface roughness of the samples was assessed using scanning probe microscopy over a grid area of 50 μm × 50 μm. After assessing the surface roughness of the samples, nanoindentation tests were performed on a square grid area. A total of 100 points were selected, with a 10 μm gap between adjacent grid points. The measurement utilised a loading sequence of a 10-second ramp-up to a peak load of 1000 μN, sustaining that load for 5 seconds, followed by a 10-second unloading period.

Following the nanoindentation test, the resin-impregnated specimens were coated with carbon using an SPI Module^{TM} carbon coater. A scanning electron microscope, equipped with an energy-dispersive X-ray spectrometer, was used to capture the changes in the morphology of the samples subjected the chloride and sulphate attack. Backscattered

electron (BSE) imaging was conducted at an accelerating voltage of 15 kV and a working distance of approximately 15 mm. Elemental EDS point analyses were performed at a magnification of ×4000, with a minimum of 10 locations chosen on each specimen. In each location, 10 points were measured with a spacing of at least 20 μm, yielding a minimum of 100 EDS points per sample. The data were utilised to evaluate the leaching of calcium from the C-S-H gel in seawater-mixed cement paste exposed to chloride and sulphate solution.

6.3 Results and discussion

6.3.1 pH of solution

Figure 6.2 presents the pH values of pore solutions of seawater-mixed cement pastes after exposure to 5% chloride, 5% sulphate, and combined chloride-sulphate solutions for one year. The reference paste displays a pH of ~12.6, consistent with typical cement pore solutions buffered by portlandite and alkali hydroxides (Zhao et al., 2023). Under chloride attack, NC, and KC, exposures maintain alkaline conditions above pH 12. Exposure to CC results in a decrease in pH, while exposure to MC yields the lowest pH of ~ 11.2. In sulphate solutions, the exposure to NS and KS further increases the pH above 13, likely due to alkali enrichment in the pore solution, while CS and MS reduce the pH. The exposure to combined solutions shows similar trends, with NCS and KCS maintaining high alkalinity (~13.0-13.3), while CCS stabilizes at ~11.9. The most significant pH reduction is observed for exposure to MCS, where values drop close to ~10.8.

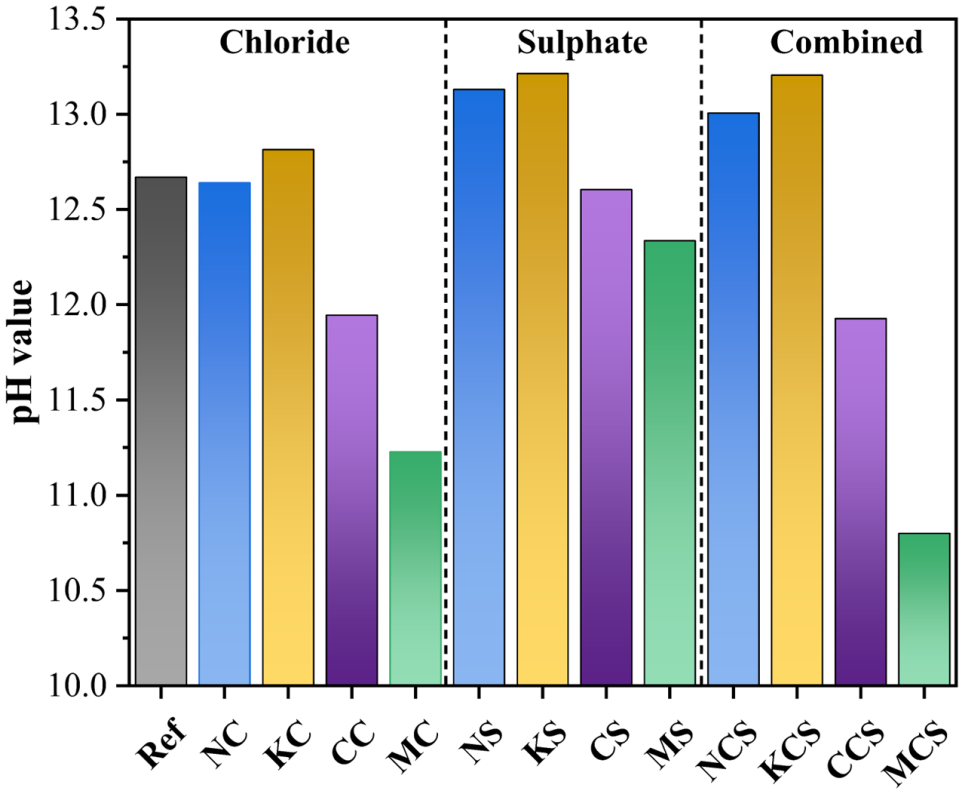

Figure 6.2. The change of pH under chloride, sulphate and combined attack.

(Note: NC, KC, CC, and CC represent NaCl, KCl, $CaCl_2$, and $MgCl_2$ respectively. NS, KS, CS, and MS represent Na_2SO_4, K_2SO_4, $CaSO_4$, and $MgSO_4$ respectively. NCS, KCS, CCS, and MCS represent NaCl+Na_2SO_4, KCl+K_2SO_4, $CaCl_2$+$CaSO_4$, and $MgCl_2$+MgSO4 respectively. All these notations are described in Table 6.3.)

6.3.2 Evolution of mineralogical composition

6.3.3 XRD analysis

Exposure to chlorides

Figure 6.3 shows the XRD spectra of seawater mixed cement paste subjected to chloride, sulphate and combined chloride-sulphate attacks. Figure 6.3a illustrates the XRD pattern of seawater mixed cement paste after exposure to different chloride salts (NC, KC, CC, and MC). The main phases identified include portlandite (CH), ettringite (AFt), Friedel's salt

(FS), and minor unreacted clinker phases. The evolution of these phases demonstrate that the type of cations associated with chloride ions is critical in determining the phase assemblage and stability of hydration products. After exposure to NC, KC, and CC, a noticeable increase in the intensity of CH peak is observed. This enhancement indicates that these salts do not destabilise CH; instead, they promote its persistence or even secondary formation through ionic exchange reactions. Exposure to MC leads to the total disappearance of the CH peak, aligning with the recognised decalcification effect of Mg^{2+} ions. Mg^{2+} aggressively interacts with CH and C-S-H, resulting in the formation of brucite ($Mg((OH)_2$) and magnesium silicate hydrates (M-S-H), which causes significant degradation of the matrix (Taylor, 1997, Bonen and Cohen, 1992, Santhanam et al., 2002). The AFt peak demonstrates different behaviours based on the cation associated with chloride. A minor decrease in AFt is noted upon exposure to NC, KC, and CC, likely due to limited ion exchange between sulphate and chloride-containing AFt phases. Conversely, exposure to MC results in an elevated AFt peak. The formation of Friedel's salt is observed in all samples exposed to chloride. The peak intensity of Friedel's salt is highest in the MC system, indicating that the destabilisation of hydration phases by Mg^{2+} enhances chloride binding by the available aluminates. This aligns with literature suggesting that Mg^{2+} attack increases chloride binding through the transformation of monosulphate to Friedel's salt (Hong and Glasser, 1999, Yang et al., 2019c).

Exposure to sulphate

Figure 6.3b displays the XRD patterns of seawater-mixed cement paste after exposure to different sulphate salts (NS, KS, CS, and MS). The results indicate significant changes in the hydration phase assemblage, illustrating that sulphate attack strongly affects the stability of cement hydrates and the formation of expansive phases. The mechanism of

sulfate attack in seawater-mixed cement paste is illustrated by equations (6.3)-(6.6) (De Weerdt et al., 2014b). As shown in Figure 6.2, equation (6.4) explains the rise in pH during NS exposure due to the formation of NaOH. In this process, Friedel's salt, CH, and C_3A present in the paste are progressively consumed, leading to the formation of gypsum and AFt. A significant increase in the AFt peak is observed for all sulphate salts, with the highest intensity in the MS-exposed system, followed by NS. The enhanced AFt formation can be attributed to the reaction of external sulphate ions with available monosulphate or unreacted aluminates in the paste (Taylor, 1997, Santhanam et al., 2002). A prominent gypsum peak is also observed after the attack of MS solution. The presence of gypsum and AFt is a well-established indicator of external sulphate attack, leading to volume instability and cracking (Skalny et al., 2003, Bonen and Cohen, 1992). The CH peak decreases significantly after sulphate attack, with complete disappearance in the MS-exposed sample. This is attributed to the aggressive decalcification effect of Mg^{2+} ions, which consume CH and react with C-S-H to form brucite and amorphous M-S-H, which can be expressed as equations (6.7), and (6.8) (Santhanam et al., 2002, Yang et al., 2019c, Bernard et al., 2017). The Friedel's salt peak disappears after sulphate attack in all systems. This observation indicates that sulphate ions displace chloride ions from the AFm phase due to higher sulphate affinity, converting Friedel's salt into monosulphate or AFt (Hong and Glasser, 1999, Yang et al., 2019c). This displacement reduces chloride-binding capacity under sulphate attack, which has important durability implications for seawater concretes exposed to mixed chloride-sulphate environments.

$$3CaO.Al_2O_3.CaCl_2.10H_2O\ (Fs) + Na_2SO_4 + 2H_2O \rightarrow$$
$$3CaO.Al_2O_3.CaSO_4.12H_2O\ (AFm) + 2NaCl$$

(6.3)

$$Ca(OH)_2 + Na_2SO_4 + 2H_2O \rightarrow CaSO_4.2H_2O + 2NaOH$$

(6.4)

$$2CaSO_4.2H_2O + 3CaO.Al_2O_3.CaSO_4.12H_2O + 16H_2O \rightarrow$$

$$3CaO.Al_2O_3.3CaSO_4.32H_2O(AFt)$$

(6.5)

$$3(CaSO_4.2H_2O) + 3CaO.Al_2O_3 + 26H_2O \rightarrow 3CaO.Al_2O_3.3CaSO_4.32H_2O$$

(6.6)

$$MgSO_4 + Ca(OH)_2 \rightarrow Mg(OH)_2 + CaSO_4.2H_2O$$

(6.7)

$$MgSO_4 + C-S-H + H_2O \rightarrow M-S-H + CaSO_4.2H_2O$$

(6.8)

Exposure to combined solution

Figure 6.3c shows the XRD patterns of seawater-mixed cement paste before and after combined chloride-sulphate attack (NCS, KCS, CCS, and MCS). The results demonstrate the strong synergistic influence of chloride and sulphate ions on the phase assemblage of cement hydrates. The intensity of AFt peak increases significantly under all combined attack conditions, with the highest AFt intensity observed in the MCS system. This indicates the significant destabilization of hydration phases by Mg^{2+}. The increase in AFt across all combined systems suggests that both chloride and sulphate ions promote transformations of AFm and aluminates into AFt, consistent with earlier findings on mixed chloride-sulphate exposures (Yang et al., 2019c, Chen and Ye, 2023). The Friedel's salt peak decreases for all cases, indicating progressive transformation of chloride-AFm phases into sulphate-bearing AFm or AFt. In particular, the Friedel's salt peak nearly disappears in

the MCS system, demonstrating that Mg^{2+}-induced decalcification and sulphate-driven ion exchange completely destabilize chloride-binding hydrates. This finding confirms that chloride binding is not durable under combined sulphate exposure and that aluminates preferentially incorporate sulphate to form additional ettringite. A clear gypsum peak is observed in the MCS case, indicating the significant consumption of Ca^{2+} from CH and C-S-H by Mg^{2+} and SO_4^{2-}, resulting in substantial gypsum precipitation. The behaviour of CH varies depending on the type of cation. The highest CH peak is observed for the KCS system, possibly due to reduced solubility of CH in the presence of K^+ ions. After NCS and CCS exposure, the CH peak is slightly enhanced, suggesting limited destabilization and possible secondary crystallization of CH in the presence of alkali and alkaline-earth salts. .

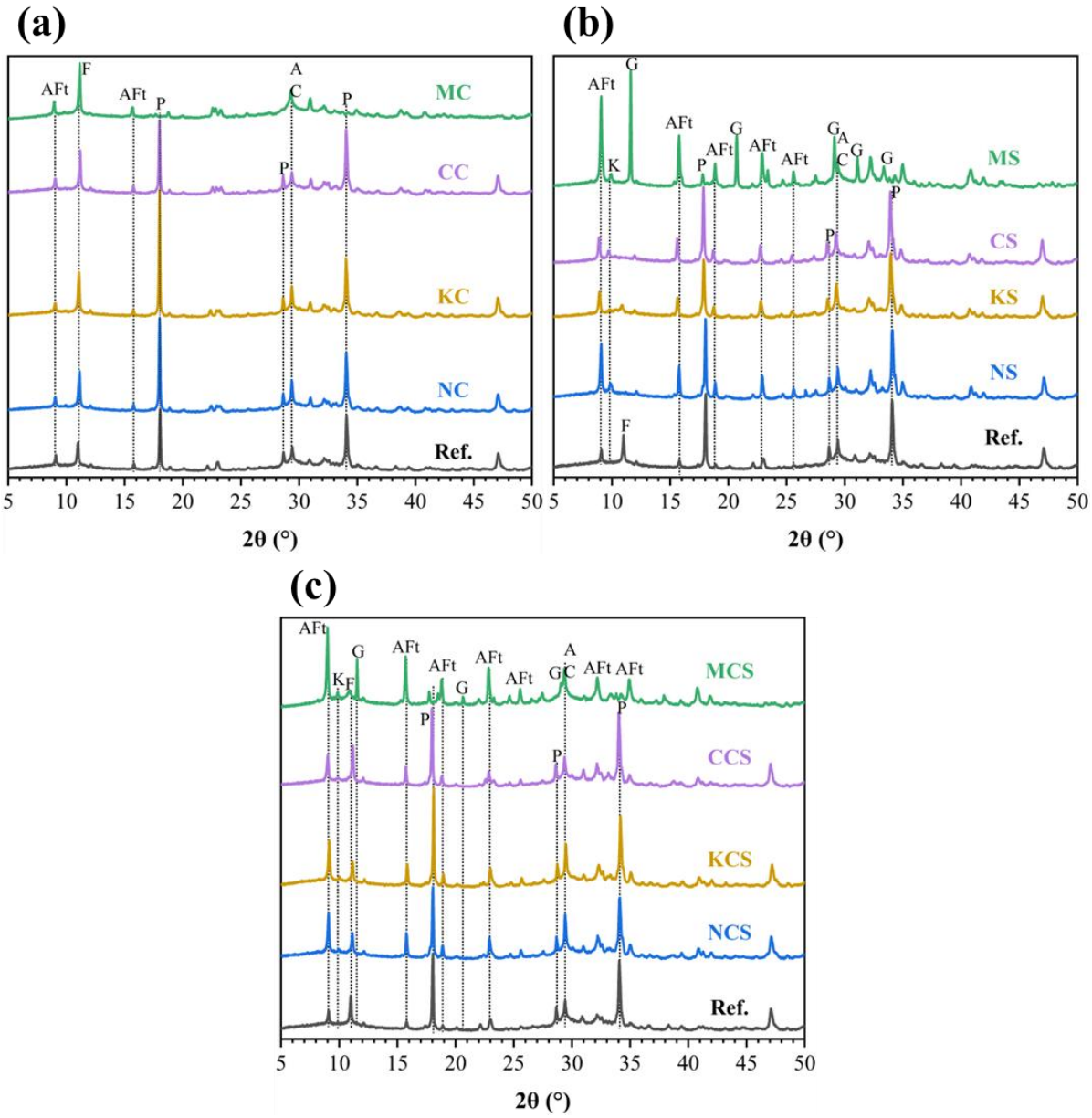

Figure 6.3. XRD patterns of seawater mixed cement paste subjected to (a) chloride attack (b) sulphate attack (a) combined chloride and sulphate attack.

(AFt: Ettringite, F: Friedel's salt, P: Portlandite (CH), A: Tricalcium silicate (C_3S), C: Calcite, K: Kuzelite, G: Gypsum).

6.3.4 Thermogravimetric/differential thermogravimetric analysis

Considering the changes in hydration phases identified by XRD after exposure to different solutions, thermogravimetric analysis (TGA) was used to quantitatively assess the stability and decomposition of hydration products in seawater cement paste. The derivative thermogravimetric (DTG) curves for chloride attack, sulphate attack, and combined chloride-sulphate attack are presented in Figure 6.4. The decomposition of hydration products occurs in different temperature ranges. A broad peak around 100 °C is associated with the dehydration of AFt and C-S-H gel, while a sharper peak near 130 °C corresponds to the decomposition of gypsum (Scrivener et al., 2016). A relatively weak peak appearing between 230-400 °C is associated with the decomposition of Friedel's salt. Finally, a pronounced peak between 400-500 °C is assigned to the decomposition of CH (Scrivener et al., 2016).

Exposure to chloride

The DTG curves for samples subjected to 5% chloride solutions (NC, KC, CC, and MC) exhibit significant changes as shown in Figure 6.4a. All chloride-exposed samples show a broad mass-loss peak centered around 100 °C, which is associated with the dehydration of C-S-H gel and AFt, indicating that these phases remain stable after chloride exposure. Compared with the reference specimens, samples exposed to MC exhibit highest mass loss in this temperature range, followed by NC, suggesting an increased amount of AFt or bound water retained within the hydrate structure. A small decomposition peak between 230-400 °C is observed for all the cases, which corresponds to decomposition of Friedel's salt, especially evident after NC and MC exposure. The CH decomposition peak (~450 °C) in samples exposed to MC and CC was lower than that of the corresponding reference, KC and NC-exposed specimens. These observations are consistent with the phase evolution identified by XRD analysis.

Exposure to sulphate

The DTG patterns considerably change for sulphate exposure (NS, KS, CS, and MS), compared to chloride attack as shown in Figure 6.4b. The low-temperature peak becomes sharper and more intense, reflecting an increase in AFt formation. A distinct additional peak at ~130 °C is present in MS-exposed samples, attributed to gypsum decomposition, confirming the strong tendency of Mg-based sulphates to form gypsum. The absence of the Friedel's salt peak (230-400 °C) in all sulphate exposures confirms the instability of chloride-binding AFm phases in the presence of sulphates, which typically convert Friedel's salt into AFt and gypsum. The CH decomposition peak at ~450 °C persists but is less pronounced, indicating the consumption of CH during sulphate reactions. Almost no CH is observed in the $MgSO_4$-exposed samples, as evidenced by the almost horizontal line at ~450 °C. All these observations are in good agreement with the corresponding XRD results.

Exposure to combined solution

In specimens subjected to combined chloride and sulphate attack, the DTG curves as shown in Figure 6.4c, exhibit overlapping characteristics of both mechanisms, reflecting the competitive phase transformations. The broad AFt/C-S-H peak at ~100 °C is intensified, indicating abundant AFt. A gypsum-related peak at ~130 °C is also evident, confirming coexistence of sulphate products. However, the Friedel's salt-related peak is weak or nearly absent, consistent with XRD findings where Friedel's salt disappeared due to its transformation into AFt and gypsum. The CH decomposition peak is retained in some cases but is nearly eliminated in the case of MCS exposure. The combined attack thus accelerates the destabilization of Friedel's salt and CH, while concurrently promoting the formation of AFt and gypsum.

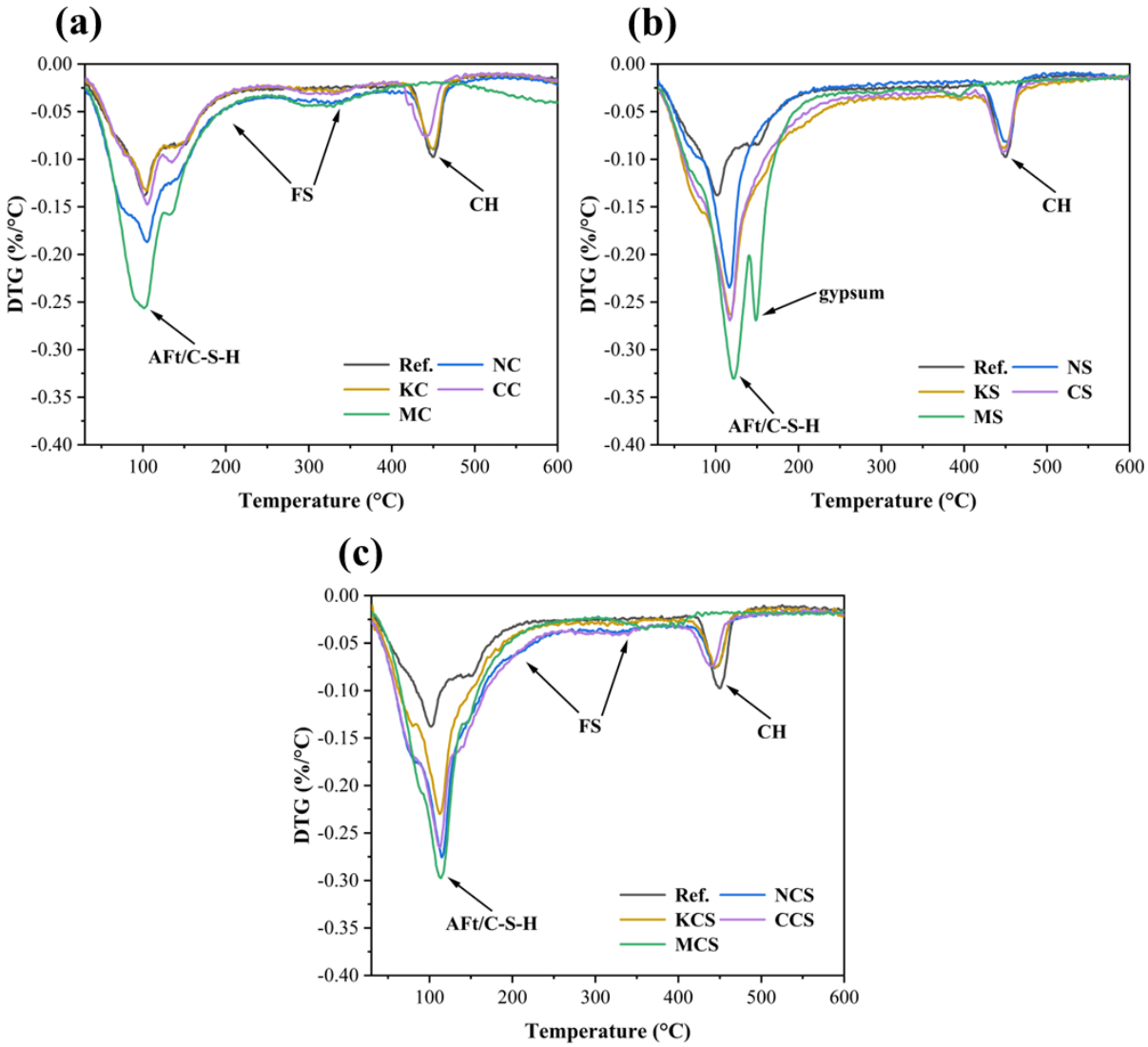

Figure 6.4. DTG curves of seawater mixed cement paste subjected to (a) chloride attack (b) sulphate attack (c) combined chloride and sulphate attack.

The quantity of CH and Friedel's salt was calculated by integrating the mass loss over the temperature range using the tangential method, as suggested in earlier research (Scrivener et al., 2016). Figure 6.5a shows the computed CH contents for seawater-mixed cement pastes exposed to chloride, sulphate, and combined chloride-sulphate solutions. Chloride exposure results in a decrease in CH content when compared to the reference paste; NC and KC retain significant amounts of CH, while the MC-exposed paste shows nearly total

CH depletion. This pattern is in line with the corresponding pH values displayed in Figure 6.2, which indicate a significantly reduced pH values when Mg^{2+} is present. Under sulphate exposure, NS and KS retain relatively higher CH contents, while the MS-exposed paste shows nearly zero CH. A similar behaviour is observed for the combined chloride-sulphate systems, where Na^{+}- and K^{+}- based solutions preserve higher CH contents, whereas the Mg^{2+}- based solutions exhibits negligible residual CH. The close correspondence between CH content and pore solution pH confirms that portlandite governs alkalinity buffering and highlights the particularly aggressive role of Mg^{2+} in destabilising CH in seawater-mixed cement paste.

Figure 6.5b shows the Friedel's salt contents, which were determined using mass loss in the 230-400 °C temperature range. The quantity of Friedel's salt is significantly increased under chloride exposure when compared to the reference paste; MC systems show the highest contents, indicating strong chemical chloride binding. On the other hand, all sulphate salts exhibit extremely low Friedel's salt contents when exposed to sulphate, which is indicative of the instability of chloride-binding AFm phases in sulphate-rich environments. Measurable amounts of Friedel's salt are retained for the combined chloride-sulphate systems, but the contents are significantly lower than those under chloride-only exposure. These findings show that even in environments containing chloride, the presence of sulphate inhibits the formation of Friedel's salt.

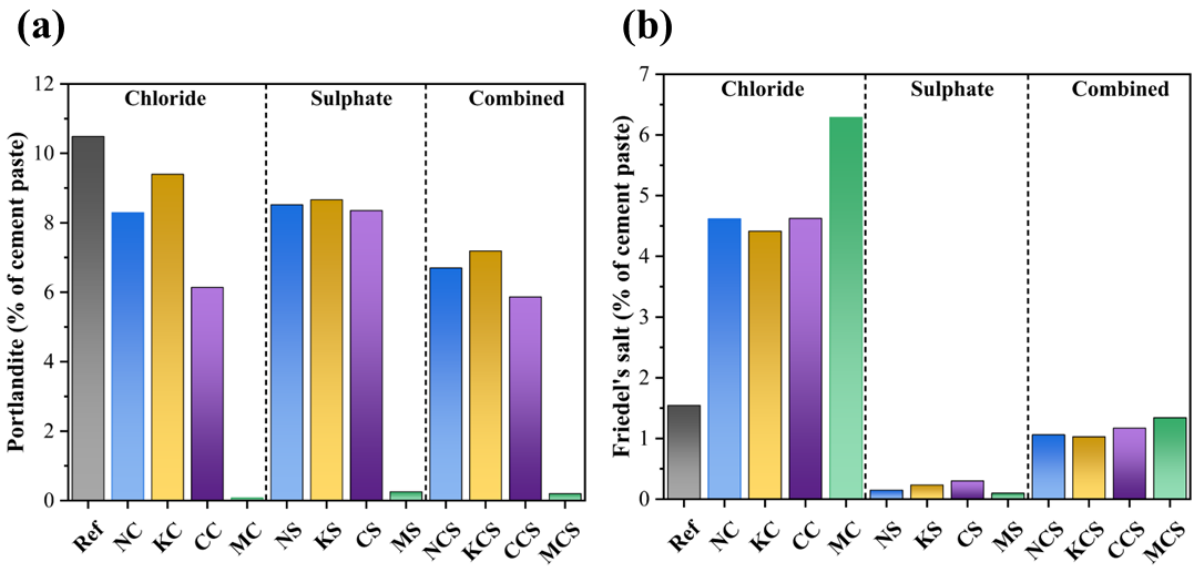

Figure 6.5. The CH and Friedel's salt content calculated from DTG curves of seawater mixed cement paste exposed to different solution (a) Portlandite (b) Friedel's salt.

6.3.5 FTIR analysis

Given the substantial changes in the structure of C-S-H resulting from exposure to different solutions, Fourier transform infrared (FTIR) analysis was conducted to assess the evolution of silicate bonding environments in seawater mixed cement paste. To study the changes in C-S-H structure and polymerisation, the spectra were mainly analysed in the 800-1200 cm^{-1} range. Figure 6.6 shows the FTIR spectra of seawater mixed cement paste subjected to chloride, sulphate and combined chloride-sulphate attack. The small peak appears at 3696 cm^{-1} corresponds to brucite (Nied et al., 2016). The intensity of band at 3643 cm^{-1} corresponds to the vibration of O-H in CH, while the bending vibration of molecular water is seen near 1646 cm^{-1} (Bakharev, 2005). The carbonate phases are indicated by the prominent v_3 CO_3^{2-} band at 1488 and 1425 cm^{-1}, together with the v_2 and v_4 doublets at 874 and 713 cm^{-1} (Dai et al., 2009, Choudhary et al., 2015). The most significant band of the silicate phase appears at around 980 cm^{-1}, indicating the asymmetric stretching of Si-O in

Q^2 silicate units in C-S-H (Li et al., 2024, Sekhar Das et al., 2025). The sulphate-bearing phases, comprising AFt and AFm, are characterised by a prominent band at 1122 cm^{-1} (Qu et al., 2022), whereas the low-wavenumber area features multiple overlapping peaks: 788 cm^{-1} (Si-O-Si bending), 672 and 620 cm^{-1} (sulphate vibrations in ettringite/gypsum), and 530-462 cm^{-1} (Si-O bending and lattice modes of sulphates and carbonates) (Zhao et al., 2023).

A clear CH O-H stretching band is observed at around 3643 cm^{-1} in the pastes that have been subjected to Na^+, K^+, and Ca^{2+}-based solutions. Additionally, a distinct Si-O stretching band is observed near 980 cm^{-1} for all the cases. There is also moderate band found in these systems at about 1122 cm^{-1} and at 672-620 cm^{-1}. These bands correspond to sulphate- or chloride-bearing AFm/AFt phases, while carbonate-related bands remain limited. However, samples exposed to Mg^{2+}-based solutions show significant suppression or complete disappearance of the CH band, accompanied by strong weakening and broadening of the Si-O stretching band, indicating extensive destabilisation of calcium-bearing hydrates. In these Mg^{2+}-based solutions, sulphate-related bands at ~1122 and 672-620 cm^{-1} dominate the spectra, and a small peak near 3696 cm^{-1} corresponding to brucite appeared. These FTIR results are consistent with XRD and TGA results, which indicate extensive formation of AFt and gypsum together with severe depletion of CH when the seawater mixed cement paste is subjected to Mg^{2+}-based solutions.

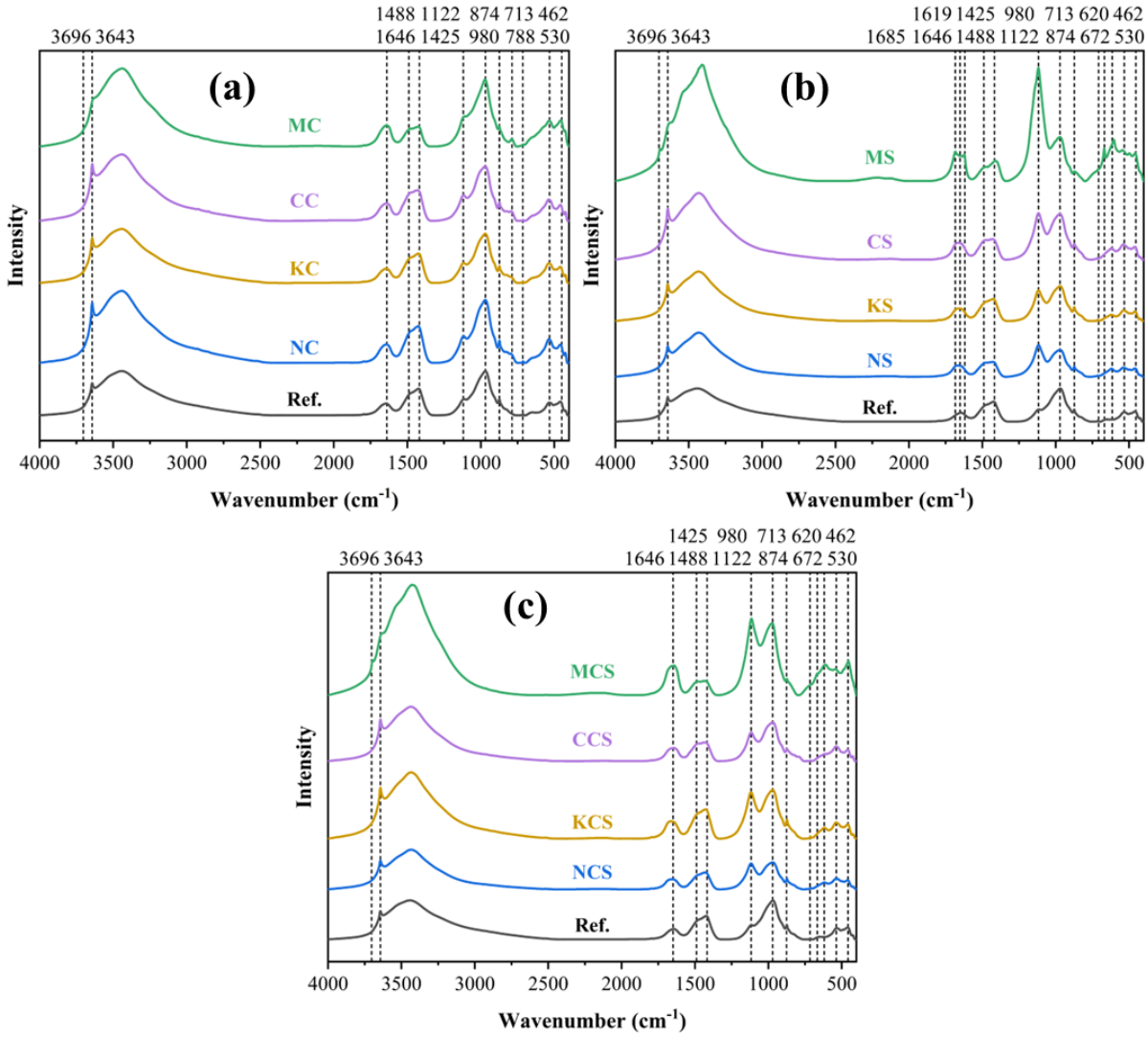

Figure 6.6. FTIR spectra of seawater mixed cement paste subjected to (a) chloride attack, (b) sulphate attack, (c) combined chloride and sulphate attack.

6.3.6 Structural evaluation of C-S-H

It is challenging to identify the change of C-S-H gel subjected to chloride, sulphate and combined chloride-sulphate attack by XRD because of its poor-crystallinity. In contrast, deconvoluted FTIR spectra in the 800-1200 cm^{-1} range provide direct insight into the structural evolution of C-S-H. The Si-O stretching bands of Q^2 (~985 cm^{-1}) and Q^1 (850-900 cm^{-1}) reveal modifications in chain structure, while the spectra also highlight shifts in polymerization (Zhao et al., 2023, Yan et al., 2023). Figure 6.7 shows the deconvolution of

seawater-mixed cement paste exposed to chloride, sulphate, and combined solutions, and the corresponding relative areas of the components are summarized in Table 6.3. The reference sample exhibits a low-wavenumber Q^2 component at ~ 958 cm^{-1} and a higher-wavenumber band at ~ 993 cm^{-1}, along with minor Q^1 contributions in the 850-900 cm^{-1} range. This suggests that the C-S-H gel comprises both Ca-rich, jennite-like structure characterised by shorter silicate chains and more polymerised, tobermorite-like structure featuring longer chains (Zhu et al., 2021, Yu et al., 1999). This duality is characteristic of prolonged cured pastes, wherein partial leaching and restructuring enable the coexistence of both structural patterns.

Exposure to chloride

In the chloride exposures, NC and KC keep the area of the Q^1 (~850-900 cm^{-1}) band small and retain a significant portion of the area of the lower-wavenumber Q^2 (~950-965 cm^{-1}) component, while slightly increasing the area of the higher-wavenumber Q^2 (~983-1000 cm^{-1}) component and the high-wavenumber shoulder (~1100-1200 cm^{-1}). This means the silicate chains remain largely intact (few new end-groups) with a shift toward longer, more polymerized chains and some alkali association at silicate sites (García Lodeiro et al., 2009). CC behaves similarly but with an even more stable lower-wavenumber Q^2 area, consistent with calcium buffering that stabilizes the chain network. In contrast, MC enhances the area of the Q^1 band and reduces the area of the lower-wavenumber Q^2 component, while simultaneously increasing the area of the higher-wavenumber Q^2 component. Table 3 therefore shows a higher share for end-groups along with a larger share for the polymerized and Si-rich bands, reflecting chain breakage alongside re-organization into more Si-rich segments (Sáez del Bosque et al., 2014).

Exposure to Sulfate

Under sulphate attack, NS and KS shift area away from the lower-wavenumber Q^2 band toward the higher-wavenumber Q^2 band, increasing the area of the high-wavenumber shoulder while maintaining a relatively small area for the Q^1 band. Table 3 indicates a greater proportion of polymerised chains and Si-rich environments, accompanied by a negligible increase in chain-end signatures, suggesting that silicon-rich C-S-H incorporates alkali ions into its structure (García Lodeiro et al., 2009, García-Lodeiro et al., 2008). CS shows a moderate transfer of area to the higher-wavenumber Q^2 band, a clearer high-wavenumber shoulder, and only a limited growth of the Q^1 band, again reflecting calcium-moderated changes. MS exhibits the most pronounced sulphate-only effect: the area of the Q^1 band significantly increases, the area of the lower-wavenumber Q^2 component decreases, and both the higher-wavenumber Q^2 band and the high-wavenumber shoulder acquire substantial contributions, indicative of simultaneous chain depolymerisation and re-polymerization into Si-rich chains. As shown in Figure 6.6 and table 6.3, the specimen exposed to MS solution exhibits the smallest C-S-H area, which is likely due to the conversion of C-S-H into M-S-H gel (Nied et al., 2016). The findings demonstrate a clear hierarchy in the severity of sulphate attack on C-S-H, with MS exerting the most detrimental impact, followed by KS and then NS.

Exposure to combined solution

In the combined chloride-sulphate exposures, NCS and KCS continue the sulphate-driven pattern. The results show elevated shares for the higher-wavenumber Q^2 band and for the high-wavenumber shoulder, while the Q^1 band remains modest, again indicating chain lengthening and Si enrichment with limited chain-end formation. The exposure to CCS results in intermediate values, with an increase in the share of the higher-wavenumber Q^2 band and high-waenumber shoulder. However, the Q^1 band remains limited, indicating

partial polymerisation while maintaining chain stability. The most severe response is observed in the exposure of MCS solution, where the Q^1 band and the lower-wavenumber Q^2 component is markedly reduced, and both the higher-wavenumber Q^2 band and the high-wavenumber shoulder account for substantial spectral contributions. This spectral configuration reflects extensive chain depolymerization accompanied by significant re-polymerization into Si-rich chains.

The results demonstrate that the type of cation significantly influences C-S-H morphology under aggressive environments. Na^+ and K^+ primarily enhance polymerization, driving the C-S-H toward more tobermorite-like structures with longer silicate chains. Ca^{2+} stabilizes the gel, preserving jennite-like domains and minimizing structural reorganization. Mg^{2+} exerts the strongest destabilizing effect, simultaneously promoting chain breakage and re-polymerization into Si-rich, tobermorite-like or even M-S-H gel. These findings confirm that the response of C-S-H under chloride, sulphate, and combined attack is not only controlled by the anions present but is strongly influenced by the associated cations.

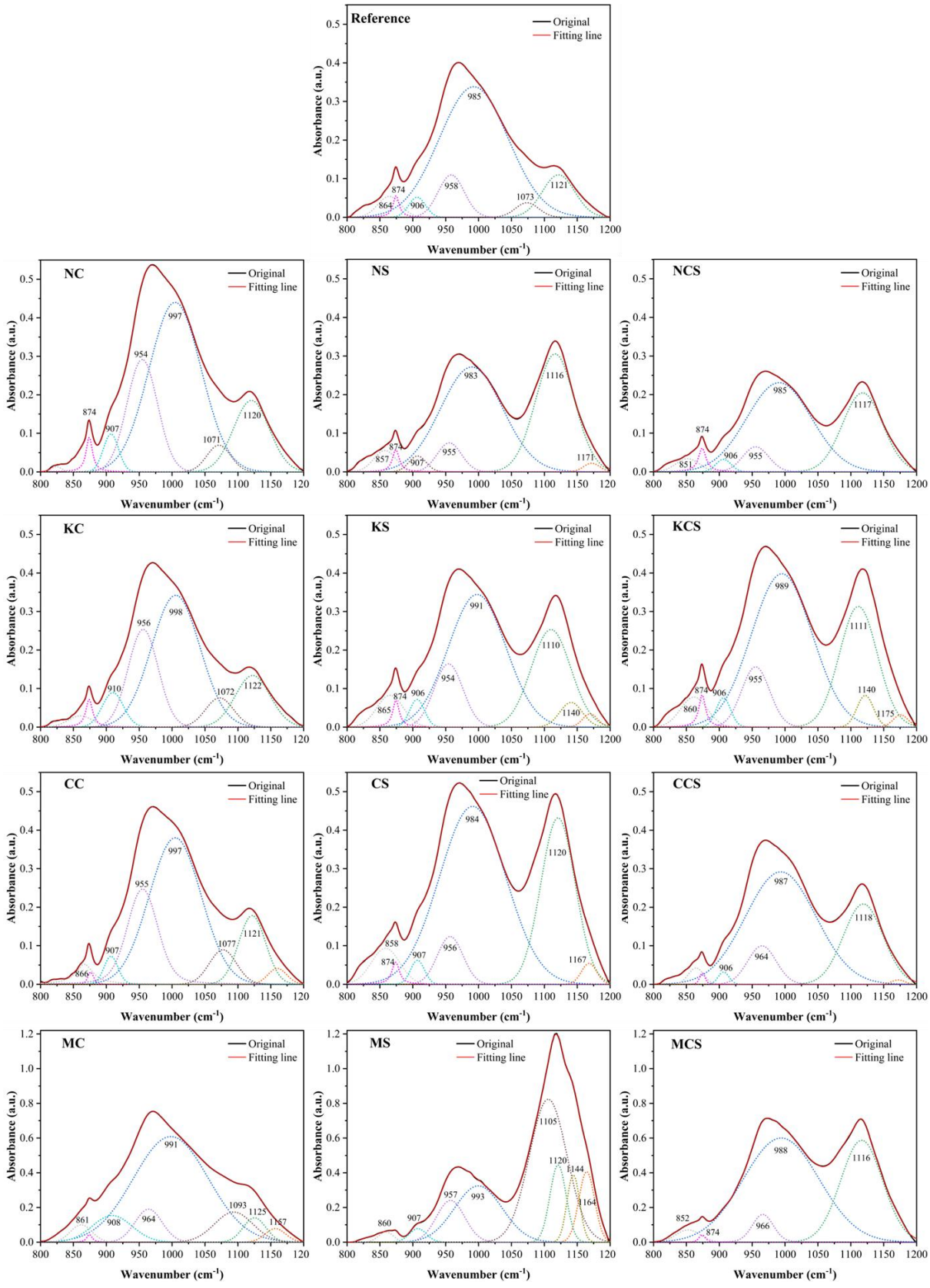
Reference
Original
Fitting line
Absorbance (a.u.)
Wavenumber (cm-1)
985
874
864
906
958
1073
1121
NC
997
954
874
907
1071
1120
NS
983
1116
857
874
907
955
1171
NCS
985
1117
874
851
906
955
KC
998
956
910
1072
1122
KS
991
1110
874
865
906
954
1140
KCS
989
1111
874
860
906
955
1140
1175
CC
997
955
907
866
1077
1121
CS
984
1120
858
874
907
956
1167
CCS
987
1118
906
964
MC
991
861
908
964
1093
1125
1157
MS
1105
1120
1144
1164
860
907
957
993
MCS
988
1116
852
874
966

Figure 6.7. Deconvoluted FTIR spectra of seawater mixed cement paste subjected to chloride, sulphate and combined chloride-sulphate attack with wavenumber from 800-1200 cm^{-1}.

Table 6.3. Relative areas of deconvoluted FTIR bands (800-1200 cm^{-1}) of seawater-mixed cement paste after chloride, sulphate, and combined exposures.

Wavenumber (cm^{-1})	**Q^1** (~850-900)	**Q^2** (~950-965)	**Q^2** (~983-1000)	**Shoulder** (~1100-1200)
Reference	7.8	8.5	68.7	13.3
NC	8.2	20.6	51.4	19
KC	10.1	21.6	47.2	19.4
CC	6.2	21.1	50.3	20.3
MC	13.1	7.4	63.3	16.2
NS	8.5	5.3	49.3	37
KS	10.4	11.2	46.5	30.7
CS	8.3	5.6	54.2	31.9
MS	3.9	9	20.5	66.4
NCS	7.9	6.2	54.1	31.6
KCS	8.9	9.8	49.4	31.8
CCS	4.3	9.9	58.7	25.5
MCS	2.7	4.5	58.7	33.1

6.3.7 EDS analysis

Considering the significant changes in C-S-H gel during exposure to the solutions containing different cations and anions, EDS point analysis was conducted to evaluate how these changes affect the Ca/Si ratio.

6.3.7.1 Calcium leaching

Figure 6.8 shows the Al/Ca ratio as a function Si/Ca atomic ratio calculated from EDS point analysis of seawater-mixed cement paste subjected to chloride, sulphate and combined chloride-sulphate attack. An increase in the Si/Ca ratio is associated with progressive Ca leaching from C-S-H, while a simultaneous rise in the Al/Ca ratio indicates

either incorporation of Al into secondary phases (ettringite, monosulphate) or substitution within decalcified C-S-H (Kobayashi et al., 2021, Wilson et al., 2022).

When seawater-mixed cement paste is exposed to chloride solutions, most systems (NC, KC, and CC) exhibit data clustered closely to the reference, suggesting that chloride primarily promotes the formation of Friedel's salt without causing extensive Ca leaching. An exception is the MC system, which displays a clear shift to higher Si/Ca and Al/Ca values. Thus, while chlorides associated with other cations have little influence over the hydration phases in seawater cement pastes, MC strongly destabilizes them through Ca leaching and CH consumption.

Sulphate attack, conversely, produces a more pronounced shift in both Si/Ca and Al/Ca ratios. Compared with the reference, NS, KS, and CS exposures show clear upward and rightward movement of the data, reflecting enhanced Ca leaching from C-S-H. MS, in particular, produces the most severe effect among the sulphates, with extensive scattering of points toward very high Si/Ca values.

The combined chloride-sulphate systems exhibit the greatest data dispersion, with points shifting significantly to higher Al/Ca and Si/Ca ratios compared to single-ion exposure. This indicates simultaneous Ca leaching and secondary phase formation. For example, the NCS and KCS cases show substantial enrichment in Al/Ca, reflecting the formation of AFt alongside destabilized Friedel's salt. The CCS case shows more moderate changes, since the external Ca buffers some of the leaching but still allows AFt formation. The most aggressive environment is MCS, where the data are scattered to the highest Si/Ca ratios

The influence of different cations shows that Na^+ and K^+ systems undergo little change under chloride attack, but exhibit marked Al/Ca enrichment under sulphate and combined

exposure. In Ca^{2+} systems, CC limits Ca leaching and keeps ratios close to the reference, whereas $CaSO_4$ and combined attack cause moderate shifts. Mg^{2+} systems are the most aggressive, with both chloride and sulphate leading to significant increases in Si/Ca and C-S-H decalcification, and combined attack producing the most severe deterioration.

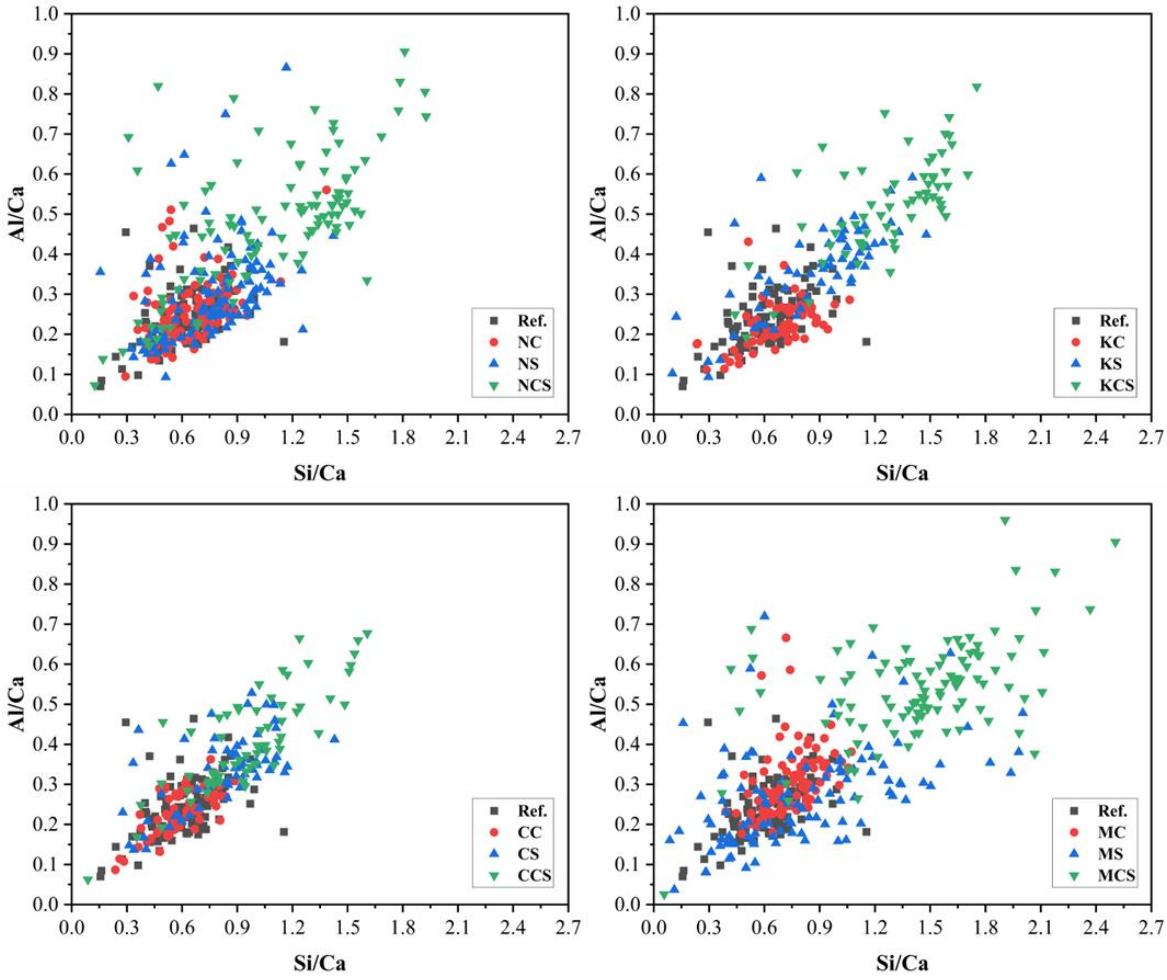

Figure 6.8. The Al/Ca ratio as a function Si/Ca atomic ratio calculated from EDS point analysis of seawater-mixed cement paste subjected to chloride, sulphate and combined attack (a) influence of Na^+ (b) influence of K^+, (c) influence of Ca^{2+}, (d) influence of Mg^{2+}.

The Ca/Si ratios of seawater-mixed cement subjected to chloride, sulphate, and combined attacks are presented in Figure 6.9. The values in the figures represent the mean value for each case. The reference sample shows an average Ca/Si of 1.67, which is typical for C-S-

H with moderate Ca enrichment. After chloride attack, only minor reductions in Ca/Si are observed for NC, KC, and CC exposures, indicating that chloride causes limited decalcification of C-S-H. The exception is MC exposure, where the Ca/Si ratio decreases to 1.44, confirming significant Ca leaching. Sulphate attack, conversely, results in a more significant decrease in Ca/Si ratios across all cation systems. Average values decrease to 1.35 for NS, 1.27 for KS, 1.30 for CS, and 1.22 for MS, reflecting progressive decalcification of C-S-H during sulphate exposure. The combined chloride-sulphate attack produces the lowest Ca/Si ratios, highlighting the synergistic aggressiveness of multi-ion exposure. The average ratios drop significantly to 1.08 for NCS, 0.918 for KCS, 1.12 for CCS, and reach a minimum of 0.768 in the MCS system. The results suggest that chloride alone has limited impact, sulphates drive stronger Ca depletion, and combined exposure, especially with Mg^{2+} results in the most severe decalcification of C-S-H. These observations are in excellent agreement with XRD, TGA, and FTIR results.

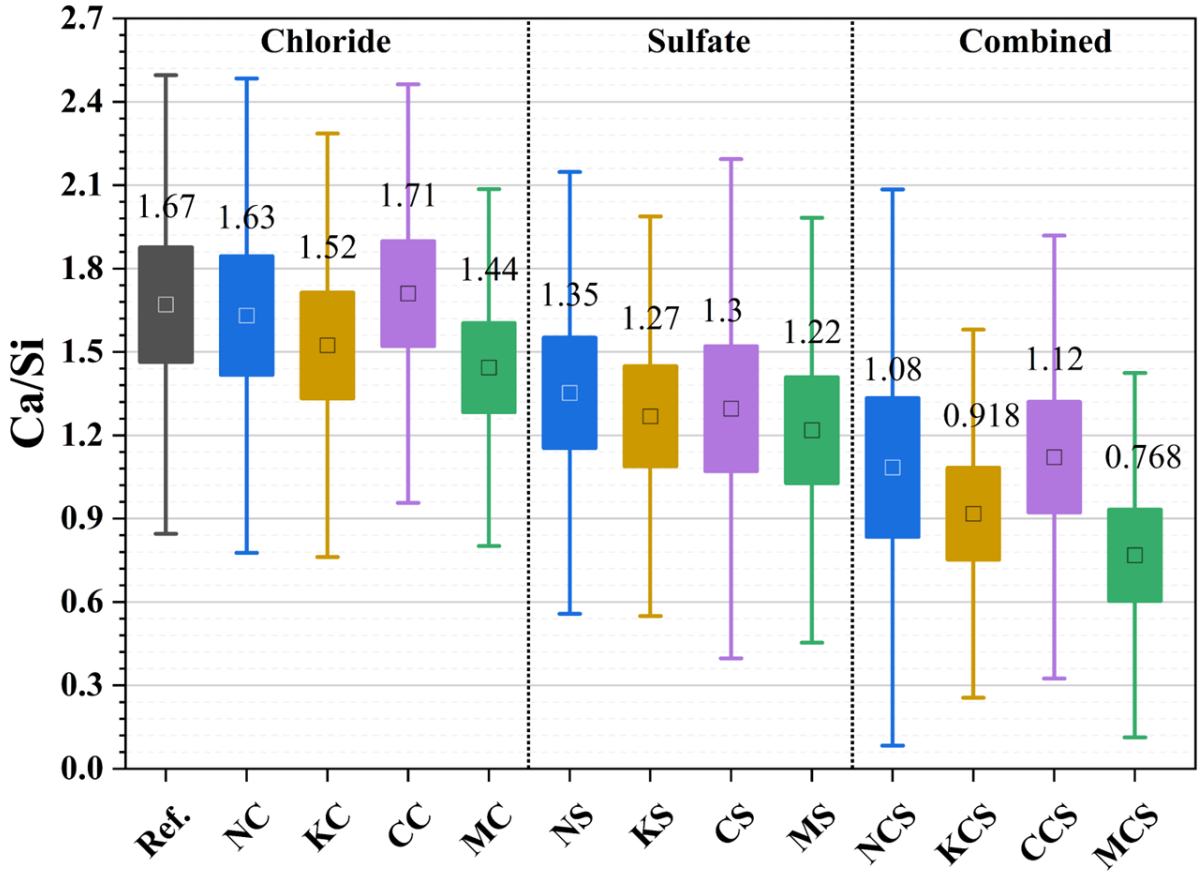

Figure 6.9. Ca/Si atomic ratio calculated from EDS point analysis of seawater-mixed cement paste subjected to chloride, sulphate and combined attack.

The Cl/Si ratios of seawater-mixed cement paste subjected to chloride, sulphate, and combined chloride-sulphate attacks are shown in Figure 6.10, where the values represent the mean for each case. The reference paste exhibits a Cl/Si ratio of ~0.004. After chloride attack, the Cl/Si ratio increases for all systems. The highest Cl/Si ratio is observed for MC, reaching ~0.017, indicating substantially greater chloride incorporation. In contrast, sulphate exposure results in consistently low Cl/Si ratios for all cation systems, indicating minimal chloride presence. For the combined chloride-sulphate systems, slightly higher Cl/Si ratios are observed as compared to sulphate only systems. The exposure of MCS shows a higher Cl/Si ratio of ~0.008. These results suggest that chloride incorporation is

most pronounced under MC exposure, remains low under sulphate-only conditions, and is partially reduced in combined chloride-sulphate environments, consistent with the phase and microstructural observations from XRD, TGA, and FTIR analyses.

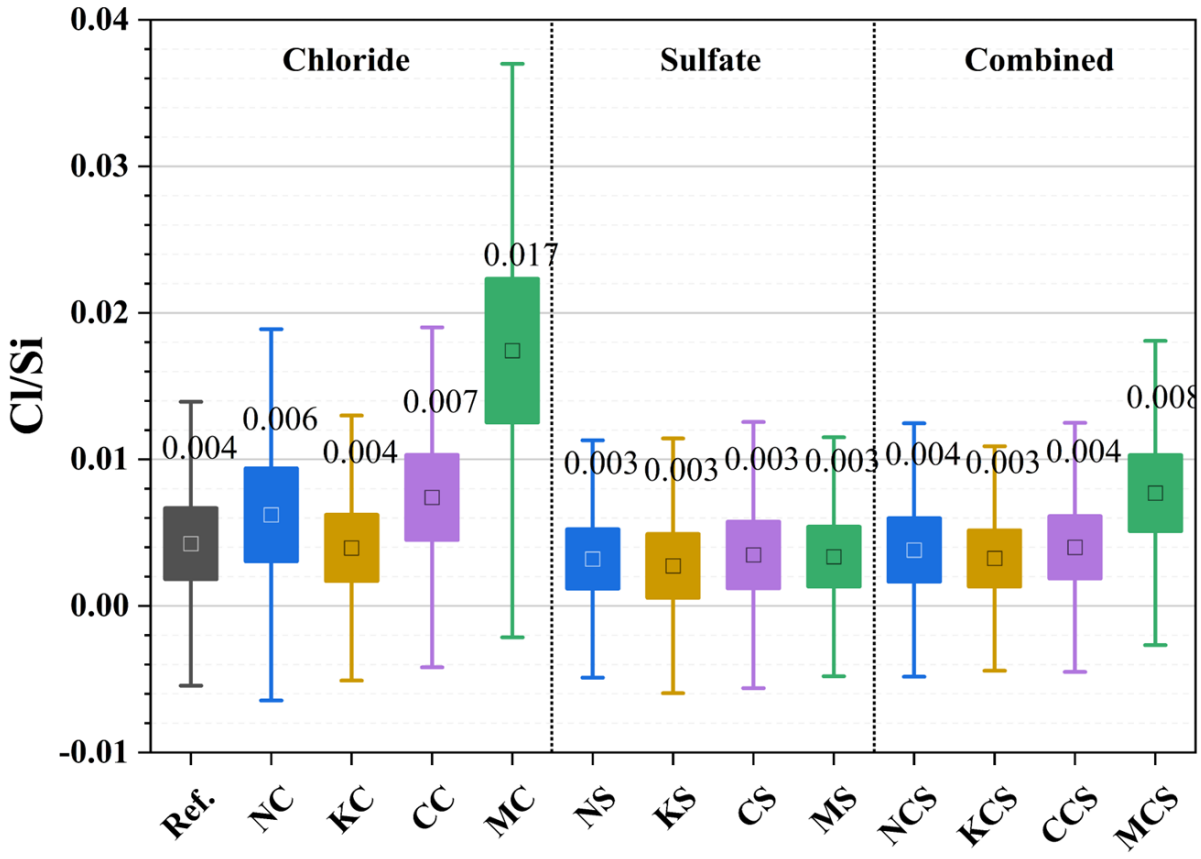

Figure 6.10. Cl/Si atomic ratio calculated from EDS point analysis of seawater-mixed cement paste after one year of exposure to chloride, sulphate, and combined chloride-sulphate solutions.

6.3.8 Micromechanical properties

In context of the microstructural and phase changes caused by exposure to different solutions, nanoindentation was utilised to assess the micromechanical properties of seawater mixed cement paste after different attacks. The results elucidate the local mechanical response of the seawater mixed cement paste after different attacks. Each

indentation curve provides the localised mechanical response of the cement paste at a specific grid point. By interpolating these discrete data points, a continuous map of nanomechanical properties can be generated over the entire indented area. These contour maps offer valuable insight into the spatial distribution of different hydration phases, within the resolution limits of the grid. Following the approach in reference (Constantinides and Ulm, 2007), equal size domains are defined around the mean values of each phase. Indentation moduli between 0-13 GPa represent macroporous regions dominated by high porosity. Values between 13-26 GPa correspond to low-density C-S-H (LD C-S-H), while 26-39 GPa indicate high-density C-S-H (HD C-S-H). Modulus values above 39 GPa are attributed to CH and un-hydrated clinker. Figure 6.11 shows the plan views of the contour plots of the indentation modulus of seawater mixed cement paste subjected to chloride, and sulphate attack.

In the reference paste, LD C-S-H forms the continuous matrix, rimmed by HD C-S-H around stiff inclusions, while scattered high-stiffness regions correspond to CH and unhydrated clinker. Limited macroporosity is also observed. This heterogeneous but balanced distribution is consistent with the EDS results (moderate Ca/Si, Al/Ca ratios), XRD identification of CH and minor secondary phases.

The overall phase morphology remains similar for seawater mixed cement paste after exposure to NC, KC, and CC, with LD C-S-H still dominating and CH-rich regions largely preserved. These maps align with EDS, which shows only minor Ca/Si reductions after chloride attack. In contrast, MC exposure leads to extensive softening: LD C-S-H and porosity expand while CH-rich domains vanish. This agrees with the higher Si/Ca ratios from EDS, and TGA curves showing no CH decomposition peak, confirming significant decalcification of C-S-H after MC attack. Sulphate attack results in a more significant

redistribution of phases, with LD C-S-H and porosity regions enlarging at the expense of HD C-S-H and CH. These changes correspond to the lower Ca/Si ratios of seawater mixed cement paste subjected to sulphate attack observed in EDS. Among sulphates, the exposure of MS causes the most severe degradation, with contour maps dominated by LD C-S-H and porosity, correlating with the pronounced Ca leaching, CH depletion, and secondary phase formation revealed by XRD and TGA results. The exposure to NS, KS, and CS also induce matrix softening, but retain slightly more HD C-S-H.

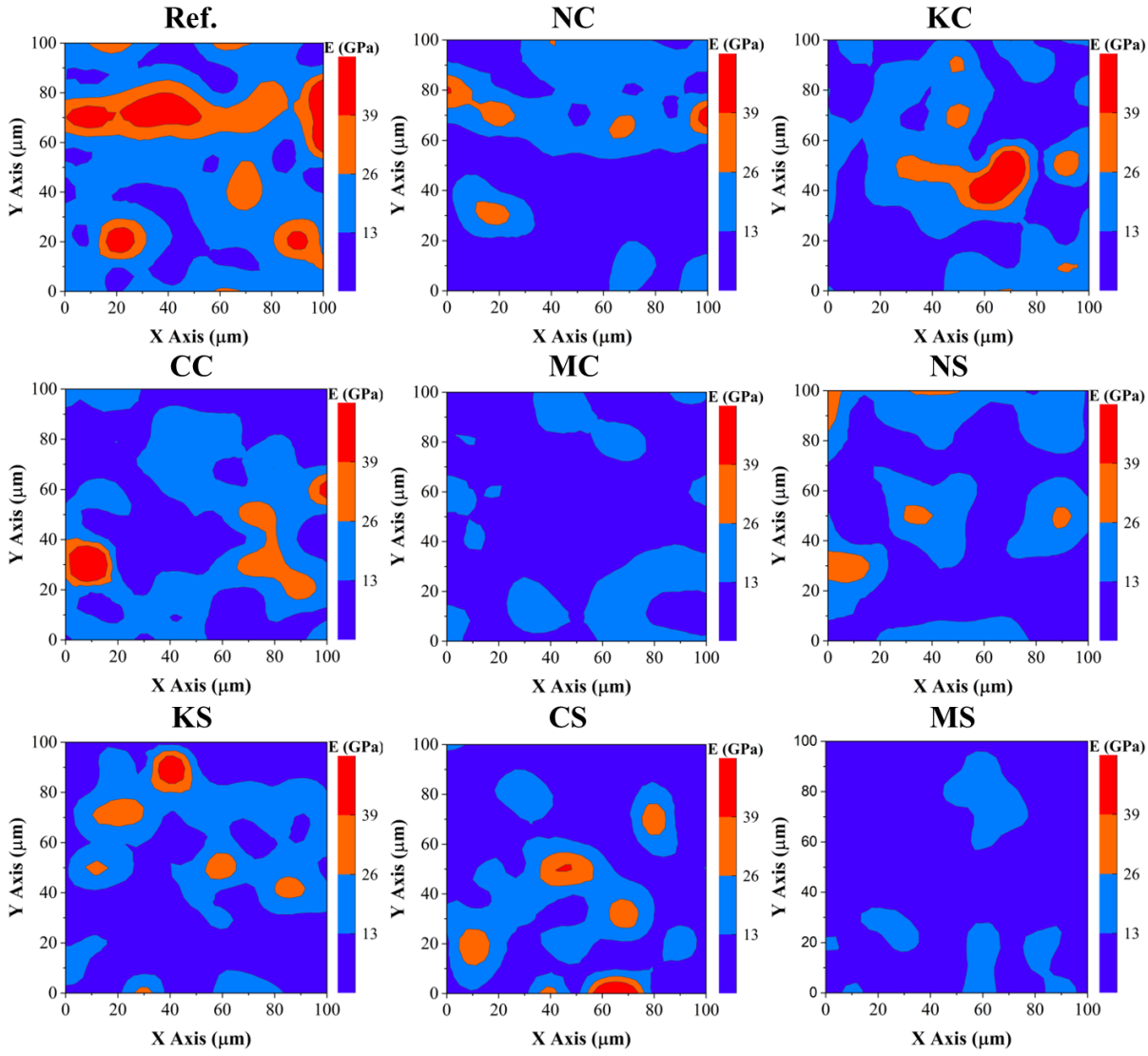

Figure 6.11. 2D contour maps of the indentation modulus values obtained from the nanoindentation data for the reference seawater mixed cement paste sample and after subjected the chloride and sulphate attack.

Figure 6.12 shows the surface condition of seawater mixed cement paste after one year exposure to chloride and sulfate solutions. Samples exposed to Na-based chloride and sulphate solutions exhibit relatively intact surfaces with limited visible damage. However, samples exposed to Mg-based solutions show clear surface cracking, indicating more severe degradation. The degree of cracking is significantly more pronounced in specimens exposed to the combined Mg-based chloride-sulphate solution, where wider and more continuous cracks are observed. These observations demonstrate that Mg-based solutions results in more pronounced surface deterioration of seawater-mixed cement paste compared with other solutions.

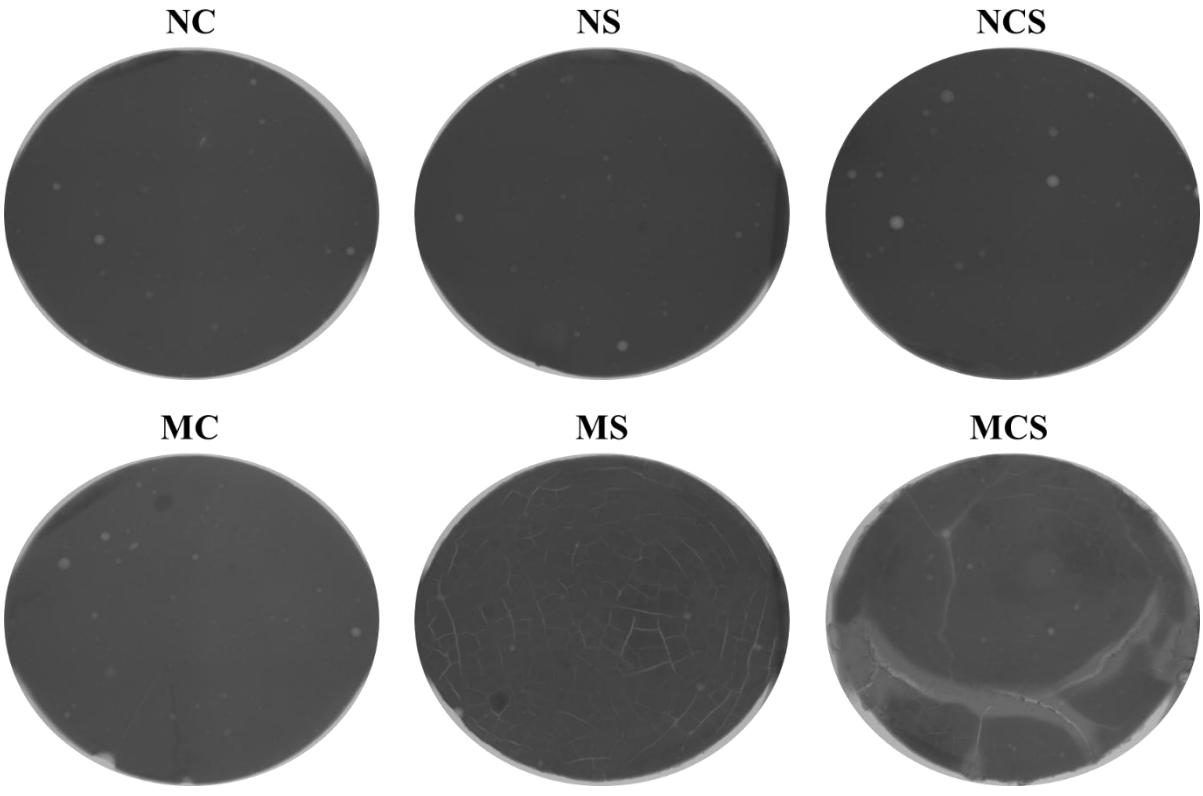

Figure 6.12. Surface degradation of seawater mixed cement pastes after one year exposure to chloride and sulfate solutions.

6.4 General discussion

The combined evidence from XRD, TGA, FTIR, EDS, and nanoindentation demonstrates that chloride and sulphate ions affect seawater-mixed cement paste in fundamentally different ways and and their combined action follows a distinct, synergistic degradation pathway.

6.4.1 Influence of anion type and synergistic effects

Chloride exposure (from NaCl, KCl, $CaCl_2$) primarily influences aluminate hydrates, leading to the formation of stable Friedel's salt with limited decalcification of C-S-H or consumption of portlandite (CH). This results in preserved micromechanical properties. In contrast, $MgCl_2$ attack is an exception, where the Mg^{2+} cation aggressively consumes CH to form brucite and initiates C-S-H decalcification. Sulphate attack is inherently more destructive to the calcium-bearing phases. It drives expansive ettringite and gypsum formation, consumes CH, and promotes significant decalcification of C-S-H, leading to increased porosity and reduced stiffness, as confirmed by nanoindentation. The simultaneous presence of chlorides and sulphates amplifies these effects, as Friedel’s salt is progressively transformed into sulphate-bearing products, CH is further depleted, and C-S-H chains undergo structural rearrangement toward more Si-rich configurations. This combined exposure results in increased decalcification, phase instability, and micromechanical softening compared to single-ion attack, confirming the synergistic impact of chloride-sulphate environments on seawater-based systems.

6.4.2 Influence of cation type and synergistic effects

The role of cations is equally critical in determining the extent of degradation. Monovalent cations (Na^+, K^+) consistently induced the least damage and facilitated moderate polymerization of C-S-H chains, shifting the gel toward tobermorite-like structures while causing relatively limited chain breakage or microstructural damage. Divalent Ca^{2+} salts act as a buffer by stabilizing jennite-like domains, maintaining chain integrity, and limiting both excessive decalcification and expansive product formation, resulting in only moderate reductions in stiffness. In contrast, Mg^{2+} Magnesium-bearing salts (MC, MS, MCS) were unequivocally the most destructive, regardless of the accompanying anion. Its action is multi-faceted. (1) direct reaction with CH to form brucite, drastically reducing pH and depleting alkalinity; (2) severe decalcification of C-S-H, promoting transformation into non-cementitious M-S-H gel; and (3) in sulphate-containing systems, supplying Ca^{2+} for excessive gypsum and ettringite formation. This led to complete CH loss, the highest C-S-H decalcification (lowest Ca/Si), and the most severe microstructural collapse, dominated by soft, porous phases. The combined attack with Mg^{2+} (MCS) represents the worst-case synergistic scenario. Here, Mg^{2+} induced decalcification and pH drop work in conjunction with sulphate-driven ion exchange and expansive product formation, creating an accelerated degradation cycle.

Taken together, the results indicate that the anion type determines the nature of secondary hydrates, while the cation influences the stability of portlandite and the nano structural integrity of C-S-H, with Mg^{2+} having the most detrimental effect on seawater-mixed cement paste.

6.5 Summary

This study systematically investigated the long-term impacts of chloride, sulphate, and combined chloride-sulphate attack on seawater-mixed cement paste. The sweater-mixed cement pastes were exposed to Na^+, K^+, Ca^{2+}, and Mg^{2+} salts for one year, and the phase assemblage, chemical stability, and micromechanical properties were examined through XRD, TGA, FTIR, EDS, and nanoindentation. The work provides insights into the impact of both anions and cations on the degradation of seawater-based cementitious systems. Based on the results and discussion, the following conclusions can be drawn:

- Chloride attack by NaCl, KCl, and $CaCl_2$ had a limited effect on phase assemblage, mainly stabilizing the system through the formation of Friedel's salt while preserving CH and C-S-H. In contrast, $MgCl_2$ markedly destabilized hydrates, causing CH depletion, brucite formation, and substantial decalcification of C-S-H.
- Sulphate attack produced extensive secondary phases, with Na_2SO_4 and K_2SO_4 leading to AFt formation, $CaSO_4$ causing moderate CH consumption, and $MgSO_4$ being the most destructive, characterized by severe CH depletion, AFt and gypsum formation, and transformation of C-S-H into M-S-H.
- Combined chloride and sulphate exposures accelerated deterioration compared to single-ion systems. Friedel's salt was transformed to AFt and gypsum, CH was depleted, and C-S-H gel underwent significant rearrangement, resulting in greater decalcification and structural softening.
- FTIR deconvolution in the range of the 800-1200 cm^{-1} indicated that Na^+ and K^+ facilitate silicate chain polymerization and a transition toward tobermorite-like structures, Ca^{2+} stabilizes jennite-like structures, and Mg^{2+} causes chain scission and re-polymerization into Si-rich, poorly ordered phases.

- EDS analysis corroborated these trends, showing relatively stable Ca/Si ratios under Na^+, K^+, and Ca^{2+} salts, but significant increases in Si/Ca and Al/Ca ratios were observed in Mg^{2+} systems, indicating extensive decalcification and aluminate incorporation into secondary products.
- Nanoindentation results linked chemical degradation to micromechanical performance: chloride systems with Na^+, K^+, and Ca^{2+} retained HD C-S-H and CH domains, while sulphate and especially Mg-bearing systems shifted the microstructure toward LD C-S-H and porosity, resulting in pronounced softening.

Chapter 7. Conclusion and Recommendations

7.1 Conclusions

Concrete is the most widely used man-made construction material, serving as the backbone for infrastructure such as buildings, bridges, pavements, pipelines, and dams. However, its substantial demand places increasing pressure on freshwater resources, a challenge that is particularly critical in regions where freshwater is already scarce, such as the Middle East, North Africa, and remote islands. In such coastal and island environments, the limited availability of freshwater makes the use of seawater as a mixing water for concrete construction a practical and often necessary alternative. The use of seawater as mixing water introduces a high concentration of aggressive ions into the concrete, which can significantly influence the mechanical properties and durability of seawater concrete.

This thesis presents a comprehensive investigation of seawater-mixed cementitious materials across multiple scales, combining MD simulations with experimental studies to provide new insights into their fundamental behaviour and long-term durability. The dissertation comprises the effect of temperature and pore size on the transport of NaCl solution in C-S-H nanopore (Chapter 4), desorption of NaCl solution confined in C-S-H nanopore (Chapter 5), degradation of C-S-H in seawater, and the durability of seawater-mixed pastes subjected chloride and sulfate attack. The important findings from the studies are given below:

- The penetration rate of NaCl solution increased with the increase of pore size and temperature, and it was faster in the middle region of the pore as compared to near the C-S-H surface due to hydrophilicity of C-S-H. A filtration effect on the ions in the NaCl solution was observed in the smaller pore size, as the pore size

increased, the filtration effect disappeared gradually, and this filtration effect became more obvious with the increase of temperature. A double layer of ions (one layer of Na^+ on the inner side and one layer of Cl^- on the outer side) were adsorbed on the C-S-H surface after penetration.

- Through MD simulations, it was observed that, under NVT conditions, where the pore size remains fixed, evaporation occurs preferentially from the central region of the nanopore. Under NPT conditions, the nanopore undergoes significant shrinkage, dynamically adapting its size as water evaporates. As the system loses water, Na^+ and Cl^- ions migrate towards the pore surface, forming a double ionic layer that alters the local ionic distribution under both NVT and NPT ensembles. Additionally, the study found that variations in the Ca/Si ratio (1.2-2.0) have a negligible impact on the overall evaporation behaviour. This indicates that water desorption mechanisms within C-S-H nanopores are largely independent of the Ca/Si ratio within this range.
- Under constant shear and tensile strain at perfect interface, the pure C-S-H system has the highest shear strength and tensile strength. The partial substitution with seawater cations results in a reduction of shear strength as well as the tensile strength, following the order: CSH $\approx$ CSH_Mg > CSH_Na > CSH_K. As the interfacial distance increases, all systems show a sharp decline in shear strength and tensile strength, with a complete loss of cohesion beyond an expansion of 0.32 nm, attributed to the transition of water in the interlayer from a bilayer to a trilayer configuration. The distribution of local shear strain demonstrates that stress relaxation is limited to the interlayer space, while the C-S-H layers remain rigid, confirming a stick-slip relaxation mechanism. Finally, micromechanical modelling

demonstrates that porosity progressively governs the macroscopic mechanical response of C-S-H gels, reducing the influence of atomic-scale differences between systems as porosity increases.

- At macroscale, chloride attack by NaCl, KCl, and $CaCl_2$ had a limited effect on phase assemblage, mainly stabilizing the system through the formation of Friedel's salt while preserving CH and C-S-H. In contrast, $MgCl_2$ markedly destabilized hydrates, causing CH depletion, brucite formation, and substantial decalcification of C-S-H. Sulphate attack produced extensive secondary phases, with Na_2SO_4 and K_2SO_4 leading to AFt formation, $CaSO_4$ causing moderate CH consumption, and $MgSO_4$ being the most destructive, characterized by severe CH depletion, AFt and gypsum formation, and transformation of C-S-H into M-S-H. Combined chloride and sulphate exposures accelerated deterioration compared to single-ion systems. Ca leaching in seawater mixed cement paste was observed exposed to sulphate solution and solution containing Mg^{2+} ions. Nanoindentation results linked chemical degradation to micromechanical performance: chloride systems with Na^+, K^+, and Ca^{2+} retained HD C-S-H and CH domains, while sulphate and especially Mg-bearing systems shifted the microstructure toward LD C-S-H and porosity, resulting in pronounced softening.

7.2 Recommendations

This thesis has made a substantial contribution to understanding the behaviour of seawater cementitious systems at the nanoscale using MD modelling, however there are still certain issues that require further exploration in order to fully comprehend the behaviour of seawater cementitious systems.

- There is a need to upscale the current atomistic models of C-S-H, which are typically based on layered crystalline structures such as tobermorite or jennite, to more realistic colloidal particle assemblies that reflect the morphology of C-S-H at larger scales. Developing mesoscale modelling frameworks that incorporate such colloidal structures would help bridge the gap between nanoscale simulations and microscale experimental observations, providing a more complete representation of ion transport and mechanical response in cementitious material.
- Future study should expand the nanoscale investigations beyond C-S-H to investigate the stability and degradation mechanisms of other hydration products that are especially important in marine environments. These include M-S-H, which forms when magnesium is attacked, as well as ettringite and other AFt/AFm phases that influence sulphate resistance. Atomistic simulations of these hydrates would provide useful insights into their structural evolution, ion exchange mechanisms, and long-term stability under severe exposures.
- There is a strong need for the development of ReaxFF parameters tailored for seawater cementitious systems. Current force fields cannot adequately capture bond-breaking and bond-forming processes such decalcification, C-S-H to M-S-H transformation, and portlandite dissolution. A reliable ReaxFF parameter set for Ca-Si-O-H systems containing Na^{+}, K^{+}, Mg^{2+}, Cl^{-}, and SO_4^{-2} would simulate reactive pathways and give a valuable tool for predicting the chemical durability of seawater concretes at the molecular level.
- At the macroscale, more experimental work is needed to investigate the durability of seawater-mixed concrete under service-like conditions. Studies should focus on partial immersion and cyclic wet-dry exposures, which simulate

tidal and splash zones in marine environments. Such studies would provide critical insights into ion transport dynamics, phase transformations, cracking initiation, and microstructural degradation under realistic boundary conditions, thus complementing laboratory immersion tests and improving the predictive accuracy of durability models.

References

A, H., YANG, Z., HU, R. & CHEN, Y. F. 2022. Roles of energy dissipation and asymmetric wettability in spontaneous imbibition dynamics in a nanochannel. *J Colloid Interface Sci,* 607**,** 1023-1035.

ABDEL-MAGID, T. I., OSMAN, O. M., IBRAHIM, O. H., MOHAMMED, R. T., HASSAN, S. O. & BAKKAB, A. A. H. 2016. Influence of Seawater in Strengths of Concrete Mix Design when Used in Mixing and Curing. *Key Engineering Materials,* 711**,** 382-389.

ABDOLHOSSEINI QOMI, M., KRAKOWIAK, K., BAUCHY, M., STEWART, K., SHAHSAVARI, R., JAGANNATHAN, D., BROMMER, D. B., BARONNET, A., BUEHLER, M. J. & YIP, S. 2014a. Combinatorial molecular optimization of cement hydrates. *Nature communications,* 5**,** 1-10.

ABDOLHOSSEINI QOMI, M. J., BROCHARD, L., HONORIO, T., MARUYAMA, I. & VANDAMME, M. 2021. Advances in atomistic modeling and understanding of drying shrinkage in cementitious materials. *Cement and Concrete Research,* 148.

ABDOLHOSSEINI QOMI, M. J., KRAKOWIAK, K. J., BAUCHY, M., STEWART, K. L., SHAHSAVARI, R., JAGANNATHAN, D., BROMMER, D. B., BARONNET, A., BUEHLER, M. J., YIP, S., ULM, F. J., VAN VLIET, K. J. & PELLENQ, R. J. 2014b. Combinatorial molecular optimization of cement hydrates. *Nat Commun,* 5**,** 4960.

ADIWIJAYA, HAMADA, H., SAGAWA, Y. & YAMAMOTO, D. 2017. Influence of seawater mixing and curing on strength characteristics and porosity of ground granulated blast-furnace slag concrete. *IOP Conference Series: Materials Science and Engineering,* 271**,** 012070.

ADIWIJAYA, A. & HAMADA, H. 2017. Evaluation of seawater-mixed concrete from th e viewpoint of strength and durability. *Proceedings of International Symposiu m on Concrete Technology, Makassar, Indonesia*.

ADIWIJAYA, A., HAMADA, H., SAGAWA, Y. & YAMAMOTO, D. Expansion characteristics o f seawater mixed concrete due to alkali-silica reaction. 40th Conference on Ou r World in Concrete & Structures, Singapore, 2015.

AIT HAMADOUCHE, S., HONORIO, T., BORE, T., BENBOUDJEMA, F., DAOUT, F. & VOURC'H, E. 2023. Dielectric permittivity of C-S-H. *Cement and Concrete Research,* 169.

ALIZADEH, R., BEAUDOIN, J. J. & RAKI, L. 2010. Viscoelastic nature of calcium silicate hydrate. *Cement and Concrete Composites,* 32**,** 369-376.

ALLEN, A. J., THOMAS, J. J. & JENNINGS, H. M. 2007. Composition and density of nanoscale calcium-silicate-hydrate in cement. *Nat Mater,* 6**,** 311-6.

ARAR, M. 2016. *Elastic properties of cement phases using molecular dynamic simulation.* Toronto Metropolitan University Toronto, ON, Canada.

ASHRAF, W., OLEK, J. & TIAN, N. 2016. Multiscale characterization of carbonated wollastonite paste and application of homogenization schemes to predict its effective elastic modulus. *Cement and Concrete Composites,* 72**,** 284-298.

BACH, T. T. H., CHABAS, E., POCHARD, I., CAU DIT COUMES, C., HAAS, J., FRIZON, F. & NONAT, A. 2013. Retention of alkali ions by hydrated low-pH cements: Mechanism and Na+/K+ selectivity. *Cement and Concrete Research,* 51**,** 14-21.

BAGHERI, A., NAZARI, A., SANJAYAN, J. G. & DUAN, W. 2018. Molecular simulation of water and chloride ion diffusion in nanopores of alkali-activated aluminosilicate structures. *Ceramics International,* 44**,** 20723-20731.
BAI, Y., WANG, Y. & XI, Y. 2020. Modeling the effect of temperature gradient on moisture and ionic transport in concrete. *Cement and Concrete Composites,* 106.
BAKHAREV, T. 2005. Durability of geopolymer materials in sodium and magnesium sulfate solutions. *Cement and Concrete Research,* 35**,** 1233-1246.
BARBHUIYA, S. & DAS, B. B. 2023. Molecular dynamics simulation in concrete research: A systematic review of techniques, models and future directions. *Journal of Building Engineering,* 76.
BASMADJIAN, D. 2003. *Mass transfer: principles and applications*, CRC press.
BAŽANT, Z. P., HAUGGAARD, A. B., BAWEJA, S. & ULM, F.-J. 1997. Microprestress-Solidification Theory for Concrete Creep. I: Aging and Drying Effects. *Journal of Engineering Mechanics,* 123**,** 1188-1194.
BERA, A., S, K., OJHA, K., KUMAR, T. & MANDAL, A. 2012. Mechanistic Study of Wettability Alteration of Quartz Surface Induced by Nonionic Surfactants and Interaction between Crude Oil and Quartz in the Presence of Sodium Chloride Salt. *Energy & Fuels,* 26**,** 3634-3643.
BERENDSEN, H. J., GRIGERA, J.-R. & STRAATSMA, T. P. 1987. The missing term in effective pair potentials. *Journal of Physical Chemistry,* 91**,** 6269-6271.
BERG, J. 1993. *Wettability (1st ed.)*, CRC Press.
BERNAL, J., JEFFERY, J. & TAYLOR, H. 1952. Crystallographic research on the hydration of Portland cement. A first report on investigations in progress. *Magazine of Concrete research,* 4**,** 49-54.
BERNARD, E., LOTHENBACH, B., LE GOFF, F., POCHARD, I. & DAUZÈRES, A. 2017. Effect of magnesium on calcium silicate hydrate (C-S-H). *Cement and Concrete Research,* 97**,** 61-72.
BHUSHAN, B., ISRAELACHVILI, J. N. & LANDMAN, U. 1995. Nanotribology: friction, wear and lubrication at the atomic scale. *Nature,* 374**,** 607-616.
BIRNIN-YAURI, U. & GLASSER, F. 1998. Friedel's salt, Ca2Al (OH) 6 (Cl, OH)· 2H2O: its solid solutions and their role in chloride binding. *Cement and Concrete Research,* 28**,** 1713-1723.
BISSCHOP, J. & WITTEL, F. K. 2011. Contraction gradient induced microcracking in hardened cement paste. *Cement and Concrete Composites,* 33**,** 466-473.
BONACCORSI, E., MERLINO, S. & TAYLOR, H. F. W. 2004. The crystal structure of jennite, Ca9Si6O18(OH)6·8H2O. *Cement and Concrete Research,* 34**,** 1481-1488.
BONEN, D. & COHEN, M. D. 1992. Magnesium sulfate attack on portland cement paste-I. Microstructural analysis. *Cement and concrete research,* 22**,** 169-180.
BONNAUD, P. A., JI, Q., COASNE, B., PELLENQ, R. J. & VAN VLIET, K. J. 2012a. Thermodynamics of water confined in porous calcium-silicate-hydrates. *Langmuir,* 28**,** 11422-32.
BONNAUD, P. A., JI, Q., COASNE, B., PELLENQ, R. J. M. & VAN VLIET, K. J. 2012b. Thermodynamics of Water Confined in Porous Calcium-Silicate-Hydrates. *Langmuir,* 28**,** 11422-11432.
BONNAUD, P. A., JI, Q. & VAN VLIET, K. J. 2013. Effects of elevated temperature on the structure and properties of calcium–silicate–hydrate gels: the role of confined water. *Soft Matter,* 9**,** 6418-6429.
BONNAUD, P. A., MANZANO, H., MIURA, R., SUZUKI, A., MIYAMOTO, N., HATAKEYAMA, N. & MIYAMOTO, A. 2016. Temperature Dependence of

Nanoconfined Water Properties: Application to Cementitious Materials. *The Journal of Physical Chemistry C,* 120**,** 11465-11480.
BREHM, M. & KIRCHNER, B. 2011. TRAVIS - A Free Analyzer and Visualizer for Monte Carlo and Molecular Dynamics Trajectories. *Journal of Chemical Information and Modeling,* 51**,** 2007-2023.
BREHM, M., THOMAS, M., GEHRKE, S. & KIRCHNER, B. 2020. TRAVIS-A free analyzer for trajectories from molecular simulation. *J Chem Phys,* 152**,** 164105.
BURLION, N., BOURGEOIS, F. & SHAO, J.-F. 2005. Effects of desiccation on mechanical behaviour of concrete. *Cement and concrete composites,* 27**,** 367-379.
CAI, Y., XUAN, D., HOU, P., SHI, J. & POON, C. S. 2021. Effect of seawater as mixing water on the hydration behaviour of tricalcium aluminate. *Cement and Concrete Research,* 149.
CAI, Y., ZHU, X., SUN, K., YIN, K., XUAN, D. & POON, C. S. 2025. Degradation mechanism of seawater-mixed cementitious material subjecting to sulphate attack. *Cement and Concrete Composites,* 155.
CAO, Y., GUO, L., CHEN, B. & WU, J. 2020. Thermodynamic modelling and experimental investigation on chloride binding in cement exposed to chloride and chloride-sulfate solution. *Construction and Building Materials,* 246.
CARSANA, M., GASTALDI, M., LOLLINI, F. & REDAELLI, E. 2019. Durability-Related Properties of Concrete Made with Chloride-Contaminated Materials. *Advances in Civil Engineering Materials,* 8.
CASAR, Z., LÓPEZ-ZORRILLA, J., MANZANO, H., DUQUE-REDONDO, E., MOHAMED, A. K., SCRIVENER, K. & BOWEN, P. 2024. pyCSH: Automated atomic-level structure generation of bulk C-S-H and investigation of their intrinsic properties. *Cement and Concrete Research,* 183**,** 107593.
CASCUDO, O., PIRES, P., CARASEK, H., DE CASTRO, A. & LOPES, A. 2021. Evaluation of the pore solution of concretes with mineral additions subjected to 14 years of natural carbonation. *Cement and Concrete Composites,* 115.
CAUPIN, F. & HERBERT, E. 2006. Cavitation in water: a review. *Comptes Rendus Physique,* 7**,** 1000-1017.
CERVENY, S., ARRESE-IGOR, S., DOLADO, J. S., GAITERO, J. J., ALEGRÍA, A. & COLMENERO, J. 2011. Effect of hydration on the dielectric properties of CSH gel. *The Journal of chemical physics,* 134.
CHANG, H. 2017. Chloride binding capacity of pastes influenced by carbonation under three conditions. *Cement and Concrete Composites,* 84**,** 1-9.
CHAPPEX, T. & SCRIVENER, K. 2012. Alkali fixation of C–S–H in blended cement pastes and its relation to alkali silica reaction. *Cement and Concrete Research,* 42**,** 1049-1054.
CHAROLA, A. E. 2000. Salts in the Deterioration of Porous Materials: An Overview. *Journal of the American Institute for Conservation,* 39**,** 327-343.
CHEN, J. J., THOMAS, J. J., TAYLOR, H. F. & JENNINGS, H. M. 2004. Solubility and structure of calcium silicate hydrate. *Cement and concrete research,* 34**,** 1499-1519.
CHEN, S., REN, J., REN, X. & LI, Y. 2022. Deterioration laws of concrete durability under the coupling action of salt erosion and drying–wetting cycles. *Frontiers in Materials,* 9**,** 1003945.
CHEN, Z. & YE, H. 2022. The role of CaO and MgO incorporation in chloride resistance of sodium carbonate-activated slag. *Cement and Concrete Composites,* 132**,** 104625.

CHEN, Z. & YE, H. 2023. Understanding the impact of main seawater ions and leaching on the chloride transport in alkali-activated slag and Portland cement. *Cement and Concrete Research,* 164.

CHENG, S., SHUI, Z., GAO, X., LU, J., SUN, T. & YU, R. 2020. Degradation progress of Portland cement mortar under the coupled effects of multiple corrosive ions and drying-wetting cycles. *Cement and Concrete Composites,* 111.

CHENG, S., SHUI, Z., SUN, T., HUANG, Y. & LIU, K. 2018. Effects of seawater and supplementary cementitious materials on the durability and microstructure of lightweight aggregate concrete. *Construction and Building Materials,* 190**,** 1081-1090.

CHOUDHARY, H. K., ANUPAMA, A. V., KUMAR, R., PANZI, M. E., MATTEPPANAVAR, S., SHERIKAR, B. N. & SAHOO, B. 2015. Observation of phase transformations in cement during hydration. *Construction and Building Materials,* 101**,** 122-129.

CONG, X. & KIRKPATRICK, R. J. 1996a. 29Si and 17O NMR investigation of the structure of some crystalline calcium silicate hydrates. *Advanced Cement Based Materials,* 3**,** 133-143.

CONG, X. & KIRKPATRICK, R. J. 1996b. 29Si MAS NMR study of the structure of calcium silicate hydrate. *Advanced Cement Based Materials,* 3**,** 144-156.

CONSTANTINIDES, G. & ULM, F.-J. 2004. The effect of two types of CSH on the elasticity of cement-based materials: Results from nanoindentation and micromechanical modeling. *Cement and concrete research,* 34**,** 67-80.

CONSTANTINIDES, G. & ULM, F.-J. 2007. The nanogranular nature of C–S–H. *Journal of the Mechanics and Physics of Solids,* 55**,** 64-90.

CORNER, H. & RIPPSTAIN, D. 1985. Effect of aqueous sodium chloride solution on ettringite. *Touindustrie-Zeitung (TIZ) Fachberichte,* 9**,** 680-683.

CUESTA, A., ZEA-GARCIA, J. D., LONDONO-ZULUAGA, D., DE LA TORRE, A. G., SANTACRUZ, I., VALLCORBA, O., DAPIAGGI, M., SANFELIX, S. G. & ARANDA, M. A. G. 2018. Multiscale understanding of tricalcium silicate hydration reactions. *Sci Rep,* 8**,** 8544.

CYGAN, R. T., GREATHOUSE, J. A., HEINZ, H. & KALINICHEV, A. G. 2009. Molecular models and simulations of layered materials. *Journal of Materials Chemistry,* 19**,** 2470-2481.

CYGAN, R. T., GREATHOUSE, J. A. & KALINICHEV, A. G. 2021. Advances in Clayff Molecular Simulation of Layered and Nanoporous Materials and Their Aqueous Interfaces. *The Journal of Physical Chemistry C,* 125**,** 17573-17589.

CYGAN, R. T., LIANG, J.-J. & KALINICHEV, A. G. 2004. Molecular models of hydroxide, oxyhydroxide, and clay phases and the development of a general force field. *The Journal of Physical Chemistry B,* 108**,** 1255-1266.

DAI, Y., QIAN, G., CAO, Y., CHI, Y., XU, Y., ZHOU, J., LIU, Q., XU, Z. P. & QIAO, S. 2009. Effective removal and fixation of Cr(VI) from aqueous solution with Friedel's salt. *J Hazard Mater,* 170**,** 1086-92.

DE WEERDT, K., JUSTNES, H. & GEIKER, M. R. 2014a. Changes in the phase assemblage of concrete exposed to sea water. *Cement and Concrete Composites,* 47**,** 53-63.

DE WEERDT, K., ORSÁKOVÁ, D. & GEIKER, M. R. 2014b. The impact of sulphate and magnesium on chloride binding in Portland cement paste. *Cement and Concrete Research,* 65**,** 30-40.

DEJONG, M. J. & ULM, F.-J. 2007. The nanogranular behavior of CSH at elevated temperatures (up to 700 C). *Cement and Concrete Research,* 37**,** 1-12.
DENG, H. & HE, Z. 2021. Interactions of sodium chloride solution and calcium silicate hydrate with different calcium to silicon ratios: A molecular dynamics study. *Construction and Building Materials,* 268.
DHONDY, T., REMENNIKOV, A. & SHIEKH, M. N. 2019. Benefits of using sea sand and seawater in concrete: a comprehensive review. *Australian Journal of Structural Engineering,* 20**,** 280-289.
DI BELLA, C., GRIFFA, M., ULRICH, T. J. & LURA, P. 2016. Early-age elastic properties of cement-based materials as a function of decreasing moisture content. *Cement and Concrete Research,* 89**,** 87-96.
DI BELLA, C., MICHEL, A., STANG, H. & LURA, P. 2017. Early age fracture properties of microstructurally-designed mortars. *Cement and Concrete Composites,* 75**,** 62-73.
DIAMOND, S. 1986. Chloride concentrations in concrete pore solutions resulting from calcium and sodium chloride admixtures. *Cement, Concrete, and Aggregates,* 8**,** 97-102.
DONGSHUAI, H., ZEYU, L., PENG, Z. & QINGJUN, D. 2016. Molecular structure and dynamics of an aqueous sodium chloride solution in nano-pores between portlandite surfaces: a molecular dynamics study. *Physical Chemistry Chemical Physics,* 18**,** 2059-2069.
DRAMÉ, H., BEAUDOIN, J. J. & RAKI, L. 2007. A comparative study of the volume stability of C–S–H (I) and Portland cement paste in aqueous salt solutions. *Journal of Materials Science,* 42**,** 6837-6846.
DU, F., JIN, Z., SHE, W., XIONG, C., FENG, G. & FAN, J. 2020. Chloride ions migration and induced reinforcement corrosion in concrete with cracks: A comparative study of current acceleration and natural marine exposure. *Construction and Building Materials,* 263.
DU, J., LIU, Z., SUN, J., LI, G., WU, X., LI, G., LV, Y. & WANG, K. 2022. Enhancing concrete sulfate resistance by adding NaCl. *Construction and Building Materials,* 322.
DUFRESNE, A., ARAYRO, J., ZHOU, T., IOANNIDOU, K., ULM, F. J., PELLENQ, R. & BELAND, L. K. 2018. Atomistic and mesoscale simulation of sodium and potassium adsorption in cement paste. *J Chem Phys,* 149**,** 074705.
DUPUIS, R., MOON, J., JEONG, Y., TAYLOR, R., KANG, S.-H., MANZANO, H., AYUELA, A., MONTEIRO, P. J. M. & DOLADO, J. S. 2021. Normal and anomalous self-healing mechanism of crystalline calcium silicate hydrates. *Cement and Concrete Research,* 142.
DUQUE-REDONDO, E., BONNAUD, P. A. & MANZANO, H. 2022a. A comprehensive review of C-S-H empirical and computational models, their applications, and practical aspects. *Cement and Concrete Research,* 156.
DUQUE-REDONDO, E., KAZUO, Y., LOPEZ-ARBELOA, I. & MANZANO, H. 2018. Cs-137 immobilization in C-S-H gel nanopores. *Phys Chem Chem Phys,* 20**,** 9289-9297.
DUQUE-REDONDO, E., LÓPEZ-ARBELOA, I. & MANZANO, H. 2019. Distinctive Diffusion Regimes of Organic Molecules in Clays: (De)Coupled Motion with Water. *The Journal of Physical Chemistry C,* 123**,** 511-516.
DUQUE-REDONDO, E., MANZANO, H., EPELDE-ELEZCANO, N., MARTÍNEZ-MARTÍNEZ, V. & LÓPEZ-ARBELOA, I. 2014. Molecular Forces Governing

Shear and Tensile Failure in Clay-Dye Hybrid Materials. *Chemistry of Materials,* 26**,** 4338-4345.
DUQUE-REDONDO, E., MASOERO, E. & MANZANO, H. 2022b. Nanoscale shear cohesion between cement hydrates: The role of water diffusivity under structural and electrostatic confinement. *Cement and Concrete Research,* 154.
DUQUE-REDONDO, E., YAMADA, K., DOLADO, J. S. & MANZANO, H. 2021a. Microscopic mechanism of radionuclide Cs retention in Al containing C-S-H nanopores. *Computational Materials Science,* 190.
DUQUE-REDONDO, E., YAMADA, K. & MANZANO, H. 2021b. Cs retention and diffusion in C-S-H at different Ca/Si ratio. *Cement and Concrete Research,* 140.
DUQUE-REDONDO, E., YAMADA, K. & MANZANO, H. 2021c. Effect of chloride and sulfate in the immobilization of Cs-137 in CSH gel. *Journal of Advanced Concrete Technology,* 19**,** 95-105.
EBEAD, U., LAU, D., LOLLINI, F., NANNI, A., SURANENI, P. & YU, T. 2022a. A review of recent advances in the science and technology of seawater-mixed concrete. *Cement and Concrete Research,* 152.
EBEAD, U., LAU, D., LOLLINI, F., NANNI, A., SURANENI, P. & YU, T. 2022b. A review of recent advances in the science and technology of seawater-mixed concrete. *Cement and Concrete Research,* 152**,** 106666.
ELAKNESWARAN, Y., NAWA, T. & KURUMISAWA, K. 2009. Electrokinetic potential of hydrated cement in relation to adsorption of chlorides. *Cement and Concrete Research,* 39**,** 340-344.
ETXEBERRIA, M., FERNANDEZ, J. M. & LIMEIRA, J. 2016. Secondary aggregates and seawater employment for sustainable concrete dyke blocks production: Case study. *Construction and Building Materials,* 113**,** 586-595.
ETXEBERRIA, M. & GONZALEZ-COROMINAS, A. 2017. Properties of Plain Concrete Produced Employing Recycled Aggregates and Sea Water. *International Journal of Civil Engineering,* 16**,** 993-1003.
FAN, D. & YANG, S. 2018. Mechanical properties of C-S-H globules and interfaces by molecular dynamics simulation. *Construction and Building Materials,* 176**,** 573-582.
FELDMAN, R. F. & SEREDA, P. J. 1968. A model for hydrated Portland cement paste as deduced from sorption-length change and mechanical properties. *Matériaux et Construction,* 1**,** 509-520.
FRENKEL, D. & SMIT, B. 2023. *Understanding molecular simulation: from algorithms to applications*, Elsevier.
FRIAS, M., GOÑI, S., GARCÍA, R. & VIGIL DE LA VILLA, R. 2013. Seawater effect on durability of ternary cements. Synergy of chloride and sulphate ions. *Composites Part B: Engineering,* 46**,** 173-178.
GALLUCCI, E. & SCRIVENER, K. 2007. Crystallisation of calcium hydroxide in early age model and ordinary cementitious systems. *Cement and Concrete Research,* 37**,** 492-501.
GALMARINI, S., AIMABLE, A., RUFFRAY, N. & BOWEN, P. 2011. Changes in portlandite morphology with solvent composition: Atomistic simulations and experiment. *Cement and Concrete Research,* 41**,** 1330-1338.
GAO, H., YU, R., LIU, J., ZHANG, W., LI, M., JIA, Y., YE, Y., ZHONG, S., ZHUANG, C., ZHU, H., SU, Q., HUANG, B.-T., WU, H., SUN, J. & HOU, D. 2025. Study on the molecular structure and mechanical properties of potassium ion uptake in calcium silicate hydrate. *Construction and Building Materials,* 481.

GARCÍA-LODEIRO, I., FERNÁNDEZ-JIMÉNEZ, A., BLANCO, M. T. & PALOMO, A. 2008. FTIR study of the sol–gel synthesis of cementitious gels: C–S–H and N–A–S–H. *Journal of Sol-Gel Science and Technology,* 45**,** 63-72.

GARCÍA LODEIRO, I., MACPHEE, D. E., PALOMO, A. & FERNÁNDEZ-JIMÉNEZ, A. 2009. Effect of alkalis on fresh C–S–H gels. FTIR analysis. *Cement and Concrete Research,* 39**,** 147-153.

GARDNER, D. W., LI, J., KUNZ, M., ZHU, C., MONTEIRO, P. J. M., MABOUDIAN, R. & CARRARO, C. 2021. Plastic deformation mechanism of calcium-silicate hydrates determined by deviatoric-stress Raman spectroscopy. *Cement and Concrete Research,* 146.

GARG, N., ÖZÇELIK, V. O., SKIBSTED, J. & WHITE, C. E. 2019. Nanoscale Ordering and Depolymerization of Calcium Silicate Hydrates in the Presence of Alkalis. *The Journal of Physical Chemistry C,* 123**,** 24873-24883.

GARTNER, E., MARUYAMA, I. & CHEN, J. 2017. A new model for the C-S-H phase formed during the hydration of Portland cements. *Cement and Concrete Research,* 97**,** 95-106.

GENG, G., VASIN, R. N., LI, J., QOMI, M. J. A., YAN, J., WENK, H.-R. & MONTEIRO, P. J. M. 2018. Preferred orientation of calcium aluminosilicate hydrate induced by confined compression. *Cement and Concrete Research,* 113**,** 186-196.

GMIRA, A. 2004. *Etude texturale et thermodynamique d'hydrates modèles du ciment.*

GRANGEON, S., CLARET, F., LINARD, Y. & CHIABERGE, C. 2013. X-ray diffraction: a powerful tool to probe and understand the structure of nanocrystalline calcium silicate hydrates. *Structural Science,* 69**,** 465-473.

GREENWELL, H. C., JONES, W., COVENEY, P. V. & STACKHOUSE, S. 2006. On the application of computer simulation techniques to anionic and cationic clays: A materials chemistry perspective. *Journal of Materials Chemistry,* 16**,** 708-723.

GROVES, G. W. 1986a. TEM Studies of Cement Hydration. *MRS Proceedings,* 85**,** 3.

GROVES, G. W. 1986b. Tem Studies of Cement Hydration. *MRS Online Proceedings Library,* 85**,** 3.

GRUTZECK, M. 1999. A new model for the formation of calcium silicate hydrate (CSH). *Material Research Innovations,* 3**,** 160-170.

GRUYAERT, E., VAN DEN HEEDE, P. & DE BELIE, N. 2013. Carbonation of slag concrete: Effect of the cement replacement level and curing on the carbonation coefficient – Effect of carbonation on the pore structure. *Cement and Concrete Composites,* 35**,** 39-48.

GU, Y., DANGLA, P., MARTIN, R.-P., OMIKRINE METALSSI, O. & FEN-CHONG, T. 2022. Modeling the sulfate attack induced expansion of cementitious materials based on interface-controlled crystal growth mechanisms. *Cement and Concrete Research,* 152.

GUO, M., HU, B., XING, F., ZHOU, X., SUN, M., SUI, L. & ZHOU, Y. 2020. Characterization of the mechanical properties of eco-friendly concrete made with untreated sea sand and seawater based on statistical analysis. *Construction and Building Materials,* 234.

HAIST, M., DIVOUX, T., KRAKOWIAK, K. J., SKIBSTED, J., PELLENQ, R. J. M., MÜLLER, H. S. & ULM, F.-J. 2021. Creep in reactive colloidal gels: A nanomechanical study of cement hydrates. *Physical Review Research,* 3.

HAMID, S. 1981. The crystal structure of the 11Å natural tobermorite Ca2. 25 [Si3O7. 5 (OH) 1.5]· 1H2O. *Zeitschrift für Kristallographie-Crystalline Materials,* 154**,** 189-198.

HAN, B., DING, S. & YU, X. 2015. Intrinsic self-sensing concrete and structures: A review. *Measurement: Journal of the International Measurement Confederation,* 59**,** 110-128.

HAN, S., ZHONG, J., DING, W. & OU, J. 2021a. Strength, hydration, and microstructure of seawater sea-sand concrete using high-ferrite Portland cement. *Construction and Building Materials,* 295.

HAN, S., ZHONG, J., YU, Q., YAN, L. & OU, J. 2021b. Sulfate resistance of eco-friendly and sulfate-resistant concrete using seawater sea-sand and high-ferrite Portland cement. *Construction and Building Materials,* 305.

HANTAL, G., BROCHARD, L., LAUBIE, H., EBRAHIMI, E., PELLENQ, R.-J.-M., ULM, F. J. & COASNE, B. 2014. Atomic-scale modelling of elastic and failure properties of clays. *Molecular Physics,* 112**,** 1294-1305.

HARRISON, W. 1990. Effect of chloride in mix ingredients on sulphate resistance of concrete. *Magazine of Concrete Research,* 42**,** 113-126.

HAYAT, U., KAI, M.-F., A, H.-B., LIEW, J.-X. & DAI, J.-G. 2024. Atomic-level investigation into the transport of NaCl solution in porous cement paste: The effects of pore size and temperature. *Journal of Building Engineering,* 86.

HIRAO, H., YAMADA, K., TAKAHASHI, H. & ZIBARA, H. 2005. Chloride binding of cement estimated by binding isotherms of hydrates. *Journal of Advanced Concrete Technology,* 3**,** 77-84.

HONG, S.-Y. & GLASSER, F. 1999. Alkali binding in cement pastes: Part I. The CSH phase. *Cement and Concrete Research,* 29**,** 1893-1903.

HONORIO, T. 2019. Monte Carlo Molecular Modeling of Temperature and Pressure Effects on the Interactions between Crystalline Calcium Silicate Hydrate Layers. *Langmuir,* 35**,** 3907-3916.

HONORIO, T. 2024. Permeability of C-S-H. *Cement and Concrete Research,* 176.

HONORIO, T. & ABAHRI, K. Non equilibrium molecular dynamics simulation of the hydrodynamics in crystalline calcium silicate hydrates nanopores. RILEM SPRING CONVENTION and SUSTAINABLE MATERIALS, SYSTEMS AND STRUCTURES CONFERENCE, 2019.

HONORIO, T., CARASEK, H. & CASCUDO, O. 2022. Water self-diffusion in C-S-H: Effect of confinement and temperature studied by molecular dynamics. *Cement and Concrete Research,* 155.

HONORIO, T., MASARA, F., HUANG, G. & BENBOUDJEMA, F. 2025. Thermal, mechanical, and transport properties of C-S-H at the molecular scale: A force field benchmark. *Cement,* 20.

HONORIO, T., MASARA, F., POYET, S. & BENBOUDJEMA, F. 2023. Surface water in C-S-H: Effect of the temperature on (de)sorption. *Cement and Concrete Research,* 169.

HOU, D. 2020a. *Molecular simulation on cement-based materials*, Springer.

HOU, D. 2020b. *Molecular simulation on cement-based materials*, Springer.

HOU, D., HU, C. & LI, Z. 2017a. Molecular Simulation of the Ions Ultraconfined in the Nanometer-Channel of Calcium Silicate Hydrate: Hydration Mechanism, Dynamic Properties, and Influence on the Cohesive Strength. *Inorg Chem,* 56**,** 1881-1896.

HOU, D., JIA, Y., YU, J., WANG, P. & LIU, Q. 2018a. Transport Properties of Sulfate and Chloride Ions Confined between Calcium Silicate Hydrate Surfaces: A

Molecular Dynamics Study. *The Journal of Physical Chemistry C,* 122**,** 28021-28032.
HOU, D., LI, D., YU, J. & ZHANG, P. 2017b. Insights on Capillary Adsorption of Aqueous Sodium Chloride Solution in the Nanometer Calcium Silicate Channel: A Molecular Dynamics Study. *The Journal of Physical Chemistry C,* 121**,** 13786-13797.
HOU, D. & LI, T. 2018. Influence of aluminates on the structure and dynamics of water and ions in the nanometer channel of calcium silicate hydrate (C-S-H) gel. *Phys Chem Chem Phys,* 20**,** 2373-2387.
HOU, D., LI, T. & WANG, P. 2018b. Molecular Dynamics Study on the Structure and Dynamics of NaCl Solution Transport in the Nanometer Channel of CASH Gel. *ACS Sustainable Chemistry & Engineering,* 6**,** 9498-9509.
HOU, D. & LI, Z. 2014. Molecular dynamics study of water and ions transport in nano-pore of layered structure: A case study of tobermorite. *Microporous and Mesoporous Materials,* 195**,** 9-20.
HOU, D., LI, Z., ZHAO, T. & ZHANG, P. 2015. Water transport in the nano-pore of the calcium silicate phase: reactivity, structure and dynamics. *Phys Chem Chem Phys,* 17**,** 1411-23.
HOU, D., MA, H., ZHU, Y. & LI, Z. 2014a. Calcium silicate hydrate from dry to saturated state: Structure, dynamics and mechanical properties. *Acta Materialia,* 67**,** 81-94.
HOU, D., YU, J., JIN, Z. & HANIF, A. 2018c. Molecular dynamics study on calcium silicate hydrate subjected to tension loading and water attack: structural evolution, dynamics degradation and reactivity mechanism. *Physical Chemistry Chemical Physics,* 20**,** 11130-11144.
HOU, D., ZHANG, W., SUN, J. & ZHANG, J. 2021. Structure, dynamics and mechanical properties evolution of calcium-silicate-hydrate induced by Fe ions: A molecular dynamics study. *Construction and Building Materials,* 287.
HOU, D., ZHANG, W., SUN, M., WANG, P., WANG, M., ZHANG, J. & LI, Z. 2020. Modified Lucas-Washburn function of capillary transport in the calcium silicate hydrate gel pore: A coarse-grained molecular dynamics study. *Cement and Concrete Research,* 136.
HOU, D., ZHENG, H., WANG, P., WAN, X., WANG, M. & WANG, H. 2022. Molecular insight in the wetting behavior of nanoscale water droplet on CSH surface: Effects of Ca/Si ratio. *Applied Surface Science,* 587**,** 152811.
HOU, D., ZHU, Y., LU, Y. & LI, Z. 2014b. Mechanical properties of calcium silicate hydrate (C–S–H) at nano-scale: A molecular dynamics study. *Materials Chemistry and Physics,* 146**,** 503-511.
HOU, D. S., ZHANG, Q. E., ZHANG, J. H. & WANG, P. 2019. Molecular Modeling of Capillary Transport in the Nanometer Pore of Nanocomposite of Cement Hydrate and Graphene/GO. *The Journal of Physical Chemistry C,* 123**,** 15557-15568.
HU, L., PENG, W., WANG, H., QI, Y. & CHENG, H. 2024. Migration behavior of water molecules and chloride ions at the nanopore scale based on molecular properties under temperature effect. *Colloids and Surfaces A: Physicochemical and Engineering Aspects,* 680.
IOANNIDOU, K., GADO, E. D., ULM, F.-J. & PELLENQ, R. J.-M. 2017. Inhomogeneity in Cement Hydrates: Linking Local Packing to Local Pressure. *Journal of Nanomechanics and Micromechanics,* 7**,** 04017003.
ISRAELACHVILI, J. N. 2011. *Intermolecular and surface forces*, Academic press.

ISTEITA, M. & XI, Y. 2017. The effect of temperature variation on chloride penetration in concrete. *Construction and Building Materials,* 156**,** 73-82.

JACKSON, M. D., CHAE, S. R., MULCAHY, S. R., MERAL, C., TAYLOR, R., LI, P., EMWAS, A.-H., MOON, J., YOON, S., VOLA, G., WENK, H.-R. & MONTEIRO, P. J. M. 2013. Unlocking the secrets of Al-tobermorite in Roman seawater concrete. *American Mineralogist,* 98**,** 1669-1687.

JACKSON, M. D., VOLA, G., VŠIANSKÝ, D., OLESON, J. P., SCHEETZ, B. E., BRANDON, C. & HOHLFELDER, R. L. Cement Microstructures and Durability in Ancient Roman Seawater Concretes. *In:* VÁLEK, J., HUGHES, J. J. & GROOT, C. J. W. P., eds. Historic Mortars, 2012// 2012 Dordrecht. Springer Netherlands, 49-76.

JAM, A. N., JAM, N. N., IZADIFAR, M. & RABCZUK, T. 2022. Molecular dynamics study on the crack propagation in carbon doped polycrystalline boron-nitride nanosheets. *Computational Materials Science,* 203**,** 111066.

JAMES, A., BAZARCHI, E., CHINIFORUSH, A. A., PANJEBASHI AGHDAM, P., HOSSEINI, M. R., AKBARNEZHAD, A., MARTEK, I. & GHODOOSI, F. 2019. Rebar corrosion detection, protection, and rehabilitation of reinforced concrete structures in coastal environments: A review. *Construction and Building Materials,* 224**,** 1026-1039.

JAWED, I. & SKALNY, J. 1978. Alkalies in cement: A review: II. Effects of alkalies on hydration and performance of Portland cement. *Cement and Concrete Research,* 8**,** 37-51.

JENNINGS, H. M. 2000. A model for the microstructure of calcium silicate hydrate in cement paste. *Cement and concrete research,* 30**,** 101-116.

JENNINGS, H. M. 2008. Refinements to colloid model of C-S-H in cement: CM-II. *Cement and Concrete Research,* 38**,** 275-289.

JENNINGS, H. M., THOMAS, J. J., GEVRENOV, J. S., CONSTANTINIDES, G. & ULM, F.-J. 2007. A multi-technique investigation of the nanoporosity of cement paste. *Cement and Concrete Research,* 37**,** 329-336.

JIANG, J., WANG, P. & HOU, D. 2017. The mechanism of cesium ions immobilization in the nanometer channel of calcium silicate hydrate: a molecular dynamics study. *Phys Chem Chem Phys,* 19**,** 27974-27986.

K. KATANO, N. T., Y. ISHIZEKI, K. IRIYA. Properties and Application of Concrete Made with Sea Water and Un-washed Sea Sand Sustainable Construction Materials and Technologies, 2013.

KAI, M.-F., HOU, D.-S., SANCHEZ, F., POON, C.-S. & DAI, J.-G. 2023a. Nanoscale Insights into the Influence of Seawater (NaCl) on the Behavior of Calcium Silicate Hydrate. *The Journal of Physical Chemistry C,* 127**,** 8735-8750.

KAI, M.-F., JI, W.-M. & DAI, J.-G. 2022. Atomistic insights into the debonding of Epoxy–Concrete interface with water presence. *Engineering Fracture Mechanics,* 271**,** 108668.

KAI, M.-F., LI, G., YIN, B.-B. & AKBAR, A. 2023b. Aluminum-induced structure evolution and mechanical strengthening of calcium silicate hydrates: an atomistic insight. *Construction and Building Materials,* 393.

KAI, M.-F., LI, G., YIN, B.-B. & AKBAR, A. 2023c. Aluminum-induced structure evolution and mechanical strengthening of calcium silicate hydrates: an atomistic insight. *Construction and Building Materials,* 393**,** 132120.

KAI, M.-F., SANCHEZ, F., HOU, D.-S. & DAI, J.-G. 2023d. Nanoscale insights into the interfacial characteristics between calcium silicate hydrate and silica. *Applied Surface Science,* 616**,** 156478.
KAI, M., ZHANG, L. & LIEW, K. 2019. Graphene and graphene oxide in calcium silicate hydrates: Chemical reactions, mechanical behavior and interfacial sliding. *Carbon,* 146**,** 181-193.
KAI, M., ZHANG, L. & LIEW, K. 2020. Carbon nanotube-geopolymer nanocomposites: a molecular dynamics study of the influence of interfacial chemical bonding upon the structural and mechanical properties. *Carbon,* 161**,** 772-783.
KAI, M. F., ZHANG, L. W. & LIEW, K. M. 2021. Atomistic insights into structure evolution and mechanical property of calcium silicate hydrates influenced by nuclear waste caesium. *J Hazard Mater,* 411**,** 125033.
KALINICHEV, A. G. & KIRKPATRICK, R. J. 2002. Molecular dynamics modeling of chloride binding to the surfaces of calcium hydroxide, hydrated calcium aluminate, and calcium silicate phases. *Chemistry of Materials,* 14**,** 3539-3549.
KALINICHEV, A. G., WANG, J. & KIRKPATRICK, R. J. 2007. Molecular dynamics modeling of the structure, dynamics and energetics of mineral–water interfaces: Application to cement materials. *Cement and Concrete Research,* 37**,** 337-347.
KANTRO, D. L., BRUNAUER, S. & WEISE, C. 1962. Development of surface in the hydration of calcium silicates. II. Extension of investigations to earlier and later stages of hydration. *The Journal of Physical Chemistry,* 66**,** 1804-1809.
KHAN, M. I. & SIDDIQUE, R. 2011. Utilization of silica fume in concrete: Review of durability properties. *Resources, Conservation and Recycling,* 57**,** 30-35.
KHATIBMASJEDI, M., RAMANATHAN, S., SURANENI, P. & NANNI, A. 2020. Compressive strength development of seawater-mixed concrete subject to different curing regimes. *ACI Materials Journal,* 117**,** 3-12.
KHATIBMASJEDI, M., RAMANTHAN, S., SURANENI, P. & NANNI, A. 2019. Shrinkage Behavior of Cementitious Mortars Mixed with Seawater. *Advances in Civil Engineering Materials,* 8**,** 64-78.
KIRKPATRICK, R., KALINICHEV, A., HOU, X. & STRUBLE, L. 2005. Experimental and molecular dynamics modeling studies of interlayer swelling: water incorporation in kanemite and ASR gel. *Materials and Structures,* 38**,** 449-458.
KIRKPATRICK, R., KALINICHEV, A. & YU, P. 2001. Chloride binding to cement phases: exchange isotherm, exp 35 Cl NMR and molecular dynamics modeling studies. *Materials Science of Concrete Special***,** 77-92.
KOBAYASHI, M., TAKAHASHI, K. & KAWABATA, Y. 2021. Physicochemical properties of the Portland cement-based mortar exposed to deep seafloor conditions at a depth of 1680 m. *Cement and Concrete Research,* 142.
KRÖNER, E. 1971. Statistical continuum mechanics.
L'HÔPITAL, E., LOTHENBACH, B., SCRIVENER, K. & KULIK, D. A. 2016. Alkali uptake in calcium alumina silicate hydrate (C-A-S-H). *Cement and Concrete Research,* 85**,** 122-136.
LAGERBLAD, B., JENNINGS, H. & CHEN, J. 2004. Modification of cement paste with silica fume-a NMR study.
LANGE, D. A., JENNINGS, H. M. & SHAH, S. P. 1994. Image analysis techniques for characterization of pore structure of cement-based materials. *Cement and Concrete research,* 24**,** 841-853.
LEACH, A. R. 2001. *Molecular modelling: principles and applications*, Pearson education.

LI, D., ZHAO, W., HOU, D. & ZHAO, T. 2017a. Molecular dynamics study on the chemical bound, physical adsorbed and ultra-confined water molecules in the nano-pore of calcium silicate hydrate. *Construction and Building Materials,* 151**,** 563-574.

LI, G., AKBAR, A., ZHANG, L.-W., ROSEI, F. & LIEW, K. 2023. Surface modification strategy for controlling wettability and ionic diffusion behaviors of calcium silicate hydrate. *Applied Surface Science,* 622**,** 156993.

LI, G., ZHANG, A., SONG, Z., SHI, C., WANG, Y. & ZHANG, J. 2017b. Study on the resistance to seawater corrosion of the cementitious systems containing ordinary Portland cement or/and calcium aluminate cement. *Construction and Building Materials,* 157**,** 852-859.

LI, H., FARZADNIA, N. & SHI, C. 2018. The role of seawater in interaction of slag and silica fume with cement in low water-to-binder ratio pastes at the early age of hydration. *Construction and Building Materials,* 185**,** 508-518.

LI, H., FARZADNIA, N., ZHAO, Y., HU, X. & SHI, C. 2024. Effects of SCMs on chloride binding capacity of ultra-low water-to-binder ratio cement paste with internally introduced chloride. *Construction and Building Materials,* 413.

LI, K., ZENG, J., TANG, L., SØRENSEN, H. E., CASTRO BORGES, P., GEIKER, M. R., PEDERSEN, M. T., ZHANG, P., SURANA, S., MADDALENA, R., WANG, J., ANDRADE, C., BAROGHEL-BOUNY, V., MARTIRENA-HERNÁNDEZ, F., GENG, G., KOVLER, K. & WANG, S. 2022. Long-term field exposure of structural concretes in marine environment: state-of-the-art review by RILEM TC 289-DCM. *Materials and Structures,* 55.

LI, L. G., CHEN, X. Q., CHU, S. H., OUYANG, Y. & KWAN, A. K. H. 2019. Seawater cement paste: Effects of seawater and roles of water film thickness and superplasticizer dosage. *Construction and Building Materials,* 229.

LI, P., LI, W., SUN, Z., SHEN, L. & SHENG, D. 2021. Development of sustainable concrete incorporating seawater: A critical review on cement hydration, microstructure and mechanical strength. *Cement and Concrete Composites,* 121.

LI, P., LI, W., YU, T., QU, F. & TAM, V. W. Y. 2020. Investigation on early-age hydration, mechanical properties and microstructure of seawater sea sand cement mortar. *Construction and Building Materials,* 249.

LI, Q., GENG, H., HUANG, Y. & SHUI, Z. 2015a. Chloride resistance of concrete with metakaolin addition and seawater mixing: A comparative study. *Construction and Building Materials,* 101**,** 184-192.

LI, W., KAWASHIMA, S., XIAO, J., CORR, D. J., SHI, C. & SHAH, S. P. 2015b. Comparative investigation on nanomechanical properties of hardened cement paste. *Materials and Structures,* 49**,** 1591-1604.

LI, Z. & MERZ, K. M., JR. 2022. Systematic Evaluation of Ion Diffusion and Water Exchange. *J Chem Theory Comput,* 18**,** 3017-3026.

LIANG, Y. 2020. Mechanical and fracture properties of calcium silicate hydrate and calcium hydroxide composite from reactive molecular dynamics simulations. *Chemical Physics Letters,* 761.

LINDGÅRD, J., ANDIÇ-ÇAKıR, Ö., FERNANDES, I., RØNNING, T. F. & THOMAS, M. D. A. 2012. Alkali–silica reactions (ASR): Literature review on parameters influencing laboratory performance testing. *Cement and Concrete Research,* 42**,** 223-243.

LIU, C., TAO, Y., NIE, S., CHEN, Y., LI, Z., POON, C. S. & YE, G. 2025. Dissolution of cations in C-(N,K-)A-S-H gels at the nanoscale. *Composites Part B: Engineering,* 297.

LIU, H. & CAO, G. 2016. Effectiveness of the Young-Laplace equation at nanoscale. *Sci Rep,* 6**,** 23936.

LIU, H., DONG, S., TANG, L., KRISHNAN, N. M. A., SANT, G. & BAUCHY, M. 2019. Effects of polydispersity and disorder on the mechanical properties of hydrated silicate gels. *Journal of the Mechanics and Physics of Solids,* 122**,** 555-565.

LIU, X., FENG, P., CHEN, J., LIU, Q., YU, X., CAI, Y., ZHU, H., QING, L. & HONG, J. 2024. A critical review on the interaction between calcium silicate hydrate (C-S-H) and different ions. *Construction and Building Materials,* 413.

LIU, X., FENG, P., YU, X. & HUANG, J. 2022a. Decalcification of calcium silicate hydrate (C-S-H) under aggressive solution attack. *Construction and Building Materials,* 342.

LIU, X., FENG, P., YU, X., SHEN, X., GENG, G. & LOTHENBACH, B. 2022b. The physiochemical alterations of calcium silicate hydrate (C-S-H) under magnesium attack. *Cement and Concrete Research,* 160.

LIU, Z., WANG, Y., XU, D., ZANG, C., ZHANG, Y. & JIANG, J. 2021. Multiple ions transport and interaction in calcium silicate hydrate gel nanopores: Effects of saturation and tortuosity. *Construction and Building Materials,* 283.

LIU, Z., XU, D., GAO, S., ZHANG, Y. & JIANG, J. 2020. Assessing the Adsorption and Diffusion Behavior of Multicomponent Ions in Saturated Calcium Silicate Hydrate Gel Pores Using Molecular Dynamics. *ACS Sustainable Chemistry & Engineering,* 8**,** 3718-3727.

LUBELLI, B., NIJLAND, T. G., VAN HEES, R. P. J. & HACQUEBORD, A. 2010. Effect of mixed in crystallization inhibitor on resistance of lime–cement mortar against NaCl crystallization. *Construction and Building Materials,* 24**,** 2466-2472.

LUO, Q., LI, Y., ZHANG, Z., PENG, X. & GENG, G. 2022. Influence of substrate moisture on the interfacial bonding between calcium silicate hydrate and epoxy. *Construction and Building Materials,* 320**,** 126252.

LUO, Q., QIN, T., CHEN, Z., PANG, B., QU, J. & GAO, Z. 2023a. The influence of moisture and epoxy bonding agents on interfacial behavior between normal concrete substrate and ultrahigh performance concrete as a repair material: Experimental and molecular dynamics study. *Construction and Building Materials,* 372**,** 130779.

LUO, Q., ZHANG, X., LI, Y., ZHANG, Z. & GENG, G. 2023b. Interfacial degradation of calcium silicate hydrate and epoxy under a hygrothermal environment: an experimental and molecular model study. *The Journal of Physical Chemistry C,* 127**,** 1607-1621.

LUPING, T. & NILSSON, L.-O. 1993. Chloride binding capacity and binding isotherms of OPC pastes and mortars. *Cement and concrete research,* 23**,** 247-253.

LUPING, T., NILSSON, L.-O. & BASHEER, M. 2012. *Resistance of concrete to chloride ingress: Testing and modelling*, Taylor and Francis.

MA, Z., LIU, M., TANG, Q., LIANG, C. & DUAN, Z. 2020. Chloride permeability of recycled aggregate concrete under the coupling effect of freezing-thawing, elevated temperature or mechanical damage. *Construction and Building Materials,* 237.

MANZANO, H., DOLADO, J. S. & AYUELA, A. 2009. Elastic properties of the main species present in Portland cement pastes. *Acta Materialia,* 57**,** 1666-1674.

MANZANO, H., MASOERO, E., LOPEZ-ARBELOA, I. & JENNINGS, H. M. 2013. Shear deformations in calcium silicate hydrates. *Soft Matter,* 9.

MANZANO, H., MOEINI, S., MARINELLI, F., VAN DUIN, A. C., ULM, F. J. & PELLENQ, R. J. 2012a. Confined water dissociation in microporous defective silicates: mechanism, dipole distribution, and impact on substrate properties. *J Am Chem Soc,* 134**,** 2208-15.

MANZANO, H., MOEINI, S., MARINELLI, F., VAN DUIN, A. C. T., ULM, F.-J. & PELLENQ, R. J. M. 2012b. Confined Water Dissociation in Microporous Defective Silicates: Mechanism, Dipole Distribution, and Impact on Substrate Properties. *Journal of the American Chemical Society,* 134**,** 2208-2215.

MARTÍNEZ, L., ANDRADE, R., BIRGIN, E. G. & MARTÍNEZ, J. M. 2009. PACKMOL: A package for building initial configurations for molecular dynamics simulations. *Journal of Computational Chemistry,* 30**,** 2157-2164.

MARUYAMA, I., NISHIOKA, Y., IGARASHI, G. & MATSUI, K. 2014. Microstructural and bulk property changes in hardened cement paste during the first drying process. *Cement and Concrete Research,* 58**,** 20-34.

MARUYAMA, I., OHKUBO, T., HAJI, T. & KURIHARA, R. 2019. Dynamic microstructural evolution of hardened cement paste during first drying monitored by 1H NMR relaxometry. *Cement and Concrete Research,* 122**,** 107-117.

MASARA, F., BENBOUDJEMA, F. & HONORIO, T. 2024. Cavitation, Hydrophilicity, and Sorption Hysteresis in C–S–H Pores: Coupled Effects of Relative Humidity and Temperature. *Langmuir,* 40**,** 27286-27298.

MASARA, F., HONORIO, T. & BENBOUDJEMA, F. 2023. Sorption in C-S-H at the molecular level: Disjoining pressures, effective interactions, hysteresis, and cavitation. *Cement and Concrete Research,* 164.

MASOERO, E., CUSATIS, G. & DI LUZIO, G. 2018. C–S–H gel densification: The impact of the nanoscale on self-desiccation and sorption isotherms. *Cement and Concrete Research,* 109**,** 103-119.

MASOERO, E. & DI LUZIO, G. 2020. Nanoparticle simulations of logarithmic creep and microprestress relaxation in concrete and other disordered solids. *Cement and Concrete Research,* 137.

MASOUMI, S., VALIPOUR, H. & ABDOLHOSSEINI QOMI, M. J. 2017. Intermolecular Forces between Nanolayers of Crystalline Calcium-Silicate-Hydrates in Aqueous Medium. *The Journal of Physical Chemistry C,* 121**,** 5565-5572.

MATSUMOTO, M. 2007. Relevance of hydrogen bond definitions in liquid water. *J Chem Phys,* 126**,** 054503.

MEHTA, P. K. & MONTEIRO, P. J. 2014. *Concrete: microstructure, properties, and materials*, McGraw-Hill Education.

MENDOZA, O., GIRALDO, C., CAMARGO, S. S. & TOBÓN, J. I. 2015. Structural and nano-mechanical properties of Calcium Silicate Hydrate (C-S-H) formed from alite hydration in the presence of sodium and potassium hydroxide. *Cement and Concrete Research,* 74**,** 88-94.

MERLINO, S., BONACCORSI, E. & ARMBRUSTER, T. 2001. The real structure of tobermorite 11A: normal and anomalous forms, OD character and polytypic modifications. *European Journal of Mineralogy,* 13**,** 577-590.

MIDDLEMAN, S. 1997. *An introduction to mass and heat transfer: principles of analysis and design*, John Wiley & Sons.

MILLER, S. A., HORVATH, A. & MONTEIRO, P. J. M. 2018. Impacts of booming concrete production on water resources worldwide. *Nature Sustainability,* 1**,** 69-76.

MODUPEOLA, A. G. & OLUTOGE, F. A. 2014. The effect of seawater on shrinkage properties of concrete. *Int J Res Eng Technol,* 2**,** 1-12.

MOHAMED, A. K., PARKER, S. C., BOWEN, P. & GALMARINI, S. 2018. An atomistic building block description of CSH-Towards a realistic CSH model. *Cement and Concrete Research,* 107**,** 221-235.

MOHAMMED, T. U., HAMADA, H. & YAMAJI, T. 2004. Performance of seawater-mixed concrete in the tidal environment. *Cement and Concrete Research,* 34**,** 593-601.

MONASTERIO, M., JANSSON, H., GAITERO, J. J., DOLADO, J. S. & CERVENY, S. 2013. Cause of the fragile-to-strong transition observed in water confined in CSH gel. *The Journal of Chemical Physics,* 139.

MONTANARI, L., SURANENI, P., TSUI-CHANG, M., KHATIBMASJEDI, M., EBEAD, U., WEISS, J. & NANNI, A. 2019. Hydration, Pore Solution, and Porosity of Cementitious Pastes Made with Seawater. *Journal of Materials in Civil Engineering,* 31.

MONTEIRO, P., WANG, K., SPOSITO, G., DOS SANTOS, M. & DE ANDRADE, W. P. 1997. Influence of mineral admixtures on the alkali-aggregate reaction. *Cement and concrete research,* 27**,** 1899-1909.

MORROW, C. P., YAZAYDIN, A. Ö., KRISHNAN, M., BOWERS, G. M., KALINICHEV, A. G. & KIRKPATRICK, R. J. 2013. Structure, Energetics, and Dynamics of Smectite Clay Interlayer Hydration: Molecular Dynamics and Metadynamics Investigation of Na-Hectorite. *The Journal of Physical Chemistry C,* 117**,** 5172-5187.

MORSHEDIFARD, A., MASOUMI, S. & ABDOLHOSSEINI QOMI, M. J. 2018. Nanoscale origins of creep in calcium silicate hydrates. *Nat Commun,* 9**,** 1785.

MORTAZAVI, B., JAVVAJI, B., SHOJAEI, F., RABCZUK, T., SHAPEEV, A. V. & ZHUANG, X. 2021. Exceptional piezoelectricity, high thermal conductivity and stiffness and promising photocatalysis in two-dimensional MoSi2N4 family confirmed by first-principles. *Nano Energy,* 82.

MOSTAFA, N. Y., KISHAR, E. A. & ABO-EL-ENEIN, S. A. 2009. FTIR study and cation exchange capacity of Fe3+- and Mg2+-substituted calcium silicate hydrates. *Journal of Alloys and Compounds,* 473**,** 538-542.

MYERS, R. J., L'HOPITAL, E., PROVIS, J. L. & LOTHENBACH, B. 2015. Composition-solubility-structure relationships in calcium (alkali) aluminosilicate hydrate (C-(N,K-)A-S-H). *Dalton Trans,* 44**,** 13530-44.

N. OTSUKI, T. N., C. YI, T. NAGATA, H. OHARA 2014. Effect of Blast Furnace Slag Powder and Fly Ash on Durability of Concrete Mixed with Seawater. *4th Int. Conf. Durab. Concr. Struct.* USA.

NIED, D., ENEMARK-RASMUSSEN, K., L'HOPITAL, E., SKIBSTED, J. & LOTHENBACH, B. 2016. Properties of magnesium silicate hydrates (M-S-H). *Cement and Concrete Research,* 79**,** 323-332.

NONAT, A. 2004. The structure and stoichiometry of C-S-H. *Cement and Concrete Research,* 34**,** 1521-1528.

NOORI, H., MORTAZAVI, B., KESHTKARI, L., ZHUANG, X. & RABCZUK, T. 2021. Nanopore creation in MoS 2 and graphene monolayers by nanoparticles impact: A reactive molecular dynamics study. *Applied Physics A,* 127**,** 1-13.

OHTOMO, N. & ARAKAWA, K. 2006. Neutron Diffraction Study of Aqueous Ionic Solutions. II. Aqueous Solutions of Sodium Chloride and Potassium Chloride. *Bulletin of the Chemical Society of Japan,* 53**,** 1789-1794.

OLESON, J. P., BOTTALICO, L., BRANDON, C., CUCITORE, R., GOTTI, E. & HOHLFELDER, R. L. 2006. Reproducing a Roman Maritime structure with Vitruvian pozzolanic concrete. *Journal of Roman Archaeology,* 19**,** 29-52.

PACK, S.-W., JUNG, M.-S., SONG, H.-W., KIM, S.-H. & ANN, K. Y. 2010. Prediction of time dependent chloride transport in concrete structures exposed to a marine environment. *Cement and Concrete Research,* 40**,** 302-312.

PÁLINKÁS, G., RADNAI, T. & HAJDU, F. 1980. Ion-solvent and solvent-solvent interactions. X-ray Study of Aqueous Alkali Chloride Solutions. *Zeitschrift für Naturforschung A,* 35**,** 107-114.

PAN, T., XIA, K. & WANG, L. 2010. Chloride binding to calcium silicate hydrates (C-S-H) in cement paste: a molecular dynamics analysis. *International Journal of Pavement Engineering,* 11**,** 367-379.

PELLENQ, R. J.-M., KUSHIMA, A., SHAHSAVARI, R., VAN VLIET, K. J., BUEHLER, M. J., YIP, S. & ULM, F.-J. 2009. A realistic molecular model of cement hydrates. *Proceedings of the National Academy of Sciences,* 106**,** 16102-16107.

PIMIENTA, L., FORTIN, J. & GUÉGUEN, Y. 2014. Investigation of elastic weakening in limestone and sandstone samples from moisture adsorption. *Geophysical Journal International,* 199**,** 335-347.

PIVONKA, P., HELLMICH, C. & SMITH, D. 2004. Microscopic effects on chloride diffusivity of cement pastes—A scale-transition analysis. *Cement and Concrete Research,* 34**,** 2251-2260.

PLIMPTON, S. 1995. Fast parallel algorithms for short-range molecular dynamics. *Journal of computational physics,* 117**,** 1-19.

POWERS, T. C. & BROWNYARD, T. L. Studies of the physical properties of hardened Portland cement paste. Journal Proceedings, 1947. 669-712.

PUERTAS, F., FERNÁNDEZ-JIMÉNEZ, A. & BLANCO-VARELA, M. T. 2004. Pore solution in alkali-activated slag cement pastes. Relation to the composition and structure of calcium silicate hydrate. *Cement and Concrete Research,* 34**,** 139-148.

QU, F., LI, W., GUO, Y., ZHANG, S., ZHOU, J. L. & WANG, K. 2022. Chloride-binding capacity of cement-GGBFS-nanosilica composites under seawater chloride-rich environment. *Construction and Building Materials,* 342.

RAMACHANDRAN, V. S. 1971. Possible states of chloride in the hydration of tricalcium silicate in the presence of calcium chloride. *Matériaux et Construction,* 4**,** 3-12.

RICHARDSON, I. G. 1999. The nature of CSH in hardened cements. *cement and concrete research,* 29**,** 1131-1147.

RICHARDSON, I. G. 2004. Tobermorite/jennite- and tobermorite/calcium hydroxide-based models for the structure of C-S-H: applicability to hardened pastes of tricalcium silicate, β-dicalcium silicate, Portland cement, and blends of Portland cement with blast-furnace slag, metakaolin, or silica fume. *Cement and Concrete Research,* 34**,** 1733-1777.

RICHARDSON, I. G. 2008. The calcium silicate hydrates. *Cement and Concrete Research,* 38**,** 137-158.

SÁEZ DEL BOSQUE, I. F., MARTÍNEZ-RAMÍREZ, S. & BLANCO-VARELA, M. T. 2014. FTIR study of the effect of temperature and nanosilica on the nano structure of C–S–H gel formed by hydrating tricalcium silicate. *Construction and Building Materials,* 52**,** 314-323.

SAMSON, E. & MARCHAND, J. 2007. Modeling the effect of temperature on ionic transport in cementitious materials. *Cement and Concrete Research,* 37**,** 455-468.

SÁNCHEZ ‐ HERRERO, M. J., FERNÁNDEZ ‐ JIMÉNEZ, A. & PALOMO, A. 2017. C3S and C2S hydration in the presence of Na2CO3 and Na2SO4. *Journal of the American Ceramic Society,* 100**,** 3188-3198.

SÁNCHEZ ‐ HERRERO, M. J., FERNÁNDEZ ‐ JIMÉNEZ, A. & PALOMO, Á. 2016. Alkaline hydration of C2S and C3S. *Journal of the American Ceramic Society,* 99**,** 604-611.

SANTHANAM, M., COHEN, M. D. & OLEK, J. 2002. Mechanism of sulfate attack: A fresh look: Part 1: Summary of experimental results. *Cement and concrete research,* 32**,** 915-921.

SANTOS REGO, J., MIRANDA, C. R. & DE KONING, M. 2022. Effects of $Ca^{2+} \rightarrow Mg^{2+}$ substitution on the properties of cementitious tobermorite. *Physical Review Materials,* 6.

SCHERER, G. W. 1999. Structure and properties of gels. *Cement and Concrete Research,* 29**,** 1149-1157.

SCRIVENER, K., SNELLINGS, R., LOTHENBACH, B. & PRESS, C. 2016. *A practical guide to microstructural analysis of cementitious materials*, CRC press Boca Raton, FL, USA:.

SEKHAR DAS, C., AHMAD, M. R., ZHAO, X.-L. & DAI, J.-G. 2025. Influences of temperatures on the physical and chemical chloride binding of calcium silicate hydrate and Friedel salt at different chloride concentrations. *Construction and Building Materials,* 476.

SHAHSAVARI, R., BUEHLER, M. J., PELLENQ, R. J. M. & ULM, F. J. 2009. First ‐ principles study of elastic constants and interlayer interactions of complex hydrated oxides: Case study of tobermorite and jennite. *Journal of the American Ceramic Society,* 92**,** 2323-2330.

SHAHSAVARI, R., PELLENQ, R. J.-M. & ULM, F.-J. 2011. Empirical force fields for complex hydrated calcio-silicate layered materials. *Physical Chemistry Chemical Physics,* 13**,** 1002-1011.

SHAO, W., LI, J. & LIU, Y. 2016. Influence of Exposure Temperature on Chloride Diffusion into RC Pipe Piles Exposed to Atmospheric Corrosion. *Journal of Materials in Civil Engineering,* 28.

SHI, C., YUAN, Q., HE, F. & HU, X. 2019. *Transport and interactions of chlorides in cement-based materials*, CRC press.

SHI, Z., GEIKER, M. R., LOTHENBACH, B., DE WEERDT, K., GARZÓN, S. F., ENEMARK-RASMUSSEN, K. & SKIBSTED, J. 2017. Friedel's salt profiles from thermogravimetric analysis and thermodynamic modelling of Portland cement-based mortars exposed to sodium chloride solution. *Cement and Concrete Composites,* 78**,** 73-83.

SHI, Z. & LOTHENBACH, B. 2020. The combined effect of potassium, sodium and calcium on the formation of alkali-silica reaction products. *Cement and Concrete Research,* 127.

SHI, Z., SHUI, Z., LI, Q. & GENG, H. 2015. Combined effect of metakaolin and sea water on performance and microstructures of concrete. *Construction and Building Materials,* 74**,** 57-64.

SHRIVASTAVA, O. P., KOMARNENI, S. & BREVAL, E. 1991. Mg2+ uptake by synthetic tobermorite and xonotlite. *Cement and Concrete Research,* 21**,** 83-90.

SKALNY, J., MARCHAND, J. & ODLER, I. 2003. Sulfate attack on concrete. Taylor & Francis.

SONG, Q., NIE, J., WU, D., HU, Y. & CHEN, Y. 2021. Effect of SO42−, Cl− and Mg2+ on the system of C-S-H and Ca(OH)2. *Construction and Building Materials,* 285.
STANDARD, A. 2013. D1141-98: Standard Practice for the Preparation of Substitute Ocean Water. *ASTM International, West Conshohocken*.
STUKOWSKI, A. 2010. Visualization and analysis of atomistic simulation data with OVITO–the Open Visualization Tool. *Modelling and Simulation in Materials Science and Engineering,* 18**,** 015012.
SUGIYAMA, D. 2008. Chemical alteration of calcium silicate hydrate (C–S–H) in sodium chloride solution. *Cement and Concrete Research,* 38**,** 1270-1275.
SUN, J., ZHANG, W., ZHANG, J. & HOU, D. 2021a. Molecular dynamics study the structure, bonding, dynamic and mechanical properties of calcium silicate hydrate with ultra-confined water: Effects of nanopore size. *Construction and Building Materials,* 280.
SUN, Y., ZHANG, Y., CAI, Y., LAM, W. L., LU, J.-X., SHEN, P. & POON, C. S. 2021b. Mechanisms on Accelerating Hydration of Alite Mixed with Inorganic Salts in Seawater and Characteristics of Hydration Products. *ACS Sustainable Chemistry & Engineering,* 9**,** 10479-10490.
SUWANMANEECHOT, P., AILI, A. & MARUYAMA, I. 2020. Creep behavior of C-S-H under different drying relative humidities: Interpretation of microindentation tests and sorption measurements by multi-scale analysis. *Cement and Concrete Research,* 132.
TANG, S., A, H., CHEN, J., YU, W., YU, P., CHEN, E., DENG, H. & HE, Z. 2019a. The interactions between water molecules and C-S-H surfaces in loads-induced nanopores: A molecular dynamics study. *Applied Surface Science,* 496.
TANG, S., HUBAO, A., CHEN, J., YU, W., YU, P., CHEN, E., DENG, H. & HE, Z. 2019b. The interactions between water molecules and CSH surfaces in loads-induced nanopores: A molecular dynamics study. *Applied Surface Science,* 496**,** 143744.
TANG, Y. & CHEN, W. 2020. Effect of magnesium on the structure and chemical composition of calcium silicate hydrate at elevated temperature. *Construction and Building Materials,* 240.
TANG, Y., SCHOLLBACH, K., BROUWERS, H. J. H. & CHEN, W. 2021. Effects of soluble magnesium on the structure of calcium silicate hydrate. *Construction and Building Materials,* 302.
TAO, Y., GAO, Y., SUN, Y., PELLENQ, R. J. M. & POON, C. S. 2024. C-S-H decalcification in seawater: The view from the nanoscale. *Cement and Concrete Research,* 175.
TAYLOR, H. & HOWISON, J. 1956. Relationships between calcium silicates and clay minerals. *Clay Minerals Bulletin,* 3**,** 98-111.
TAYLOR, H. F. 1986. Proposed structure for calcium silicate hydrate gel. *Journal of the American Ceramic Society,* 69**,** 464-467.
TAYLOR, H. F. 1997. *Cement chemistry*, Thomas Telford London.
THOMAS, J. J., BIERNACKI, J. J., BULLARD, J. W., BISHNOI, S., DOLADO, J. S., SCHERER, G. W. & LUTTGE, A. 2011. Modeling and simulation of cement hydration kinetics and microstructure development. *Cement and Concrete Research,* 41**,** 1257-1278.
TING, M. Z. Y., WONG, K. S., RAHMAN, M. E. & SELOWARA JOO, M. 2020. Mechanical and durability performance of marine sand and seawater concrete

incorporating silicomanganese slag as coarse aggregate. *Construction and Building Materials,* 254.
TOUIL, B., GHOMARI, F., BEZZAR, A., KHELIDJ, A. & BONNET, S. 2017. Effect of Temperature on Chloride Diffusion in Saturated Concrete. *Materials Journal,* 114**,** 713-721.
TREJO, D., SHAKOURI, M., VADDEY, N. P. & ISGOR, O. B. 2018. Development of empirical models for chloride binding in cementitious systems containing admixed chlorides. *Construction and Building Materials,* 189**,** 157-169.
UKPATA, J. O., MUHAMMED BASHEER, P. A. & BLACK, L. 2019. Expansion of CEM I and slag-blended cement mortars exposed to combined chloride-sulphate environments. *Cement and Concrete Research,* 123.
ULM, F.-J., COUSSY, O. & BAŽANT, Z. P. 1999. The "Chunnel" fire. I: Chemoplastic softening in rapidly heated concrete. *Journal of engineering mechanics,* 125**,** 272-282.
ULM, F. J., VANDAMME, M., BOBKO, C., ALBERTO ORTEGA, J., TAI, K. & ORTIZ, C. 2007. Statistical Indentation Techniques for Hydrated Nanocomposites: Concrete, Bone, and Shale. *Journal of the American Ceramic Society,* 90**,** 2677-2692.
VANDAMME, M. & ULM, F.-J. 2009. Nanogranular origin of concrete creep. *Proceedings of the National Academy of Sciences,* 106**,** 10552-10557.
VERLET, L. 1968. Computer" experiments" on classical fluids. II. Equilibrium correlation functions. *Physical Review,* 165**,** 201.
VIEHLAND, D., YUAN, L. J., XU, Z., CONG, X. D. & KIRKPATRICK, R. J. 1997. Structural studies of jennite and 1.4 nm tobermorite: disordered layering along the [100] of jennite. *Journal of the American Ceramic Society,* 80**,** 3021-3028.
VU-BAC, N., RAFIEE, R., ZHUANG, X., LAHMER, T. & RABCZUK, T. 2015. Uncertainty quantification for multiscale modeling of polymer nanocomposites with correlated parameters. *Composites Part B: Engineering,* 68**,** 446-464.
WANG, F., ZHANG, Y., JIANG, J., YIN, B. & LI, Z. 2020a. Effect of temperature on the capillary transport of sodium sulfate solution in calcium silicate hydrate nanopore: A molecular dynamics study. *Construction and Building Materials,* 231.
WANG, J., LIU, E. & LI, L. 2018. Multiscale investigations on hydration mechanisms in seawater OPC paste. *Construction and Building Materials,* 191**,** 891-903.
WANG, J., XIE, J., WANG, Y., LIU, Y. & DING, Y. 2020b. Rheological properties, compressive strength, hydration products and microstructure of seawater-mixed cement pastes. *Cement and Concrete Composites,* 114.
WANG, P., ZHANG, Q., WANG, M., YIN, B., HOU, D. & ZHANG, Y. 2019. Atomistic insights into cesium chloride solution transport through the ultra-confined calcium-silicate-hydrate channel. *Phys Chem Chem Phys,* 21**,** 11892-11902.
WANG, X., LI, T., XIE, W., ZHANG, L., LI, D. & XING, F. 2024. Molecular dynamics study on the structure and mechanical properties of tobermorite. *Materials Science and Engineering: B,* 299.
WEGIAN, F. M. 2010. Effect of seawater for mixing and curing on structural concrete. *The IES Journal Part A: Civil & Structural Engineering,* 3**,** 235-243.
WEN, R., CHEN, Y., GUO, T., YUAN, L., WANG, T., YU, Q., TU, Y., SAS, G. & ELFGREN, L. 2022. Effects of temperature on ion transport in C–A–S–H gel nanopores: insights from molecular dynamics simulations. *Journal of Materials Science,* 57**,** 18437-18455.

WILSON, W., GONTHIER, J. N., GEORGET, F. & SCRIVENER, K. L. 2022. Insights on chemical and physical chloride binding in blended cement pastes. *Cement and Concrete Research,* 156.

WITTMANN, F. 1973. Interaction of hardened cement paste and water. *Journal of the American ceramic society,* 56**,** 409-415.

WITTMANN, F. 1979. Trends in research on creep and shrinkage of concrete. *Cement Production and Use***,** 143-161.

WOJDYR, M. 2010. Fityk: a general-purpose peak fitting program. *Applied Crystallography,* 43**,** 1126-1128.

XIANG-PENG, F., LI-PING, G., JIAN-DONG, W., BANG-CHENG, L., YING-JIE, C. & XU-YAN, S. 2023. Impact of temperature, pH value and multiple ions on the physisorption of chloride ion on C-S-H gel surface. *Construction and Building Materials,* 392.

XIAO, J., QIANG, C., NANNI, A. & ZHANG, K. 2017. Use of sea-sand and seawater in concrete construction: Current status and future opportunities. *Construction and Building Materials,* 155**,** 1101-1111.

XIE, Q., XIAO, J. & ZONG, Z. 2022. Strength and microstructure of seawater and sea sand mortar after exposure to elevated temperatures. *Construction and Building Materials,* 322.

XIE, Y. & LUO, Q. 2023. Atomistic insights into the effect of temperature on capillary transport of water molecules in epoxy-modified calcium silicate hydrate nanopore: diffusion, kinetics, and mechanism. *Journal of Materials Science***,** 1-15.

YAMAMOTO, A. H. H. Y. S. D. 2017. Influence of seawater mixing and curing on strength characteristics and porosity of ground granulated blastfurnace slag concrete. *Materials Science and Engineering.*

YAN, Y., BERNARD, E., MIRON, G. D., RENTSCH, D., MA, B., SCRIVENER, K. & LOTHENBACH, B. 2023. Kinetics of Al uptake in synthetic calcium silicate hydrate (C-S-H). *Cement and Concrete Research,* 172.

YAN, Y., YANG, S.-Y., MIRON, G. D., COLLINGS, I. E., L'HÔPITAL, E., SKIBSTED, J., WINNEFELD, F., SCRIVENER, K. & LOTHENBACH, B. 2022. Effect of alkali hydroxide on calcium silicate hydrate (C-S-H). *Cement and Concrete Research,* 151.

YANG, J., HOU, D. & DING, Q. 2018. Ionic hydration structure, dynamics and adsorption mechanism of sulfate and sodium ions in the surface of calcium silicate hydrate gel: A molecular dynamics study. *Applied Surface Science,* 448**,** 559-570.

YANG, J., JIA, Y., HOU, D., WANG, P., JIN, Z., SHANG, H., LI, S. & ZHAO, T. 2019a. Na and Cl immobilization by size controlled calcium silicate hydrate nanometer pores. *Construction and Building Materials,* 202**,** 622-635.

YANG, J., ZHAO, G., YIN, H., FENG, Y. & ZHANG, P. 2023. Effects of C-S-H gel surface structure on sodium chloride evaporation crystallization in C-S-H gel nanopores with molecular dynamics analysis. *Applied Surface Science,* 639.

YANG, Y., PATEL, R. A., CHURAKOV, S. V., PRASIANAKIS, N. I., KOSAKOWSKI, G. & WANG, M. 2019b. Multiscale modeling of ion diffusion in cement paste: electrical double layer effects. *Cement and Concrete Composites,* 96**,** 55-65.

YANG, Z., JIANG, J., JIANG, X., MU, S., WU, M., SUI, S., WANG, L. & WANG, F. 2019c. The influence of sodium sulfate and magnesium sulfate on the stability of bound chlorides in cement paste. *Construction and Building Materials,* 228**,** 116775.

YAPHARY, Y. L., LAU, D., SANCHEZ, F. & POON, C. S. 2020. Effects of sodium/calcium cation exchange on the mechanical properties of calcium silicate hydrate (C-S-H). *Construction and Building Materials,* 243.

YASEEN, S. A., YISEEN, G. A., POON, C. S. & LI, Z. 2020. Influence of Seawater on the Morphological Evolution and the Microchemistry of Hydration Products of Tricalcium Silicates (C3S). *ACS Sustainable Chemistry & Engineering,* 8**,** 15875-15887.

YE, H., JIN, X., CHEN, W., FU, C. & JIN, N. 2016. Prediction of chloride binding isotherms for blended cements. *Computers and Concrete,* 17**,** 655-672.

YOUNIS, A., EBEAD, U., SURANENI, P. & NANNI, A. 2018. Fresh and hardened properties of seawater-mixed concrete. *Construction and Building Materials,* 190**,** 276-286.

YU, J., HOU, D., MA, H. & WANG, P. 2022. Nanomodified Cement-Based Materials: Review (2015–2020) of Molecular Dynamics Studies. *Journal of Materials in Civil Engineering,* 34.

YU, J., ZHENG, Q., HOU, D., ZHANG, J., LI, S., JIN, Z., WANG, P., YIN, B. & WANG, X. 2019. Insights on the capillary transport mechanism in the sustainable cement hydrate impregnated with graphene oxide and epoxy composite. *Composites Part B: Engineering,* 173.

YU, P. & KIRKPATRICK, R. J. 2001. 35Cl NMR relaxation study of cement hydrate suspensions. *Cement and concrete research,* 31**,** 1479-1485.

YU, P., KIRKPATRICK, R. J., POE, B., MCMILLAN, P. F. & CONG, X. 1999. Structure of Calcium Silicate Hydrate (C-S-H): Near-, Mid-, and Far-Infrared Spectroscopy. *Journal of the American Ceramic Society,* 82**,** 742-748.

YUAN, Q. 2009. *Fundamental studies on test methods for the transport of chloride ions in cementitious materials.* Ghent University.

YURTDAS, I., PENG, H., BURLION, N. & SKOCZYLAS, F. 2006. Influences of water by cement ratio on mechanical properties of mortars submitted to drying. *Cement and Concrete Research,* 36**,** 1286-1293.

ZEHTAB, B. & TARIGHAT, A. 2016. Diffusion study for chloride ions and water molecules in C-S-H gel in nano-scale using molecular dynamics: Case study of tobermorite. *Advances in concrete construction,* 4**,** 305-317.

ZHA, Y., YU, J., WANG, R., HE, P. & CAO, Z. 2018. Effect of ion chelating agent on self-healing performance of Cement-based materials. *Construction and Building Materials,* 190**,** 308-316.

ZHANG, C.-L., CHEN, W.-K., MU, S., ŠAVIJA, B. & LIU, Q.-F. 2021a. Numerical investigation of external sulfate attack and its effect on chloride binding and diffusion in concrete. *Construction and Building Materials,* 285.

ZHANG, L., LIN, Z. & LI, Z. 2012. The structure of silicate ions in C-S-H discussed from chemical composition. *Advances in Cement Research,* 24**,** 263-281.

ZHANG, P., HOU, D., LIU, Q., LIU, Z. & YU, J. 2017. Water and chloride ions migration in porous cementitious materials: An experimental and molecular dynamics investigation. *Cement and Concrete Research,* 102**,** 161-174.

ZHANG, Y., ZHOU, Q., JU, J. W. & BAUCHY, M. 2021b. New insights into the mechanism governing the elasticity of calcium silicate hydrate gels exposed to high temperature: A molecular dynamics study. *Cement and Concrete Research,* 141.

ZHANG, Z. H., SANG, Z. Q., ZHANG, L. Y., MA, Z. X. & ZHANG, Y. 2013a. Experimental Research on Durability of Concrete Made by Seawater and Sea-Sand. *Advanced Materials Research,* 641-642**,** 385-388.

ZHANG, Z. H., SANG, Z. Q., ZHANG, L. Y., MA, Z. X. & ZHANG, Y. 2013b. Experimental research on durability of concrete made by seawater and sea-sand. *Advanced Materials Research,* 641**,** 385-388.

ZHAO, G., LI, J. & SHAO, W. 2018. Effect of mixed chlorides on the degradation and sulfate diffusion of cast-in-situ concrete due to sulfate attack. *Construction and Building Materials,* 181**,** 49-58.

ZHAO, Y., HU, X., SHI, C., ZHANG, Z. & ZHU, D. 2021. A review on seawater sea-sand concrete: Mixture proportion, hydration, microstructure and properties. *Construction and Building Materials,* 295.

ZHAO, Y., HU, X., YUAN, Q. & SHI, C. 2023. The change of phase assemblage and desorption of bound chloride for seawater cement paste under sulfate attack. *Cement and Concrete Composites,* 139.

ZHOU, Y., HOU, D., JIANG, J., LIU, L., SHE, W. & YU, J. 2018. Experimental and molecular dynamics studies on the transport and adsorption of chloride ions in the nano-pores of calcium silicate phase: The influence of calcium to silicate ratios. *Microporous and Mesoporous Materials,* 255**,** 23-35.

ZHOU, Y., HOU, D., JIANG, J. & WANG, P. 2016. Chloride ions transport and adsorption in the nano-pores of silicate calcium hydrate: Experimental and molecular dynamics studies. *Construction and Building Materials,* 126**,** 991-1001.

ZHU, Q., JIANG, L., CHEN, Y., XU, J. & MO, L. 2012. Effect of chloride salt type on chloride binding behavior of concrete. *Construction and Building Materials,* 37**,** 512-517.

ZHU, X., BROCHARD, L., VANDAMME, M. & JIANG, Z. 2023. Scaling of nanoscale elastic and tensile failure properties of cementitious calcium-silicate-hydrate materials at cryogenic temperatures: A molecular simulation study. *Cement and Concrete Research,* 172.

ZHU, Z., WANG, Z., ZHOU, Y., CHEN, Y., ZHOU, L. & SHE, A. 2021. Evaluation of the nanostructure of calcium silicate hydrate based on atomic force microscopy-infrared spectroscopy experiments. *Nanotechnology Reviews,* 10**,** 807-818.

ZIBARA, H., HOOTON, R. D., THOMAS, M. D. A. & STANISH, K. 2008. Influence of the C/S and C/A ratios of hydration products on the chloride ion binding capacity of lime-SF and lime-MK mixtures. *Cement and Concrete Research,* 38**,** 422-426.

Appendix 1

Methodology for building the C-S-H models

The atomic structure of C-S-H in pyCSH is built from chains of SiO_4 tetrahedra, where the basic structural unit is the silicate dimer. The key parameter controlling the Ca/Si ratio is the mean chain length (MCL): shorter chains contain more dimers per Si atom, which requires more Ca^{2+} ions per Si to ensure electroneutrality, and thus a higher Ca/Si ratio. By holding the Ca^{2+}/dimer ratio constant and reducing MCL, pyCSH systematically increases Ca/Si without introducing arbitrary structural defects. Additionally, Ca^{2+} ions can be positioned either in bridging sites (within the silicate chain) or in interlayer regions (between C-S-H sheets). Their distribution is automatically managed by the code to yield physically realistic arrangements.

Figure A1.1 presents the input parameters used to generate the calcium-silicate-hydrate structure with a Ca/Si ratio of 1.2-2.0. The study generated five distinct C-S-H structures with each specific Ca/Si composition, and the code output for these structures is provided below. The pyCSH code used to generate the C-S-H models is publicly available at the following link, allowing for further exploration and utilisation of this computational tool: https://github.com/hegoimanzano/pyCSH.git and https://github.com/akmiitm/pyCSH.

Ca/Si=1.2

```
seed = 23137
shape = (6,6,3)   # Minimum (1,1,1)
Ca_Si_ratio = 1.2
W_Si_ratio  = 0.45

prefix = "CaSi1.2"

N_samples = 5
make_independent = True


offset_gaussian = True
width_Ca_Si = 0.05
width_SiOH = 0.05
width_CaOH = 0.05

create =True
check = False


write_lammps = True
write_lammps_erica = True
write_vasp = True
write_siesta = False
```

Ca/Si=1.4

```
seed = 23137
shape = (6,6,3)   # Minimum (1,1,1)
Ca_Si_ratio = 1.4
W_Si_ratio  = 0.55

prefix = "CaSi1.4"

N_samples = 5
make_independent = True


offset_gaussian = True
width_Ca_Si = 0.05
width_SiOH = 0.05
width_CaOH = 0.05

create =True
check = False


write_lammps = True
write_lammps_erica = True
write_vasp = True
write_siesta = False
```

Ca/Si=1.6

```
seed = 23137
shape = (6,6,3)   # Minimum (1,1,1)
Ca_Si_ratio = 1.6
W_Si_ratio  = 0.65

prefix = "CaSi1.6"

N_samples = 5
make_independent = True


offset_gaussian = True
width_Ca_Si = 0.05
width_SiOH = 0.05
width_CaOH = 0.05

create =True
check = False


write_lammps = True
write_lammps_erica = True
write_vasp = True
write_siesta = False
```

Ca/Si=1.8

```
seed = 23137
shape = (6,6,3)   # Minimum (1,1,1)
Ca_Si_ratio = 1.8
W_Si_ratio  = 0.7

prefix = "CaSi1.8"

N_samples = 5
make_independent = True


offset_gaussian = True
width_Ca_Si = 0.05
width_SiOH = 0.05
width_CaOH = 0.05

create =True
check = False


write_lammps = True
write_lammps_erica = True
write_vasp = True
write_siesta = False
```

Ca/Si=2.0

```
seed = 23137
shape = (6,6,3)   # Minimum (1,1,1)
Ca_Si_ratio = 2.0
W_Si_ratio  = 0.75

prefix = "CaSi2.0"

N_samples = 5
make_independent = True


offset_gaussian = True
width_Ca_Si = 0.05
width_SiOH = 0.05
width_CaOH = 0.05

create =True
check = False


write_lammps = True
write_lammps_erica = True
write_vasp = True
write_siesta = False
```

Figure A1.1. Snapshot of the input parameters used to generate C-S-H structure with Ca/Si=1.2-2.0.

Figure A1.2 shows the output parameters for the 5 samples generated for a C-S-H model with Ca/Si ratios between 1.2-2.0.

```
Sample:     2     Ca/Si:  1.207000     SiOH/Si:  0.314500    CaOH/Ca:  0.163400    MCL:  3.764700
Sample:     5     Ca/Si:  1.208300     SiOH/Si:  0.289800    CaOH/Ca:  0.208500    MCL:  4.400000
Sample:     3     Ca/Si:  1.209700     SiOH/Si:  0.297100    CaOH/Ca:  0.165300    MCL:  3.872200
Sample:     1     Ca/Si:  1.211500     SiOH/Si:  0.301900    CaOH/Ca:  0.192100    MCL:  4.062500
Sample:     4     Ca/Si:  1.212200     SiOH/Si:  0.312400    CaOH/Ca:  0.157200    MCL:  3.661900

Sample:     1     Ca/Si:  1.396700     SiOH/Si:  0.204800    CaOH/Ca:  0.434600    MCL:  5.113200
Sample:     4     Ca/Si:  1.397100     SiOH/Si:  0.205900    CaOH/Ca:  0.442100    MCL:  5.230800
Sample:     2     Ca/Si:  1.399600     SiOH/Si:  0.202600    CaOH/Ca:  0.423600    MCL:  4.890900
Sample:     3     Ca/Si:  1.402200     SiOH/Si:  0.206700    CaOH/Ca:  0.426300    MCL:  4.837800
Sample:     5     Ca/Si:  1.402600     SiOH/Si:  0.206000    CaOH/Ca:  0.416600    MCL:  4.684200

Sample:     5     Ca/Si:  1.589600     SiOH/Si:  0.107900    CaOH/Ca:  0.497000    MCL:  4.023300
Sample:     4     Ca/Si:  1.592000     SiOH/Si:  0.141800    CaOH/Ca:  0.529500    MCL:  4.142900
Sample:     2     Ca/Si:  1.593500     SiOH/Si:  0.120200    CaOH/Ca:  0.523400    MCL:  4.225800
Sample:     3     Ca/Si:  1.596100     SiOH/Si:  0.110700    CaOH/Ca:  0.492700    MCL:  3.872200
Sample:     1     Ca/Si:  1.600000     SiOH/Si:  0.144200    CaOH/Ca:  0.532500    MCL:  4.062500

Sample:     2     Ca/Si:  1.787800     SiOH/Si:  0.055000    CaOH/Ca:  0.606600    MCL:  3.661900
Sample:     4     Ca/Si:  1.789300     SiOH/Si:  0.029800    CaOH/Ca:  0.576700    MCL:  3.469000
Sample:     5     Ca/Si:  1.792200     SiOH/Si:  0.056900    CaOH/Ca:  0.613800    MCL:  3.695700
Sample:     1     Ca/Si:  1.793000     SiOH/Si:  0.035200    CaOH/Ca:  0.607800    MCL:  3.764700
Sample:     3     Ca/Si:  1.797300     SiOH/Si:  0.042500    CaOH/Ca:  0.631600    MCL:  3.984600

Sample:     1     Ca/Si:  1.989200     SiOH/Si:  0.000000    CaOH/Ca:  0.598900    MCL:  2.541000
Sample:     2     Ca/Si:  1.991500     SiOH/Si:  0.000000    CaOH/Ca:  0.612400    MCL:  2.620100
Sample:     5     Ca/Si:  1.995700     SiOH/Si:  0.000000    CaOH/Ca:  0.612400    MCL:  2.600000
Sample:     4     Ca/Si:  2.000000     SiOH/Si:  0.000000    CaOH/Ca:  0.594400    MCL:  2.465200
Sample:     3     Ca/Si:  2.002200     SiOH/Si:  0.000000    CaOH/Ca:  0.607900    MCL:  2.541000
```

Figure A1.2. Output parameters for the generated models with a Ca/Si ratio of 1.2, 1.4, 1.6, 1.8, and 2.0.

Model characterization

The Ca/Si, Si-OH/Si, Ca-OH/Ca, MCL, and 2H/S ratios, as well as the mean chain length (MCL) of the models used in this study are shown in Figure A1.3(a1-a5). The mean chain length, H/Si ratio, and Ca-OH/Ca and Si-OH/Si ratios are comparable with the experimental data , as can be seen in Figure A1.3(b1-b5), (c1-c5), and (d1-d5), respectively for the C-S-H with Ca/Si ratios between 1.2-2.0.

(1) Ca/Si = 1.20

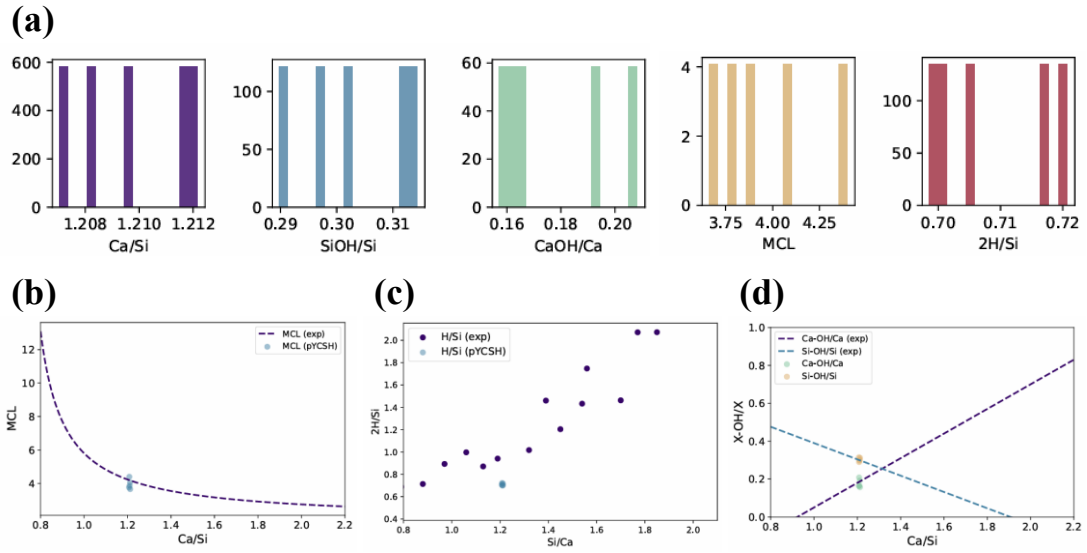

(2) Ca/Si = 1.40

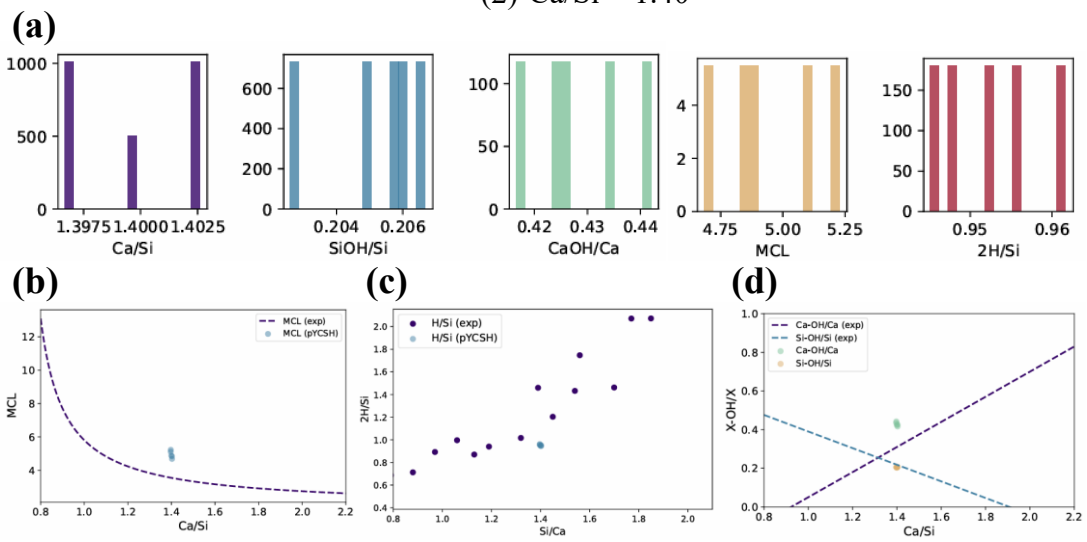

(3) Ca/Si = 1.60

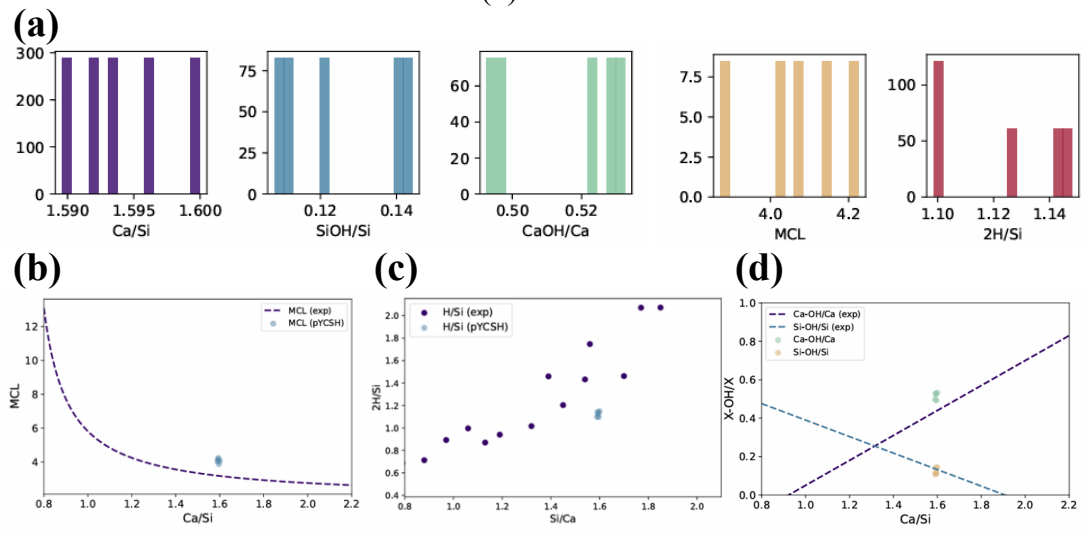

(4) Ca/Si = 1.80

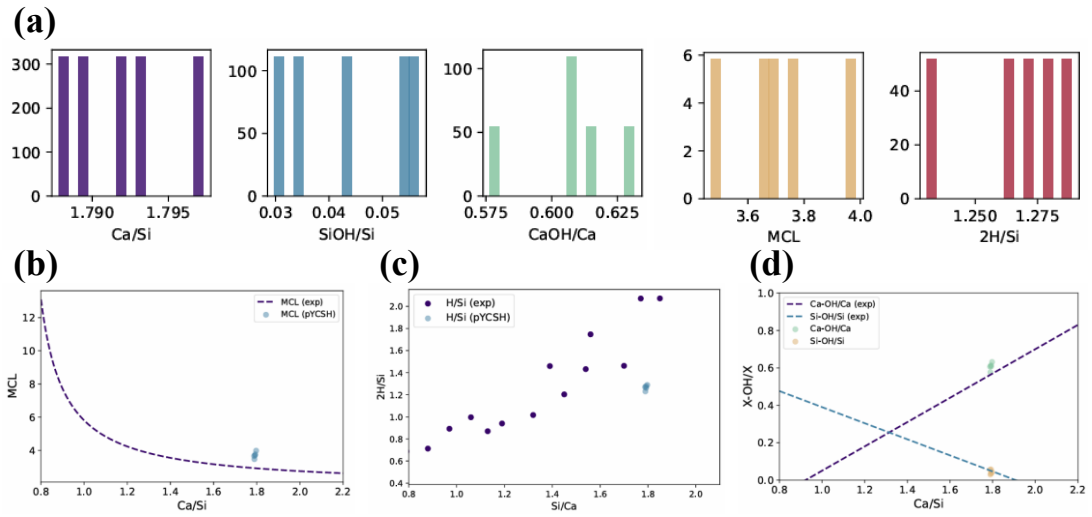
(a)
Ca/Si
SiOH/Si
CaOH/Ca
MCL
2H/Si
(b)
MCL (exp)
MCL (pYCSH)
MCL
Ca/Si
(c)
H/Si (exp)
H/Si (pYCSH)
2H/Si
Si/Ca
(d)
Ca-OH/Ca (exp)
Si-OH/Si (exp)
Ca-OH/Ca
Si-OH/Si
X-OH/X
Ca/Si

(5) Ca/Si = 2.00

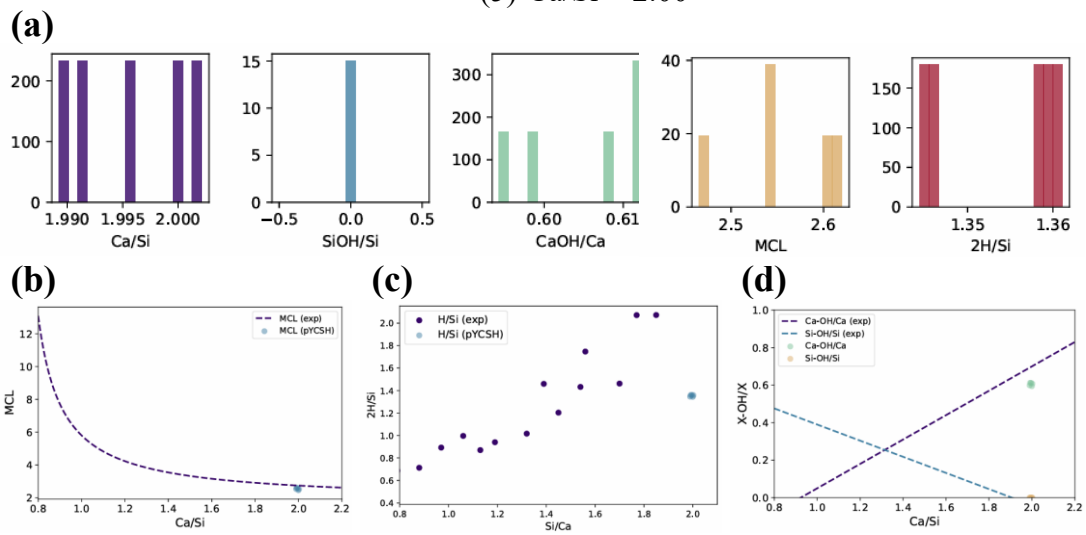

Figure A1.3. (a1-a5) Characteristic properties (Ca/Si, Si-OH/Si, Ca-OH/Ca, MCL, and 2H/Si), (b1-b5) mean chain length (MCL), (c1-c5) 2H/Si ratio, and (d1-d5) Ca-OH/Ca and Si-OH/Si ratios of bulk C-S-H for the generated structures with Ca/Si ratios between 1.2-2.0, with the comparison with experimental data from Duque-Redondo et al. (Duque-Redondo et al., 2022a).

Table A1.1. ClayFF parameters for all the species used to simulate C-S-H and NaCl solution (Cygan et al., 2004).

Species	**Charge (e)**	**D_o (kcal/mol)**	**R_o (Å)**
Interlayer Ca (cah)	1.2203	$5.0298 \cdot 10^{-6}$	6.2428
Intralayer Ca (cao)	1.3600	$5.0298 \cdot 10^{-6}$	6.2428
Tetrahedral silicon (st)	2.1000	$1.8405 \cdot 10^{-6}$	3.7064
Bridging oxygen (ob)	-1.0500	0.1554	3.5532
Non-Bridging oxygen (obos)	-1.1808	0.1554	3.5532
Hydroxyl oxygen (oh)	-0.9500	0.1554	3.5532
Hydroxyl hydrogen (ho)	0.4250	0.0000	0.0000
Water oxygen (o*)	-0.8200	0.1554	3.5532
Water hydrogen (h*)	0.4100	0.0000	0.0000
Na	1.0000	0.1301	2.6378
Cl	-1.0000	0.1001	4.9388

Density profile of Si

The density profile of Si along the z-direction, shown in Figure A1.4, provides valuable insights into the structural characteristics of the C-S-H phase with a Ca/Si ratio of 1.6. The shaded regions in the plot represent the boundaries of the C-S-H layer, which are determined based on the density profile of Si. This analysis enables a more detailed understanding of the spatial distribution and organization of the C-S-H phase within the system. The density profile of Si serves as a crucial tool for identifying the C-S-H surfaces that define the extent of the gel pore. This information is essential for further analysis and interpretation of the system's properties, such as its evolution during the evaporation process or its interactions with other components.

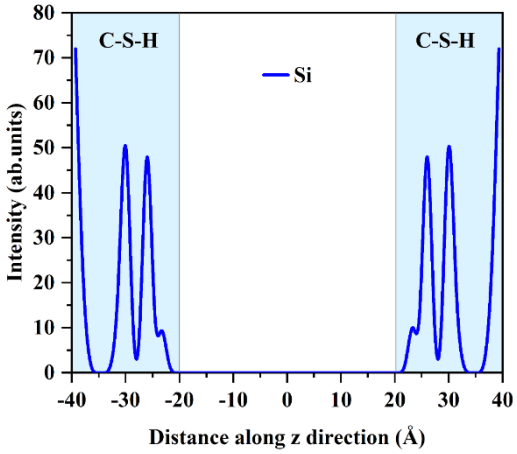

Figure A1.4. Density profiles of Si inside the C-S-H gel pore with a Ca/Si ratio of 1.6. 0 Å is assigned as the centre of the nanopore.

Density Profile of Ca ions under NVT

Figure A1.5 shows the spatial distribution of Ca^{2+} ions along the z-direction in the C-S-H nanochannel during different stages of water evaporation under the NVT ensemble. At 0 ns, the density profile's sharp peaks revealed localised regions of higher Ca^{2+} concentration near the surface. The density profiles of Ca^{2+} ions in the C-S-H gel pore maintain a high degree of consistency across the different time intervals, with only minor variations observed throughout the water evaporation process (Tang et al., 2019a). This suggests that

the spatial arrangement of the Ca^{2+} ions is not significantly disrupted by the loss of water. However, a minor change is observed at 80 ns, where the Ca^{2+} ion density profile indicates a slight increase in their proximity to the gel surface compared to the previous profiles.

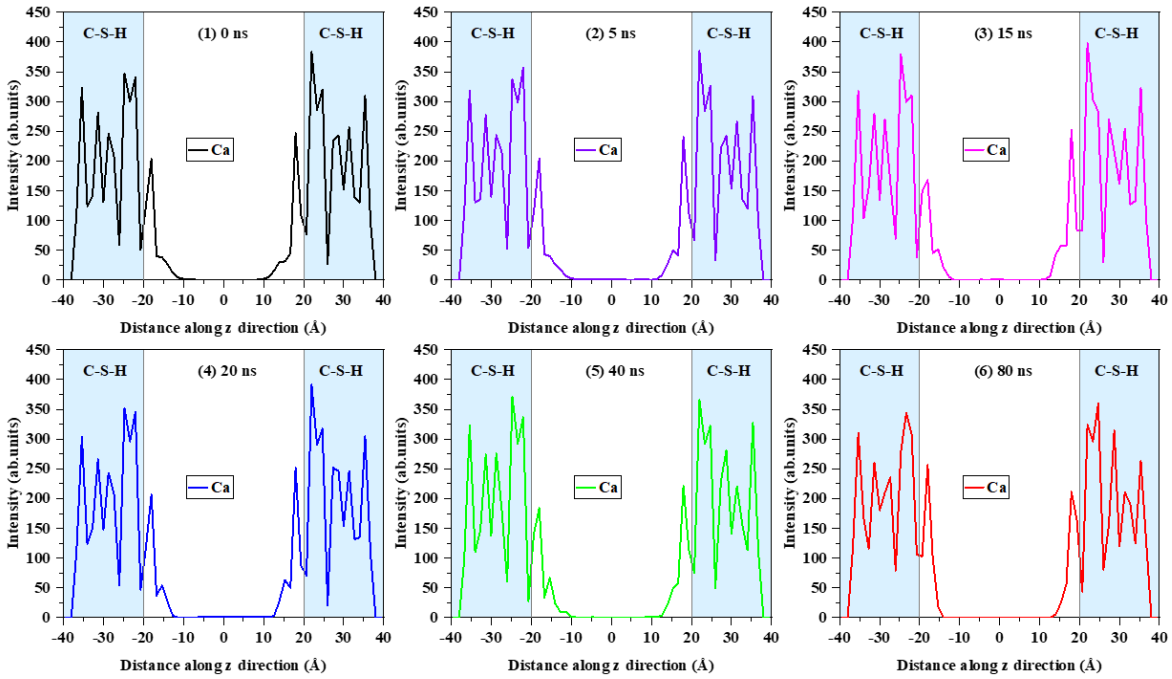

Figure A1.5. Density profiles of Ca^{2+} ions inside the C-S-H gel pore at different water content under NVT ensemble.

Figure A1.6 presents the radial distribution function (RDF) of Ca^{2+} ions with oxygen atoms from water molecules, revealing a coordination number of 0.96 during evaporation at Ca/Si = 1.6 under the NVT ensemble. The peak in the RDF indicates that water molecules are directly coordinated with surface Ca^{2+} ions, forming a stable hydration shell. Additionally, hydrogen bonding analysis shows that each water molecule forms on average 0.39 hydrogen bonds with deprotonated silanol oxygens ($Si–O^-$). This suggests that water molecules at the C-S-H surface are simultaneously coordinated to Ca^{2+} ions and form hydrogen bonds with the silicate oxygens.

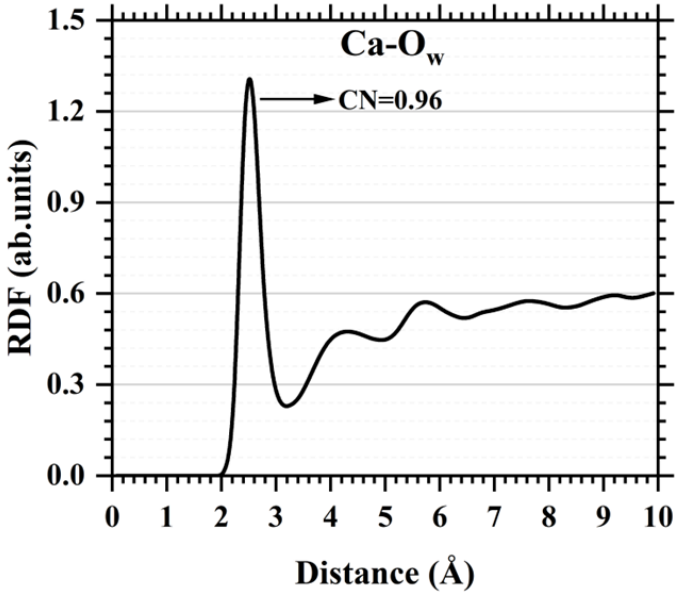

Figure A1.6. RDF of Ca^{2+} ions with oxygen atoms from water molecules in the C-S-H gel pore at a Ca/Si ratio of 1.6 under NVT ensemble during the evaporation.

Density profile of Ca under NPT

Figure A1.7 depicts the spatial distribution of Ca^{2+} ions in the C-S-H nanopore at various times (from 0 to 80 ns) during the water evaporation process under the NPT ensemble. The yellow-shaded region shows the pore shrinkage during evaporation. During the initial stages of water evaporation (5–15 ns), the Ca^{2+} ion density profiles maintain a similar shape, indicating that the distribution of Ca^{2+} ions is not significantly affected by the early phases of water evaporation. At 20 ns, the nanopore shrinkage becomes more obvious, as evidenced by the larger yellow-shaded region in the density profile, despite the overall shape of the profile remaining mostly consistent. At 40 ns, a small change in the distribution of Ca^{2+} is noticed. The Ca^{2+} ions accumulate in higher concentration along the C-S-H nanopore surfaces. At 80 ns, the density profile exhibits that the majority of Ca^{2+} ions are concentrated near the surfaces, where a limited number of water molecules are preserved, but Ca^{2+} can also be found in the centre of the pore. This indicates that when the pore shrinks and the system approaches a nearly dry condition, Ca^{2+} ions relocate within the pore and the C-S-H surfaces.

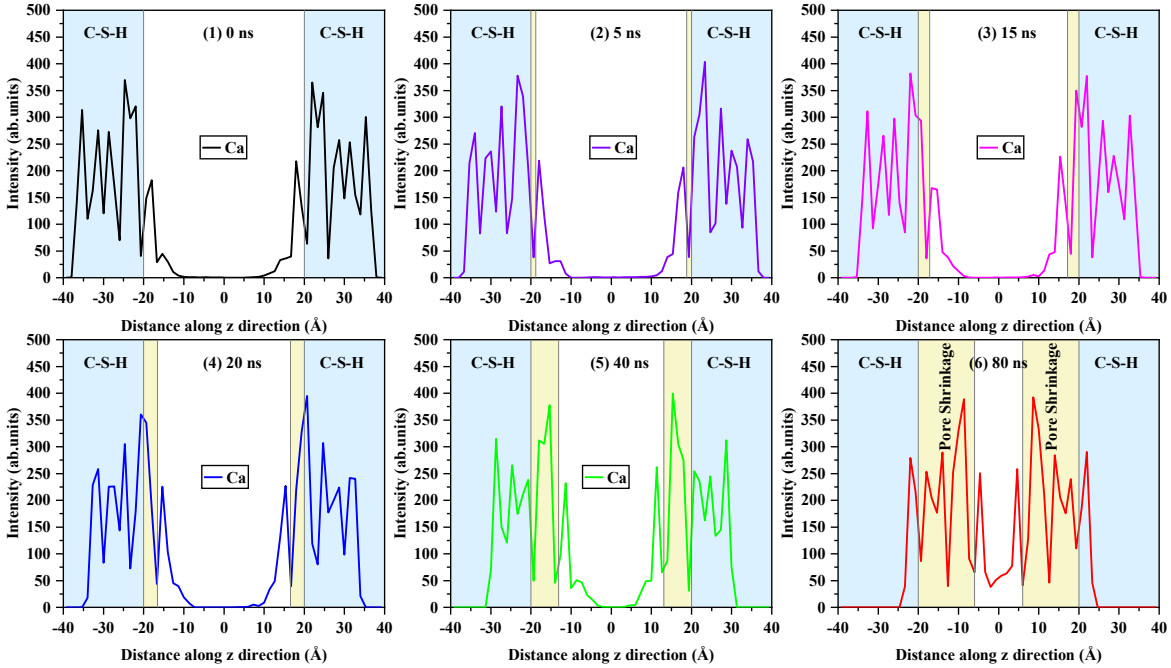

Figure A1.7. Density profiles of Ca^{2+} ions inside the C-S-H gel pore at different water content under NPT ensemble.

Density profile of Ca at different Ca/Si ratios

Figure A1.8 depicts the density profiles of Ca^{2+} ions in the C-S-H nanopores at different Ca/Si ratios during the evaporation process. At the initial stage of evaporation, the density profile shows pronounced peaks near the C-S-H surface across all ratios, indicating a high concentration of Ca^{2+} ions at the pore surface due to their strong binding interactions with the C-S-H surface (Zhou et al., 2018). Although the density profiles vary slightly with different Ca/Si ratios, the overall shape remains similar, suggesting that Ca^{2+} ions consistently remained near the surfaces irrespective of the specific ratio. As evaporation progresses, the peaks in the Ca^{2+} density profiles remain stable and substantial, indicating that Ca^{2+} ions do not significantly disperse into the centre of the nanopore, but instead remain concentrated at the surface. This stability highlights the important role Ca^{2+} ions play in maintaining the structural integrity of the C-S-H matrix during the desorption process.

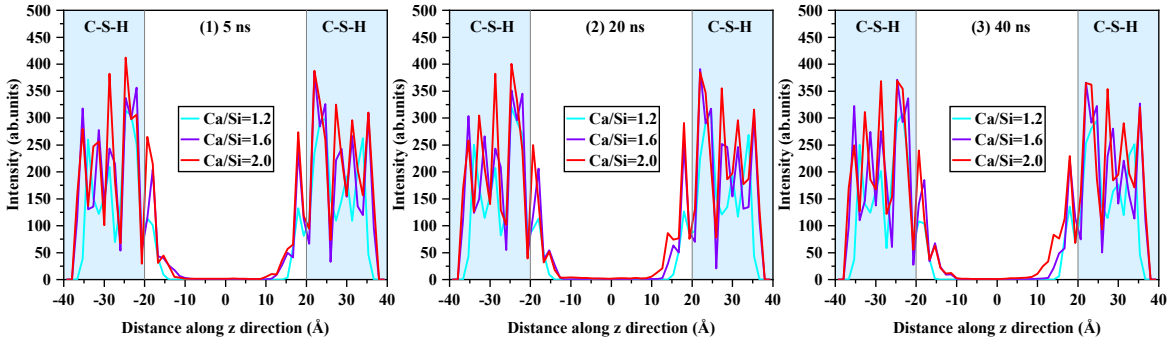

Figure A1.8. Density profiles of Ca^{2+} ions inside the C-S-H gel pore with different Ca/Si ratios at different water content under the NVT ensemble.

Density profile of water, Na^+ and Cl^- ions at different Ca/Si ratios

The density profiles of water inside the C-S-H nanopore at different Ca/Si ratios from 1.2 to 2.0 under the NPT ensemble are shown in Figure A1.9. The peaks inside the dashed line region represent the presence of other interlayer water. At the initial stage of evaporation, the density plateau is similar across all the Ca/Si ratios, indicating that the water distribution within the nanopore is not significantly affected by the compositional variations. This suggests a consistent initial hydration state irrespective of the Ca/Si ratio. As the evaporation progresses to 40 ns, a considerable shrinkage of the nanopore is observed as a result of the water loss. Interestingly, even as the evaporation continues, the density profile of water maintains a similar shape, with only minor differences observed among the various Ca/Si ratios. This observation implies that the evaporation of the aqueous solution within the C-S-H nanopore is not significantly influenced by the Ca/Si ratio.

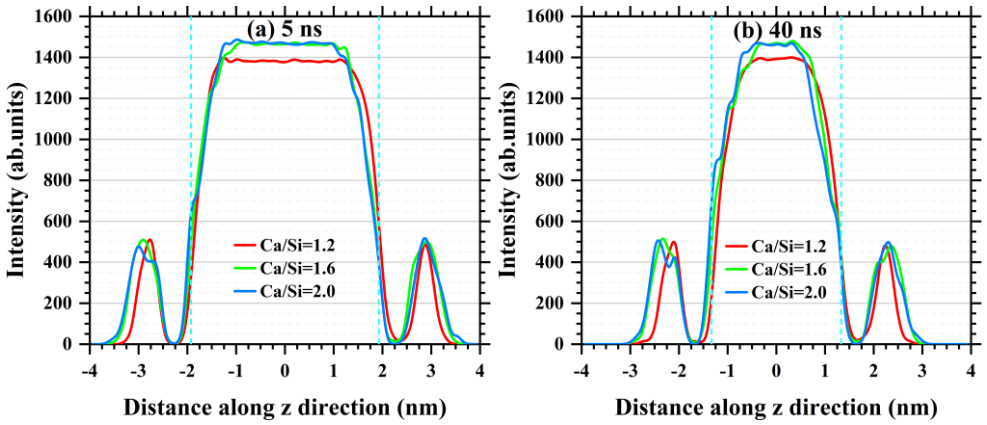

Figure A1.9. Density profiles of water within the C-S-H gel pore with different Ca/Si ratios during evaporation under the NPT ensemble at (a) 5 ns and (b) 40 ns. Dashed lines represent the C-S-H surface.

The corresponding density profiles for Na^+ and Cl^- ions are shown in Figure A1.10. At the initial stage of evaporation (5 ns), the density profile of Na^+ ions exhibits a random distribution across all the Ca/Si ratios, with a higher concentration of ions present near the surface. At lower Ca/Si ratios, when less Ca^{2+} is present, there are more Na^+ ions near the surfaces due to lower repulsive interactions between Na^+ and Ca^{2+} ions. For Cl^- ions, the density profiles at the initial stage of evaporation exhibit a distinct pattern depending on the Ca/Si ratio, see Figure A1.9 (b). For Ca/Si ratios of 1.6 and 2.0, the Cl^- ions are almost exclusively adsorbed near the C-S-H surface. This indicates strong electrostatic interactions between Cl^- ions and the increased concentration of Ca^{2+} ions on the surface at higher Ca/Si ratios. In contrast, for the lower Ca/Si ratios, as 1.2, a noticeable number of Cl^- ions are present in the central region of the nanopore. This behaviour can be attributed to the reduced availability of Ca^{2+} ions at lower Ca/Si ratios, which weakens the electrostatic attraction between Ca^{2+} and Cl^-. As a result, Cl^- ions experience less binding to the surface and exhibit a more dispersed distribution within the pore. As the evaporation progresses (40ns), the density profiles of both Na^+ and Cl^- ions show a trend towards increased adsorption near the surface, suggesting that the loss of water during the evaporation process leads to a reorganisation of the ionic species, with the ions becoming

more strongly associated with the surface regions of the C-S-H, although the rearrangement of Na^+ and Cl^- ions during the evaporation process does not appear to be significantly influenced by the Ca/Si ratio. This indicates that the ionic behaviour is primarily driven by the loss of water and the resulting changes in the local environment, rather than being strongly dependent on the specific Ca/Si composition of the C-S-H phase.

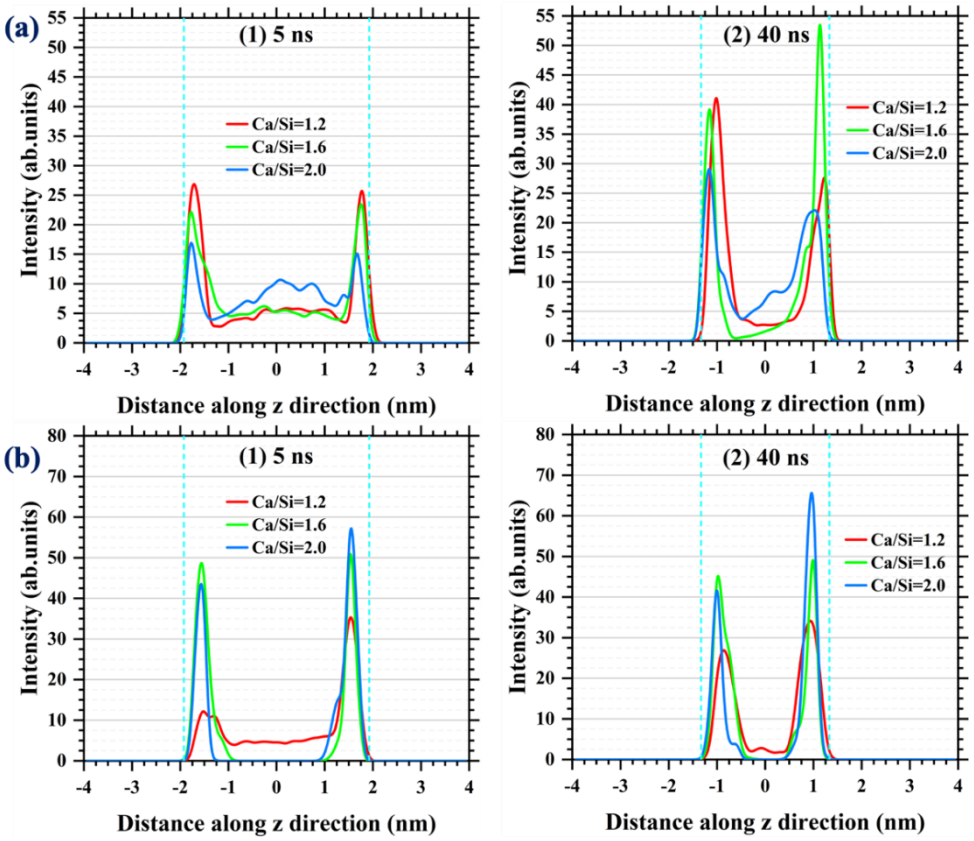

Figure A1.10. Density profiles of (a) Na^+ and (b) Cl^- ions within the C-S-H gel pore with different Ca/Si ratios during evaporation under NPT ensemble. (Note: Dashed lines represent the C-S-H surface).

Diffusion coefficients and surface charge density.

To evaluate the impact of the C-S-H surface on ion mobility, the diffusion coefficients of Cl^- ions were calculated for three representative Ca/Si ratios (1.2, 1.6, and 2.0) using the TRAVIS based on the analysis of mean squared displacement (MSD) under NVT conditions. The results are presented in Figure A1.11. A clear decreasing trend in Cl^-

diffusivity is observed with increasing Ca/Si ratio: from $2.998 \cdot 10^{-11}$ m^2/s at Ca/Si = 1.2 to $0.1 \cdot 10^{-11}$ m^2/s at 1.6 and 2.0, respectively.

This behaviour is correlated with the density of exposed Ca^{2+} ions at the nanopore surface, used here as a proxy for the effective surface charge. For each system, the number of Ca^{2+} ions located at the inner surface of the pore was divided by the accessible surface area to estimate this density. Values of 5.38, 8.78, and 10.93 Ca^{2+}/nm^2 were obtained for Ca/Si = 1.2, 1.6, and 2.0, respectively. The net electrostatic charge of each system is calculated, and the values are -2.12 e/nm^2, +5.81 e/nm^2, and +11.73 e/nm^2 for Ca/Si ratio of 1.2, 1.6, and 2.0, respectively, it reflects the increasing positive character of the surface with higher Ca/Si. The inverse correlation between this Ca^{2+} density and the Cl^- diffusion coefficients supports the idea that stronger electrostatic attraction to the C-S-H surface hinders Cl^- mobility at high Ca/Si.

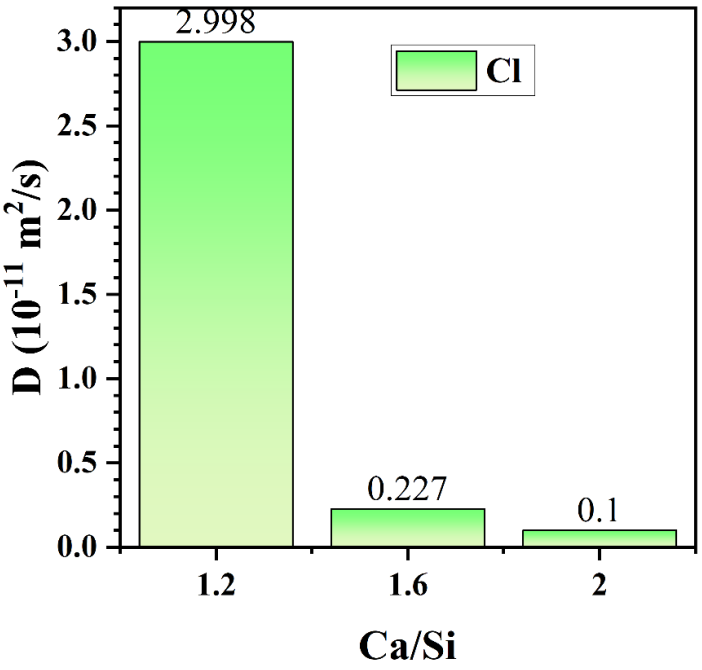

Figure A1.11. Diffusion coefficient of Cl^- ions within the C-S-H nanopore at different Ca/Si ratios (1.2, 1.6, and 2.0) during the evaporation process.

Appendix 2

Methods

Figure A2.1 depicts the stress-strain curves of a pure C-S-H system under shear deformation in the xz-direction without partial substitution of sweater ions, evaluated at various strain rates. The results show that using strain rates higher than 10^{-8} fs^{-1} leads to an overestimation of stress, as molecules do not have enough time to relax during deformation. Based on these observations, a strain rate of 10^{-8} fs^{-1} was employed in this study for both shear and tensile deformations.

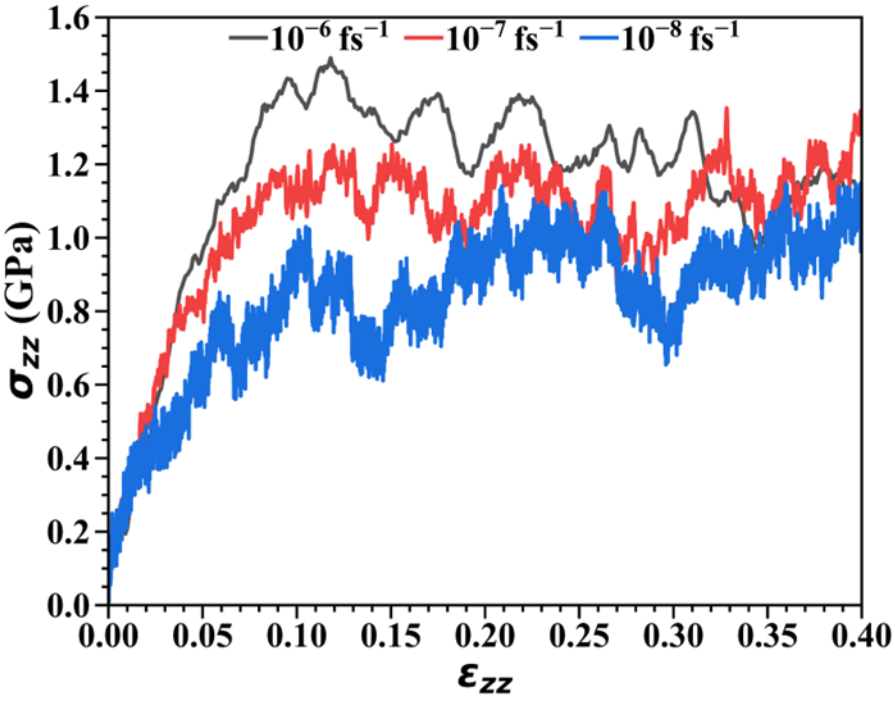

Figure A2.1. Stress-strain curves under shear deformation in the xz direction at different strain rates.

Table A2.1 shows the exact number of Na^+, K^+, and Mg^{2+} ions added, along with the corresponding Ca^{2+} ions removed, to ensure full reproducibility of the simulations for all the cases. Interlayer Ca^{2+} ions were partially removed, and cations were added as shown below in the table.

Table A2.1. Amount of interlayer Ca^{2+} replaced by seawater cations for all the investigated cases.

Model name	Cation/Si	Removed interlayer Ca	Cations added	Remaining interlayer Ca	Ca/Si (After)
CSH	-	-	-	403	1.60
CSH_Mg	0.1	54	54	349	1.49
	0.3	162	162	241	1.28
CSH_Na	0.1	27	54	376	1.54
	0.3	81	162	322	1.43
CSH_K	0.1	27	54	376	1.54
	0.3	81	162	322	1.43

Results

Figure A2.2 shows the shear strength as a function of the additional interfacial distance for the systems with and without partial replacement by seawater ions with a cation/Si ratio of 0.1. For all cases, shear strength decreases sharply as the interfacial distance increases. The overall shear strength performance order is as follows: CSH $\approx$ CSH_Mg > CSH_Na > CSH_K.

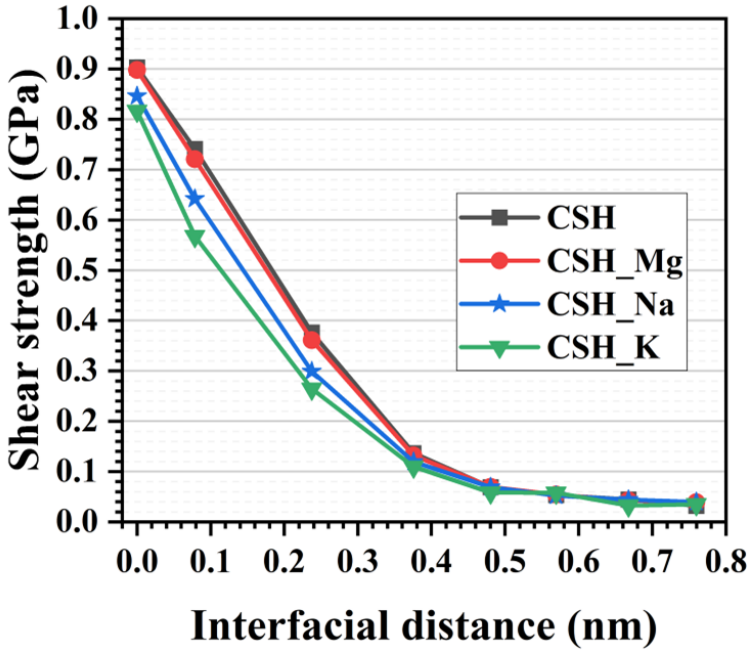

Figure A2.2. Shear strength as a function of the additional interfacial distance for C-S-H with and without seawater ions with cation/Si = 0.1.

H Bond network

Figure A2.3 presents a linear Sankey diagram illustrating the hydrogen bond network between donors (left) and acceptors (right) for all systems with an interfacial expansion of 0.48 nm. The values shown in the Figure represent the average number of hydrogen bonds for each donor/acceptor. The average hydrogen bond count decreases in the order: CSH > CSH_Mg > CSH_Na > CSH_K, which correlates directly with their respective shear strength.

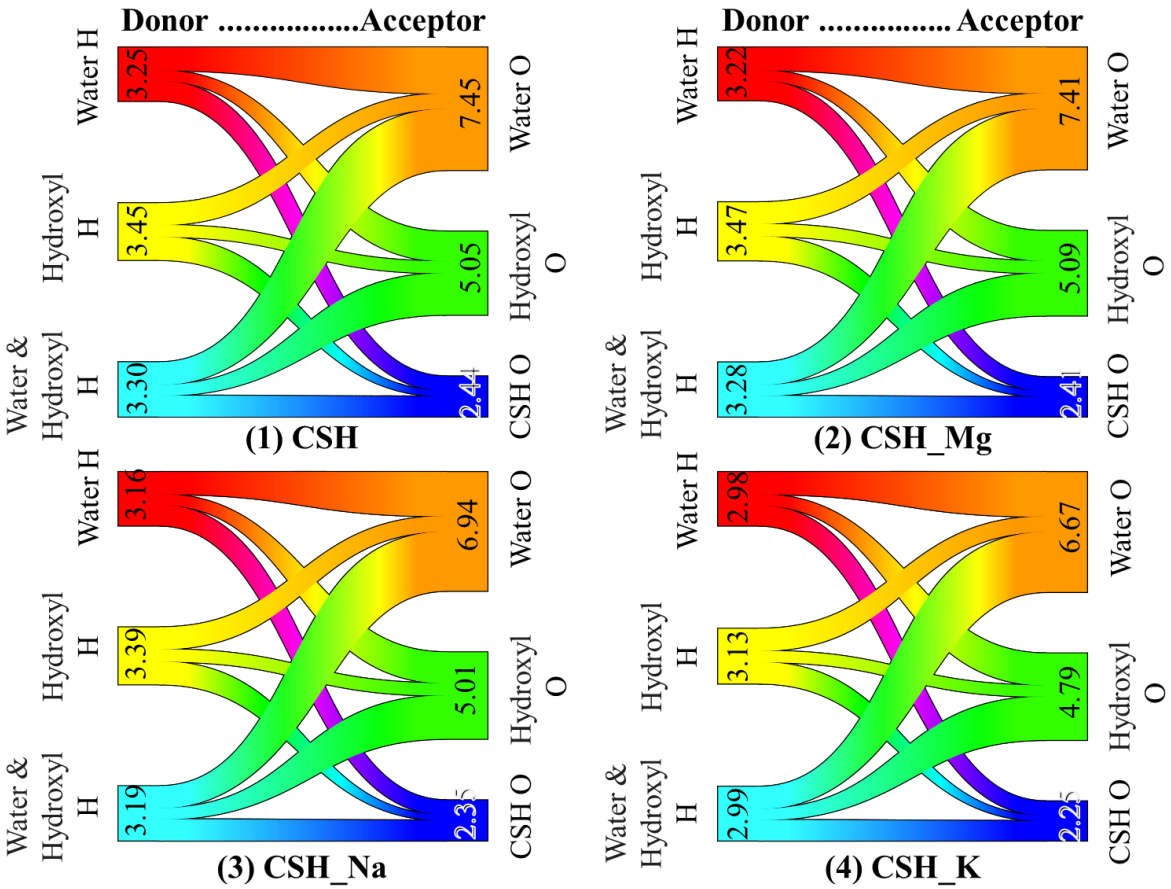

Figure A2.3. Linear Sankey diagram illustrating the hydrogen bonding topology of interlayer species at an interfacial expansion of 0.48 nm. Numbers indicate the average number of hydrogen bonds per donor/acceptor.

Density profiles

Figure A2.4 shows the density profiles of cations (Mg^{2+}, Na^{+}, and K^{+}) and their corresponding interlayer Ca^{2+} for each system at different interfacial distances. At small interfacial expansions (0.08 nm), Mg^{2+} ions are located in the same areas as interlayer Ca^{2+} ions, indicating strong adsorption near the silicate surfaces. In contrast, Na^{+} and K^{+} ions are more uniformly distributed throughout the interlayer space. Or higher interlayer expansions (0.48 nm), Mg^{2+} ions remain closely associated with the position of interlayer Ca^{2+}, and Na^{+} and K^{+} exhibit similar behaviour.

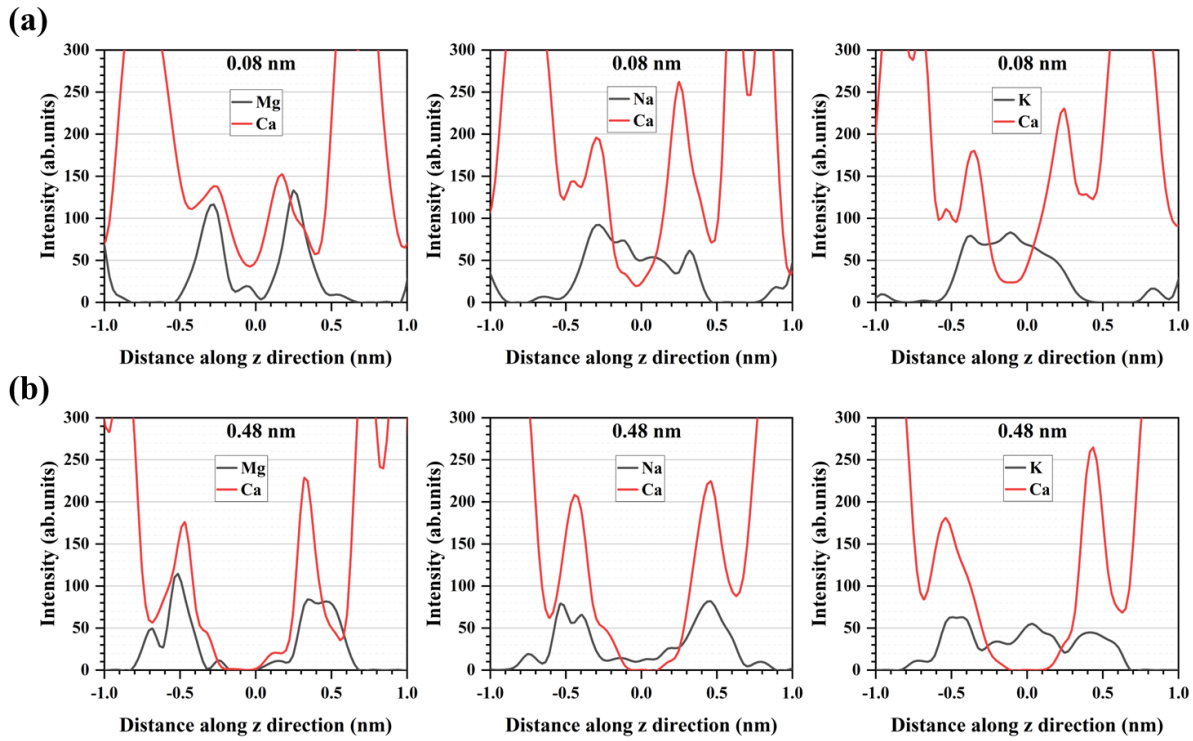

Figure A2.4. Density profiles of seawater cation and the corresponding interlayer Ca^{2+} at interfacial expansions of (a) 0.08 nm and (b) 0.48 nm.

Mechanism under tensile loading

Figure A2.5 depicts snapshots of the structural configurations of the CSH and CSH_K systems under tensile deformation with an average strain of 0.15. These images, taken during tensile testing, show additional interfacial expansions of 0 (perfect contact), 0.08, and 0.48 nm, demonstrating how the structure changes as it deforms under tensile strain. As tensile strain increases, small cavities emerge in the interlayer space, corresponding to the peak of the stress-strain curve. With further strain, the stress decreases, but residual stress remains due to the presence of an electrolyte bridge connecting the two surfaces. When this electrolyte bridge breaks, the stress drops to zero, indicating complete tensile failure. The interlayer space is consistently identified as the primary location where tensile failure occurs and propagates. At the interfacial expansion of 0 nm, both CSH and CSH_K systems do not separate and remain intact at the strain of 0.15. However, when the

additional interfacial expansion is increased to 0.08 nm and 0.48 nm, separation of the two layers occurs upon reaching a strain of 0.15. This behaviour indicates that tensile strength decreases as the interfacial expansion increases, as the weakened interlayer cohesion leads to earlier failure.

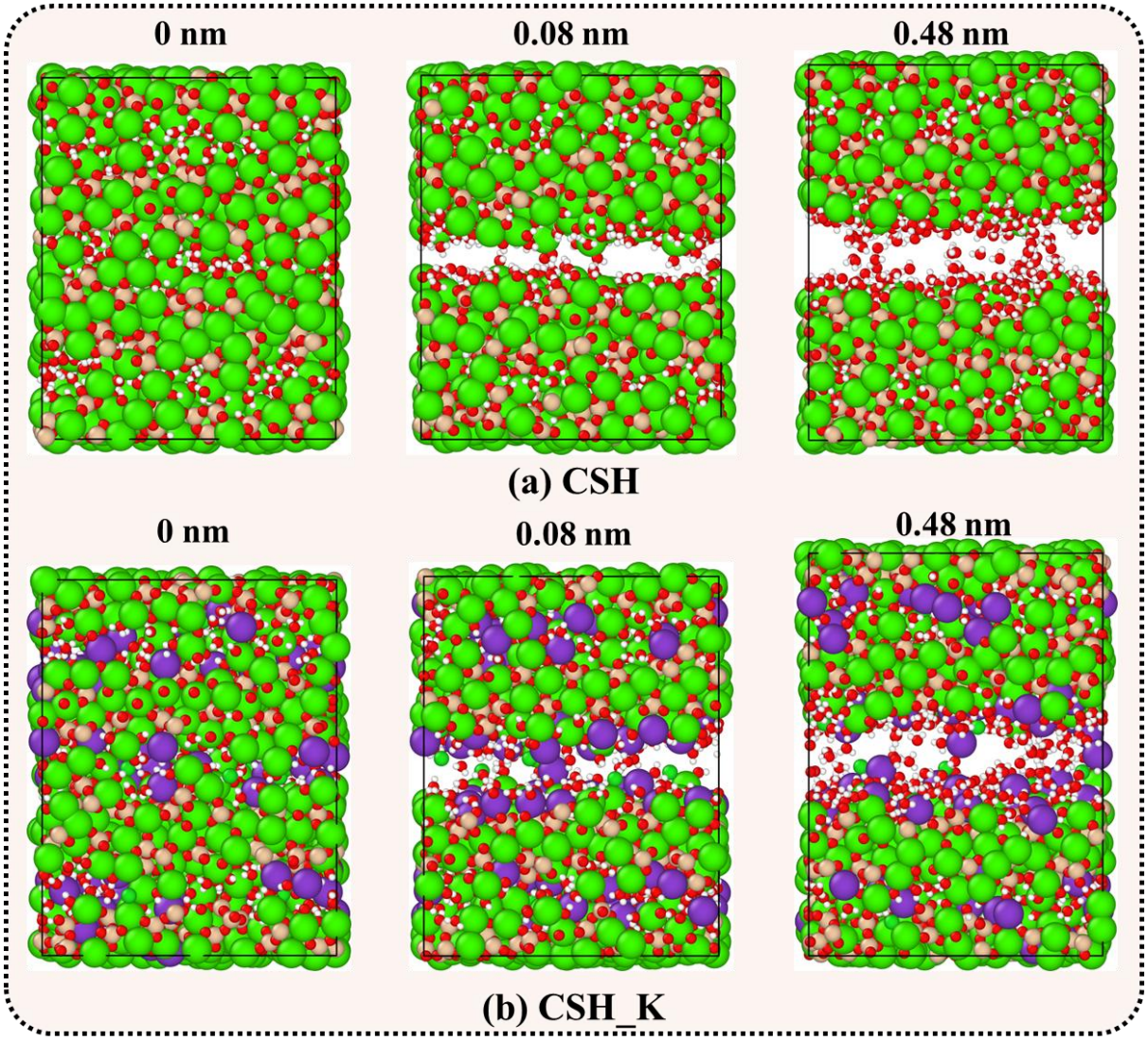

Figure A2.5. Snapshot of the configurations of (a) pure C-S-H and (b) CSH_K, at an average strain of 0.15 for additional interfacial expansions of 0 nm, 0.08 nm, and 0.48 nm. K^+ and Ca^{2+} ions are shown as purple and green balls, respectively; O, H, and Si atoms are represented as red, white, and light brown balls.